The University of Sheffield

Characterisation and Nanophotonic Device Integration of Droplet Epitaxy Quantum Dots Emitting in the Telecom C-Band

Max Robert Godsland

Submitted in partial fulfilment of the requirements
for the degree of Doctor Of Philosophy

Department of Electronic and Electrical Engineering
The University of Sheffield

October, 2022

Abstract

Quantum dots are well established as a source of single photons for applications in quantum cryptography. Having their emission in the telecommunication C-band (1530-1565 nm) is a desirable property as it allows for compatibility with existing low-loss fibre infrastructure. InAs/InP quantum dots grown by droplet epitaxy using metal organic vapour-phase epitaxy are the basis of the work presented in this thesis. Optical characterisation shows the quantum dots to emit in the C-band with narrow linewidths. Further growth development of quantum dots through capping layer engineering, which blue shifts emission wavelengths to the telecommunication O-band, and growth on InGaAs and InGaAsP interlayers, producing high density quantum dots, is presented with the results demonstrating a versatile growth method. Further characterisation of the quantum dots on distributed Bragg reflectors explicitly reveals the presence of undesirable background emission, the origin of which is explored.

It is desirable to have high repetition rates for single photon sources which can be achieved with Purcell enhancement of quantum dot emission. A fabrication process for photonic crystal cavities in the InP material system is established which produces high Q factor emission with the aim to achieve enhanced quantum dot emission. Further fabrication development is presented which successfully integrates high density quantum dots on an InGaAsP interlayer in the photonic crystal cavities resulting in candidate quantum dots for Purcell enhancement in the telecommunication C-band.

Acknowledgements

First of all I would like to thank my supervisor, Jon Heffernan, for extremely helpful guidance and encouragement over this project. Also to Luke Wilson, Mark Fox and Maurice Skolnick.

I have been very fortunate to work with many talented and wonderful people over this last four years- standing (in my case barely standing and more of a decrepit lean) on the shoulders of giants and all that. A huge thank you to Elisa Sala for growing all the samples that I have studied in this thesis, none of this would have been possible without your work. Aristotelis Trapalis for training me on the micro-PL setup and always offering helpful advice and support. Nasser Babazadeh for training me in the dark arts of device fabrication and endless knowledge on all things fabrication related. René Dost for EBL and assistance with photonic crystal fabrication, also to Tommi Isoniemi for going to York and doing the EBL for the final sample. A huge thanks to Catherine Phillips for a great collaboration on the InP photonic crystals and for doing the final measurements and also to Andrew Foster. To Paul Haines and the technicians for keeping the cleanroom functioning and enabling a large amount of this work to go ahead and to Ian Farrer for being a font of knowledge on all things and a great source of advice throughout the years

Also a thank you to my fellow PhD students/Post Docs with whom I've had the pleasure of either sharing an office, a lab or lunchtimes with. Charlotte Ovendon, Henry Francis, Yunran Wang, Si Chen, Matthew Fenton-Jones, Henry Chan, Paige Baldwin-McDonald, Young In Na and Matthew Carr.

Thank you to my parents, Maggie and Ian, for your endless love, support and belief throughout these years. I dedicate this thesis to you. Also to the rest of my family, Holly, Amber, Chris and Kat for all your encouragement and support. And of course, little Effie, the real hero behind all of this.

And finally to Rosie, it's hard to sum up my gratitude to you but I'll try. How fortunate I am to be with you and receive your constant love and support. Without you I really would have given up on this many times over. Thank you for helping me see the wood for the trees and for being your amazing, kind and funny self.

How To Handle Imposter Syndrome, Part Two.

You have found a solution- which may be temporary, it may be permanent, you don't know, but you will try it out. It is this: to tell yourself every morning:

Imagine what you would do if you were confident, and then do it.

It is an excellent way to trick yourself into productivity. You contact a company to ask if they would like to work with you, you write to a producer and ask for a beat, you ask someone on a date. The company is keen, the producer politely declines, and the potential date says yes. But most importantly, you asked- you gave yourself a chance. You return home one evening and you see the signs on your hallway mirror, your kitchen wall. You have a lot to offer, they say. You can do it, they say. Yes I do, you think, and yes I can.

Musa Okwonga

In The End, It Was All About Love.

Publications

Sala, E.M., Na, Y.I., **Godsland, M.**, Trapalis, A. and Heffernan, J., 2020. InAs/InP quantum dots in etched pits by droplet epitaxy in metalorganic vapor phase epitaxy. physica status solidi (RRL)–Rapid Research Letters, 14(8), p.2000173.

Sala, E.M., **Godsland, M.**, Trapalis, A. and Heffernan, J., 2021. Effect of Cap Thickness on InAs/InP Quantum Dots Grown by Droplet Epitaxy in Metal–Organic Vapor Phase Epitaxy. physica status solidi (RRL)–Rapid Research Letters, 15(9), p.2100283.

Sala, E.M., **Godsland, M.**, Na, Y.I., Trapalis, A. and Heffernan, J., 2021. Droplet epitaxy of InAs/InP quantum dots via MOVPE by using an InGaAs interlayer. Nanotechnology, 33(6), p.065601.

Abbreviations

AFM	Atomic Force Microscopy
CPD	Critical Point Drying
DBR	Distributed Bragg Reflector
DE	Droplet Epitaxy
EBL	Electron Beam Lithography
EDX	Energy-Dispersive X-ray
FDTD	Finite Difference Time Domain
FSS	Fine Structure Splitting
ICP	Inductively Coupled Plasma
MBE	Molecular Beam Epitaxy
MOVPE	Metal Organic Vapour Phase Epitaxy
NIR	Near Infrared
PECVD	Plasma Enhanced Chemical Vapour Deposition
PBG	Photonic Band Gap
PhC	Photonic Crystal
PhCC	Photonic Crystal Cavity
QC	Quantum Cryptography
QD	Quantum Dot
QKD	Quantum Key Distribution
QCSE	Quantum Confined Stark Effect
QRE	Quasi Resonant Excitation
RE	Resonant Excitation
RIE	Reactive Ion Etch
SEM	Scanning Electron Microscopy
SK	Quantum Key Distribution
TEM	Transmission Electron Microscopy
X-STM	Cross-Sectional Scanning Tunnelling Microscopy

Contents

1 Introduction **1**

1.1 Quantum 1.0 and 2.0 1

1.1.1 Quantum Computing 3

1.1.2 Quantum Cryptography 4

1.2 Quantum Dots and the Telecommunication C-Band 4

1.3 Outline and Scope 6

2 Background **9**

2.1 Semiconductor Quantum Dots and Single Photons 9

2.1.1 Quantum Dots as Single Photon Emitters 12

2.1.2 Electronic Substructure and Fine Structure 13

2.1.3 Excitation Techniques 15

2.1.4 Tuning Quantum Dot Emission Wavelength 17

2.2 Quantum Dot Growth Techniques and Emission in the C-band 18

2.3 Light Confinement at the Nanoscale 22

2.3.1 One Dimensional Photonic Crystals 23

2.3.2 Two Dimensional Photonic Crystals 25

2.3.3 Weak Coupling and the Purcell Effect 27

2.4 Summary 31

3 Methods **33**

3.1 Quantum Dot Growth 33

3.2 Sample Cooling for Optical Measurements 35

3.3 Optical Characterisation Of Quantum Dots 37
3.3.1 Microphotoluminescence with the Flow Cryostat 37
3.3.2 Microphotoluminescence with the Bath Cryostat 40
3.4 Device Design with Finite Difference Time Domain Methods 42
3.5 Photonic Crystal Device Fabrication 43
3.6 Sample Inspection 47
3.6.1 Scanning Electron Microscopy 47
3.6.2 Energy-Dispersive X-ray Spectroscopy 48
3.6.3 Cross-sectional scanning tunnelling microscopy 49

4 Characterisation of Quantum Dots 51

4.1 InAs/InP Quantum Dots 52
4.1.1 Crystallisation Temperature 53
4.1.2 Varying Cap Thickness 57
4.2 QDs grown on Interlayers 60
4.2.1 InGaAs Interlayer 61
4.2.2 InGaAsP Interlayer 66
4.3 Quantum Dots on DBRs 67
4.4 The Background Emission Problem 71
4.4.1 Presence of the Background Emission 71
4.4.2 Investigations into the Origin of the Background Emission 75
4.5 Summary 80

5 Establishing InP Photonic Crystals 83

5.1 Design of InP-Based Photonic Crystal Cavities in Lumerical 84
5.1.1 H1 Cavity Simulations 85
5.1.2 L3 Cavities 90
5.2 Fabrication of Photonic Crystal Cavities 91
5.2.1 Sample 91
5.2.2 Hard Mask Patterning 92

5.2.3 InP Etch 97

5.2.4 Sacrificial Layer Removal 99

5.3 Optical Characterisation of Photonic Crystal Cavities 101

5.4 Summary 106

6 High Density Quantums Dots in Photonic Crystal Cavities 109

6.1 InAs/InGaAs/InP QDs for Devices 110

6.1.1 Fabrication and Characterisation 111

6.2 Optimisation of High Density QDs in Devices 117

6.2.1 Ferric Chloride Wet Etch Tests 119

6.3 New Sample Structure and Fabrication 123

6.3.1 Wafer Characterisation 123

6.3.2 Unintentional Layer Problem 124

6.4 Micro-PL of Fabricated Structures 127

6.4.1 PhCC Micro-PL 130

6.5 Initial Candidates for Purcell Enhancement 136

6.5.1 First Device 136

6.5.2 Third Device 142

6.6 Initial Investigations into Electrical Tuning 148

6.7 Summary 151

7 Summary and Outlook 155

7.1 Summary 155

7.2 Outlook 157

7.2.1 The Background Emission Problem 157

7.2.2 Improving the Number of QD Lines in Photonic Crystals 158

7.2.3 Further Measurements of Photonic Crystal Cavities 159

7.2.4 Deterministic Device Fabrication 159

A Appendix 161

A.1 Optical Setups 161

A.1.1 Flow Cryostat System 161

A.1.2 Bath Cryostat System 162

Bibliography **162**

Chapter 1

Introduction

1.1 Quantum 1.0 and 2.0

The field of Quantum physics originated from Max Planck's law of blackbody radiation in which he described the radiation spectrum of a black body with electrically charged oscillators that could only change energy by a discrete amount [1]. This quantisation of energy was simply a mathematical trick for Planck but in reality he had started the great scientific revolution of the twentieth century [2].

Albert Einstein built upon Planck's work to explain the photoelectric effect by considering light to exist as discrete packets of energy known as photons. What followed was the establishment of the theory of quantum mechanics by Erwin Schrödinger, Paul Dirac, Werner Heisenberg and Wolfgang Pauli, amongst other physicists. Quantum mechanics is used to describe the behaviour of atoms and subatomic particles and resulted in better understanding and controlling of the behaviour of particles at the microscopic level. This advancement in our understanding of physics ultimately led to the development of semiconductor materials and semiconductor devices, which have come to define much of our modern lives through the technological innovations they have enabled. These technological advancements include the advent of computers, telecommunications, lasers, light emitting diodes (LEDs), medical imaging and much more. These technologies have enabled the information age and have been labelled as "Quantum 1.0" [3].

Further scientific advances have led us to a position where we can start to exploit some of the fundamental phenomena of quantum mechanics: super position and entanglement. The exploitation of these phenomena can lead to advances in computation, security and sensing. These new technologies, which have been dubbed as "Quantum 2.0", include quantum computing, quantum cryptography, and quantum telecommunications. Superposition and entanglement are two fundamental properties of particles in quantum mechanics. The quantum mechanical description of a particle's state is a superposition of the possible values of this state. How long a particle stays in its quantum state is described by its coherence time.

For example, the polarisation of a photon (in the horizontal and vertical basis) is both horizontal and vertical until the photon polarisation is measured. This is mathematically described with the wave function as,

$$|\psi\rangle = \frac{\alpha |H\rangle + \beta |V\rangle}{\sqrt{2}} \tag{1.1}$$

.

Where α and β can be any complex number and fulfill the condition $|\alpha|^2 + |\beta|^2 = 1$. $|\alpha|^2$ and $|\beta|^2$ are the probability amplitudes for the photon being in state $|H\rangle$ and $|V\rangle$, respectively. Upon measurement of the photon's polarisation, the wave function collapses and the photon is now in one of the possible states. This is true for all manner of quantum states including electron spins, nuclear spins and the path taken by a photon through a beam splitter. A result of this behaviour is that measuring a system fundamentally changes its state.

The principle of superposition extends beyond single particles with quantum entanglement, where two or more particles can share a quantum state. Using the example of photon polarisation again, two polarisation entangled photons (where in this example they must have the same polarisation) have the wave function,

$$|\psi\rangle = \frac{\alpha |HH\rangle + \beta |VV\rangle}{\sqrt{2}} \tag{1.2}$$

. Where the shared state is a superposition of the two possible states of the individual photons.

Measuring the polarisation of one of the photons projects the other into a state as described by the wave function. In this example, measuring a polarisation of $|H\rangle$ for one of the photons projects the other into the $|H\rangle$ state and the wave function of the entangled state collapses. This correlation remains true regardless of the distance in time or space between the particles.

1.1.1 Quantum Computing

The concepts of superposition and entanglement are a fundamental aspect of quantum computing. In 1982 Richard Feynman famously set out the idea of a computer able to solve complex mathematical problems that a classical computer could not solve [4]. A classical computer uses bits to represent information whereas quantum computation uses quantum bits (qubits). Bits either exist as 0 or 1 whereas qubits exist as a superposition of 0 and 1. As for the wave function describing the quantum state of a particle, we have the same for a qubit,

$$|\psi\rangle = \frac{\alpha|0\rangle + \beta|1\rangle}{\sqrt{2}} \tag{1.3}$$

.If we have two entangled qubits, qubit A and qubit B, the state is written as,

$$\psi = \alpha|0_A 0_B\rangle + \beta|0_A 1_B\rangle + \gamma|1_A 0_B\rangle + \delta|1_A 1_B\rangle \tag{1.4}$$

.

For the case of two qubits there are four possible states available for computational tasks. It can be seen that increasing the number of qubits exponentially increases the number of usable states as 2^N, where N is the number of qubits. In contrast, bits used in classical computers scale linearly. Though real life quantum computers are still in their relative infancy, such a device has great potential for solving computational tasks exponentially faster than classical computing.

Peter Shor demonstrated the theoretical advantage of a quantum computer over a classical computer in 1994. Using Shor's algorithm, the factoring of large numbers into their constituent primes is exponentially faster than by classical computation [5]. The importance of this demonstration lies in the fact that the RSA algorithm, which is the basis for much of the encryption used today, relies

on the use of large numbers which are computationally difficult to factorise into prime numbers [6].

As a result, a quantum computer has the potential to make current encryption methods easily countered by Shor's algorithm and as such, new security protocols will be required once these technologies become commonplace.

1.1.2 Quantum Cryptography

Quantum cryptography (QC) is another field that falls under the umbrella of Quantum 2.0. Using the fundamental characteristics of quantum mechanics, it offers truly secure communications which are not susceptible to the threat of a quantum computer as RSA-based encryption methods are. QC offers true security based on the fundamental principle of quantum mechanics that a measurement of a system changes the state of the system.

The convention for describing QC uses information exchange from Alice to Bob with an eavesdropper, Eve. Alice and Bob can share information by encoding it in individual photons. If Eve were to steal the information through a measurement, then Bob would receive photons that were perturbed. If Bob were to receive unperturbed photons, then it would be clear that no eavesdropping had taken place.

Clearly this isn't fully secure communication as eavesdropping is only confirmed after the information is transferred. However, these principles are used in quantum key distribution (QKD) to achieve the goal of full security. QKD is based on keys being shared over a quantum channel using photons and such keys being used to encrypt and decrypt information sent over a classical channel. Should Eve able to successfully steal a key, this will be known to Alice and Bob and they can disregard the key. Eve will not have gained any of the information sent over the classical channel because her stolen key will be useless. It is on this premise that QKD offers truly secure data transfer [7].

1.2 Quantum Dots and the Telecommunication C-Band

Semiconductor quantum dots can act as the single photon source (SPS) for QKD applications [8, 9, 10, 11]. They have been shown to possess highly coherent [12] and pure [13] single photon

emission. Furthermore, QDs exist in a semiconductor matrix which means well-established processing techniques can be applied in order to build emission-enhancing structures around the QDs and photonic integrated circuits on-chip [14].

QD growth in the GaAs-based material system has been well established over the last few decades with such QDs emitting around 900 nm in the near infrared (NIR) [15, 16, 17]. More recently, there has been an increase in attention on QDs emitting in the telecom C-band. This wavelength region is of interest due to the low losses (∼0.2 dB/km) compared to 900 nm (∼1 dB/km) in the optical fibres used globally for telecommunications.

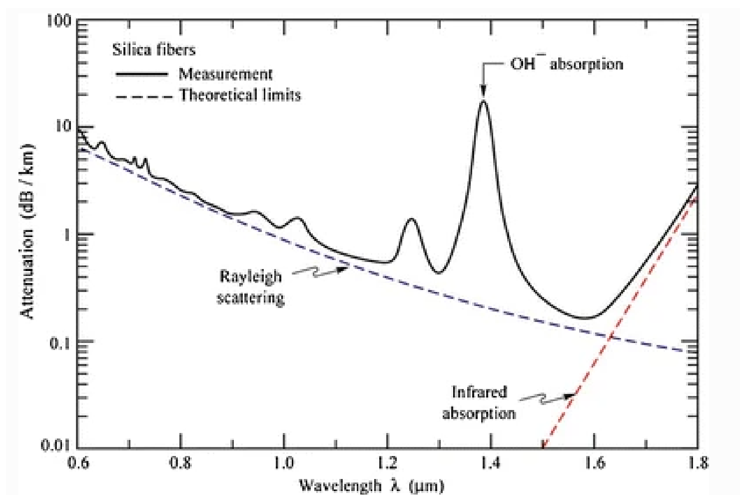

Figure 1.1: *Attenuation in Silica optical fibres for various wavelengths of light. The lowest losses 0.2 dB/km are for wavelengths of 1530 nm to 1560 nm. Reprinted with permission from [18].*

The low losses at this wavelength has meant it has been possible to demonstrate QKD over a distance of 120 km using C-band emitting QDs [19]. Furthermore, QKD can also be implemented from ground to earth orbiting satellites [20]. Again, the telecom C-band is advantageous over ∼900 nm due to the low daytime noise levels from the sun at these wavelengths [21].

This thesis characterises the growth of InAs/InP QDs emitting around the telecom C-band using optical spectroscopy. The QDs are grown by droplet epitaxy (DE) using metal organic vapour phase epitaxy (MOVPE) which is the favoured industry tool for mass production of optical semiconductor devices. Device design and fabrication techniques are then developed in order to produce photonic crystal cavities (PhCCs) which can enhance the emission from the QDs.

1.3 Outline and Scope

This thesis consists of seven chapters, this first chapter has introduced the reader to the concepts of quantum computing and quantum cryptography as the context for the motivation of this work. Chapter 2 gives a background overview to epitaxial QDs and their emission properties. Also included in this chapter is a review of relevant work published on QDs emitting in the telecom C-band with light confinement using nanophotonics also introduced.

Chapter 3 gives an overview of the experimental methods used in this thesis. These include the QD growth method and optical characterisation setups, device design using finite difference time domain methods and the subsequent device fabrication. Finally, sample inspection methods using electron beam methods are also introduced.

Chapter 4 covers the optical characterisation of various QD growths and the assessment of a background emission problem associated with these QDs. Chapter 5 details the device design, fabrication method and characterisation of photonic crystal cavities. Chapter 6 builds on the work of chapter 5 by outlining the integration of high density QDs in the photonic crystal devices. Candidates for QDs enhanced by the cavities are then presented.

Finally, the work presented in this thesis will be summarised followed by an outline of directions for future work.

The following outlines what work in this thesis was performed by the author and what work was performed by collaborators.

In chapter 4 all micro-PL measurements and related analysis was performed by the author. The sample growth was performed by Dr Elisa Sala, AFM measurements were performed by Dr Young In Na and EDX measurements were performed by Raja Sekhar Gajjela at Eindhoven University of Technology.

In chapter 5 the FDTD simulations of the H1 cavities were performed by the author and the simulations for the L3 cavities and GSII file creation were performed by Dr Catherine Phillips. Micro-PL of the sample prior to fabrication, hard mask deposition, resist spinning and resist baking were performed by the author. The sample EBL and development were performed by Dr Rene Dost.

The hard mask etching, InP etching and SEM imaging were performed by the author. The hard mask removal was performed by Dr Rene Dost. The sample underetching and the critical point drying was performed by the author. The high power micro-PL to characterise the cavities was performed by the author with Dr Catherine Phillips and the low power micro-PL to look for QDs in cavities was performed by Dr Catherine Phillips.

In chapter 6 sample fabrication was performed by the author and Dr Rene Dost as set out for chapter 5. Micro-PL measurements and related analysis of both sets of cavity samples were performed by the author. The wet etch tests to develop the second set of samples were also performed by the author. EDX measurements were performed by the author and Dr Aristotelis Trapalis. Time-resolved micro-PL measurements were performed by Dr Catherine Phillips. The fabrication of the diode sample was performed by Toshiba Research Europe in the Cavendish laboratory Cambridge and the micro-PL and electrical measurements of the diode sample was performed by the author.

Chapter 2

Background

This chapter introduces the relevant theory of semiconductor QDs and their emission properties. Their growth techniques are outlined and previous studies of C-band emitting QDs are reviewed. This is followed by an introduction to nanophotonics and the enhancement of QD emission through the Purcell effect.

2.1 Semiconductor Quantum Dots and Single Photons

Quantum information processing and quantum cryptography with photons require single photon sources (SPS). In quantum optics, light and photons can be described as fitting into three main categories- anti-bunched, coherent and bunched. These are visualised in Figure 2.1 A single photon source is described as having anti-bunched emission, here the photon stream consists of individual photons spaced out in time. Coherent light consists of photons separated by random time intervals and bunched light consists of groups of photons where each group is separated in time.

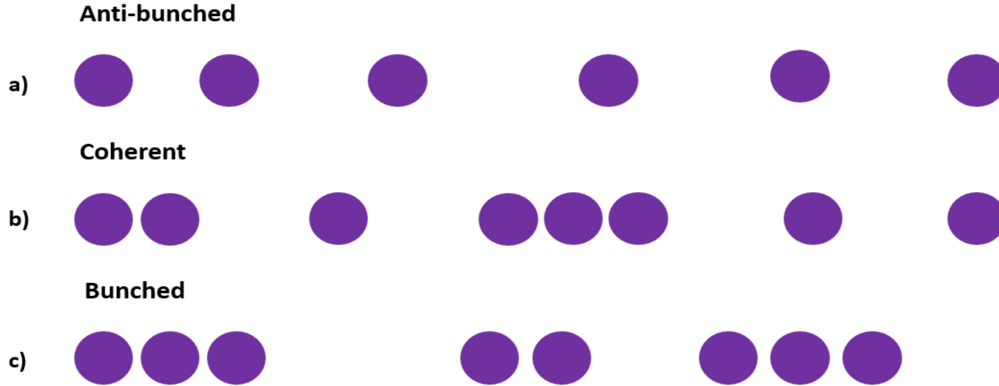

Figure 2.1: *When using photons to describe light there are three categories, anti-bunched, coherent and bunched light.*

A stream of photons can be described mathematically using the second order correlation function. Here we consider a photon stream impinging on a beamsplitter and two detectors on each of the output arms of the beamsplitter. The second order correlation function is defined as:

$$g^{(2)}(\tau) = \frac{\langle n_1(t)n_2(t+\tau)\rangle}{\langle n_1(t)\rangle\langle n_2(t+\tau)\rangle} \tag{1}$$

.

Where $n_i(t)$ is the number of photon counts measured on a detector i at time t. The angled brackets $\langle ... \rangle$ represent photon counting over a large time range of t. $g^{(2)}(0)$ represents the probability of two photons arriving at a detector at the same time which is important for characterising the photon stream. For the case of antibunched light, photons are separated out in time, making it unlikely to measure two photons at each detector at the same time. In this case $g^{(2)}(0) < 1$. For Coherent light, there are random time intervals between photon arrivals, so there is equal chance of measuring photons at the same time and for large time intervals. In this case $g^{(2)}(0) = 1$. For bunched light, photons arrive together so there is a high chance of measuring photons at the same time. In this case $g^{(2)}(0) > 1$ [22].

There are a variety of possible sources of single photons including spontaneous parametric down conversion [23], nitrogen vacancy centres in diamond [24], trapped atoms [25], carbon nanotubes [26] and quantum dots [27], which are the focus of this work.

Crucial to explaining QDs is the concept of quantum confinement. Electrons and holes can be confined within semiconductor crystals when one or more of the dimensions of the crystal are comparable to the De Broglie wavelength

$$\lambda = \frac{h}{p} = \frac{h}{\sqrt{3m_{eff}k_BT}} \tag{2.1}$$

where h is Planck's constant, p is the momentum, m_{eff} is the effective mass of the carriers in the semiconductor crystal,k_B is the Boltzmann constant and T is the temperature [22].

Different degrees of confinement determine the density of states (DOS) of carriers within semiconductor structures. A bulk crystal structure has no confinement, a quantum well has 1D confinement, a quantum wire has 2D confinement and a QD has 3D confinement. The DOS for these structures is given in Figure 2.2.

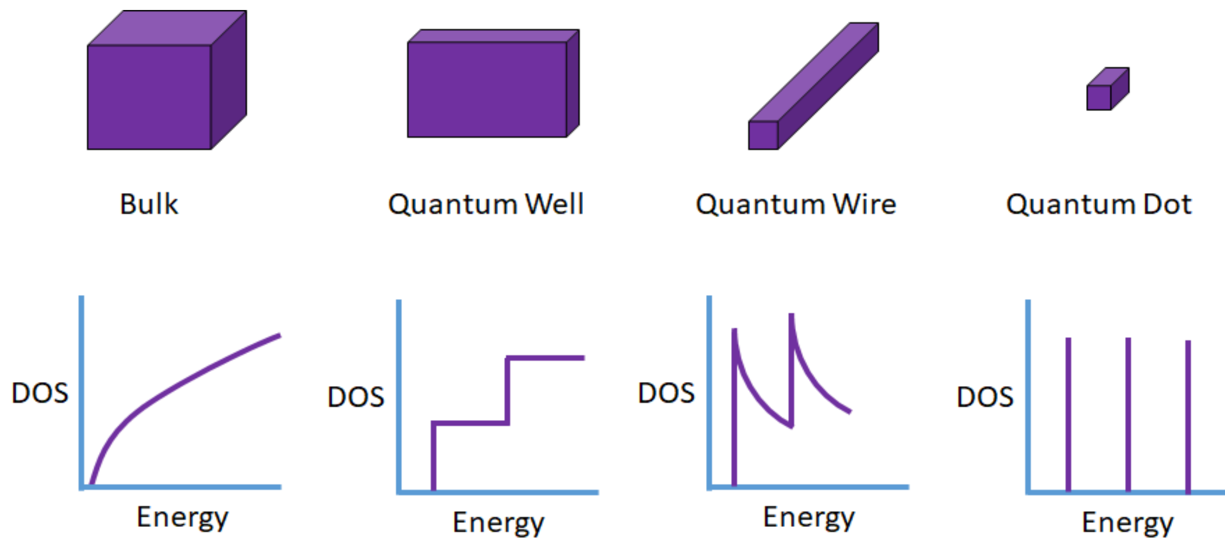

Figure 2.2: *DOS for varying degrees of confinement, ranging from bulk structures which exhibit continuous DOS functions to QDs which give delta functions DOS.*

Semiconductor quantum dots (QDs) are small islands of lower band gap semiconductor material (eg InAs) surrounded by a larger bandgap semiconductor material (eg InP) with a size of the order of tens of nanometres. This is a realisation of a 0D structure where carriers are confined spatially in all three dimensions to a size of tens of nanometres.

The band gap offset of the QD and the surrounding material confines electrons and holes within the

QD, with the size of the confining potential dependent on the size, strain environment and barrier material of the QD and the material of the QD itself.

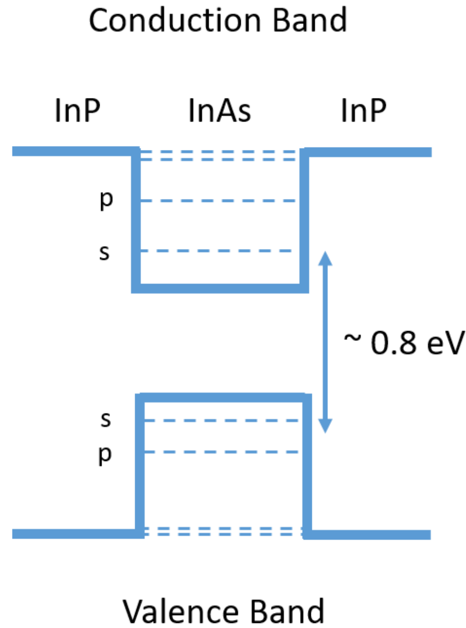

Figure 2.3: *Smaller band gap InAs surrounded by larger band gap InP causing quantum confinement and the formation of energy levels. The InAs QD has a band gap close to 0.8 eV.*

These quantised energy levels within a QD resemble atomic shells which has led to QDs often being described as 'artificial atoms'. As with atomic physics, these energy levels are labelled s and p shells for electrons in the conduction band and holes in the valence band [28].

2.1.1 Quantum Dots as Single Photon Emitters

A single QD can be described as a two level system in which electrons are excited from the ground state to an excited state, leaving behind a corresponding hole. This forms a quasi-particle known as an exciton. The electron and hole then recombine through the emission of a photon, a process known as radiative decay, with the energy of the emitted photon governed by the energy difference between the excited and ground states and the binding energy between the two. The binding energy originates from the coulomb interaction between electrons and holes in their respective shells. It is from this process that QDs act as single photon sources.

Although emission from QD transitions should only occur at specific energies, intrinsically there is a variation in energy of photons emitted from a certain transition. This is due to the radiative decay being a spontaneous process in which the time that an electron is in the excited state, typically a few ns, is determined by an exponentially decaying probability in time with an associated time constant. This time constant is known as the lifetime of the transition, T_1. The decaying probability in time determines the energy of the emitted photon as described by the Heisenberg uncertainty principle which links the energy distribution uncertainty to the lifetime distribution uncertainty.

This varying photon energy presents itself during the detection of emission from a QD transition. Over an accumulation time a histogram of photon detections of different energies is built, for a QD transition this takes the form of a characteristic Lorentzian distribution. The full width half maximum of this distribution is inversely proportional to the coherence time, T_2, of the transition. So narrow measured linewidths correspond to longer coherence times. Ideally the coherence time, and therefore linewidth, of a transition is simply dictated by the lifetime of the transition, $T_2 = 2T_1$ [29].

This ideal case does not account for various mechanisms by which the coherence of a transition is affected, these include pure dephasing and spectral wandering. Pure dephasing is mainly caused by interactions between the excited state electron and the semiconductor lattice via phonons. These interactions introduce a phase difference between the excited and ground states [30]. Spectral wandering is the change in energy of QD transitions due to the influence of time varying electric fields near to a QD. These electric fields originate from charge traps in the semiconductor lattice due to defects or surface effects or free charges in the semiconductor [31].

2.1.2 Electronic Substructure and Fine Structure

Although QDs are described as a two level system, in reality they possess multiple different optical transitions. The transitions most important to quantum optics with QDs take place from carriers in the first excited state (s shell) of the quantum dot. The simplest is the neutral exciton (X) comprising of a single electron-hole pair of opposite spin states. The biexciton (XX) consists of two pairs of electrons and holes of opposite spin states and exists at a different energy to the exciton due to the coulomb interaction between carriers. Both the X and XX transition emit either vertical or

horizontal linearly polarised light when the opposite spin states recombine. An X with an additional electron is a negatively charged exciton (X^-) whereas an X with an additional hole is a positively charged exciton (X^+). These charged states emit circularly polarised light [29].

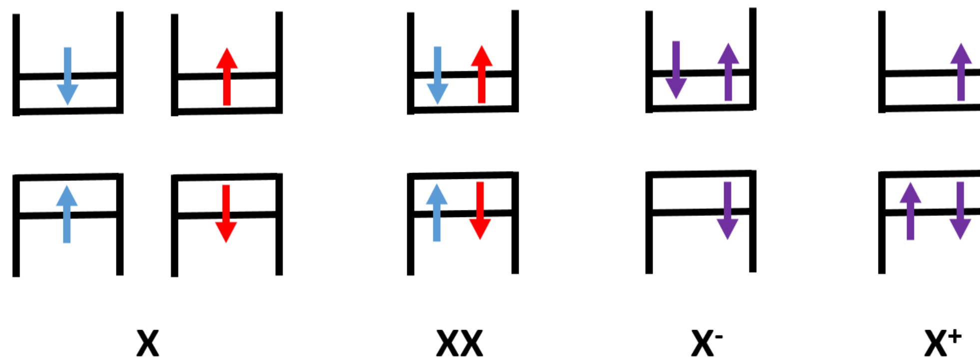

Figure 2.4: *Electronic configurations for exciton, biexciton and charged exciton states in a quantum dot.*

Electron and hole recombination from the XX state leaves the QD in the X state and subsequent photon emission then leaves the QD in the ground state. This photon pair emission is known as the biexciton cascade where the XX and X are of the same polarisation and either horizontally or vertically polarised. The emission from the biexciton cascade is very important in QDs because it results in entangled photon pairs. In an ideal QD, the emission from the orthogonal polarisation paths is degenerate, making the photons indistinguishable which is beneficial for high levels of entanglement [32].

In reality there can be an energy difference, known as the fine structure splitting (FSS), between the orthogonally polarised XX and X states. This is shown as a schematic in Figure 2.5. The energy difference arises most often due to geometric asymmetry in QDs giving different confining potentials along orthogonal crystal directions, where emission polarisation is parallel to these crystal directions. The presence of FSS reduces indistinguishability between the orthogonally polarised photons from the biexciton cascades which is detrimental to polarisation based entanglement schemes [33]. It is therefore favorable for QDs to have low FSS values, ideally less than the natural linewidth of the transition. A reduction in FSS can be achieved by application of a magnetic field [34], electric field [35], strain field [36] and growing symmetrically shaped QDs [37].

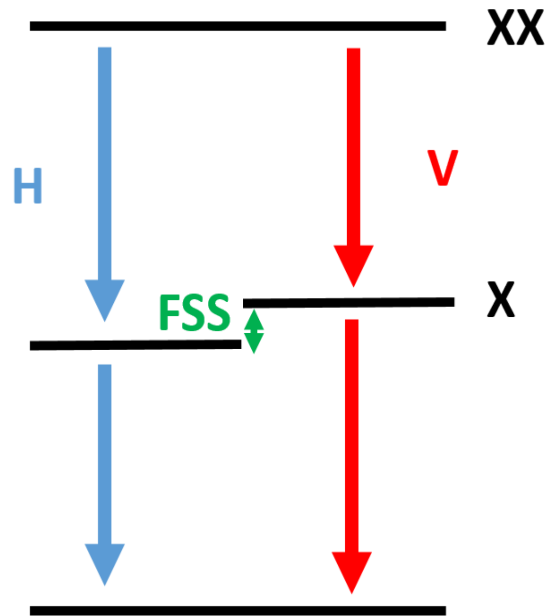

Figure 2.5: *Schematic of biexciton cascade within a QD with the FSS giving a difference in energy between the orthogonally polarised transitions.*

2.1.3 Excitation Techniques

The main techniques for exciting QDs are non-resonant, quasi-resonant and resonant optical excitation and electrical injection. These are shown in Figure 2.6. In non-resonant excitation, a laser of energy above the QD barrier band gap is used to excite carriers in the barrier material. There are several routes to recombination of excited carriers. These include recombination in the bulk barrier layers themselves, emission following relaxation via phonon emission and scattering into the wetting layer or barrier material (depending on sample structure) where emission of photons is of an energy equivalent to their respective band gaps. Finally, and of most interest in this thesis, a QD can capture the carriers, which then relax via phonon emission into the QD exciton levels with radiative emission from these exciton levels [38].

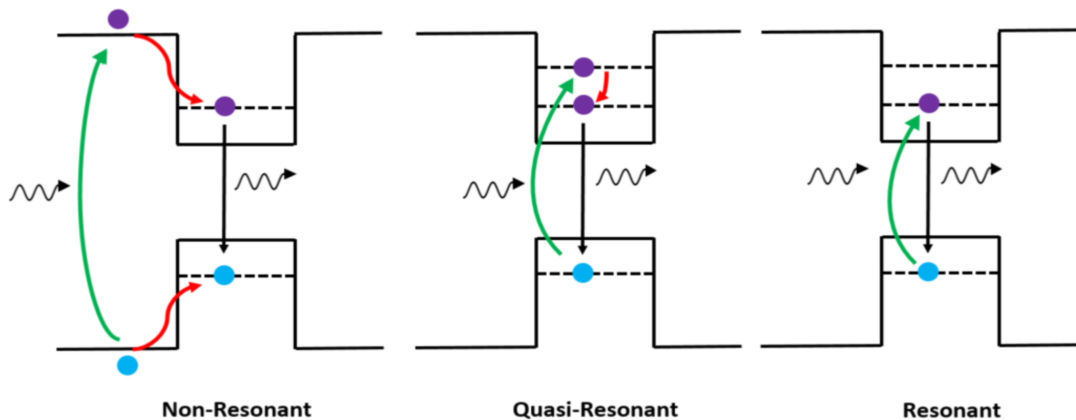

Figure 2.6: *Three QD optical excitation techniques, consisting of non-resonant, quasi-resonant and resonant excitation.*

Non-resonant excitation benefits from using a laser source at a fixed energy usually spectrally far from the emission and hence the laser signal can easily be removed from the measurement by simple filtering. Additionally, the sample structure can be investigated due to emission from the different layers within a sample. This technique has the advantage of being a relatively simple method but it does reduce the single photon purity of the QD emission due to emission from continuum states [39] and relaxation processes are susceptible to energy loss through non-radiative states or traps.

Enhanced single photon purity can be achieved by using the more complex techniques of quasi-resonant excitation (QRE) or resonant excitation (RE). QRE excites either higher energy states within the p shell of a QD which relax via phonon emission to an excitonic state [40] or excite a longitudinal-optic (LO) phonon [41]. QRE uses photon absorption at discrete energy intervals to excite an LO phonon and leave the dot in the exciton state. Resonant excitation requires exciting at the same energy of the desired optical transition with no other relaxation mechanisms and leads to the highest purity single photon emission [42].

QRE and resonant excitation schemes require a tuneable laser to access the exact energies required for exciting the various transitions in the QD. To find the excitation transitions for QRE one must also perform photoluminescence excitation (PLE) where the measurement energy is fixed on a desired emission energy, the X state for example, and the excitation energy is swept. The different excitation transitions are revealed by resonances in the measured transition. Crucial to RE is the requirement for complex filtering mechanisms in order to remove the excitation source from the

measured spectrum.

The previously mentioned excitation techniques use an optical source to excite the QDs. Electrical injection can also be used to create emitting states in electroluminescence and works by directly pumping carriers into a sample. As with non-resonant excitation, carriers can relax into the various layers of the sample, including QDs, and emit at their respective band gaps. This requires the QDs to be grown within the undoped region of a p-i-n structure, where the p layer is positively doped and the n layer is negatively doped. When applying a bias across the device, carriers are injected into the undoped region where they can recombine in the QD [43, 44, 45].

2.1.4 Tuning Quantum Dot Emission Wavelength

It is often the case that we wish to tune the emission of quantum dots, especially when used in nanophotonic structures where spectral overlap with photonic resonances may be needed. There are multiple methods for tuning QD emission, the first of which employs the quantum confined Stark effect (QCSE). Applying a forward bias across a QD produces electroluminescence, but the application of a reverse bias can be used to deterministically tune the emission wavelength of optical transitions in a QD. The applied electric field displaces electron and holes within the QD which in turn causes a change in confinement energy of a given transition due to the increased spatial separation [46].

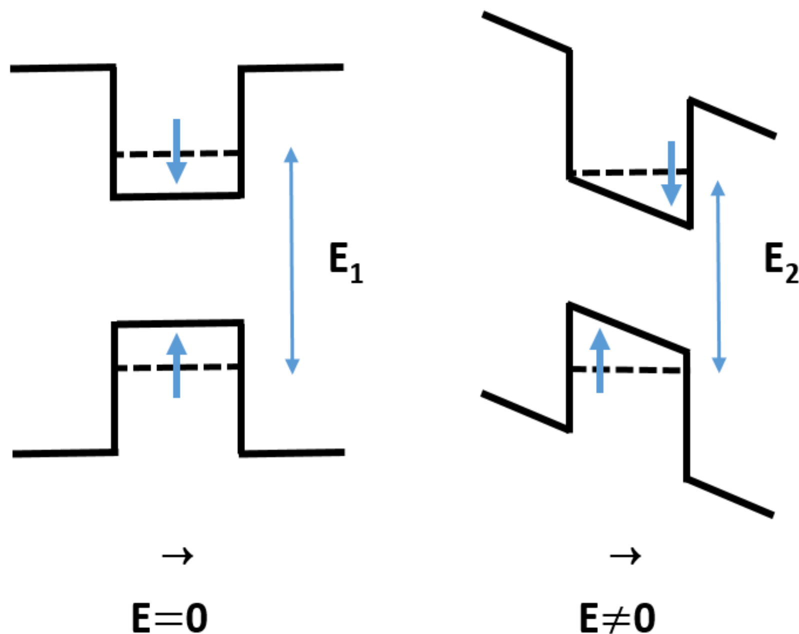

Figure 2.7: *Exciton energy level for a QD with no electric field applied with energy difference of E_1. When an electric field is applied the energy difference reduces to E_2 due to the QCSE.*

A reverse bias across a QD can also negate the effects of spectral wandering by filling states within charge traps which reduces the charge fluctuations near to a QD. This improves the linewidth of given transitions and thus the coherence time of the photons emitted [31].

Emission wavelength tuning can also be achieved by the application of an out of plane magnetic field [47], applying strain to a QD sample [48] and changing the temperature of the QD sample [49].

2.2 Quantum Dot Growth Techniques and Emission in the C-band

QDs can be epitaxially grown either using Molecular Beam Epitaxy (MBE) or Metal Organic Vapour Phase Epitaxy (MOVPE). MBE consists of an ultra-high vacuum chamber attached to which are individual effusion cells containing elements such as Gallium, Arsenic, Indium and Phosphorus. These elements are heated to produce atomic beams which impinge on the substrate and react to form compounds such as GaAs, InAs and InP.

MOVPE, on the other hand, does not take place in an ultra-high vacuum environment due to the elements for epitaxy being contained within organic compounds. These compounds include trimethylindium (TMIn), trimethylgallium (TMGa), phosphine (PH_3) and arsine (AsH_3). Epitaxial growth occurs when gases are released into the growth chamber, are pyrolised and react close to a substrate, depositing semiconductor compounds onto the substrate. The reduced equipment downtime for MOVPE systems compared to MBE systems make MOVPE more suited to use on an industrial scale though it suffers from the use of considerably more toxic materials for growth compared to MBE and can also be affected by impurities associated with the pyrolysis of organic ligands in the precursor gases [50].

There are also two main growth techniques used to produce semiconductor QDs- Stranski-Krastanow (SK) and Droplet Epitaxy (DE). SK growth is a strain driven process in which thin layers of one semiconductor material are grown on another material which has a larger lattice constant. Initial group III and V elements are supplied and form a two dimensional wetting layer and as further layers are deposited, strain accumulates up to a critical thickness. Eventually it becomes energetically favourable for the top layer to relax into three dimensional islands, forming the QDs [51]. In this work we use droplet epitaxy and this is described next in detail.

Unlike SK growth, DE growth does not depend on lattice mismatch between growth materials. In this method a group III material is grown under conditions which form metallic droplets on a substrate. These droplets are then crystallised with group V material to form the QDs [52]. In DE growth there is no wetting layer as seen in SK growth. In order to provide the 3D confinement and for optical studies, both SK and DE QD growth then require the dots to be buried with a capping layer, typically of the same material as the substrate on which the dots sit.

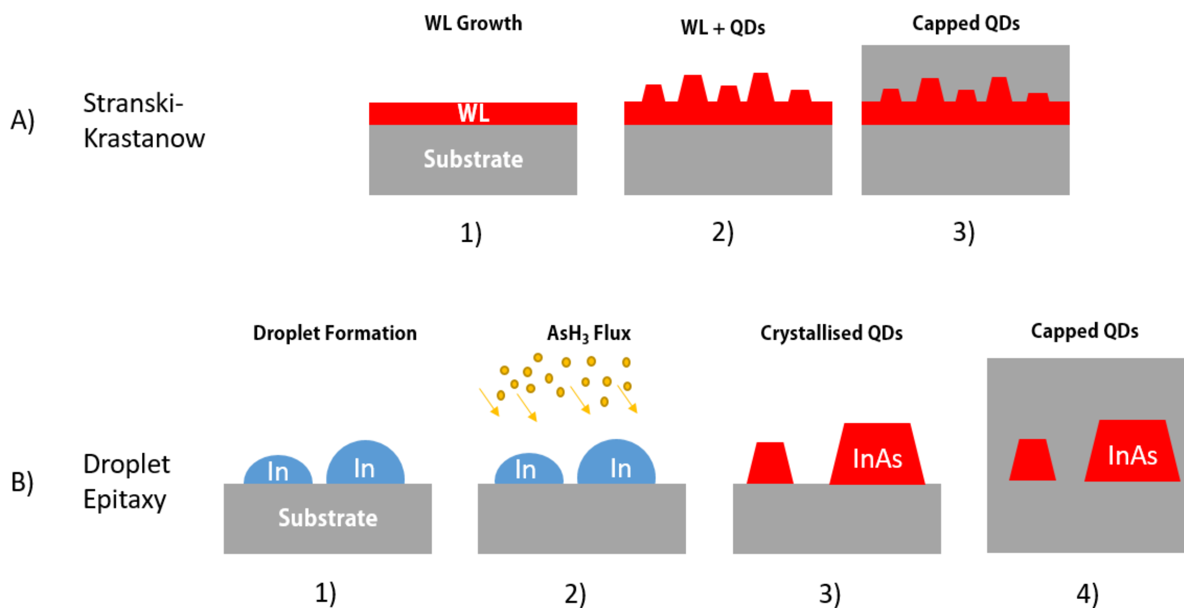

Figure 2.8: *A) Stranski-Krastanow QD growth in which a smaller lattice constant material is deposited on a larger lattice constant material. QDs form due to the build and subsequent release of strain energy. B) Droplet epitaxy growth of QDs. In this example Indium droplets are formed and crystallised into InAs QDs.*

InAs on GaAs QDs grown through the SK method have been the most widely studied semiconductor QD system [53], they have a difference in lattice constant of 7% allowing them to be well suited to the SK growth method. Such dots emit light in the near infrared (NIR) which is less suited to long distance fibre networks, though the emission wavelength of QDs of this material system can be increased to the telecom O-band through the use of strain reducing InGaAs capping layers [54]. Further emission extension up to the telecom C-band can be achieved through growing the QDs on InGaAs metamorphic buffer layers [55, 56]. Such structures are formed from an InGaAs layer in which the In content is increased over the thickness of the layer which results in a reduced strain environment and even larger QDs. This growth method has been used in demonstrating X-XX polarisation entanglement around 1550 nm [57] and the tuning of emission wavelength of a QD line in the C-band by 0.25 nm through the application of strain [58].

Larger QDs and therefore emission in the telecom C-band can also be achieved by changing material system to InP which has a lattice mismatch of 3% with InAs [59]. There is, however, a tendency in the SK mode for the formation of elongated QDs on InP, known as quantum dashes [60]. Such

asymmetry is undesirable due to the large FSS values meaning the emitters are not appropriate for polarisation entanglement schemes [61]. This FSS issue has been addressed by controlling the cooling time after InAs deposition on InP, known as a ripening technique, resulting in highly symmetric QDs emitting in the telecom C-band with a FSS below 1 μeV [62]. An example spectrum for these types of QDs is shown in Figure 2.9.

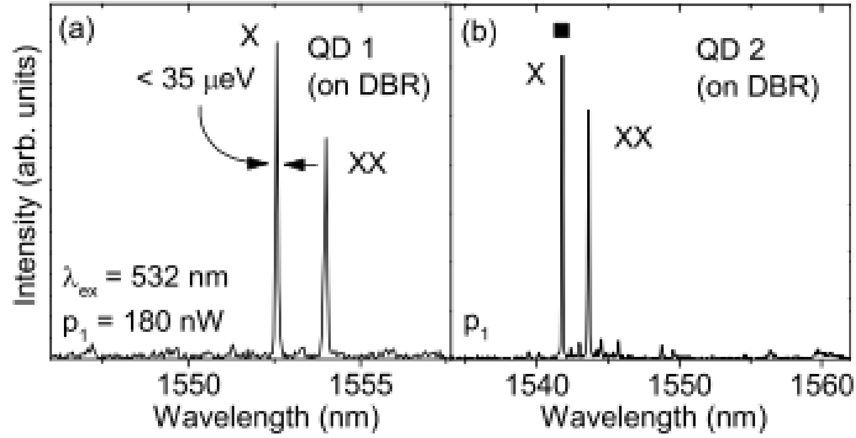

Figure 2.9: *Example QD X and XX emission spectra in the telecom C-band. The X line in panel a has a resolution limited linewidth <35 μeV. These spectra are for InAs/InP QDs grown in MBE using the ripening technique. Reprinted with permission from [62].*

The double capping method is another variation of SK growth to produce InAs/InP QDs emitting in the telecom C-band. After the strain driven dot formation the cap is deposited in two steps. A thin (few nm) layer of InP is deposited, followed by a growth interruption in which As-P exchange takes place and finally the rest of the cap is deposited [63]. These dots formed the basis of the earliest demonstrations of single photon measurements from QDs emitting in the C-band [64], followed by the first demonstration of single photon emission from an electrically driven QD emitting in the C-band [65]. The same group employed the use of QRE to excite an electron to an excited state within a QD with extremely pure single photon emission from the subsequent electron relaxation [39]. QRE was also used for high purity single photon generation in fibre based QKD experiments [19].

Droplet epitaxy QDs are not limited by the strain conditions associated with SK growth and as such, QDs based on material systems not possible in SK are achievable. For example, GaAs/AlGaAs QDs have been grown to emit at shorter wavelengths (~700 nm) than possible with the more standard

InAs/GaAs QDs with very low (<5 μeV) values of FSS [66]. Such wavelengths are of interest due to Rb atoms being used as quantum memories for these wavelengths.

InAs/InP DE QDs emitting in the telecom C-band are a more recent development with fewer demonstrations than their SK counterparts. This growth method benefits from a lack of additional growth steps required to achieve C-band emitting dots that are symmetric such that they have good polarisation properties. A comparison between C-band SK and DE dots demonstrated factor of four times reduced FSS of the DE dots with a mean FSS of 42 $\pm$ 9 μeV compared to the SK QDs mean of 176 $\pm$ 9 μeV [67]. A further study comparing coherence properties of DE and SK C-band emitting QDs demonstrated that, on average, the DE QDs showed longer coherence times by a factor of 3 and a reduced amount of dephasing [68]. Such dots have also been employed in a QLED (quantum light emitting diode) structure. Here entangled pairs of XX-X photons were generated through electrical injection up to a temperature of 96 K [69]. Additionally, these QDs have been used in quantum teleportation experiments [70].

2.3 Light Confinement at the Nanoscale

One of the main advantages of QDs is the versatility of the semiconductor matrix in which they are housed. We have seen how controlling the doping of the semiconductor layers can lead to electrical pumping schemes and the ability to control emission wavelength and quality of the QD transitions. The fabrication of nanophotonic structures can enhance and guide the emission [71].

Nanobeam waveguides form the simplest structure to guide emission from QDs on chip, they consist of a suspended beam of height and width of a few hundred nanometres, an example is shown in Figure 2.10. Light is confined to only travel along one axis due to total internal reflection (TIR) confining light in the other two spatial directions.

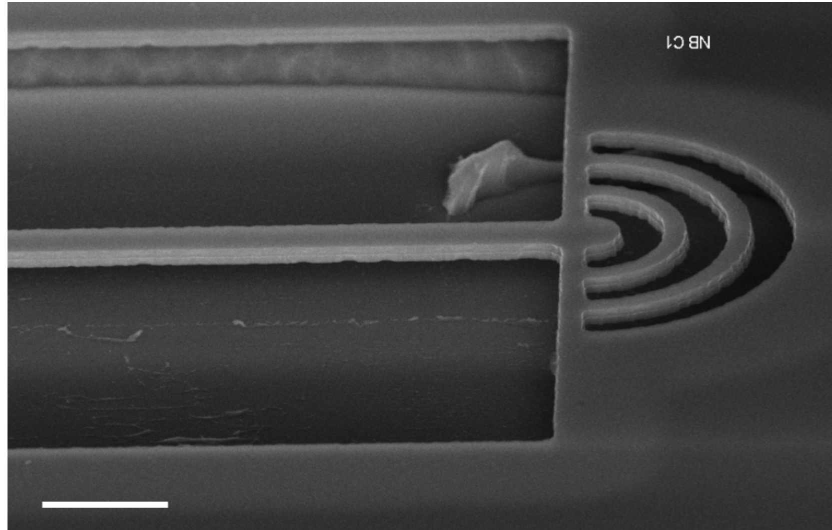

Figure 2.10: *Titled SEM image of a nanobeam waveguide featuring a Bragg grating coupler which scatters light out of plane for measurement. Scale bar is 2 μm.*

2.3.1 One Dimensional Photonic Crystals

A more intricate way to confine and enhance dot emission is through the use of a photonic crystal which consists of alternating materials of different dielectric constant. A one dimensional photonic crystal has alternating dielectric constants in only one direction [72]. A Distributed Bragg reflector (DBR) is a one dimensional photonic crystal widely used in studies of QDs in order to increase their measured count rates.

This type of structure is made of alternating layers of material with different refractive indices. The thicknesses of the layers are grown to be equal to $\lambda/4$n where λ is the wavelength of the light in air and n is the refractive index of the layer. This thickness is required in order to fulfill the constructive interference condition [53]. Partial reflections at each layer boundary cause an overall constructive interference of reflected light of wavelengths in a band around λ. So overall, the DBR acts as a mirror for QDs emitting light of wavelengths around λ, increasing the brightness of the source.

Figure 2.11: *Simple DBR structure formed of alternating layers of $\lambda/4n$ thick material. Where λ is the wavelength of device operation and n is the refractive index of the constituent material. The QDs sit within a cavity of thickness λ/n with an additional top DBR.*

This mirror effect can be improved up by growing the dots in a layer of thickness $m\lambda/2n$ where m is an integer, this produces a cavity effect which improves the vertical directionality of the dot emission increasing count rates even further. GaAs based QD systems benefit from the large refractive index contrast of AlAs/GaAs ($\Delta n = 0.48$) [73]. This technique has been adopted for metamorphic buffer layer-based C-band emitting dots to significantly increase count rates from QDs with a 20 pair AlAs/GaAs DBR [56].

DBRs for InP-based C-band systems are less straightforward than their GaAs counterparts. There are no binary materials which are lattice matched to InP that can be employed for DBRs and ternary alloys are not suitable either. For InGaAs there is a large index contrast for InGaAs/InP ($\Delta n > 0.45$) but the band gap of InGaAs means it will absorb at the C-band, making it unsuitable for telecom wavelengths DBRs. InAlAs/InP features a refractive index contrast that is too low ($\Delta n < 0.1$) to be appropriate for a DBR [74].

The more complex growth of quaternary alloys must be used in order to make InP based DBRs for C-band applications [75]. AlInGaAs/InP ($\Delta n > 0.34$) gives a DBR that is appropriate for C-band emitting QDs. An order of magnitude increase in count rates has been demonstrated with

20 DBR (AlInGaAs/InP) pairs [76]. Though the growth is complicated by the use of quaternary alloys compared to GaAs-based systems, clearly InP-based DBRs are of the quality required to significantly increase QD count rates.

25 pair DBR has been shown to enhance the count rate of QDs emitting at 1.55 μm by an order of magnitude [62].

2.3.2 Two Dimensional Photonic Crystals

A two dimensional photonic crystal has alternating dielectric constants in two dimensions, for semiconductor systems this can take the form of a suspended semiconductor slab with an array of air holes within the slab. Light confinement in the X-Y plane is provided by Bragg reflections due to the semiconductor-air hole interface. These Bragg reflections lead to the formation of photonic bands within the crystal, the photonic bands are the modes of light that can pass through the X-Y plane due to constructive interference. Between the bands is an area known as the photonic band gap (PBG). In this region certain wavelengths of light cannot pass through the photonic crystal due destructive interference. The wavelength range of the PBG depends on the refractive index of the slab, the hole radii and the lattice constant of the holes [77].

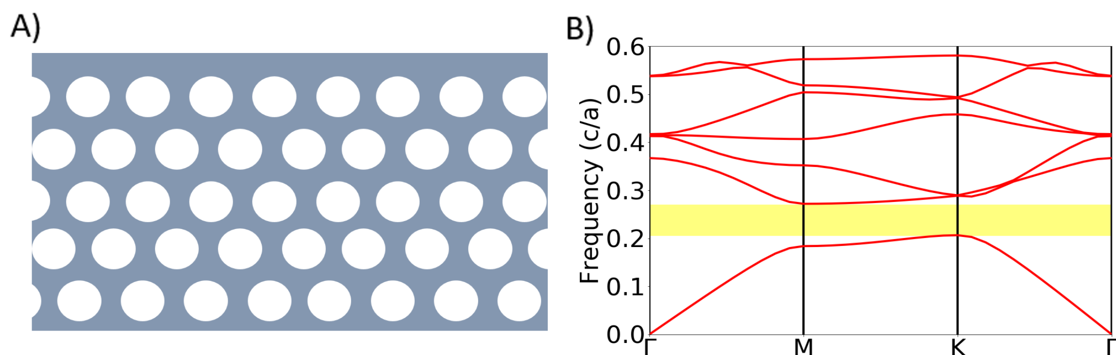

Figure 2.12: *A) Top down view of a two dimensional photonic crystal made from a hexagonal array of air holes in a semiconductor slab. B) Band diagram showing the photonic bands across four lattice directions. The photonic band gap is highlighted in yellow. This diagram was produced using MIT Photonic Bands software [77].*

By introducing defects in the photonic crystal one can create photonic crystal cavities (PhCCs) where cavity modes form at certain wavelengths within the photonic bang gap. A PhCC can be

realised by removing a single hole, creating an H1 cavity, or removing a line of three holes to create an L3 cavity. These are shown in Figure 2.13. Removing a line of holes forms a W1 waveguide.

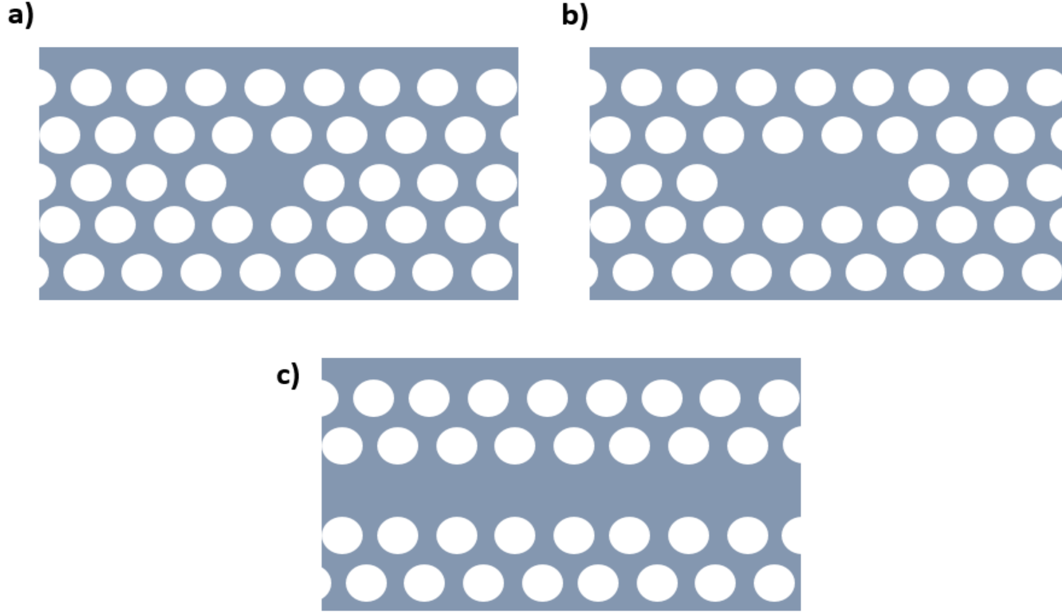

Figure 2.13: *A) Unmodified H1 cavity, formed by excluding one hole from the photonic crystal. B) Unmodified L3 cavity, formed by excluding three holes from the photonic crystal. C) W1 waveguide, formed by excluding a row of holes from the photonic crystal.*

The cavity modes related to PhCCs are described by their quality (Q) factor, this quantifies how well light is confined within the cavity. It is defined as

$$Q = \frac{\omega_o}{\Delta\omega} \tag{2.2}$$

.

Where ω_o is the frequency of the mode and $\Delta\omega$ is the cavity mode width.

PhC structures benefit from the ability to be able to combine cavities and waveguides on a single chip with the view to creating a "system on a chip". In such a system, there would be no need for large scale optical setups due to the single photon source, photon routing via waveguides and detection would all be on the same semiconductor chip [29].

2.3.3 Weak Coupling and the Purcell Effect

While a DBR type structure can be formed exclusively through epitaxial growth, a photonic crystal structure must combine growth and fabrication techniques in order to realise the suspended semiconductor slab with arrays of holes. Though a more involved process, having a QD emitting within a PhCC can enhance the emission rate through the Purcell effect [78].

This occurs when the wavelength of a QD transition sufficiently overlaps with the cavity mode wavelength. Due to this overlap the QD has an increased number of states into which it can emit. Fermi's Golden rule states that the transition rate of a system is proportional to number of final possible states the system can be in. Therefore, a QD within a PhCC with a transition overlapping with a PhCC mode has a reduced lifetime compared a QD in bulk. This is a highly desirable effect as it increases the repetition rate of a QD-based single photon source [79].

The Purcell factor (F_p) is described as:

$$F_p = \frac{3}{4\pi^2}\left(\frac{\lambda}{n}\right)^3\frac{Q}{V} \tag{2.3}$$

.

Where λ is the wavelength of the emitter/cavity, n is the refractive index of the medium from which the cavity is made, Q is the cavity mode quality factor and V is the volume of the mode. This formula assumes that the emitter is located in the cavity electric field antinode and the emission wavelength of the QD is equal to the cavity mode wavelength.

Experimentally, the Purcell factor is defined as:

$$F_p = \frac{t_{QD}}{t_{QD_{cav}}} \tag{2.4}$$

.

Where t_{QD} is the transition lifetime for a non-cavity coupled QD and $t_{QD_{cav}}$ is the lifetime of a QD transition for a QD within a cavity. The QD lifetime is measured using time-resolved measurements in which the emission from a QD line is spectrally filtered and arrival times of QD photons relative

to an excitation laser pulse are recorded. A histogram of photon arrival times is then recorded which typically has the form of an exponential decay. By fitting this the lifetime of the transition can be attained.

A Purcell enhanced QD can therefore appear very bright when it is being measured due to the short transition lifetime causing high count rates from the transition. For the case of QDs in PhCCs it should be noted that a particularly bright QD can occur when the QD is in the bulk PhC and emitting at a wavelength within the PBG. In this scenario the QD emission cannot propagate in the PhC plane, so emission is directed in the vertical direction [80]. Such a QD is therefore inhibited by the PhC and its transition lifetime is increased due to the reduced number of states available to the QD.

The shortening of a transition's lifetime can also affect the excitation power at which a QD emission line saturates. As the excitation power is increased when measuring a QD, its emission rate increases due to the increased number of carriers recombining within the QD. This occurs up to the point of saturation, when the QD transition lifetime limits the amount of recombination. A Purcell enhanced QD therefore exhibits a higher saturation power than a non-Purcell enhanced QD due the reduced transition lifetime, this is shown in Figure 2.14 [81].

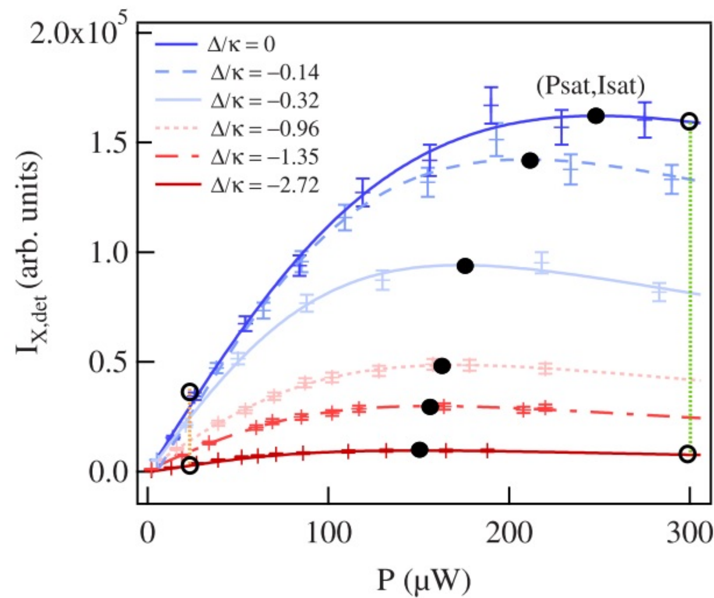

Figure 2.14: *Saturation behaviour of a QD transition as it is tuned into resonance with a cavity mode. The saturation power (black dots) is seen to increase as the QD line approaches resonance ($\Delta/\kappa = 0$). Reprinted from [81].*

Equation 2.3 tells us that the Purcell factor is proportional to $\frac{Q}{V}$ so cavities with high Q factors and small mode volumes will produce high values for F_P. Indeed, this is true in simulation where values of F_p in the millions are calculated for cavities with Q factors also in the millions [82]. Fabrication of real PhCCs cannot perfectly reproduce the Q factors given in simulation. This is due to fabrication imperfections where there is a variation in fabricated hole size and sidewall verticality, and also roughness in the fabricated holes acting as scattering centres.

As with equation 2.3, in simulation the emitter is assumed to be exactly in the cavity mode electric field antinode with perfect spectral overlap. The experimental reality, however, is that such high values are yet to be achieved. In the well-studied GaAs based QD systems, $F_p = 43 \pm 2$ represents a very high measured Purcell factor value [83], though such values are very rare due to the reliance on randomly positioned QDs being in the correct location with respect to the cavity and being perfectly spectrally aligned to the cavity resonance.

Typically, QDs are grown by self-assembly methods such as SK growth with QDs forming in random locations on the wafer and showing a distribution in QD size and corresponding emission wavelengths. As in [83], the wavelength can be tuned through the QCSE to match the cavity wavelength but there is still a reliance on finding randomly located dots within fabricated cavities. Not having control over the positioning of the QDs and cavities with respect to each other forms a major barrier to reliably achieving high Purcell factors.

This issue can be addressed by taking a deterministic approach to both cavity and QD locations. One method is through Quantum Dot Registration which is a post growth technique whereby QDs with appropriate wavelengths and linewidths have their position defined and recorded with respect to some form of alignment markers, following which PhCCs are fabricated around the pre-selected dots [84, 85]. Such an approach has been used to deterministically demonstrate a Purcell factor of 5 for a QD for a GaAs based PhCC [86].

In comparison with GaAs-based QD work, C-band QDs are still in their infancy with respect to demonstration of QDs within PhCCs and measuring Purcell enhancement, so there are only a few examples. Due to the need for the PhC slabs to be thin (few 100 nm), the metamorphic buffer layer GaAs-based dots are not appropriate for this application. This is due to the buffer layers being of thicknesses close to 1 μm [56].

The first example and benchmark for Purcell enhancement for C-band QDs gives a Purcell enhancement of 5 for a PhCC. In this paper a QD XX line ($\lambda \sim 1560$ nm) is temperature tuned into resonance with a PhCC mode. The lifetime of the transition is measured to be 0.2 ns when on resonance with the cavity mode. This is compared to a reference XX line with a lifetime of 1 ns, giving a Purcell factor of 5. The data for these are shown in Figure 2.15. Though a good value for Purcell enhancement, the study is limited by optical properties of the XX transition. The linewidth of the emission is ~240 μeV indicating the quality of the QDs to be limited [87].

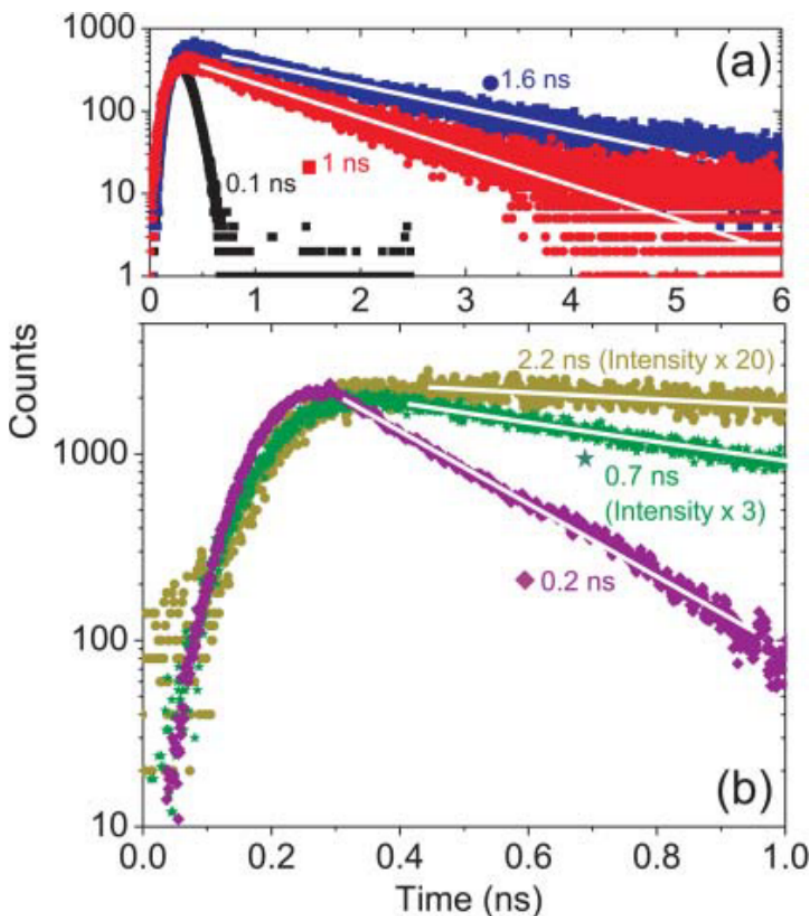

Figure 2.15: *Time resolved measurements of QD lines. a) Reference lifetime measurements, for X (blue circles) and XX (red squares). Black squares are the instrument resolution. b) Inhibited XX transition in bulk PhC (golden circles), XX in cavity out at 4 K (green star) and XX in resonance with cavity mode at 22 K (purple diamond). The XX lifetime is shorter than the reference lifetime, demonstrating a Purcell enhancement. Reprinted with permission from [87].*

More recent work shows a spectral overlap between a QD emitting around 1508 nm and an L3 cavity mode. Here the emission lines improve upon the previous work with linewidths that are

spectrometer resolution limited to 50 μeV. Where this study lacks however is the lack of directly measured F_p. A Purcell enhancement is inferred from the increase in intensity from a QD as it is temperature tuned across a cavity mode [88]. This same group has demonstrated similar results for a QD emitting at ~1510 nm, again a Purcell enhancement is inferred but not measured with QD lifetime measurements [89].

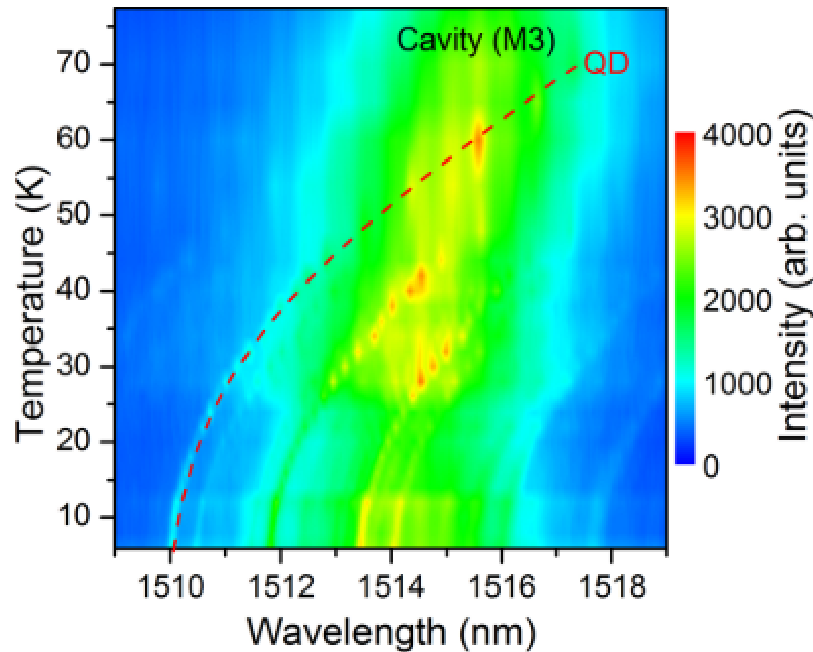

Figure 2.16: *Temperature dependent colour plot of a QD transition and a cavity mode. The QD transition exhibits a factor of four intensity increase as the QD is temperature tuned into resonance with a cavity mode. The intensity increase is due to the Purcell effect. Reprinted from [88].*

2.4 Summary

Overall this chapter has introduced QDs, covering the relevant physics of QD optical behaviour and their growth. Methods to enhance their emission with nanophotonics has also been covered, with a focus of PhCCs. Finally the concept of Purcell enhancement and the work done for C-band emitting QDs has been reviewed. There have been few demonstrations of Purcell enhancement in the C-band and this work aims to build upon existing work by exploring Purcell enhancement using DE QDs grown by MOVPE.

Chapter 3

Methods

The following chapter outlines the experimental and computational methods used in this work. First there is an overview of the quantum dot growth procedure and atomic force microscopy (AFM) of non-buried QDs. These are performed by Dr Elisa Sala and Dr Young In Na, respectively. This is followed by details of the cryogenic methods used for optical characterisation of samples. Micro photoluminescence for optical measurements is then introduced. This is followed by PhCC device design with finite difference time domain methods and device fabrication with nanofabrication techniques. Methods for further characterisation of samples are presented. These consist of scanning electron microscopy, energy dispersive X-ray spectroscopy and cross-sectional scanning tunnelling microscopy.

3.1 Quantum Dot Growth

The QDs measured in this thesis were grown in a vertical flow Aixtron 3x2" closed coupled showerhead MOVPE reactor using the droplet epitaxy growth method. The precursors used were trymethylindium (TMIn), trymethylgallium (TMGa), phosphine (PH_3) and arsine (AsH_3). The growth procedure is as follows: an InP buffer is grown on an InP substrate through the reaction of TMIn and PH3 at a substrate temperature of 610 ^oC. Substrate temperature was measured using an emissivity corrected pyrometer. The sample temperature is then reduced to 320 ^oC over a 200s period and Indium droplets are formed on the InP surface through exposing the sample to TMIn

for 35s. Indium droplets which form on the surface are then crystallised into InAs QDs by raising the sample temperature to 520 ^{o}C whilst exposing the sample to Arsine. During this crystallisation step there is As-P exchange due to the InP surface being exposed to Arsine which forms a thin $InAs_xP_{1-x}$ layer [90]. This is referred to as the quasi-wetting layer.

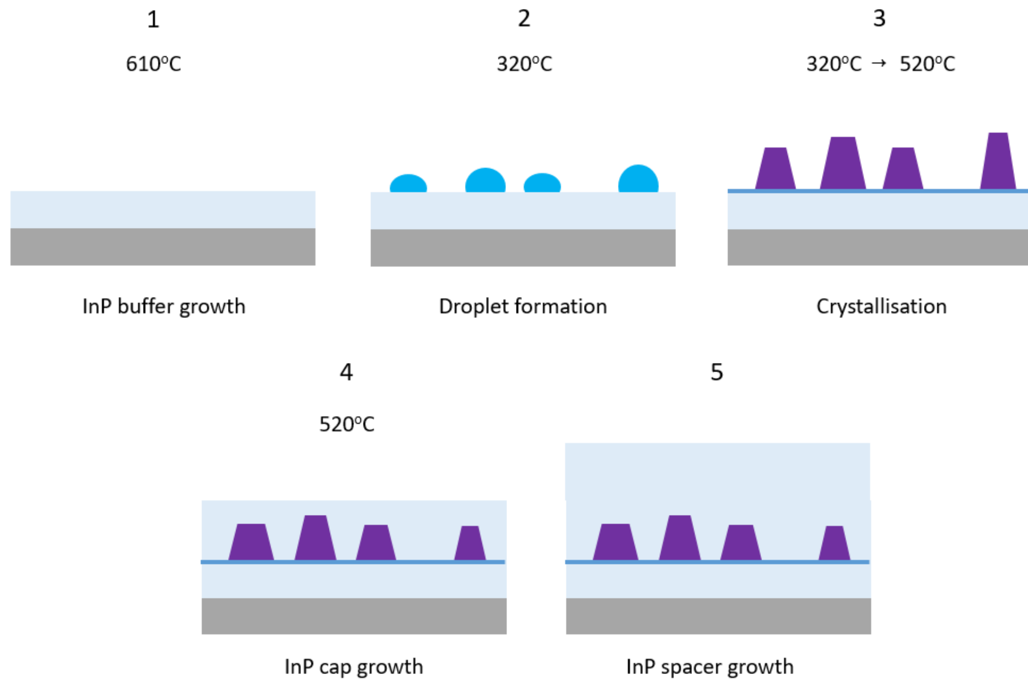

Figure 3.1: *QD growth procedure used for the samples presented in this work. The dark grey layer is the InP substrate, the light grey layers are the grown InP, the light blue semi circles are the Indium droplets, the thin dark blue layer is the quasi wetting layer and the purple trapezoids are the InAs QDs.*

The sample temperature is kept the same and the InAs QDs are then capped by growing an additional 20 nm of InP. Finally, a 80 nm thick InP spacer is grown at a temperature of 620 ^{o}C.

Some samples feature additional uncapped QD growth on the buried QDs. This allows for the uncapped QDs to be investigated by AFM which can give be used to give values for QD sizes and densities, these are referred to as surface QDs in this thesis. It should be noted that the size and shape of the QDs changes during the capping procedure so the results for the uncapped QDs are not representative of the true size of the capped QDs. However, these results are useful to compare sizes between different growth runs.

AFM uses a very thin tip with a radius on the order of tens of nanometres which is attached to a cantilever. The tip is scanned over a sample surface and moves in the vertical direction when it encounters changes in the sample surface height. This causes the cantilever to deflect in response to sample height changes. A laser is reflected off the cantilever onto a position sensitive photodiode, so movement of the cantilever is measured as a change in measured laser signal. This change in laser signal can then be converted into an image and the height and radius of the object is measured. AFM measurements presented in this thesis were performed using a Bruker Dimensions ICONAFM.

3.2 Sample Cooling for Optical Measurements

Optical characterisation measurements presented in this thesis were undertaken at low temperature (∼5K) using two types of cryostatic systems.

The first is a closed cycle cryostat, namely a Montana Instruments Cryostation s100, shown in Figure 3.2. The cryostat operates with the continual compression and expansion of Helium gas. Briefly, compressed Helium gas isothermally expands which results in the cooling of a cold head. The cold head is thermally connected to a sample stage within the vacuum sample chamber. The temperature of the cold head, and therefore sample temperature, can be controlled by adjusting the cryostat pump rate. In this system, sample temperatures down to 5 K are achievable. Sample temperatures are based on a temperature measurement of the sample stage which is measured using a thermocouple.

Samples are attached to the sample stage with thermally conductive silver paint and can be optically accessed through a glass sample window on the top of the sample chamber. Thermal grease is another option for thermally coupling the sample to the cold head, however it was only initially used on this setup due its reliability issues. These issues consisted of proper thermal contact not always being achievable and cool downs therefore failing.

The optical stack is attached to micrometer stages. Navigating across a sample or between samples is achieved by moving the optical stack outside of the sample chamber with the micrometre piezo stages in the x,y and z directions. This moves the laser spot relative to the samples which are in a fixed position within the cryostat. This type of system allows for easy sample changing and for

many samples to be mounted and measured during one cool down. Thus it is ideal for relatively quick sample characterisation.

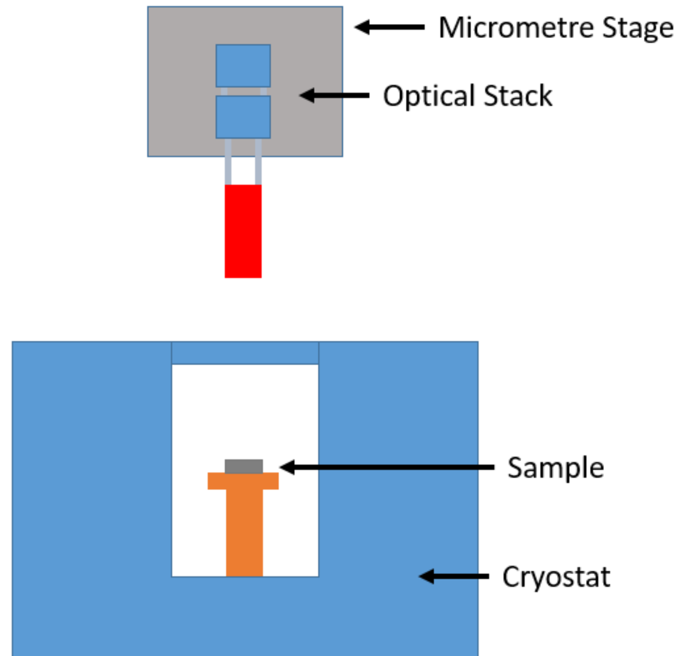

Figure 3.2: *Basic schematic of flow cryostat system used for the majority of optical measurements presented in this thesis.*

The second cryogenic system is a bath cryostat and is used for more detailed longer term measurements on a single sample, it is shown in Figure 3.3. Samples sit inside an evacuated chamber within a liquid Helium filled dewar. The sample chamber is then partially filled with a small amount of Helium gas which facilitates thermal exchange between the sample and the liquid Helium, cooling the sample down to low temperature.

The sample is again fixed to a sample plate with thermally conductive silver paint. This sample plate sits atop an x,y and z piezo stack which enables sample navigation by moving the sample relative to the fixed optical path. Again, the sample is optically accessed through a sample window at the top of the sample chamber. The piezo stack sits above a sample heater which is used to change the temperature of samples in the cryostat.

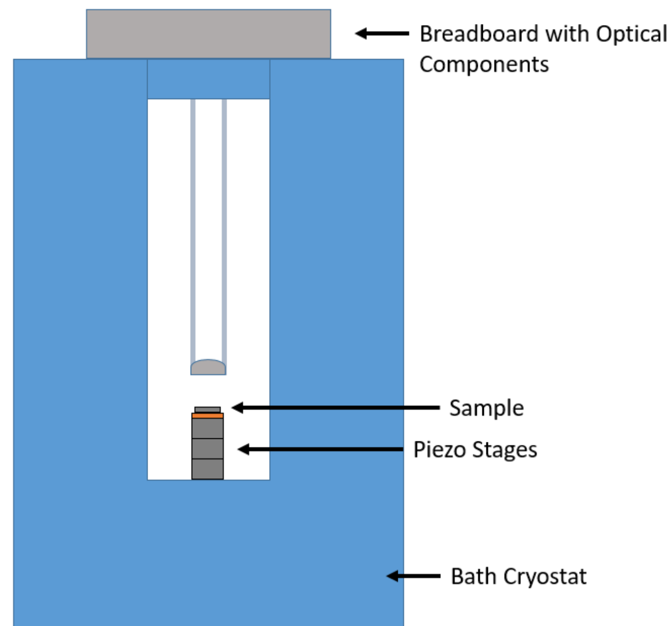

Figure 3.3: *Basic schematic of bath cryostat system used in this work.*

3.3 Optical Characterisation Of Quantum Dots

3.3.1 Microphotoluminescence with the Flow Cryostat

The measurement setup for the flow cryostat system is shown in Figure 3.4. This setup uses a 635 nm diode laser for sample excitation where the output power can be controlled by changing the laser current. The laser is fibre coupled into a cage system which allows optical elements to be easily mounted and aligned. The laser path passes through a variable neutral density filter for continual laser power adjustment. This is then followed by a 50:50 beamsplitter, with one path leading to a reference power meter. The reading from the reference power meter is used to indicate the power on the sample. This is achieved by previously measuring the output power of the laser from under the objective and comparing to the power reading measured by the reference power meter. The other beam splitter path is used to input the white light from a white light source for sample imaging.

The excitation path then goes through a dichroic mirror which reflects the laser down to a 100x, NA=0.5 Mitutoyo objective lens which has a working distance of 10 mm. This objective lens

focuses the laser light down to a ∼5 μm diameter spot onto the sample housed within the closed cycle cryostat.

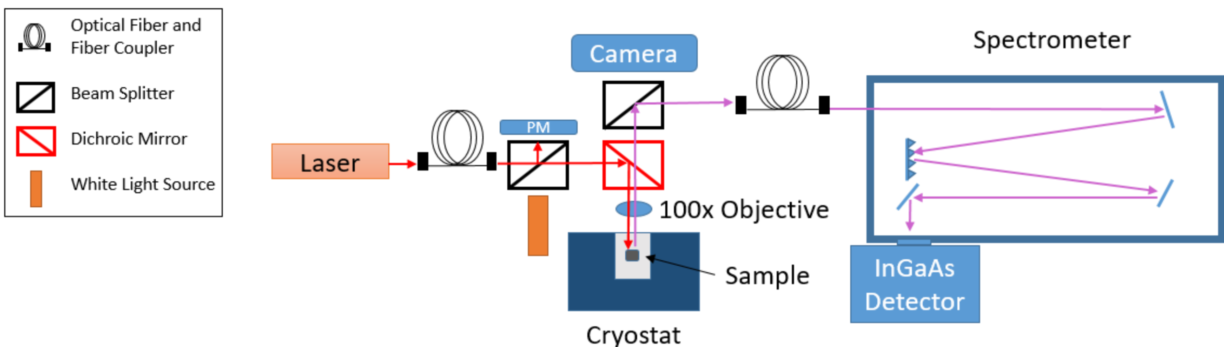

Figure 3.4: *Micro-PL setup used for sample characterisation.*

Emission from the sample is collected by the objective and transmitted through the dichroic mirror. Next there is a 90:10 beam splitter, the lower transmission path leads to a CMOS camera which can image the laser spot and sample surface. The higher transmission path goes to a fibre coupling lens which couples sample emission into an optical fibre. This optical cage system is mounted to x,y and z piezo stages which are used for moving the laser spot across a sample and focusing the laser spot.

The collection optical fibre leads to a set of lenses which focuses the optical fibre output into the spectrometer. The spectrometer uses a 600 and 900 g/mm gratings with pixel to pixel spacings at 1550 nm of 25 and 12 μeV, respectively. An InGaAs array cooled with liquid nitrogen is used for detection.

This system has a measurement range of 800-1600 nm with a spatial resolution of 5 μm. There were two main types of measurement taken on this setup. The first was micro-PL taken at 100 μW laser excitation power. This relatively high power was used as it allows for emission from the individual sample layers to be measured. Such measurements will be referred to as high power measurements in this thesis. A typical high power measurement is shown in Figure 3.5 Where the emission from the InP can be seen at 875 nm, emission relating to the quasi-wetting layer is at 960 nm and 1080 nm and broad QD-related emission begins from 1400 nm.

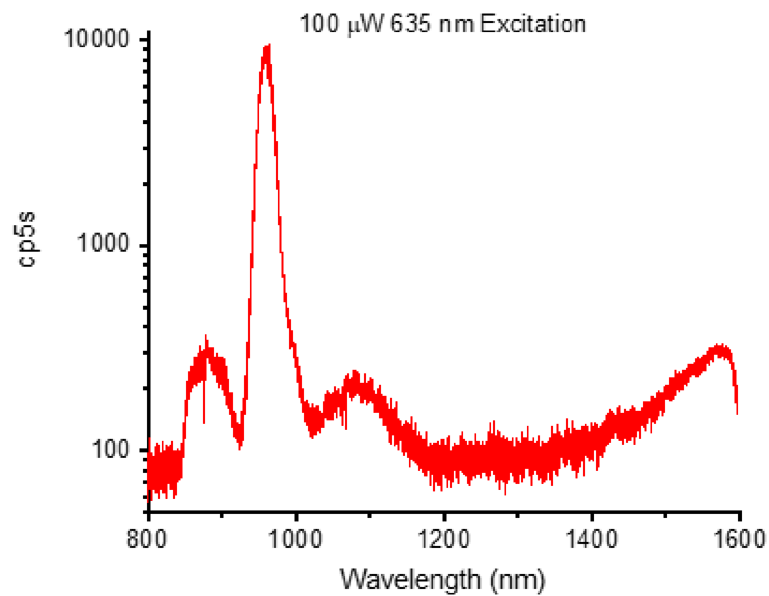

Figure 3.5: *Typical high power micro-PL spectrum for an InAs/InP QD sample.*

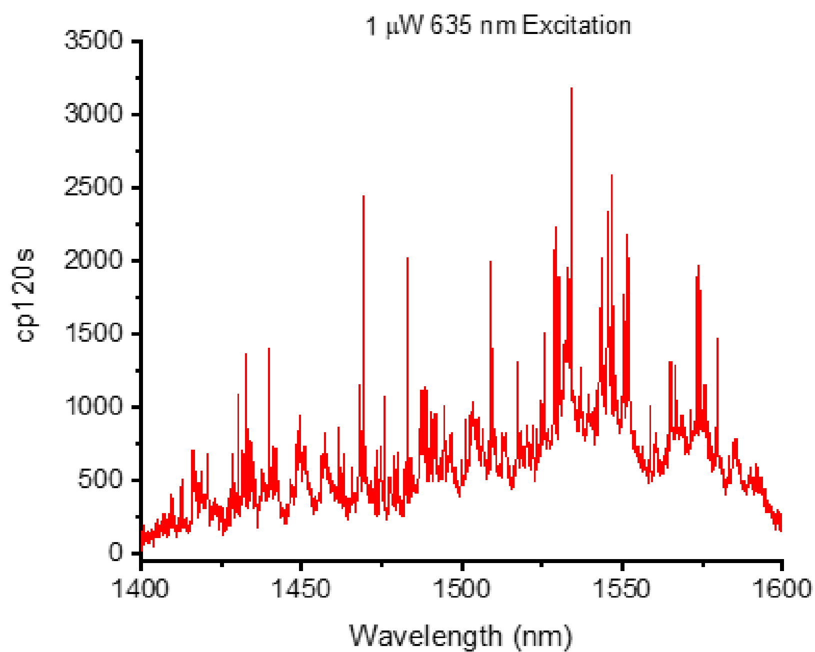

Figure 3.6: *Example low power micro-PL spectrum for an InAs/InP QD sample. The sharp lines originate from the QD transitions. It should be noted that some of the QD lines measured in this thesis are resolution-limited.*

The second type of measurement used 1 μW laser excitation power to measure emission from the

QDs. The typical integration time used was 120 seconds, which can be seen on the y-axis of Figure 3.6. This power was used as it provided relatively high count rates from the QDs whilst also being below saturation power for a lot of the QD lines. By exciting below saturation, a lower QD-ensemble background emission was seen so the QD lines were not masked by this emission. Exciting at 10 μW or 50 μW, for example, would have masked the QD emission lines with the QD-ensemble type emission. Figure 3.6 gives a typical low power QD spectrum. The spectrum shows narrow emission lines which originate from the QDs, where one QD can have multiple emission lines. For the sample shown in this spectrum the QD density is of the order of 10 μm^{-2} so for a laser spot area of $\sim$20 μm^2 we can expect to excite a few hundred QDs.

Low power spectra were not taken over the full 800-1600 nm wavelength range. This was due to the large amount of experimental time this would have taken. Instead such spectra were taken at longer wavelengths (generally $>$1300 nm) as this was where QD lines were generally found. Such spectra were repeatable for the same measurement location. QD lines could be differentiated from cosmic rays by the QD lines consisting of 5-10 pixels compared to the 1-2 pixels seen for cosmic rays. Also QD lines had much lower count rates ($<$10 cps) compared to cosmic rays ($\sim$100 cps). It should be noted that spectra presented in this thesis have a y axis of counts for a given integration time, this is not the raw number of photons from a QD line but rather a value of analogue signal that represents the intensity of the light emitted from the QDs.

3.3.2 Microphotoluminescence with the Bath Cryostat

Optical measurements were also performed in the bath cryostat system in the Department of Physics and Astronomy at the University of Sheffield. This setup features two excitation lasers, an 850 nm diode laser for above band excitation and a tuneable laser with a wavelength range of 1480-1640 nm. The optical components sit on a breadboard above the cryostat where a combination of mirrors and a dichroic mirror guide the excitation lasers towards a beamsplitter which directs the laser down to the sample. A reference power meter measures the laser power from the other arm of the beamsplitter.

This setup also features a white light source which is used to image the sample. Sample luminescence and reflected white light are directed back towards the beamsplitter and go to a 90:10 beamsplitter. Here the low reflection path is used to image the white light on an InGaAs camera. The high

transmission path leads to the spectrometer which houses a liquid nitrogen cooled InGaAs array detector for measurement.

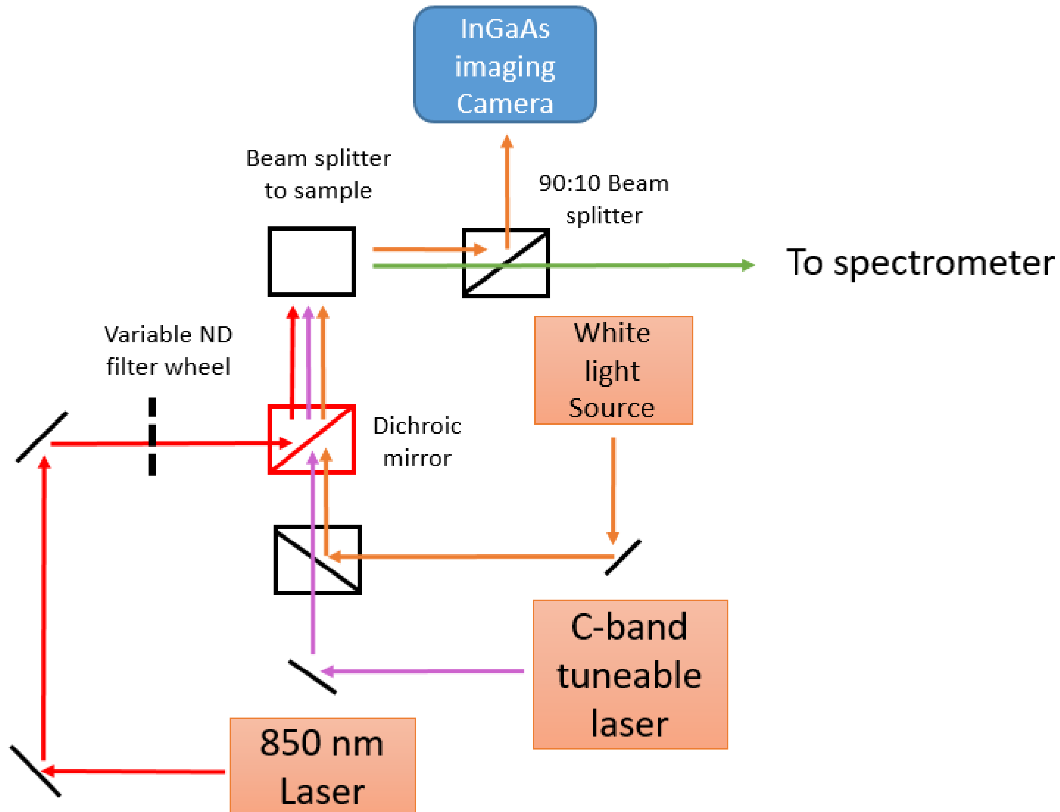

Figure 3.7: *Microphotoluminescence setup used for the bath cryostat system. Here two lasers can be used, an 850 nm diode laser for above band excitation and a tuneable laser for PLE measurements. This system is located in the Department of Physics and Astronomy and was used for characterisation of PhCCs presented in Section 5.3 and QD measurements presented in Section 6.5.2.*

Time resolved measurements can also be performed with this setup. This uses a tsunami Ti:Sapphire pulsed laser at 850 nm with a repetition rate of 80 MHz and pulse length of ∼3 ps to excite the sample, emission from a QD line is spectrally filtered and counted with superconducting nanowire detectors. Such detectors operate at ∼4 K which allows the nanowires to be in a superconducting state. The absorption of a photon causes local heating of a nanowire which means part of the nanowire is no longer superconducting. This in turn causes and increase in resistance and a measureable voltage pulse. The arrival time of photons with respect to the laser pulse is then recorded,

building up a histogram which can be fitted to extract a transition lifetime of a QD. The detector has an efficiency of 75% and a response time of 12 ps.

3.4 Device Design with Finite Difference Time Domain Methods

The design of the nanophotonic devices, which were later fabricated, and measured was done in Lumerical Finite Difference Time Domain (FDTD) solutions [91]. Lumerical uses the FDTD method to simulate the behaviour of electromagnetic fields within dielectric media. Core to the FDTD method is the solving of Maxwell's equations across a grid of points in three dimensional space, known as the mesh. This is then iterated over many time steps, with the total time either being chosen by the user or when certain conditions are met relating to the total power remaining in the system. By solving Maxwell's equations in this way the propagation and confinement of light within different structures can be ascertained.

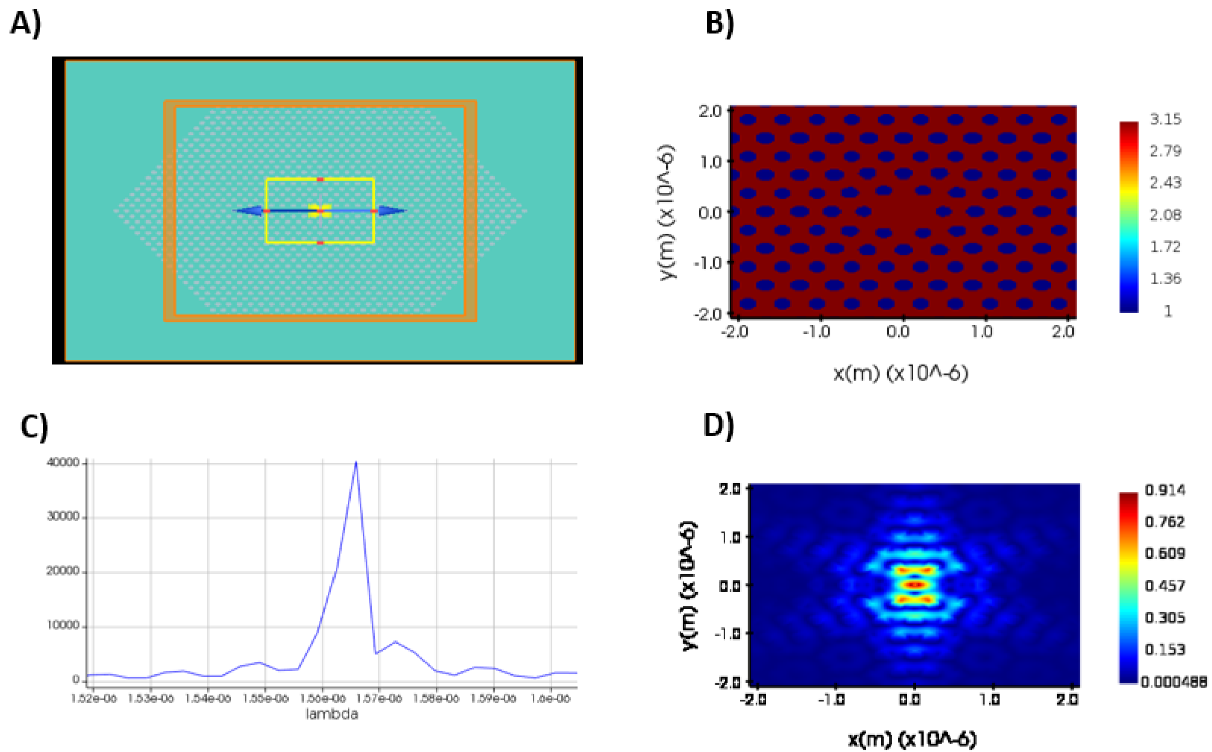

Figure 3.8: *Images of simulations from Lumerical.a) Top down view showing the dipole source in the centre of the H1 cavity. Note, the dipole source can be oriented at 90 degrees to the arrangement shown- this will excite the orthogonally polarised fundamental H1 cavity mode. b) Refractive index profile of the H1 cavity within the photonic crystal. c) Generated spectrum for the fundamental mode of the H1 cavity. d) Generated electric field profile of the fundamental mode.*

In this thesis the confinement of light within InP photonic crystal structures was simulated with a dipole emitter acting as a quantum dot. From these simulations the wavelengths and Q factors of photonic crystal cavity modes for differing device parameters were simulated. Note that the refractive index of InP is set to the low-temperature value of 3.15 in the simulations [92]. Simulations of H1 cavities were performed by the author and simulations of L3 cavities were performed by Dr Catherine Phillips.

3.5 Photonic Crystal Device Fabrication

This thesis includes the fabrication of PhCCs in InP, here the overall device fabrication procedure is introduced. The process is shown in Figure 3.9.

Prior to device fabrication the sample must be cleaned to avoid any contamination which would disrupt later deposition and patterning steps. The sample undergoes an initial clean in hot acetone and IPA and is then exposed to an oxygen plasma ash.

A Silicon Nitride hard mask is then deposited on the sample. Hard mask deposition takes places using plasma enhanced chemical vapour deposition (PECVD). In this process, thin (few hundred nanometer) films of dielectric material are deposited on a wafer. Deposition occurs when reactant gases are ionised in a vacuum chamber due to an RF bias. Radicals from the reactant gases react to form a film on the sample surface. For a Silicon Nitride hard mask, SiH_4 and NH_4 are ionised and react to form $Si3N_4$. For the samples fabricated in this thesis ∼200 nm Silicon Nitride was used as a hard mask.

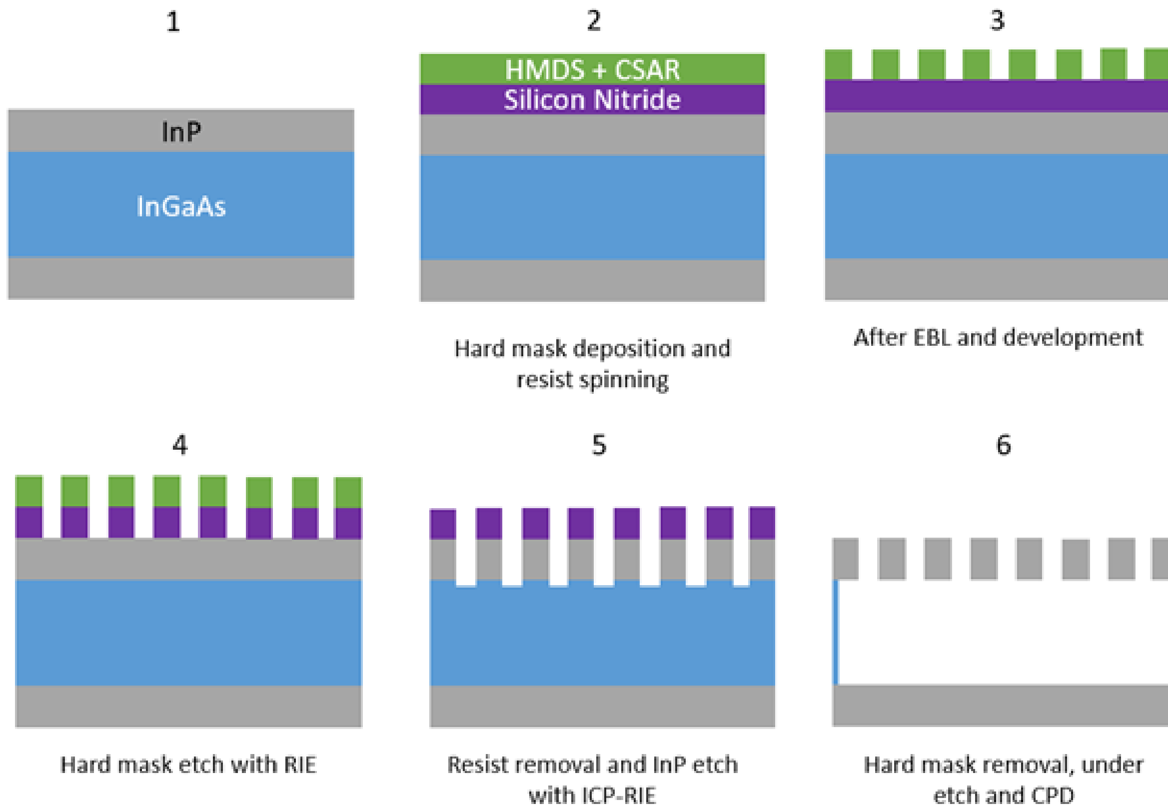

Figure 3.9: *Process overview for PhCC fabrication.*

The next step in electron beam lithography (EBL). For the work presented in this thesis a Wraith EBL system was used. The beam voltage was 50 kV with a resolution of ∼ 10 nm. Hexamethyldisilazane (HMDS) is spin coated onto the sample which aids the adhesion of EBL resist (Undiluted

CSAR) to the hard mask. The EBL resist is then immediately spun onto the sample and the sample is then baked for 5 minutes at 180°C. Patterns are then written into the EBL resist using electron beam lithography. In this process a beam of electrons is incident on the sample surface which causes the exposed CSAR to become soluble. Due to the short wavelength of electrons, features of sizes down to 11 nm can be written using EBL. The sample is then developed in Xylene at 23°C which removes the exposed areas of CSAR.

The pattern in the CSAR is transferred to the hard mask and then into the semiconductor wafer using dry etching techniques. Pattern transfer to the hard mask is done with reactive ion etching (RIE) and the subsequent pattern transfer from the hard mask to the semiconductor is done with inductively coupled plasma (ICP) etching.

Both the RIE etching and ICP etching were performed using an Oxford Instruments PlasmaLab-System100. RIE etching used etchant gases of Ar_2 and CHF_3 whilst the ICP etching using etchant gases of Cl_2, H_2 and Ar_2. For RIE etching, etchant gases are released into a vacuum chamber and ionised with an RF field originating from electrodes at the top and bottom of the chamber. Ionised electrons move up and down the chamber and hit the sample. These electrons build up on the sample giving the sample plate a negative charge which attracts the positively charged etchant ions. These ions then etch away the exposed hard mask, transferring the pattern from the EBL resist to the hard mask. After the hard mask etch the remaining EBL resist is removed with using plasma ashing and then submerging the sample in positrip.

ICP etching uses the same premise as RIE etching but includes an additional RF source. This additional RF source creates a magnetic field which controls the ion flux. Using high ion fluxes enables high etch rates which are appropriate for etching the semiconductor surface exposed by the hard mask pattern. The etch rate can be controlled by adjusting the ICP and RF power and the ICP pressure. Etch rates are calculated by recording the time of etch and the vertical etch distance of etched features. For this work, SEM imaging was required to measure the vertical etch distance for the PhC holes.

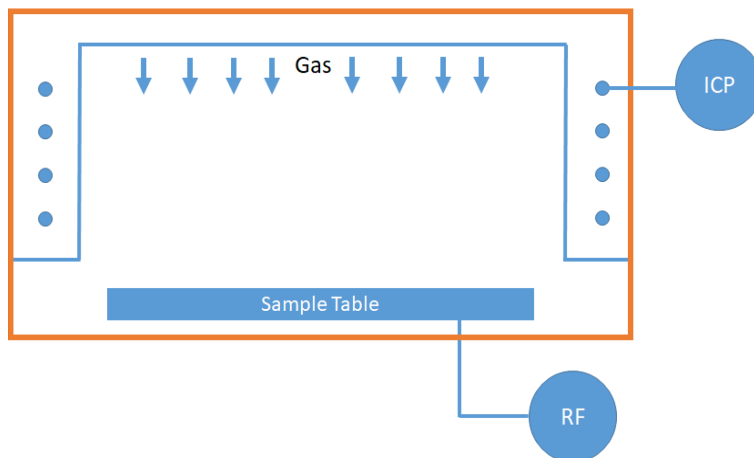

Figure 3.10: *ICP-RIE chamber schematic.*

After the semiconductor etch the hard mask is removed by soaking the sample in 10% hydrofluoric acid solution for 4 minutes. Below the semiconductor membrane is a sacrificial layer which is etched away using Ferric Chloride ($FeCl_3$). The etchant is cooled to $\sim$7 ^{o}C by submerging its beaker in a chiller, etching at lower temperatures allows a high level of etch selectivity to InP. This leaves free standing patterned membranes which must be dried after the wet etching step.

After the sacrificial layer removal samples are submerged in acetone and undergo critical point drying (CPD). The CPD step is used to avoid membrane collapse which can occur when a structure is dipped in water after the sacrificial layer removal step. Droplets from the water dip will stay between the membrane and the substrate and pull the substrate down during drying due to surface tension. As the membranes are only a few hundred nm thick this effect is enough to cause bending or collapse of the membrane.

CPD avoids any surface tension related effects on the membrane by making use of supercritical CO_2. After the sample is submerged in water post-under etch, is it then submerged in acetone and put into a CPD chamber. The chamber is cooled to $<$293K and the chamber pressure is increased to $>$50 Atm. Liquid CO_2 is then introduced to the chamber and replaces the acetone. The chamber temperature is increased to $>$300 K and chamber pressure increased to $>$70 Atm. With these conditions the liquid CO_2 is now a supercritical fluid. The chamber is vented and the supercritical CO_2 transitions to the gaseous phase thus avoiding any surface tension related effects resulting from the liquid-gas phase boundary. CPD was performed by both the author and Dr Rene Dost.

3.6 Sample Inspection

Electron beam based characterisation techniques allow for the imaging of samples down to a resolution of tens of nanometres. This is useful for wafer inspection to assess epitaxially grown layers and post fabrication imaging to ascertain the success of a given process. Additionally, the QDs themselves can be imaged with advanced techniques.

3.6.1 Scanning Electron Microscopy

An important post-fabrication process is scanning electron microscopy (SEM) which allows for imaging resolution down to tens of nanometres. In the fabrication of PhC devices, for example, the quality of etched holes and the success of a wet etch can be assessed. SEM works by using a beam of electrons incident on the sample. These electrons can ionise the atoms within a sample, producing secondary electrons. Such secondary electrons have a low energy which provides a short mean free path so they can only originate from a few nanometres into the sample surface. By using a secondary electron detector an image of the sample can then be built. Here the beam voltage was 10 kV and it should be noted that no sample damage was observed. Brightfield conditions were used, with an aperture size of 30 μm and a typical magnification of 45 kX in order to image PhC holes. All SEM images presented in this thesis were taken by the author.

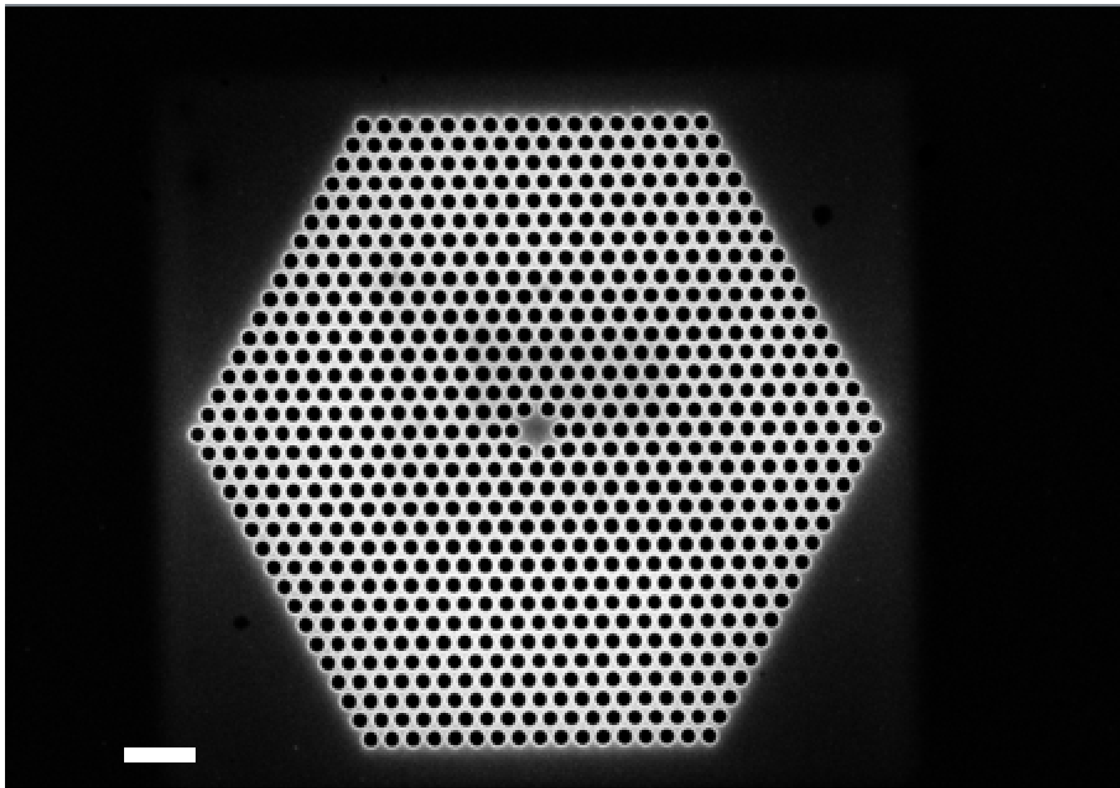

Figure 3.11: *SEM image of a fabricated H1 cavity. The scale bar is 1 μm.*

3.6.2 Energy-Dispersive X-ray Spectroscopy

While SEM can be used to build a highly magnified image of a sample, Energy-dispersive X-ray spectroscopy (EDX) allows for the identification of the elements present in a sample. This technique is particularly useful when trying to identify unknown sample contamination that can occur during fabrication. As with SEM, a beam of electrons is incident on the sample. Another process that can occur is the ionisation of electrons from the inner shell of the atoms within the sample with the subsequent relaxation of higher shell electrons into the hole left behind. This relaxation takes place by the emission of a high energy photon, known as a characteristic X-ray, of an energy equivalent to the difference in energy of the electron shells. By detecting the characteristic X-ray spectrum, the elemental makeup of a sample can be identified due to the energy of these X-rays matching the atom-specific orbital energies.

3.6.3 Cross-sectional scanning tunnelling microscopy

Finally, there is cross-sectional scanning tunnelling microscopy (X-STM) which can be used to image QDs down to atomic resolution. X-STM takes place within a high vacuum and uses a very sharp tip close to the sample surface. A bias is applied between the tip and the sample which causes electrons to tunnel from the tip to the sample. This is known as the tunnelling current which is used to form an image of the surface being probed. Samples are cleaved so that the growth layers can be accessed by the tip. X-STM measurements presented in this thesis were performed by Raja Sekhar Reddy Gajjela and Paul M. Koenraad from Eindhoven University of Technology.

Chapter 4

Characterisation of Quantum Dots

This chapter presents micro-PL measurements and analysis of QD samples. The micro-PL measurements formed an important characterisation step for the QD growth as such measurements were able to confirm whether the individual QDs were emitting. Additionally, the wavelengths and linewidths of the QD emission could also be characterised. Where it was desirable to measure narrow linewidths which indicate high quality QD growth as there will be fewer defects close to the QDs which would cause linewidth broadening via spectral wandering.

Measurements were performed in the closed cycle cryostat system presented in Chapter 3. Samples were measured using high and low power micro-PL, as explained in Chapter 3. The general procedure was to take one high power micro-PL measurement in order to assess the different layers that were emitting in the sample. Then low power micro-PL was performed on at least four locations on a sample in order to establish whether the QDs were emitting. Low power micro-PL spectra shown in this chapter are representative of the multiple locations measured.

With the overall aim of the project to achieve Purcell enhancement around 1550 nm it was aimed to have QDs emitting within or close to the telecom C-band. It was also desirable for these QDs to have narrow linewidths in agreement with previously reported values of 50 μeV or less [93], 130 μeV [94] and a mean value of 59$\pm$24 μeV [56].

An additional purpose of this work was the more general aim of characterising the effect of changing growth conditions on the emission of the QDs. Telecom C-band wavelength InAs/InP QDs grown

by DE in MOVPE is a technique developed relatively recently with the first work being published in 2017 [67]. As such there is a lack of published work outlining the effect of growth parameters on their emission. Here the crystallisation temperature and capping thickness for QD growth are investigated in micro-PL measurements. Furthermore, the growth is developed by growing QDs on 5 nm InGaAs and InGaAsP interlayers and the effect on dot emission investigated.

Finally, QDs are grown within DBR structures which explicitly reveals the presence of a background emission problem. This background emission is characterised and its potential causes are investigated.

Sample growths were performed by Dr Elisa Sala, AFM measurements were performed by Dr Young In Na, TEM measurements were performed by Professor Richard Beanland and X-STM measurements were performed by PhD candidate Raja Gajjela in Professor Paul Koenraad's group at Eindhoven.

4.1 InAs/InP Quantum Dots

Prior to the work presented in this thesis, growth experiments were conducted by Dr Elisa Sala and Dr Young In Na to investigate the formation of InAs QDs on InP by DE. Crucial to growth of QDs by DE is the formation of Indium droplets on the InP buffer, it is from these droplets that QDs are formed. Therefore, the size and density of the droplets directly influences the size, corresponding emission wavelength, and density of the QDs. The growth conditions need to be such that the deposited Indium can diffuse and coalesce to form droplets.

Investigations were conducted into droplet formation by varying the following growth parameters; Indium deposition time (s), substrate temperature (^{o}C) during Indium deposition, TMIn flow rate (sccm) and growth interruption time (s). The established values are summarised in Table 4.1.

Figure 4.1 presents an example AFM image of a droplet sample where the growth conditions are those presented in Table 4.1. The droplet density was measured to be 3x10^{9} cm^{-2}, this value was the maximum achievable density from the growth experiments. The mean droplet height and width was (35±7) nm and (6±2) nm as measured by AFM, this was a standard distribution for droplet

Parameter	Value
Indium Deposition Time	35 s
Indium Deposition Temperature	320 ^{o}C
TmIn Flow	20 sccm
Growth Interruption Time	60s

Table 4.1: *Summary of investigated growth parameters for the formation of Indium droplets on an InP buffer layer*

growth.

QDs were then formed by performing the full growth procedure where droplets are grown on an InP buffer using the established growth parameters. The droplets were then crystallised by increasing the temperature from 350 ^{o}C to a given crystallisation temperature over a 2-minute time period under an Arsine flow of 0.5 sccm. The sample was then held at the crystallisation temperature for a further 5 minutes. This was followed by 20 nm InP cap growth at the crystallisation temperature and 80 nm InP spacer growth at 600 ^{o}C.

4.1.1 Crystallisation Temperature

The temperature at which the QDs were crystallised with Arsine was varied between 480 ^{o}C and 520 ^{o}C and micro-PL measurements were taken for each sample. Figure 4.2A shows high power micro-PL spectra of each temperature. Each sample shows InP emission around 875 nm and emission due to the $InAs_xP_{1-x}$ quasi-wetting layer between 900 and 1200 nm. X-STM measurements performed by Raja Gajjela estimate that the layer varies in thickness between 2-4 monolayers and contains 30-40% Arsenic [95].

The QD ensemble-type emission can be seen for wavelengths longer than 1400 nm for the crystallisation temperatures of 500 ^{o}C and greater. No QD ensemble-type emission is observed for the crystallisation temperature of 480 ^{o}C which indicates that carriers are not being captured by the QDs but instead being captured by the quasi-wetting layer.

The spectra show that as the crystallisation temperature is increased, the emission from the quasi-

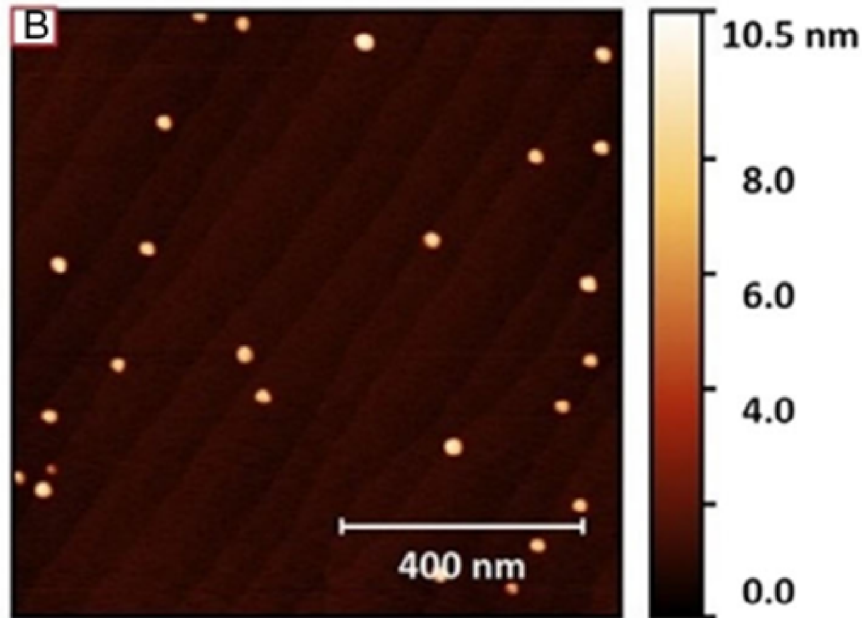

Figure 4.1: *AFM image of Indium droplets formed using the growth parameters presented in Table 4.1. From [95] with permission.*

wetting layer becomes weaker and blue shifts whilst the QD emission is shown to increase in intensity. Figure 4.2B gives a low power micro-PL comparison for the various crystallisation temperatures, it can be seen that a crystallisation temperature of 520 ^{o}C gives emission from the QDs at low powers which indicates efficient carrier capture by the QDs. This can explain the reduction in quasi-wetting layer intensity with increasing crystallisation temperature.

The QD lines are seen to be sitting on a weak background which is seen as a hump in the spectrum for wavelengths longer than 1500 nm. It is proposed that this background contributes to the emission for wavelengths longer than 1400 nm seen in the high power spectrum in Figure 4.2A. As such, this emission will be referred to as "QD-related emission" as it is unclear if it solely originates from the QD ensemble. For crystallisation temperatures below 520 ^{o}C no emission from the QDs or background emission can be seen at low powers.

AFM characterisation of the QD samples presented here shows the existence of an etched pit around the base of the QDs for crystallisation temperatures above 500 ^{o}C. This etching likely originates from the high crystallisation temperatures dissolving the InP surface and In being incorporated into the droplet [95]. Figure 4.3 shows AFM measurements of surface QDs crystallised at 510 ^{o}C and

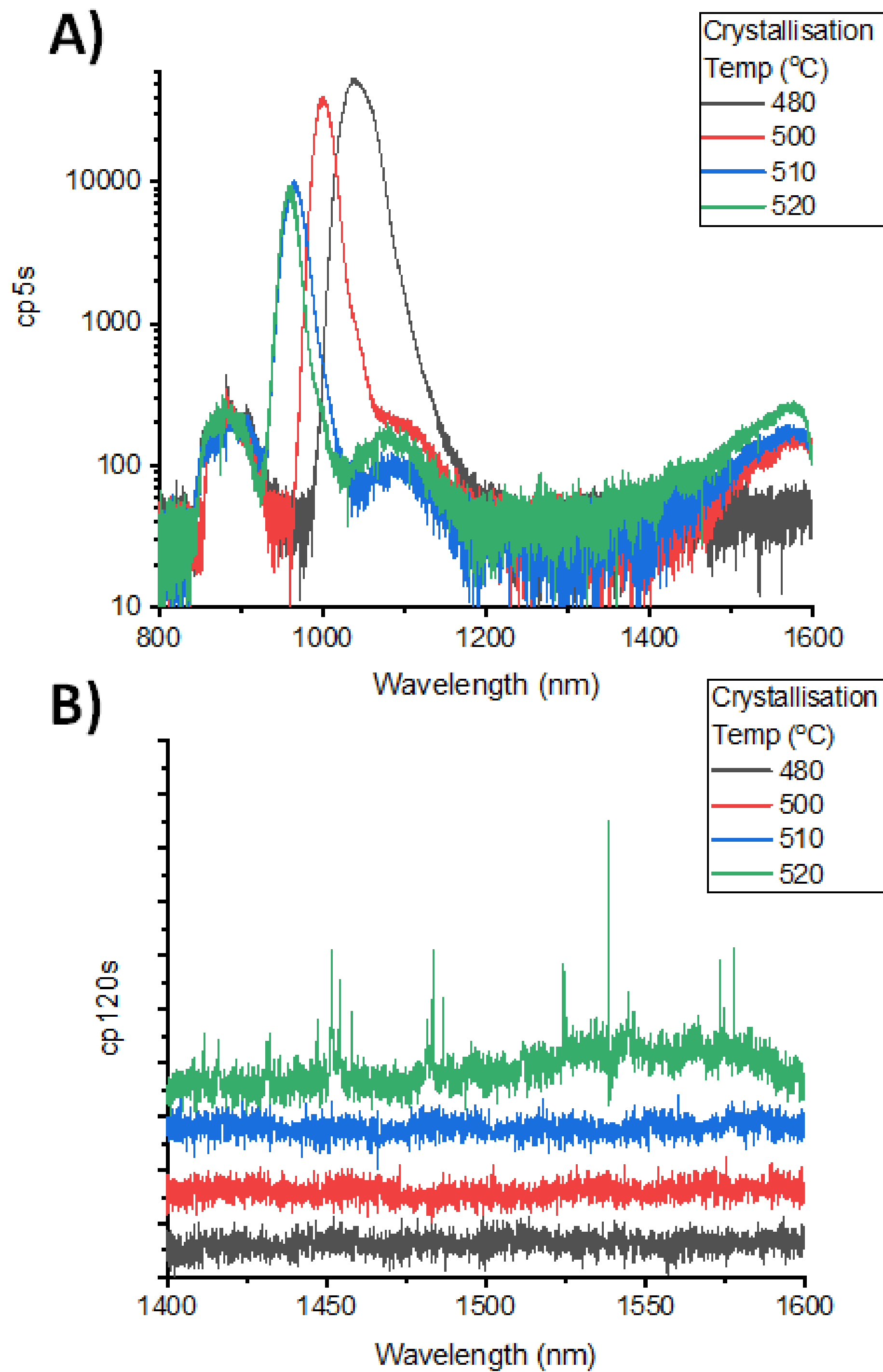

Figure 4.2: *A) High power micro-PL for samples with crystallisation temperatures from 480 °C to 520 °C. B) Low power micro-PL spectra for the same set of samples. Emission from the QDs can be seen for a crystallisation temperature of 520 °C.*

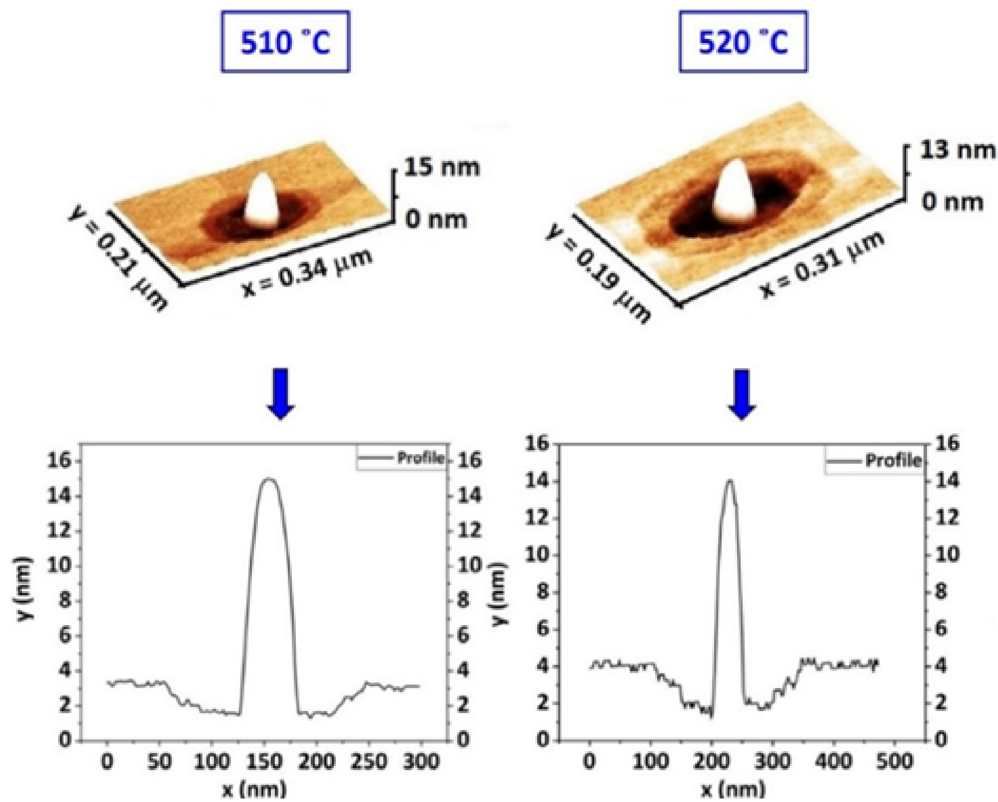

Figure 4.3: *Example AFM images for crystallisation temperatures of 510 ^{o}C and 520 ^{o}C. Both show the QDs to be in an etched pit. The lower temperature growths did not feature an etched pit. Reprinted with from [95].*

520 ^{o}C.

The depth of etching around the QDs is 1 nm, 1.8 nm and 2.7 nm for crystallisation temperatures of 500 ^{o}C, 510 ^{o}C and 520 ^{o}C, respectively. This increased etching would reduce the average quasi-wetting layer thickness thus causing the blue shifting seen in Figure 4.2A. We can also conclude for the growth presented here, the ability to measure QD emission at low powers is related to the presence of the etched pit around the QDs. Such etched pits have also been observed in later works featuring InAs/InP QD growth by DE in MOVPE. These QDs also showed emission when measuring in low power micro-PL [96].

Low power micro-PL measurements were taken from 22 different locations on the 520 ^{o}C crystallisation temperature sample with a total of 51 single lines measured. A histogram of linewidths is shown in Figure 4.4A, the mean linewidth is (80±27) μeV where the uncertainty is the standard deviation of the linewidth values. This matches well with the values published in the literature as set

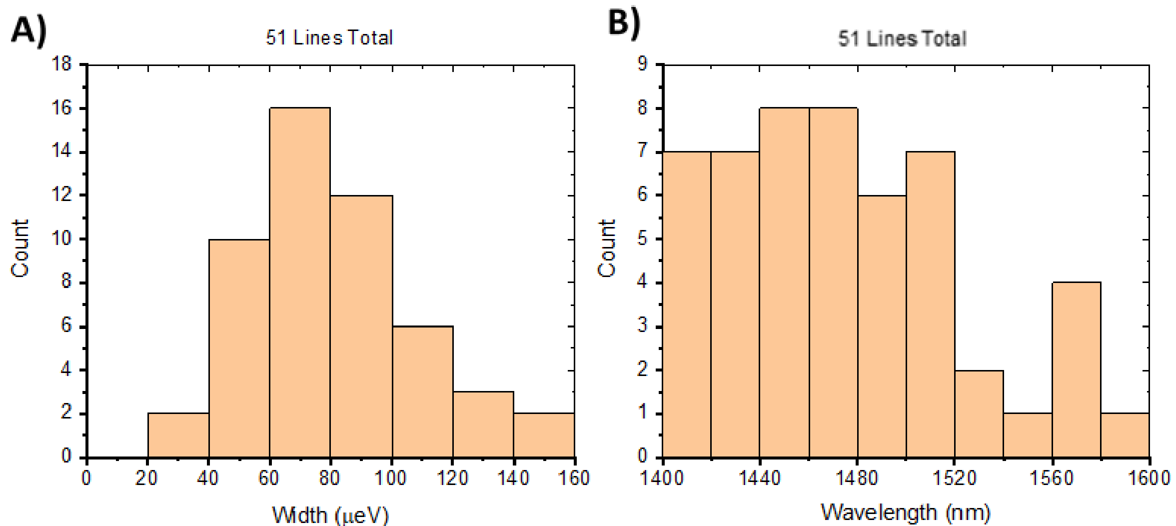

Figure 4.4: *A) Linewidths for 51 QD lines measured across 12 locations. B) Wavelength distribution for the same set of QDs as in Figure 4.4A.*

out at the start of this chapter. Additionally, there are lines that are resolution limited with widths less than 50 μeV, where the spectrometer resolution is defined as the width in energy separating two pixels at 1550 nm.

The wavelengths of the same population of lines are plotted in a histogram in figure 4.4B. This shows the majority of QDs lines to be at wavelengths shorter than 1500 nm. Though there are still lines present near to and within the telecom C-band. It can be seen that the InAs/InP QDs grown are of good optical quality with relatively narrow linewidths.

4.1.2 Varying Cap Thickness

Further QD growths were performed with the capping layer thickness varied. This has been demonstrated for InAs QDs on InP with varying InAlGaAs cap thicknesses. A thicker cap produced larger QDs which in turn was showed to red shift the QD ensemble from PL measurements [97]. The aim here was to investigate this effect for the InAs/InP QDs measured in the previous section [98]. The samples featured caps of thickness, 8 nm, 10 nm, 15 nm and 20 nm, respectively.

The samples were imaged with TEM which allowed the dimensions of the QDs to be measured. Figure 4.5 shows the average QD height and width as a function of capping thickness, showing

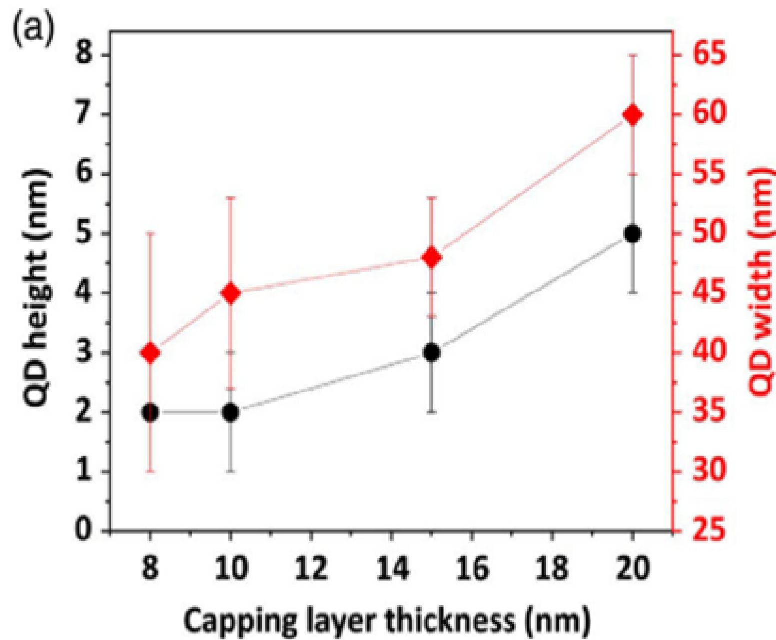

Figure 4.5: *Average QD heights and widths for various capping thicknesses. The QD heights and widths are increase with increasing cap thickness. From [98].*

thinner caps produce QDs of smaller dimensions.

The DE growth method produces QDs of varying size due to their self-assembly. By using a thinner cap, only the QDs lower in height are fully buried by the InP cap. The large QDs are not fully buried and therefore protruding out of the cap. These protruding parts of the QDs are then evaporated away when the temperature is increased from 520 ^{o}C to 620 ^{o}C for the InP spacer growth. Uncapped QDs measured in AFM were measured to have heights in the range of 10-15 nm, whereas we can see in Figure 4.5 that the height of the QDs after capping are reduced compared to these values.

Additionally, it can be seen that the QD width is less for thinner capping layers. The reduced QD heights and presence of wider QDs for thicker caps can be explained by the QDs going through a demolition process during the capping. For InAs/GaAs QDs it has been proposed that during the capping, Indium from the uncapped QD flows out from its top causing a height reduction for the QDs [99]. This process is believed to occur here where Indium and Arsenic are released from the QD and then accumulate at the base of the QD. This causes a reduction in QD height and increase in its width during the capping step.

Furthermore, it can be seen that the QD heights in Figure 4.5 are much lower than the given height

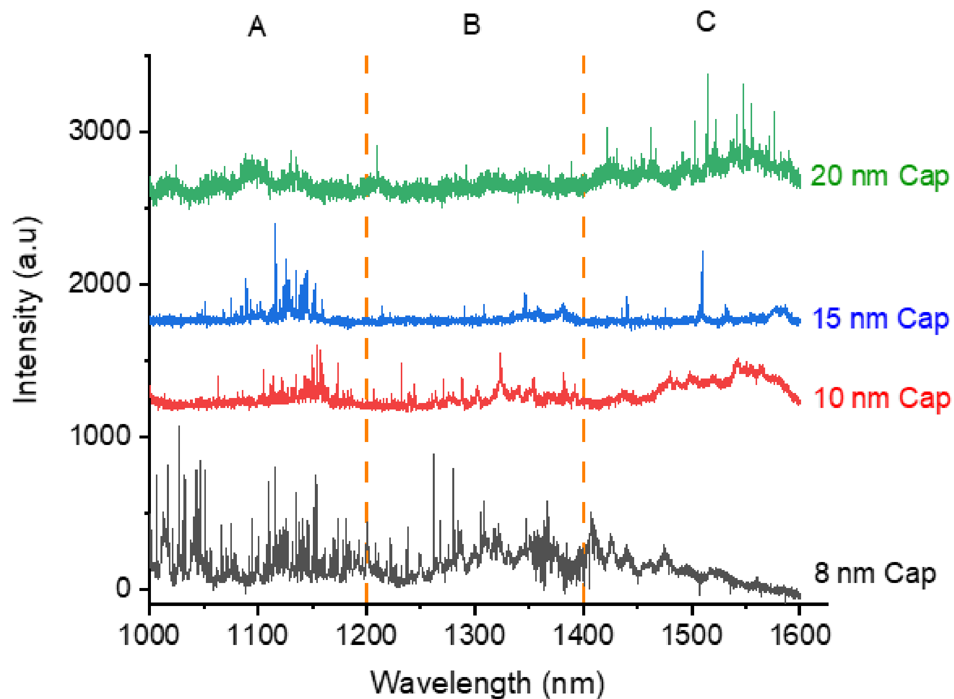

Figure 4.6: *Low power micro-PL measurements for QD caps of thickness 20 nm (green), 15 nm (blue), 10 nm (red) and 8 nm (black). QD emission lines are seen at longer wavelengths for thicker caps, reflecting the increase in QD size.*

of the InP cap. This is believed to be due to the actual InP cap thickness being less than the nominal thickness. The nominal thickness is based on growth rates of thick InP layers grown on InP. The InP growth rate is believed to be reduced when growing on the uncapped QDs due to the growth surface consisting of the QDs and the $InAs_xP_{1-x}$ quasi-wetting layer instead of planar InP.

Figure 4.6 shows low power micro-PL spectra for samples with cap thickness of 8, 10, 15 and 20 nm. Three wavelength regions are labelled, A is 1000-1200 nm, B is 1200-1400 nm and C is 1400-1600 nm. The samples consistently feature a population of sharp lines in the wavelength range of 1100-1200 nm, these are attributed to either smaller QDs or emission from exciton trapping at thickness fluctuations of the order of monolayers in the quasi-wetting layer [100]. These thickness fluctuations have been observed in X-STM measurements of the QD samples presented in this thesis [101].

For the 20 nm cap sample, emission from QDs can be seen covering the telecom C-band and up to the detector cut off wavelength of 1600 nm. The 15 nm cap features shorter wavelength QDs with a maximum emission wavelength of 1510 nm. The 10 nm and 8 nm cap samples shows a greater

population of QDs in wavelength region B with the 8 nm cap showing the shortest wavelength QD emission.

The blue shifting of QD emission wavelengths with reducing cap thicknesses is indicative of a population of smaller QDs. Additionally, there is a dearth of emission in wavelength region A for the 20 nm cap sample. We would still expect there to be smaller QDs present here but this suggests that the larger QDs present in these samples capture carriers more effectively.

Finally, for the 8 and 10 nm capped samples, there is some broad emission in wavelength region C. This is likely due to carrier recombination in QDs that are not fully formed when using thinner caps so are not detected as the sharp emission lines expected of high quality QDs.

Overall it has been shown that changing the thickness of the InP cap gives a control parameter which can change the size of the buried QDs. It can be seen that this gives the ability to control the emission wavelength of the QDs over a large range. Emission in the telecom C-band is achievable with a 20 nm cap whilst emission down to the telecom O-band is achieved using 8 nm and 10 nm caps, demonstrating a versatile QD growth method.

4.2 QDs grown on Interlayers

One of the advantages of DE compared to SK QD growth is the lack of wetting layer required for the formation of the QDs. Such a layer can produce unwanted carrier recombination which stop carriers from recombining in the QDs and can act as a layer interconnecting QDs [52]. However, this is not the case for InAs/InP QDs due the As-P exchange occurring during the droplet crystallisation step which produces an unintentional quasi-wetting layer. By growing the QDs on an $In_{0.53}Ga_{0.47}As$ interlayer, lattice matched to InP, it was aimed to stop the formation of this layer by suppressing the As-P exchange reaction that occurs for InAs QDs grown on InP [102].

Such an approach has been used before to successfully grow of InAs QDs on a 2 nm thick InGaAs layer on InP via the SK growth mode in MOVPE [103]. Furthermore, there has also been a demonstration of InAs QDs grown by DE on InGaAs using MBE [104]. This section presents micro-PL measurements of InAs QDs grown on a 5 nm InGaAs interlayer on InP using MOVPE. This

Indium Deposition Time (s)	**Mean Height (nm)**	**Mean Diameter (nm)**	**QD Density (cm^{-2})**
20	9.2 ± 1.7	53 ± 21	$6x10^8$
25	6.2 ± 1.7	47 ± 16	$5x10^9$
35	5.4 ± 2.0	41 ± 21	$1x10^{10}$

Table 4.2: *Uncapped QD height, width and density for Indium deposition times of 20s, 25s and 35s.*

growth method appears to supress the formation of the quasi-wetting layer and high QD densities ($\sim 10^{10}$ cm^{-2}) are also achieved.

Measurements of QDs on an alternative interlayer formed of InGaAsP are also introduced. Due to the timing of their growth development, the full characterisation of the various growth parameters is out of the scope of this project. However, such QDs are used in Chapter 6 and form a useful alternative material system to the InGaAs interlayer.

4.2.1 InGaAs Interlayer

The growth procedure is largely the same as stated in Chapter 3 apart from the inclusion of a 5 nm thick InGaAs layer after the InP buffer growth. In order to achieve the formation of droplets, the temperature for the Indium deposition was increased from 350 ^{o}C to 400 ^{o}C. The study by Stevens et al showed Indium diffusion to be reduced on an InGaAs surface compared to InP [104], so a higher temperature is required for the Indium to have enough mobility in order to form droplets.

Samples were grown with Indium deposition times of 15, 20, 25 and 35s. AFM measurements on surface are shown in Figure 4.7 and revealed no etch pit formation as seen in the InAs/InP QDs. Values for QD diameter, height and density are shown in Table 4.2.

Overall it can be seen that no QD formation occurs for a 15s Indium time, QD formation occurs for 20, 25 and 35s Indium supplies times. The AFM measurements show that for increasing Indium supply times, the QD size reduces and the QD density increases. Additionally, no droplet etching is observed for these QDs in contrast to the InAs/InP QDs.

What should be noted from these measurements is that the final QD density for the 25s and 35s Indium time samples is over an order of magnitude greater than the initial droplet density ($\sim 3x10^8$

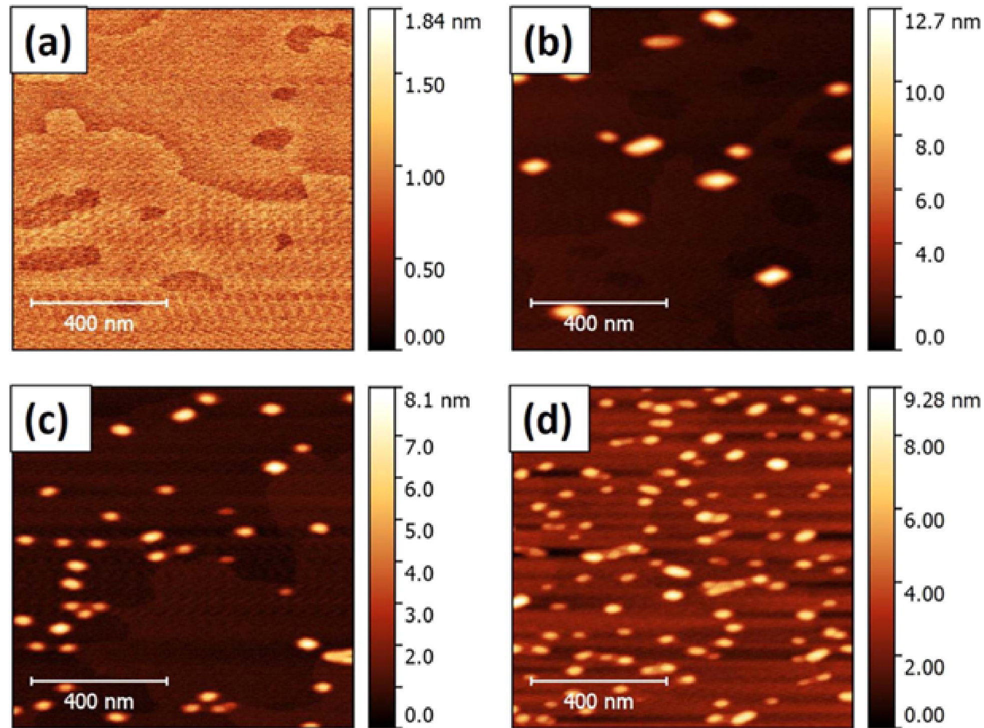

Figure 4.7: *AFM measurements for Indium deposition times of A) 15s B) 20s C) 25s D) 30s. QDs are seen to form for Indium depostion times greater than 15s. From [102].*

cm^{-2}). For the previously presented InAs/InP QDs the QD density is slightly reduced ($\sim$9x10^{8} cm^{-2}) compared to the initial droplet density ($\sim$3x10^{9} cm^{-2}).

An explanation for this increase in density originates from non-droplet Indium being present on the InGaAs surface after the Indium deposition stage. This Indium would then coalesce and crystallise during the temperature increase and crystallisation step resulting in additional QD formation from the non-droplet indium. This modified growth method leads to high QD densities being achieved. It is possible that this does not occur for QDs grown on InP due to the increased Indium mobility causing all Indium to form droplets.

High power micro-PL spectra for 20s, 25s and 35s Indium supply time are shown in Figure 4.8A,B and C respectively. All samples feature emission from the InP around 900 nm and this is seen to be weaker for the 35s Indium supply sample. This is possibly due to the high density of QDs causing even more carrier relaxation from the InP to the QDs. The samples do not feature emission from the quasi-wetting layer that is seen in the InAs/InP QD samples. This indicates that the inclusion of the InGaAs layer suppresses the As-P exchange between the InP and Arsine during the droplet

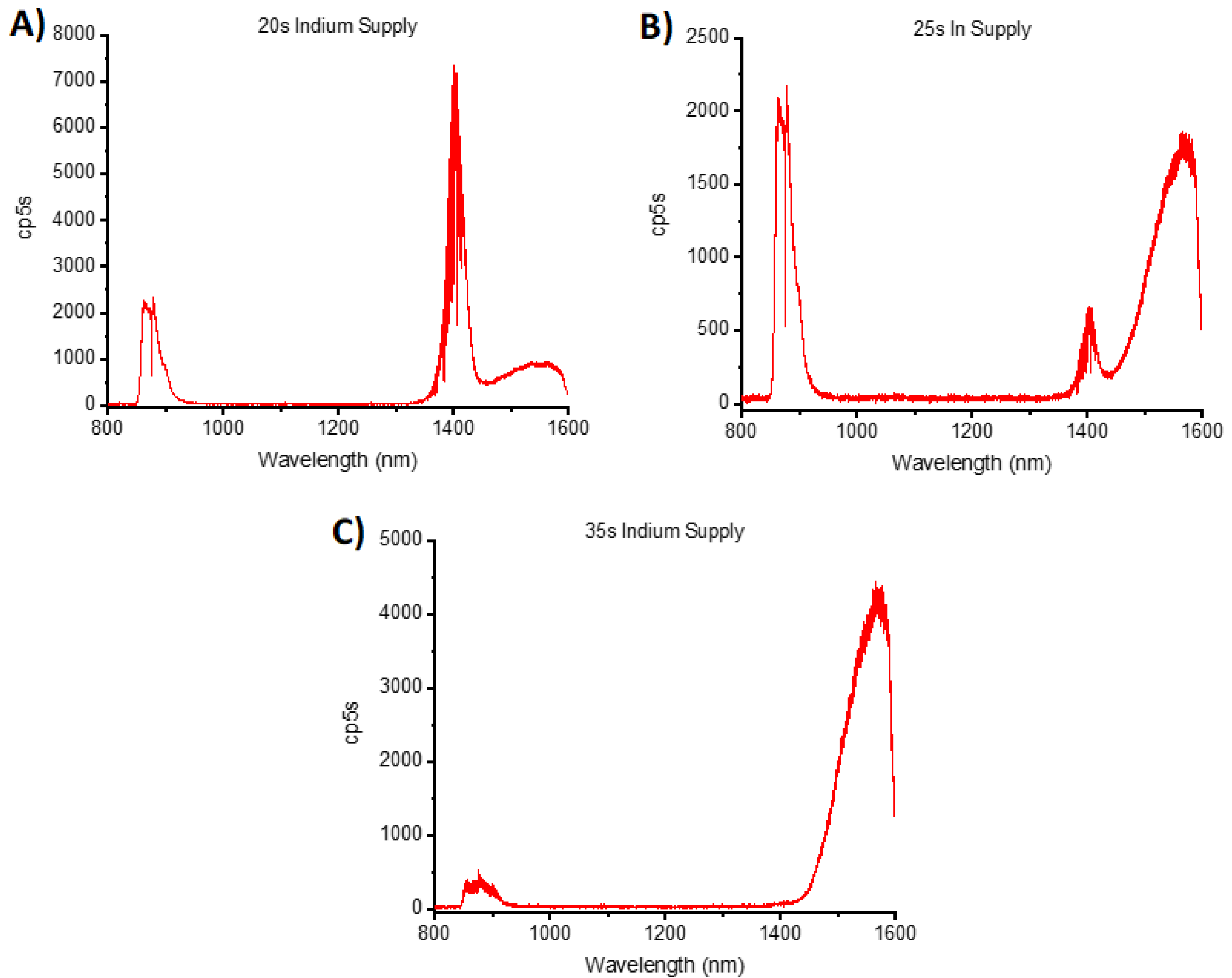

Figure 4.8: *High power micro-PL measurements for A) 20s B) 25s C) 35s Indium deposition times. The QD-related emission intensity is seen to increase with increasing Indium deposition time. This is reflective of the increase in density of the QDs.*

crystallisation stage. This was also confirmed by X-STM measurements where the quasi-wetting layer was seen to be 1-2 monolayers thick compared to the 2-4 monolayers for the InAs/InP QDs [101].

For the 20 and 25s Indium supply, emission from the 5 nm InGaAs peak can be seen at 1400 nm, this can also be seen as a very weak shoulder in the 35s Indium supply sample. Emission relating to the QDs is seen for all samples for wavelengths greater than 1400 nm. As the Indium supply time is increased the emission from the InGaAs interlayer gets weaker and the QD emission becomes stronger. This implies a higher levels of carrier capture from the QDs as their density increases.

Representative low power micro-PL spectra of the 20, 25 and 30s Indium supply samples are pre-

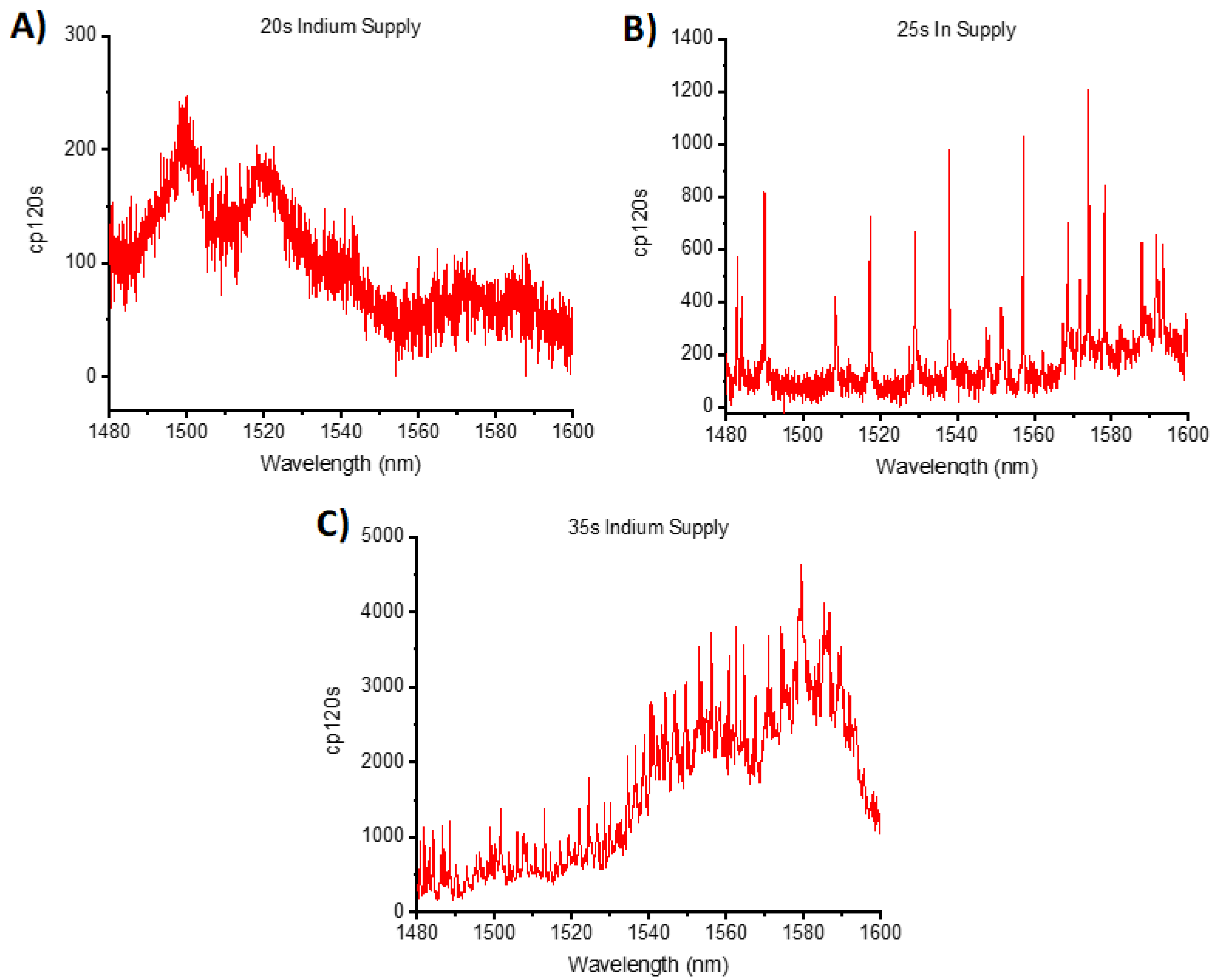

Figure 4.9: *Low power micro-PL measurements for A) 20s B) 25s and B) 25s Indium deposition times. Sharp emission lines are seen for the 25 and 35s Indium deposition times.*

sented in Figure 4.9 A,B and C respectively. The 20s Indium supply time sample shows no sharp emission lines. This could due to the QDs the large size causing charge noise to the extent that emission lines are significantly broadened or the large size causing their emission wavelength to be beyond the range of the InGaAs detector.

Low power micro-PL measurements were taken for 15 locations for the 25s Indium supply sample and 7 locations for the 35s In supply time samples. Figure 4.10A and b gives the wavelength and linewidth distribution of a total of 63 fitted lines. Figure 4.10A reveals the majority of lines to be at wavelengths greater than 1500 nm, this is an improvement on the InAs/InP QDs with respect to having QDs in the telecom C-band.

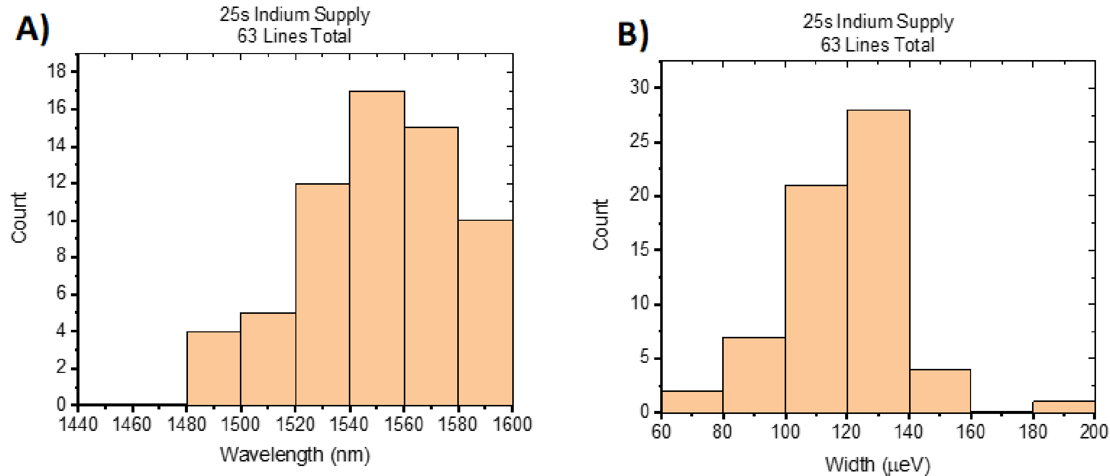

Figure 4.10: *A) Wavelengths of 63 QD lines for 25s Indium deposition sample, showing the majority of lines to emit at wavelengths greater than 1500 nm. B) Corresponding linewidths of measured QD lines.*

The linewidths presented in Figure 4.10B give a mean value of (119±18) μeV, this is a larger value than for the InAs/InP QDs which had an average linewidth of (80±27) μeV. A key difference between the two types of QDs is the presence of an etched pit around the QDs for the InAs/InP QDs which does not occur for the InAs/InGaAs/InP QDs. The etching process that caused the etched pits may remove defects close to the QDs which would improve their local environment and reduce unwanted spectral wandering from the defects.

Figure 4.11A and B gives the measured wavelengths and linewidths for the 35s Indium deposition sample. Figure 4.11A shows the presence of lines with wavelengths shorter than 1400 nm. The shorter emission wavelengths are attributed to a population of smaller QDs for these growth conditions as seen in the AFM measurements presented in Table 4.2. Figure 4.11B gives a mean linewidth of (130±34) μeV. These broader values for linewidth, compared to the 25s Indium sample, may originate from the high density of QDs. Here each QDs would then be in closer proximity to other QDs and potential defects which would broaden emission through spectral wandering.

Overall we can see that growing on the QDs on an InGaAs interlayer has suppressed the formation and emission of the quasi-wetting layer and resulted in QDs without etched pits. The linewidths of these samples are broader than the InAs/InP QDs which did feature etched pits around the QDs. These results indicate that the etched pits may be fundamental to having good quality QDs.

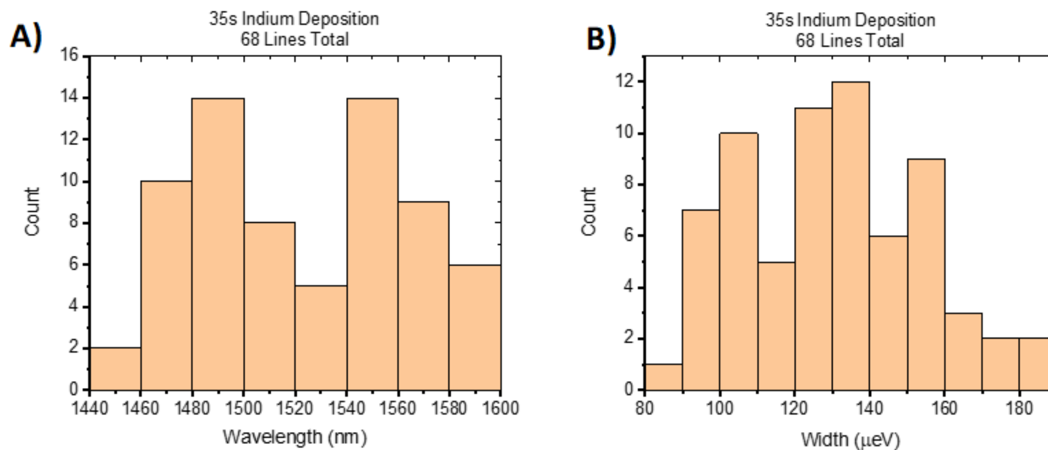

Figure 4.11: *a) Wavelengths of 68 QD lines for the 35s Indium deposition sample, this sample shows an increased proportion of lines with emission wavelengths shorter than 1500 nm compared to the 25s Indium deposition sample. b) Corresponding linewidths of measured QD lines.*

These QDs also feature a greater proportion of QD lines emitting at wavelengths longer than 1500 nm which helps to fulfil the aim of having QDs emit in the C-band. Finally, these samples allow for optically active QDs with high densities of $\sim10^{10}$ cm^{-2} which indicates a growth mechanism that is altered compared to the standard DE method. This is an improvement upon the InAs/InP QDs where 9x10^{8} cm^{-2} represented the highest QD density.

4.2.2 InGaAsP Interlayer

Growth experiments performed by Dr Elisa Sala and Dr Young In Na also resulted in the growth of high density (1.4x10^{10} cm^{-2}) QDs using a 5 nm $InGa_{0.281}As_{0.608}P$ interlayer, lattice matched to InP. This allowed further investigations into the QD growth as InGaAsP acts as an intermediate material between InP and InGaAs.

Figure 4.12A show a high power micro-PL measurement, where InP emission can be seen at 875 nm and the QD-related emission is seen from 1300 nm. No quasi-wetting layer emission can be seen which suggests that the InGaAsP interlayer suppresses the As-P exchange and the quasi-wetting layer formation.

Figure 4.12B shows a low power micro-PL spectrum where the exposure time is 90s, the spectrum shows sharp QD emission lines across a wide wavelength range from 1300 nm to 1600 nm. The high

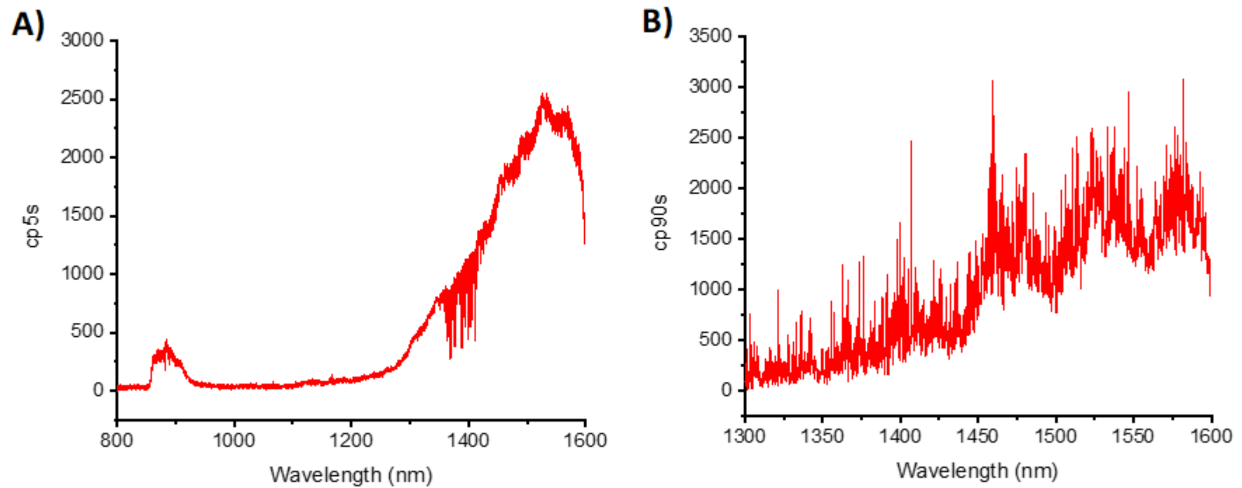

Figure 4.12: *A) High power micro-PL spectrum for QDs on InGaAsP. InP emission is at 875 with the QD-related emission starting from 1300 nm. B) Low power micro-PL spectrum showing a high density of QD emission lines from 1300 nm.*

density of QDs can be seen from the large number of lines.

Figure 4.13A shows wavelengths of QDs measured in three locations, these QDs are seen to have a broad wavelength range with QDs emitting at wavelengths shorter than 1400 nm. This indicates that some of the QDs on InGaAsP may be smaller than those on InGaAs. Figure 13b gives the linewidths of same set of QDs, the mean linewidth is (92 ±42) μeV. The linewidths for QDs on InGaAsP are narrower than for QDs grown on InGaAs presented in the previous section. It should also be noted that no etched pit formation was measured in AFM measurements for this sample. This indicates that the previous conjecture that narrow linewidths are related to the presence of the etched pit may not be the case for in the limited number of samples grown here. Further X-STM and TEM investigations are required to get a full characterisation of these samples to compare to the InAs/InP QDs and the InAs/InGaAs/InP QDs.

4.3 Quantum Dots on DBRs

So far the growth of InAs/InP QDs and InAs QDs on interlayers have been measured and characterised. In this section InAs/InP QDs as part of a DBR structure are presented. In the work described so far, QD count rates were generally <10 cps as measured on the spectrometer software-hence a requirement for 120 s integration times. This low count rate is partially due to the objective

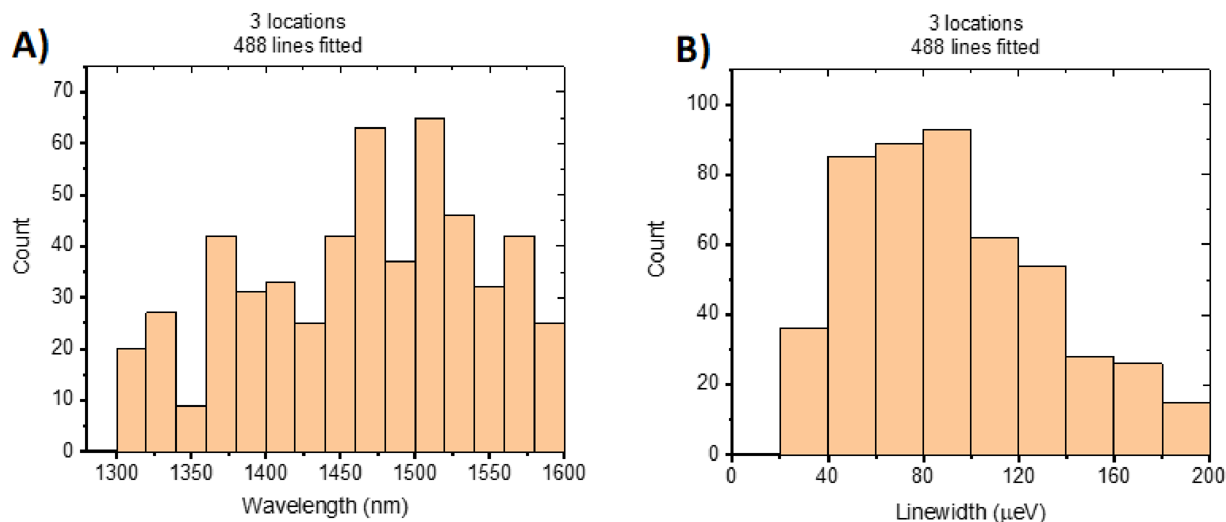

Figure 4.13: *a) Wavelengths for QDs grown on InGaAsP. These QDs are seen to emit over a broad wavelength range. b) Corresponding linewidths, showing the presence of lines with resolution limited widths (<50 μeV).*

lens used in the flow cryostat system having a transmission of ~55% at 1550 nm but is also a general feature of micro-PL measurements on QDs which emit around 1550 nm. This is due to the InGaAs detectors required for these measurements featuring relatively high noise levels. As discussed in Chapter 2, the use of DBRs featuring AlInGaAs and InP mirrors and growing the QDs in an InP cavity can result in QD count rate increases of an order of magnitude.

The QDs were grown on a wafer provided by IQE. The wafer schematic is shown in Figure 4.14A. It consists of a 300 nm InP buffer with 18x pairs of AlInGaAs and InP of a thickness 113.64 nm and 124.76 nm, respectively. These thicknesses are equal to a $\lambda/4$n, where the wavelength is 1550 nm and n is the refractive index of the respective material. This is followed by an additional $\lambda/4$n layer of AlInGaAs and a 50 nm InP layer. Figure 4.14B shows the reflectivity spectrum of white light on a wafer which shows the DBR stop band centred around 1550 nm.

Growth was then performed on the wafer shown in Figure 4.14A, this consisted of 74.6 nm of InP which completed the $\lambda/4$n InP layer. InAs QDs were grown on the InP and a final 623.8 nm of InP, equivalent to $\lambda/$n, was grown on the QDs. The final structure is shown in Figure 4.15, overall the structure consists of 18 $\lambda/4$n AlInGaAs/InP mirror pairs with an additional AlInGaAs $\lambda/4$n layer. Onto these mirror pairs is grown a $\lambda/4$n InP cavity where the QDs are grown at $\lambda/4$n within the cavity.

A)

B)

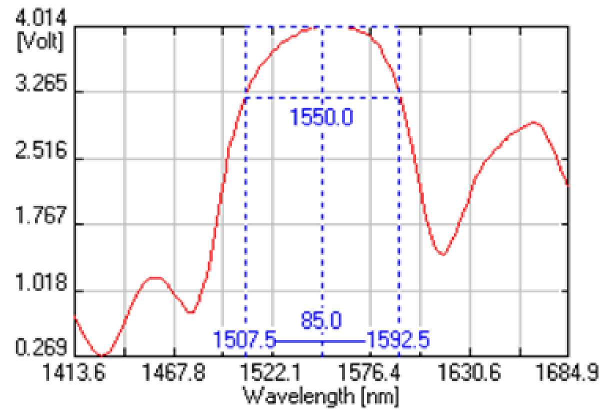

Figure 4.14: *a) Schematic of DBR structure on which the QDs were grown. B) Reflectivity spectrum provided by IQE showing the centre of the DBR stop band at 1550 nm.*

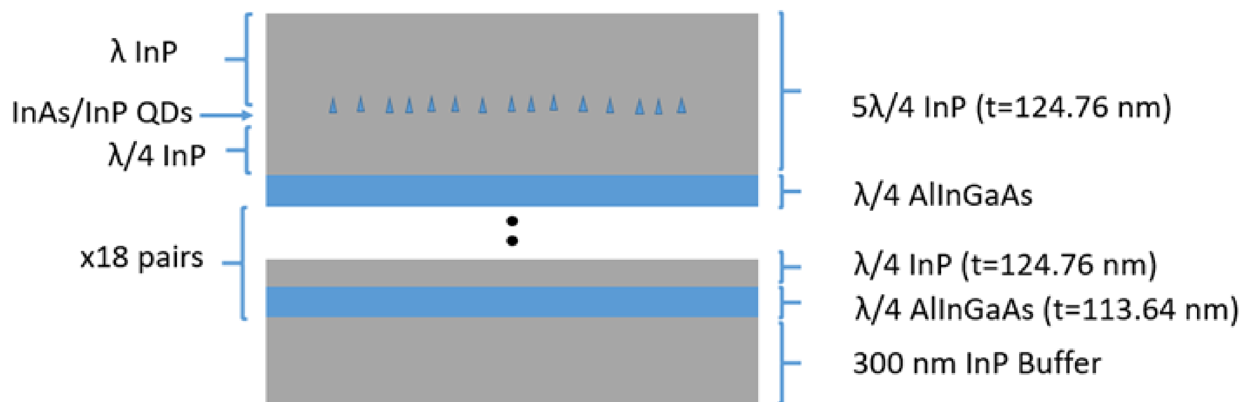

Figure 4.15: *Final DBR growth structure. This consists of an 18 pair AlInGaAs/InP DBR with an additional mirror pair. This is followed by a $\lambda/4$ InP layer onto which QDs are grown. This is finished with a λ/n InP layer. So overall, the QD layer is at $\lambda/4n$ in a $5\lambda/4n$ InP cavity.*

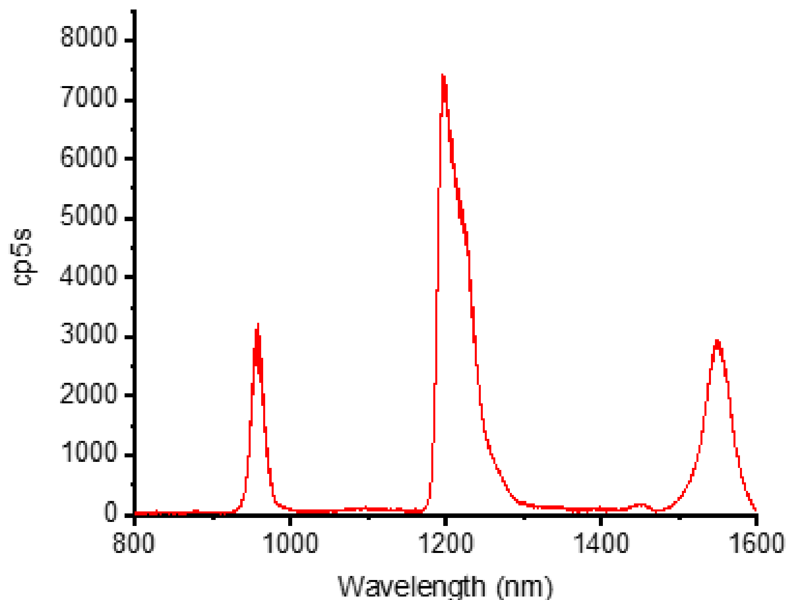

Figure 4.16: *High power micro-PL spectrum of the DBR and cavity structure presented in Figure 15. InP emission is seen at 960 nm, the emission at 1250 nm is attribute to the AlInGaAs and the peak at 1550 nm is attributed to the QD-related emission which is enhanced by the DBR.*

Figure 4.16 shows a high power micro-PL spectrum of the sample. Emission relating to the quasi wetting layer can be seen at 960 nm and emission from the AlInGaAs can be seen at 1250 nm. The bright peak at 1550 nm is due to the DBR enhancing the QD-related emission and a DBR sideband visible at 1450 nm.

Figure 4.17 shows a representative low power micro-PL spectrum taken at 1 μW and 0.5 μW for the same location. Sharp lines are seen on the spectrum taken at 0.5 μW which confirms the presence of QDs. Interestingly, the lines sit on a bright and broad background which spans the DBR stopband. The emission line at 1525 nm is approximately 1500 counts for a 120s exposure time and 1μW excitation power, such a brightness has been observed for non-DBR samples measured in this work for the same excitation conditions. This indicates that the DBR may not be enhancing the QD emission as expected. Previous work by Kors et al [62] has shown approximately an order of magnitude increase for QD brightness when growing on similar DBR structures. It is also possible that the background is masking the QD emission hence the lack of clear brightness increase.

The clear presence of the background would be problematic when doing time-resolved measurements.

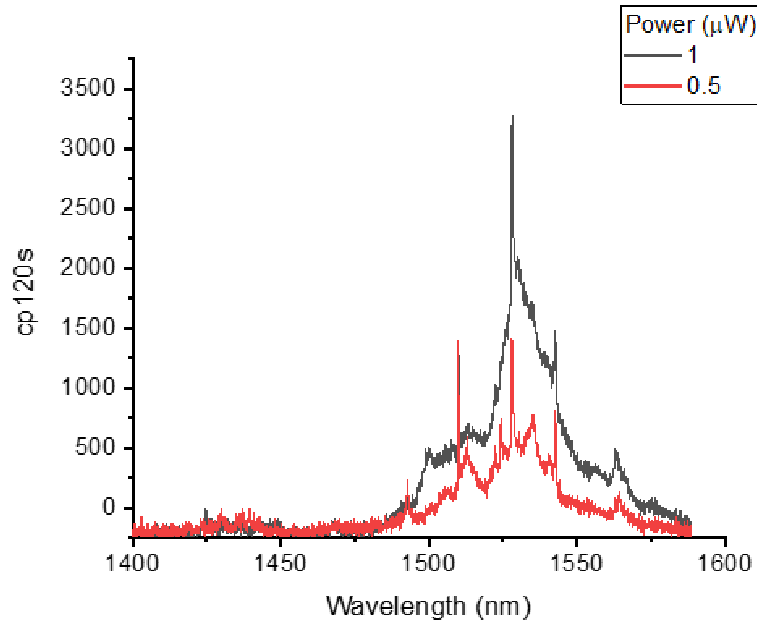

Figure 4.17: *Low power micro-PL spectrum of the DBR sample for powers of 1 μW and 0.5 μW. QD emission lines can be seen for both powers as well as a large amount of background emission.*

In such measurements the collected emission is spectrally filtered and light within the filtered wavelength range is measured in the time domain. If such a measurement were to be done on the QD at 1528 nm, for example, then the undesired background emission would also be measured. Overall this background emission would limit these QDs as a single photon source due to reduced single photon purity. The next section will explore this background emission its possible origins.

4.4 The Background Emission Problem

4.4.1 Presence of the Background Emission

The presence of a background emission can be seen for both the InAs/InP QD samples and the InAs/InGaAs/InP QD samples. Example spectra are shown in Figure 4.18, for A) InAs/InP QDs and B) the lower density InAs/InGaAs/InP QDs. The higher density InAs/InGaAs/InP QDs are not considered here due to the background emission being hard to distinguish from the overlap in QD emission lines due to the QD high density- which itself appears as a background.

Both samples presented Figure 4.18 appear to show background emission that is of greater intensity for longer wavelengths. To investigate this further, the amount of background for QD lines was estimated for each of the growth types. This was done by taking a baseline for each spectrum, denoted by the black dashed lines in Figure 4.18, and estimating the amount of background for a given QD line relative to the baseline. For the InAs/InP QDs this was done for 18 locations on the sample with a total of 50 lines estimated. The InAs/InGaAs/InP QDs had 11 locations with 44 lines estimated. This data is plotted in Figure 4.19A for the InAs/InP QDs and Figure 4.19B for the InAs/InGaAs/InP QDs.

The InAs/InP QDs show a clear increase in background intensity as the wavelength of the QD lines increases from 1400 nm to 1500 nm. There is a less obvious trend for the InAs/InGaAs/InP QDs, which can be partially attributed to the lack of QDs emitting at wavelengths shorter than 1500 nm. Fundamentally the wavelength range over which to measure the background is shorter for the InAs/InGaAs/InP QDs compared to the InAs/InP QDs. What can be seen, however, is that there is a presence of QD lines of emission wavelength longer than 1520 nm which have higher levels of background than lines shorter than 1500 nm.

Further information can be gained from these background estimations by considering whether the presence of the background affects the QD emission lines. Figure 4.20 shows the background estimates and linewidths of QDs from the same set of data as presented in Figure 4.19. Figure 4.20A is for the InAs/InP QDs and Figure 4.20B is for the InAs/InGaAs/InP QDs.

Both sets of data give no obvious correlation between the amount of background for a QD line and the linewidth of the QD line. Furthermore, the background of QD lines and their intensities are plotted in Figure 4.21. Again, no clear correlation can be seen. These results for the linewidth and QD line intensities indicate that the background is not detrimental to the QD emission lines themselves.

Overall these background estimates indicate that the background emission is wavelength dependent, where a greater amount of background is seen with increasing emission wavelength. Though the background would be problematic with respect to single photon purity of the QD emission lines, its presence does not appear to be detrimental to the intensity or linewidths of the QD emission lines. The next section looks to investigate the origin of the background emission.

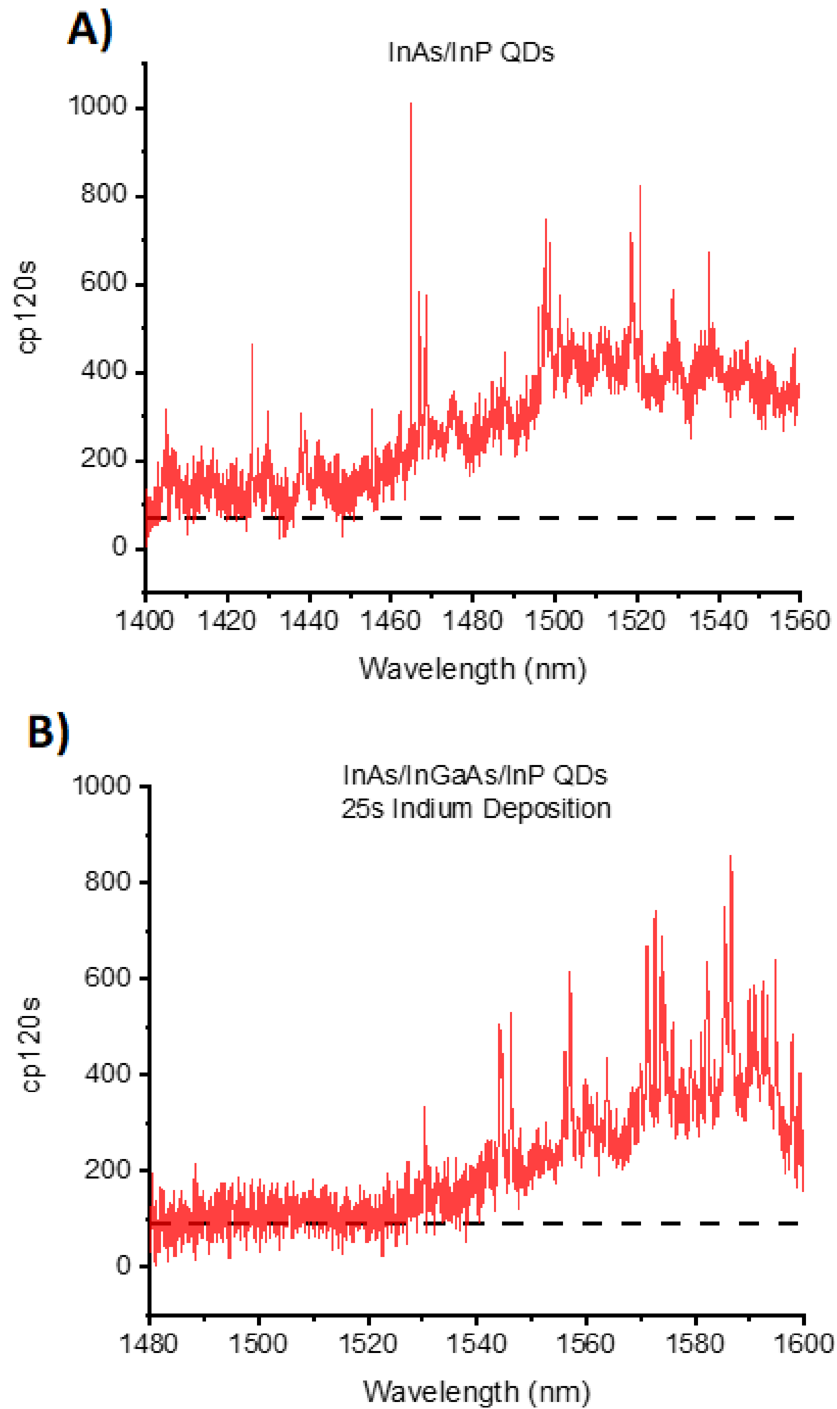

Figure 4.18: *Low power micro-PL measurements of a) InAs/InP QDs and b) InAs/InGaAs/InP QDs. Both show QD emission lines on top of a background emission. A dashed line is inserted to make the background clearer.*

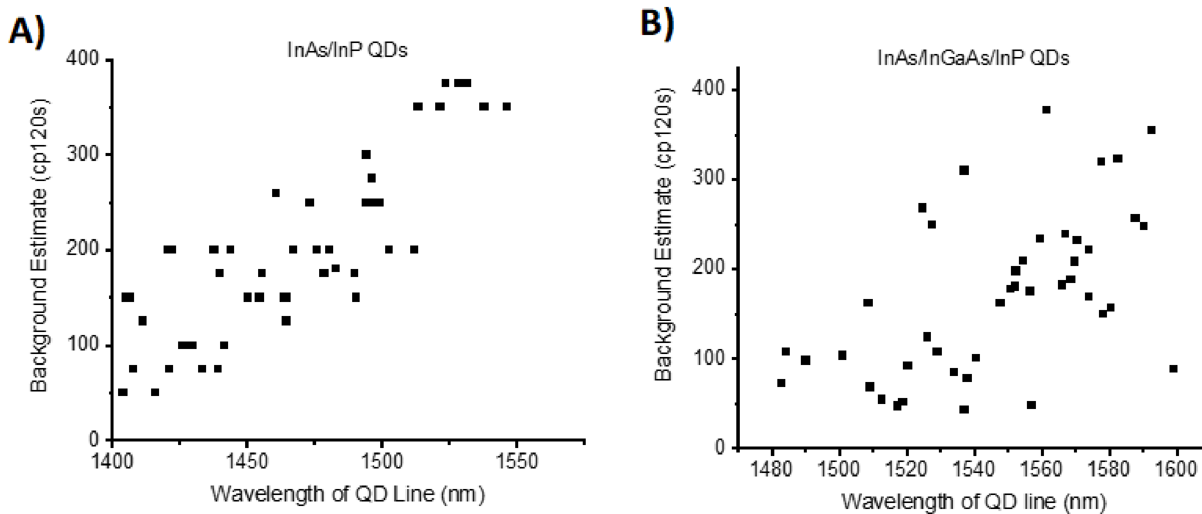

Figure 4.19: *Background estimations for QD lines and their emission wavelengths for a) InAs/InP QDs and b) InAs/InGaAs/InP QD samples.*

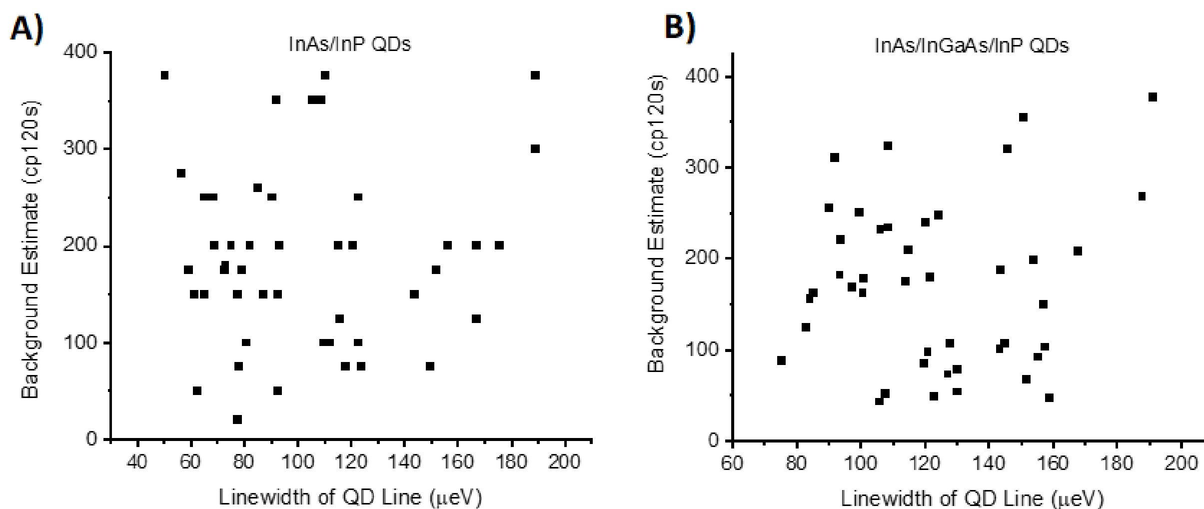

Figure 4.20: *Background estimations for QD lines with respect to the linewidths of the QD lines for a) InAs/InP QDs and b) InAs/InGaAs/InP QDs. No clear trend is seen.*

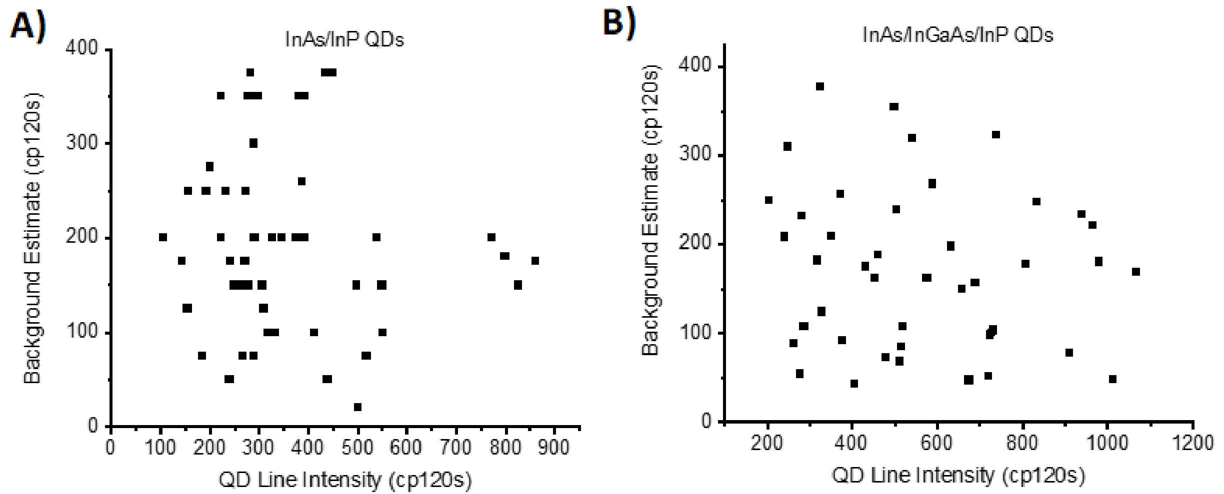

Figure 4.21: *Background estimations for QD lines and the intensities of the QD lines for a) InAs/InP QDs and b) InAs/InGaAs/InP QDs. No clear trend is seen*

4.4.2 Investigations into the Origin of the Background Emission

Micro-PL of Constituent Sample Layers

In order to begin to address this background emission problem, the cause needed to be found. It was possible that the origin of the emission was from the various growth layers used for the QD samples. The presence of deep levels in InP has been observed with PL with emission around 0.8 eV (∼1550 nm) [105] so it was possible that a similar process was occurring here.

A set of samples were measured in micro-PL to check if they exhibited any unexpected emission at the longer wavelengths where the background emission had been seen on the fully grown samples. These samples consisted of the growth substrates and growth of InP layers. Also a sample was grown in which the growth was equivalent to a full QD sample but no droplets were grown. This was to create an As-P exchange layer which would be similar to the quasi wetting layer seen in QD samples. These investigation samples are summarised in Table 4.3.

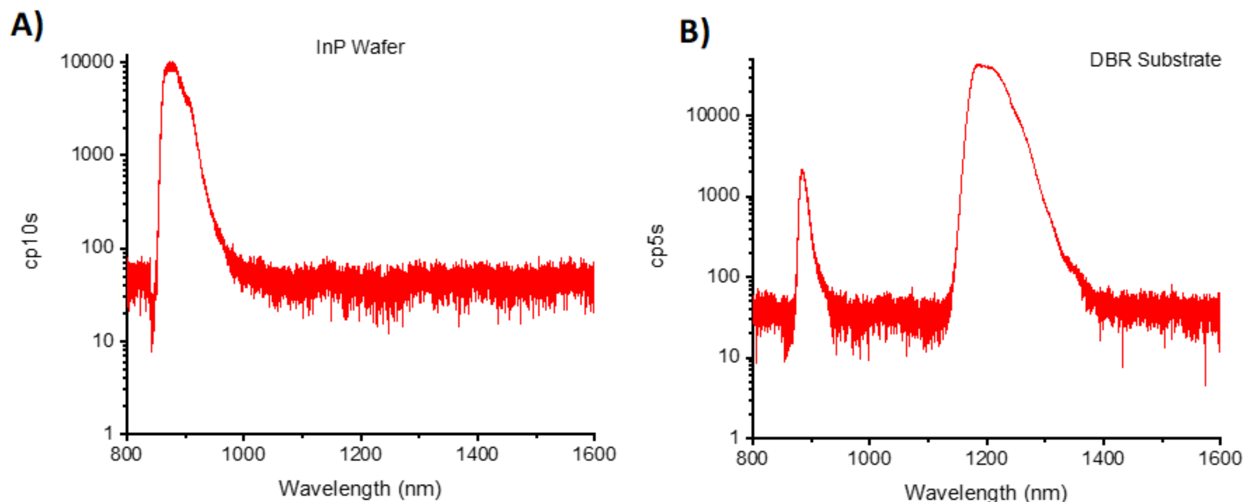

Figure 4.22: *High power micro-PL of A) InP substrate and B) DBR substrate. Both show no indication of emission for wavelengths greater than 1400 nm.*

Sample	Growth
InP Substrate	None
IQE DBR Substrate	None
InP Substrate + InP Buffer	InP Grown at 610 ^{o}C
InP Substrate + InP Cap	InP Grown at 520 ^{o}C
InP Substrate + InP Buffer + Arsine Exposure +InP Cap + InP Buffer	InP buffer exposed to Arsine at 520 ^{o}C

Table 4.3: *Summary of growth structures investigated with micro-PL to investigate whether they showed emission similar to the background emission.*

Micro-PL measurements were performed using high power conditions but for a longer exposure time of 10s. High power excitation was used as this would produce the most emission from any background. Data is plotted on log scales to help identify any weak emission.

Figure 4.22A and figure 4.22B give representative high power micro-PL spectrum of the InP substrate and the DBR substrate. The InP substrate only shows emission relating to the InP with no additional emission resembling the background emission. This is also the case for the DBR substrate presented in Figure 4.22B, emission can only be seen from the InP and the AlInGaAs. Note that the exposure time for this sample was 5s due to the brightness of the AlInGaAs emission saturating the detector for a 10s exposure time.

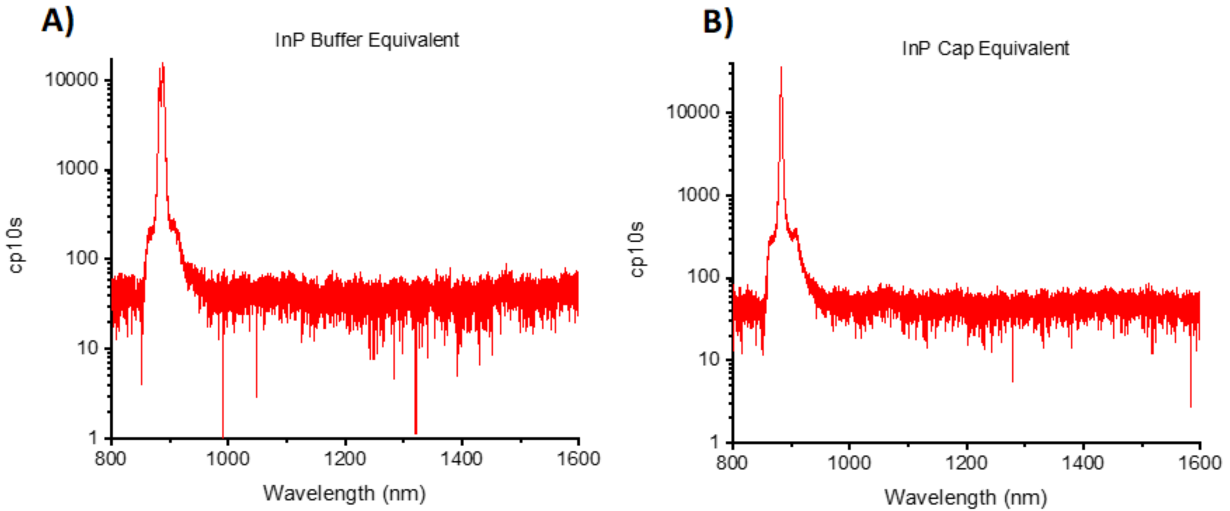

Figure 4.23: *High power micro-PL of a) InP buffer layer b) InP cap layer. Both samples show no emission for wavelengths longer than 1400 nm.*

Next we consider the InP grown on InP substrates, the micro-PL measurements for the buffer growth equivalent and the capping layer growth equivalent are given in Figure 4.23A and figure 4.23B respectively. Again, both show InP related emission at 900 nm with no long wavelength emission detected.

Finally, micro-PL measurements were taken on the As-P exchange sample. Figure 4.24 shows a high power micro-PL spectrum of the sample where the InP emission can be seen around 900nm and the $InAs_xP_{1-x}$ emission can be seen at 990 nm. The exposure time was reduced to 5s due to the emission of this layer saturating the detector over a 10s exposure. With respect to the quasi-wetting layer, it should be noted that background emission is seen in the QDs grown on the InGaAs interlayer. These samples do not feature the quasi-wetting layer emission which further indicates that the background emission is not related to this layer.

Furthermore, the InAs/InP QDs sit within an etched pit but the InAs/InGaAs/InP QDs do not. This indicates that possible background emission relating to etched pit is not responsible for the background emission due to background emission being present for both sample types.

This sample set has shown that the background emission is unlikely to originate from the substrates, InP grown layers or the 2D $InAs_xP_{1-x}$ exchange layer. These results indicate that the origin of this background emission is related to the growth of the QDs themselves.

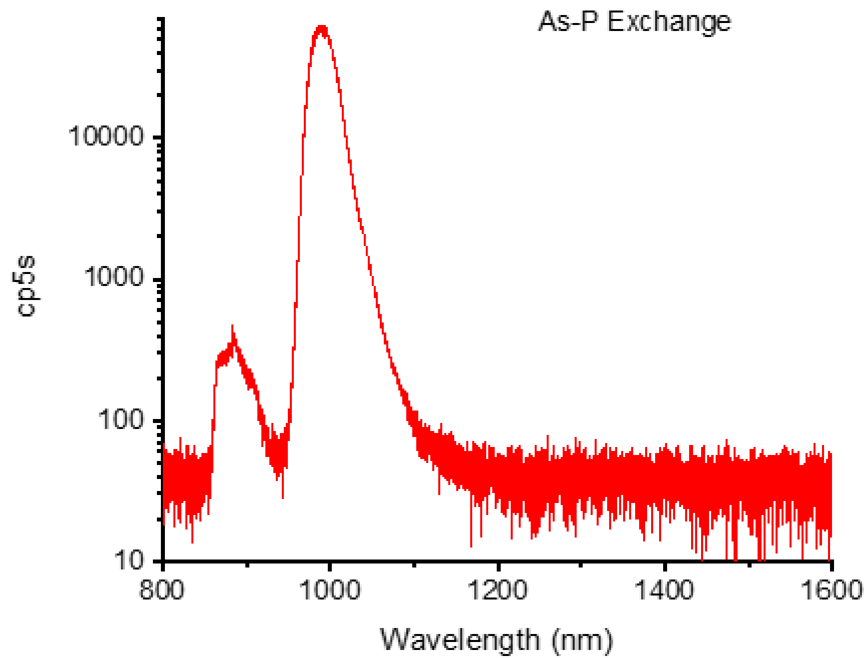

Figure 4.24: *High power micro-PL measurement of the As-P exchange sample. The emission at 1000 nm originates from the* $InAs_XP_1{-}x$ *layer. No long wavelength emission that resembles the background is seen.*

QD Growth Conditions

We have seen that it is unlikely that the background emission originates from the constituent sample layers and therefore an aspect of QD growth may give rise to the background emission. InAs/InP QDs and InAs/InGaAs/InP QDs were imaged using X-STM. This method allows the characterisation of samples at the atomic level and information can be gained about the size, shape and composition of the QDs. Furthermore, the composition of the layers surrounding the QDs can also be characterised. The full study by Gajjela et al is published in [101] and the conclusions will be considered here.

The study looked at InAs/InP QDs crystallised at 520 ^oC and 480 ^oC. These two temperatures were studied in order to looks at QDs with etched pits (520 ^oC) and without etched pits (480 ^oC). Also the InAs/InGaAs/InP QDs crystallised at 520 ^oC were studied. It was found that both the InAs/InP and InAs/InGaAs/InP QDs showed a significant amount of arsenic present in the InP capping layer for crystallisation temperatures of 520 ^oC. This arsenic is thought to originate from the quasi-wetting layers for each type of sample.

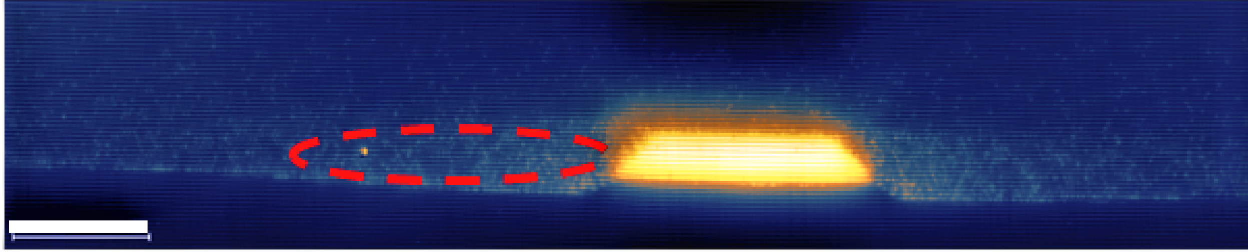

Figure 4.25: *X-STM image of an InAs/InP QD crystallised at 520 ^{o}C. The QD has the shape of a truncated pyramid and sits within an etched pit. The red dashed circle indicates where As ca be seen in the InP cap. The scale bar is 20 nm. Image credit to Raja Gajjela.*

An example is shown in Figure 4.25 for an InAs/InP QD crystallised at 520 ^{o}C. The As-containing material is gold/yellow colour, showing the QD to be a truncated pyramid shape and sitting within an etched pit. The presence of As in the InP cap either side of the QD is also seen and indicated by the red dashed circle.

For the InAs/InP QD samples crystallised at 480 ^{o}C, the As in the InP cap was found to be significantly less than the 520 ^{o}C crystallisation temperature samples. This is relevant because previous work by Skiba-Szymanska et al [67] on InAs/InP QDs grown by DE in MOVPE used a lower crystallisation temperature of 500 ^{o}C. These QDs did not show the same kind of background emission as presented in this thesis, this is further backed up by private communications with Dr Ginny Shooter from Toshiba Research Europe.

It must be noted that these QDs were grown in a different MOVPE reactors and the correspondence between temperature measurements for different growth chambers is not exact. However, the low-background Toshiba QDs did not not exhibit the same type of etched pit formation as the 520 ^{o}C crystallisation temperature QDs presented in this thesis, this is shown in X-STM measurements presented in [106]. As seen in Section 4.1.1, etched pit formation is not observed for QDs with crystallisation temperatures below 500 ^{o}C. Therefore the lack of etched pit formation for these lower background Toshiba QDs indicate that the crystallisation temperature is indeed lower than for the background-exhibiting QDs presented in this thesis.

These initial investigations indicate that the crystallisation temperature is related to the presence of background emission. Where significant amounts of As in the InP cap can be seen for both the InAs/InP QD sample and the InAs/InGaAs/InP sample when the crystallisation temperature is

520 ^{o}C and both types of sample show background emission. The QDs with a lower crystallisation temperature of 480 ^{o}C show significantly less As in the InP cap. However, from the literature there is no evidence or study of the emission properties of InP containing arsenic due to arsenic segregation. Therefore it is not clear at present how As in the cap could lead to background emission but by comparing with previous work we have seen that a lower crystallisation temperature and much reduced arsenic in the InP cap does not result in the background emission seen in this thesis.

4.5 Summary

Overall this chapter has presented micro-PL characterisation of various InP-based QD samples. We have seen that InAs/InP QDs emit in low power micro-PL for a crystallisation temperature of 520 ^{o}C. Their emission appears to be related to the formation of an etched pit around the QD during the crystallisation stage. These QDs are shown to emit within the C-band with an average linewidth of (80±27) μeV. By reducing the thickness of the InP capping layer we can see that the size of the buried QDs also reduces which results in shorter wavelength emission from the QDs when measured in low power micro-PL.

Next InAs QDs on a 5 nm InGaAs interlayer were characterised. These samples showed no etched pits around the QDs and no quasi-wetting layer emission- unlike the InAs/InP QDs. Using a 25s Indium deposition time produced QDs of a destiny of 5x10^{9} cm^{-2} with the majority of QD lines measured in low power micro-PL having emission wavelengths longer than 1500 nm. By increasing the Indium deposition time to 35s a high density of the order of 10^{10} cm^{-2} was accessible. These QDs also had emission wavelengths mostly longer than 1500 nm but included an increased proportion of emission wavelengths shorter than 1500 nm. The average linewidths from these InGaAs interlayer samples are $>$ 100 μeV which is broader than for the InAs/InP samples initially presented. Additionally, this growth appears to be a modified version of DE due to the increase in QD density of two orders of magnitude compared to the non-crystallised droplets.

Furthermore, the growth of QDs on an InGaAsP interlayer were introduced. These QDs also presented high QD densities of the order of 10^{10} cm^{-2} and showed a large wavelength range of emission from 1300 nm-1600 nm. Interestingly the average linewidth for these QDs was (92±42)

μeV which is reduced when compared to the InGaAs interlayer samples.

The InAs/InP QDs were grown within a DBR structure and the structure was shown to have a large amount of background emission as well as QD emission lines. This background emission has been shown to be present on the non-DBR samples and to be strongest for longer wavelengths. The presence of this background emission does not appear to be detrimental to the linewidths or count rate of the QDs but would be problematic with respect to measuring single photon purity from the QDs. Further growth experiments have shown that it is unlikely that the background emission originates from the constituent sample layers and is more likely to originate from the details of the QD growth mechanism.

Finally, it appears that the origin of the background may be related to the temperature at which the QDs were crystallised. X-STM measurements show a significant amount of As in the InP cap for both InAs/InP and InAs/InGaAs/InP QDs both crystallised at 520 ^{o}C. InAs/InP QDs crystallised at 480 ^{o}C show significantly less As in the InP cap and comparisons to previous works on InAs/InP QDs show that a lower crystallisation temperature of 500 ^{o}C has produced QDs with significantly less background emission.

Chapter 5

Establishing InP Photonic Crystals

In order to demonstrate a Purcell enhanced emission from QDs in a PhCC structure, the structures themselves needed to be fabricated. This was a many stage and challenging process with the overall process outlined in Figure 5.1. First the PhCCs needed to be simulated, for this work H1 cavities and L3 cavities were simulated. These simulations are used to find the device parameters which would produce mode wavelengths around 1550 nm with high Q factors.

Once devices had been simulated, a fabrication process needed to be established. The university of Sheffield has extensive experience of fabricating PhC devices in GaAs with operation wavelengths around 900 nm. This formed the foundation for the fabrication, where the process had to altered to account for the change to the InP material system and increase in operation wavelength.

Once the PhCCs had been fabricated it was necessary to characterise them with micro-PL measurements. If the fabricated PhCCs exhibit cavity modes of high Q, then the fabrication was deemed to be successful. Finally, more micro-PL measurements were required to look for QDs within the PhCCs.

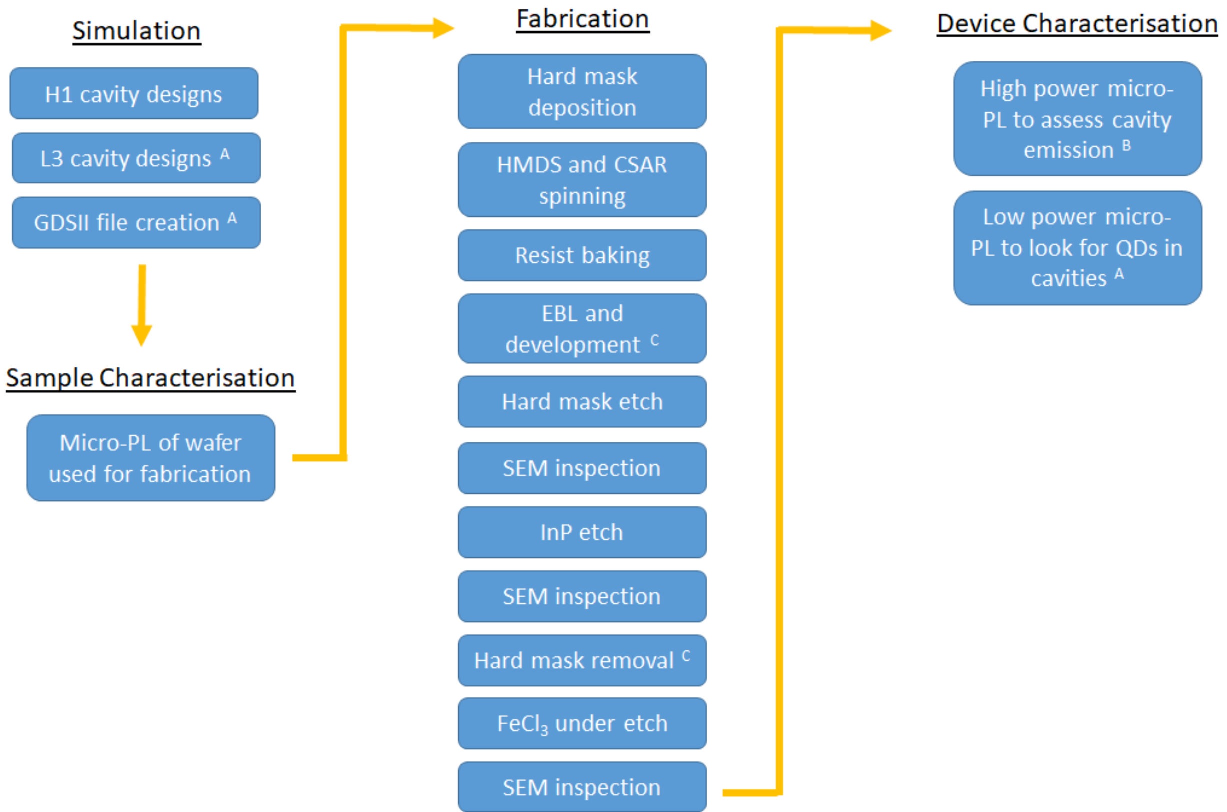

Figure 5.1: *The process flow for the simulation, sample characterisation, fabrication and device characterisation sections presented in this chapter. Steps marked A were performed by Dr Catherine Phillips, steps marked B were performed in collaboration with Dr Phillips and steps marked C were performed by Dr Rene Dost.*

5.1 Design of InP-Based Photonic Crystal Cavities in Lumerical

Over the last decade there has been a great amount of work at the University of Sheffield on PhC devices in GaAs. These devices have embedded QDs which emit around 900 nm, as we have seen in Chapter 2, the hole radii, lattice constant and slab thickness for a PhC must be designed such that the devices operate at the desired wavelength. This has resulted in PhC device designs that feature a 140 nm thick GaAs slab, hole radii of 60 nm and a lattice constant of 200 nm [107].

The work presented in this thesis is concerned with the telecom C-band in the InP material system so the PhC devices must be redesigned with respect to the existing GaAs device designs. In general, this means that device parameters need to be of a larger size in order to reflect the operation wavelength being increased to around 1550 nm.

Previously published work from Kors et al presented the simulation and fabrication of InP based L3 cavities [88], where they were able to achieve simulated Q factors close to 100,000 and fabricated Q factors up to 8700. The authors used a slab thickness of 310 nm and lattice constant (a) of 420 nm, these parameters were used as a starting point for the simulations here.

In addition, the air gap thickness between the InP membrane and the InP slab was set to 1.5 um, shown in Figure 5.2. This was based on simulations performed by Dr Catherine Phillips. Cavity modes emit light both down towards the substrate and up towards where the light is being collected. This emission can reflect off the substrate and back up towards the slab. After further reflections at the slab interfaces some of the light reflected off the substrate will be collected above the cavity [108]. An air gap value of 1.5 μm gave the optimum signal for light collected above the cavity due to constructive interference which would increase the amount of cavity emission collected.

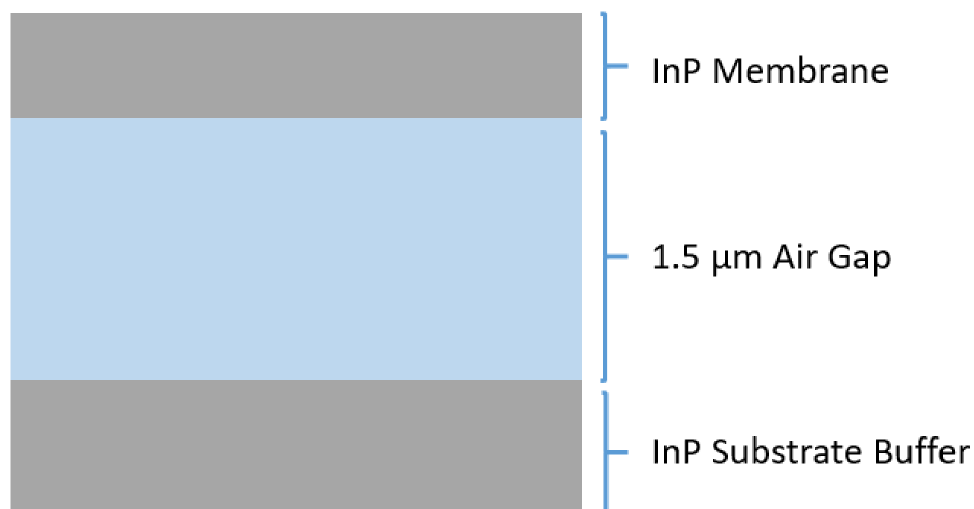

Figure 5.2: *Schematic showing cross section of a generic photonic crystal sample. These samples feature a membrane with air above and below. The air gap below the membrane is set to 1.5 μm.*

5.1.1 H1 Cavity Simulations

The parameters of the H1 cavity simulations are shown in Figure 5.3 where r and a are the radii and lattice constant of the bulk PhC holes, respectively, which define the wavelength range of the photonic band gap of the surrounding PhC and therefore the mode wavelength. Adjusting the parameters of the first central ring of holes around the cavity is a commonly used method to increase

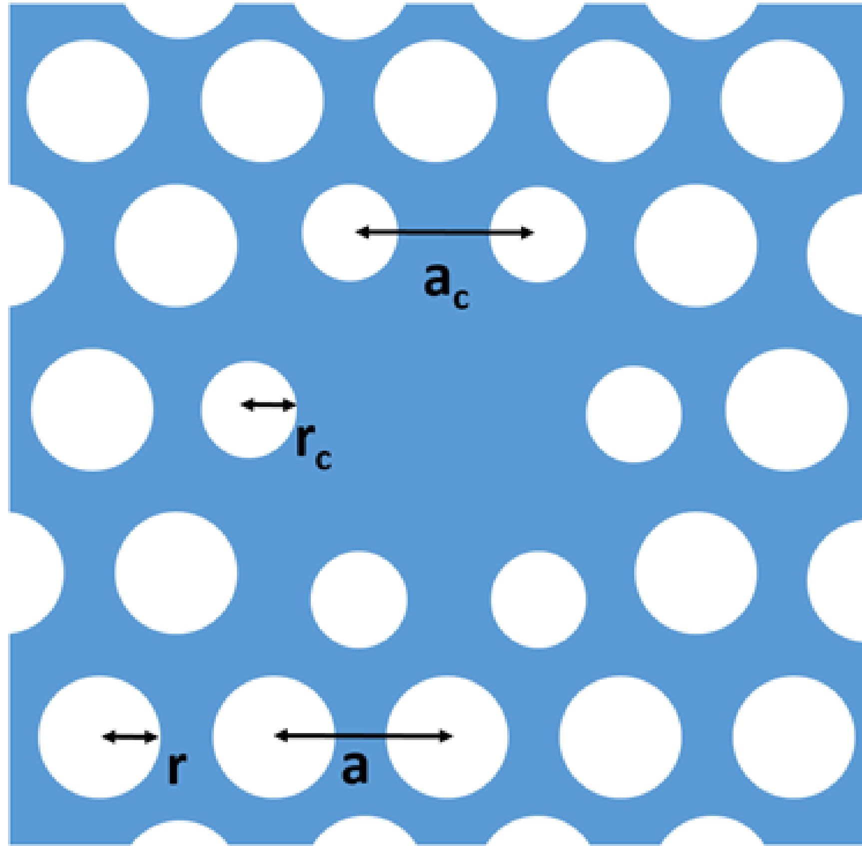

Figure 5.3: *Top-down diagram of an H1 cavity, a is the lattice constant and r is the radius of the PhC holes. These parameters for the central holes around the cavity are denoted by the subscript c.*

the Q factor of the cavity mode for PhCCs, this is method is referred to as gentle confinement. When considering an H1 cavity with the inner holes unchanged, there is an abrupt interface between the cavity and the surrounding PhC which causes out of plane leakage. By shifting the central holes outwards and reducing their radii, there is a smoother boundary, reducing out of plane leakage [109]. The radii and lattice constant of the central ring of holes surrounding the cavity are labelled r_c and a_c. The values for r_c and a_c are expressed as a multiple of r and a, respectively.

The initial H1 simulations varied the hole radius for a lattice constant of a=420 nm, a_c=a and r_c=r, where the central holes have the same parameters as the bulk PhC holes. The simulated mode wavelength and Q factor are presented in Figure 5.4 for hole radius values between 75 and 115 nm. The mode red shifts and increases in Q factor with reducing hole radius due to the increase in the size of the cavity. It can be seen that a mode wavelength close to 1550 nm is achieved with a hole radius of 85 nm. The Q factor for this mode is a relatively low value of ∼1600.

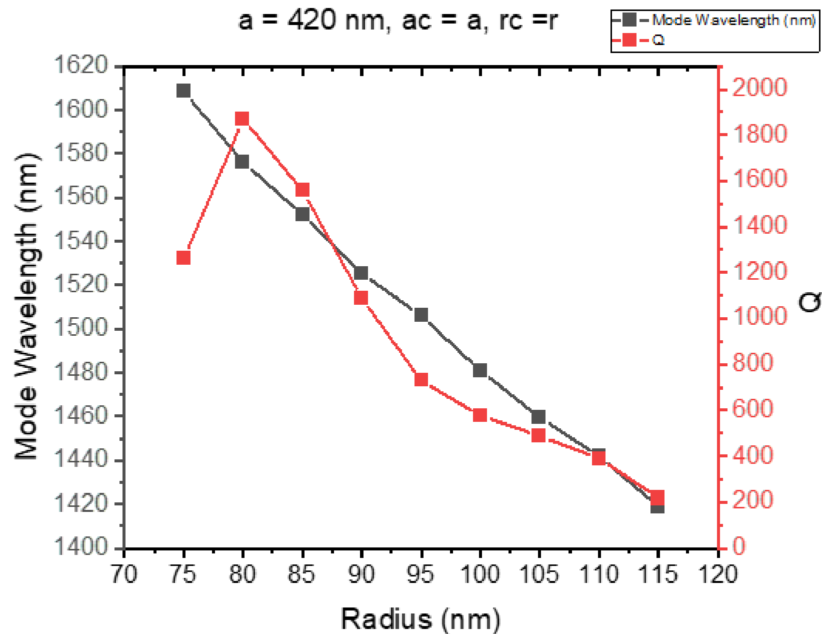

Figure 5.4: *Initial H1 cavity simulation results showing the wavelength and Q of the fundamental mode with varying hole radius.*

In order to increase the Q of the mode the effect of r_c was investigated. In previous work by Coles et al [107] the value of r_c had been set to $0.91r$, so simulations were performed between r_c values of (0.85-0.95)r. The lattice constant was 420 nm, radius 85 nm and a_c=a, the data is presented in Figure 5.5.

It can be seen that reducing r_c red shifts the mode, due to an increase in the size of the cavity, and produces an increase in Q due to the gentle confinement effect. Compared to the data presented in Figure 5.4, where r_c=r, the mode wavelength has red shifted from 1558 nm to 1576 nm when r_c=0.85r. There is a corresponding increase in Q from 1558 to 4445.

Though a smaller value of r_c produces a greater increase in Q factor, smaller holes will etch at a slower rate in fabrication which could result in the inner holes not fully etching. It was decided to use the intermediate value of r_c=$0.9r$ to reduce the potential effect of this. Using this value of r_c gives a Q factor of 2992, an increased value compared to Q=1558 for r_c=r.

Further simulations were performed to assess the effect of changing a_c on the mode wavelength and Q factor. The lattice constant was set to 420 nm, radius to 85 nm and r_c=0.9r. The value of a_c was varied from (1.1-1.24)a. The results are shown in Figure 5.6 where it can be seen that a value

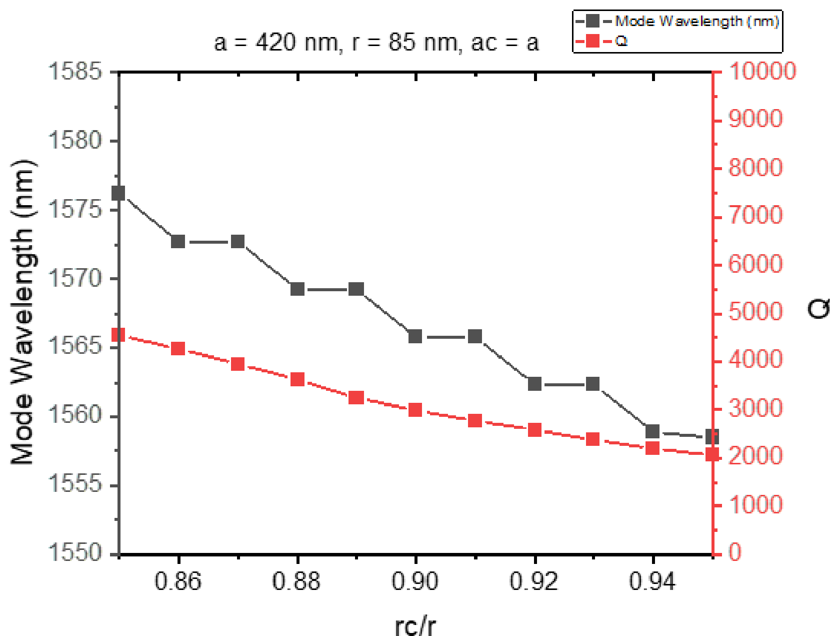

Figure 5.5: *The effect of varying r_c on the mode wavelength and mode Q factor. The mode wavelength is seen to red shift and Q factor increase as r_c is reduced.*

of a_c=1.16a gives a very high Q factor of 80,000 due to the effect of gentle confinement. The mode wavelength for this optimum value of a_c is 1620 nm which is too long a wavelength compared to the desired operation wavelength of the device.

In order to bring the mode wavelength to around 1550 nm the radius of the holes was increased. With reference to Figure 5.4, we can see that the use of larger holes blue shifts the cavity mode due to the size of the cavity reducing. Increasing the hole radius to 110 nm was found to bring the mode back into the desired wavelength range. Figure 5.7 shows the effect of changing the ac for a=420 nm, r= 110 nm and r_c =0.9r.

It can be seen that a maximum Q of 19,395 for a wavelength of 1542 nm is achieved for a_c=1.14a. This fulfils the aim of bringing the mode wavelength back to the telecom C-band, though the Q factor is reduced compared the Q factor of 80,000 shown in Figure 5.6 for a hole radius of 85 nm. This reduction in Q factor was deemed acceptable due to a hole radius of 110 nm being more likely than a hole radius of 85 nm to etch through the 310 nm InP membrane. This matches with previous InP-based PhC work from Birowosuto et al [87] where a hole radius of 100 nm was used and Kors et al [88] which used holes of a 115 nm radius, both showing successful PhCC fabrication for larger

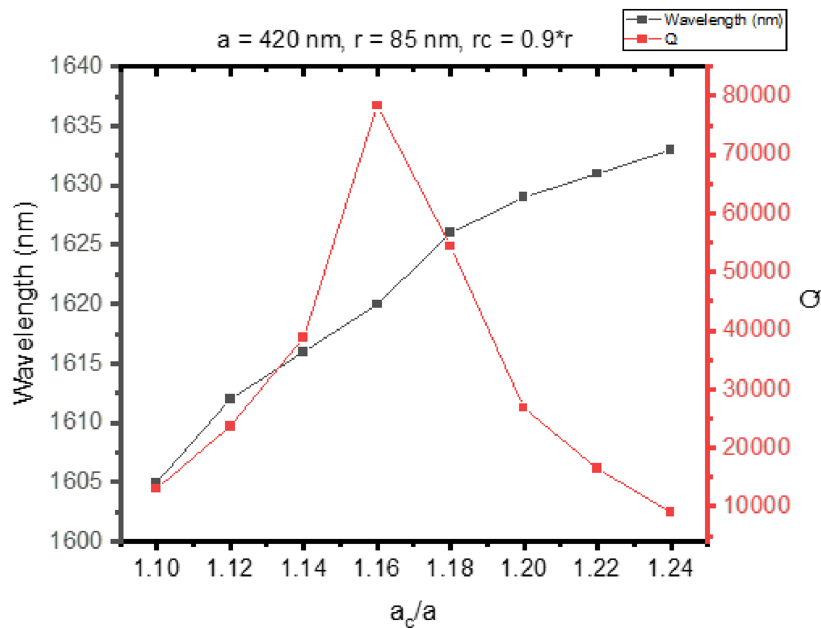

Figure 5.6: *The effect of changing a_c on the mode wavelength and Q factor. A maximum Q factor of ∼80,000 is achieved with a_c=1.16a*

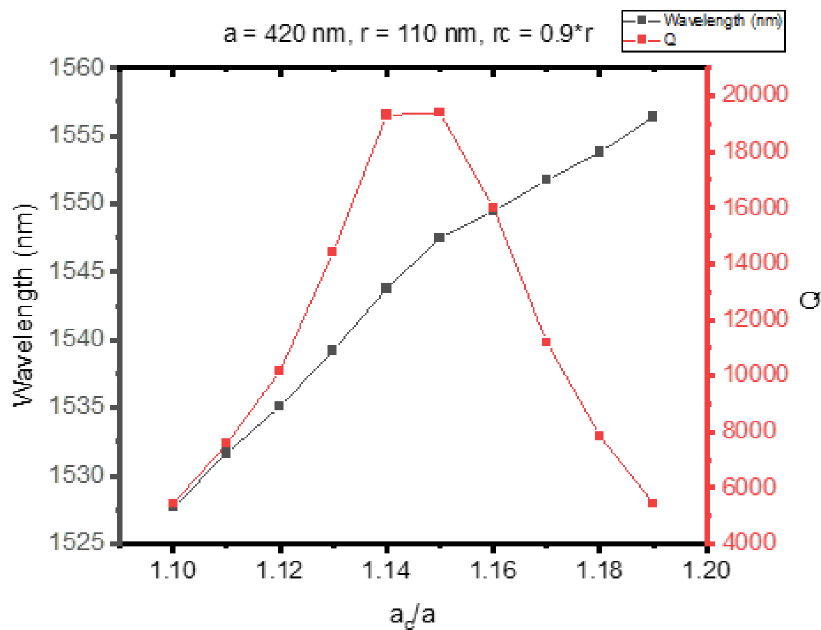

Figure 5.7: *The effect of changing a_c on the mode wavelength and Q factor for a=420 nm, r=110 nm and r_c=0.9r. By using a larger hole radius than previously, the mode wavelength has blue shifted back into the telecom C-band.*

hole radii.

In the case of an H1 cavity, the size of the cavity is small due to it consisting of the exclusion of only one hole. This reduces the chance of having spatial overlap between the QD and the cavity mode. By having a reduced Q factor, there is an increased chance of spectral overlap with the QD due to the width of the mode increasing. So a reduced Q can help increase the overall chance of getting a Purcell enhanced QD for an H1 cavity. Overall, the H1 design used as the basis for fabrication was a=420 nm, r=110 nm, r_c=0.9r and a_c= 1.14a. This gave a mode wavelength of 1543 nm and Q factor of 19,300.

5.1.2 L3 Cavities

L3 cavities were also simulated with the aim of creating a design that featured a high Q factor fundamental mode. L3 cavities are of a larger size than H1 cavities, this is due to L3 cavities being formed by the exclusion of 3 holes from the PhC compared to 1 hole for an H1 cavity. This increase in cavity size increases the chance of finding a QD that spatially overlaps with the cavity mode, therefore it was deemed acceptable to have cavity designs with higher Q factors than the H1 cavity designs.

As with the H1 cavities in Section 5.1.1 the holes around the cavity were shifted with respect to the cavity centre in order to access higher Q factors. The hole radii were kept equal, this was to simplify future fabrication where etch rates change depending on hole size. Figure 5.8 gives the L3 cavity structure with the shifted holes highlighted. For the row of holes of the cavity, the first, second and third holes closest to the cavity are shifted by 0.13a, 0.09a and 0.04a, respectively, away from the cavity in the x direction. The second and third rows above and below the cavity are shifted by 0.06a and 0.3a, respectively, in the y direction towards the cavity. This cavity design achieved a Q of approximately 100,000 for the fundamental mode at 1545 nm, fulfilling the previously stated aims of a PhCC emitting at in the telecom C-band with a high Q factor.

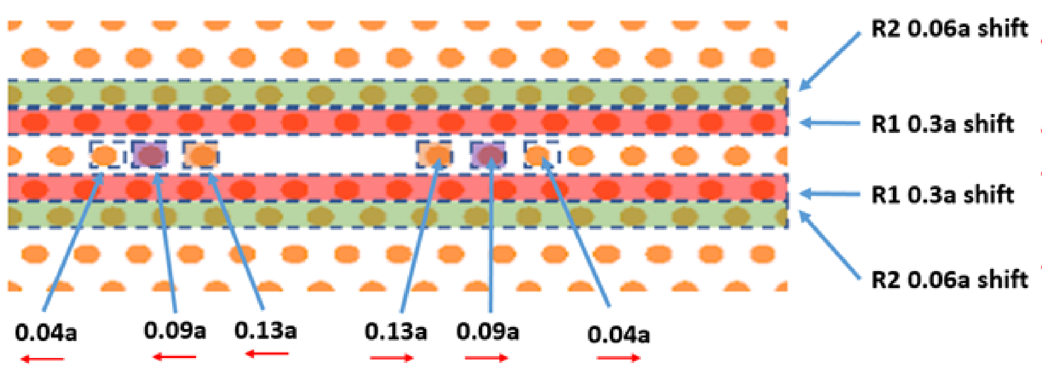

Figure 5.8: *L3 cavity design by Dr Catherine Phillips. Arrows indicated shifted holes and rows.*

5.2 Fabrication of Photonic Crystal Cavities

At the beginning of this PhD work, fabrication of PhC structures had been previously established in GaAs material at the University of Sheffield but InP-based PhC fabrication had not. This section outlines the establishment of the PhC fabrication process used in this work. The process outline was given in Section 3.5 and the following section will give more specific details of the fabrication process.

For sample processing it is key to assess the quality of each fabrication step, which was done by SEM imaging. Key goals in the fabrication included etched holes that were uniformly the intended size, and that the etch profile was close to vertical into the InP membrane. Additionally, the sacrificial layer removal needed to produce suspended membranes which retained the etched patterns with minimal damage to the membranes themselves.

5.2.1 Sample

The sample used for developing the fabrication of PhC devices consisted of a 300 nm InP buffer, 1500 nm InGaAs sacrificial layer and a 310 nm InP membrane in which QDs were grown. Figure 5.9 gives the basic sample structure. This sample used the InAs/InP QDs presented in the previous chapter.

The sample was checked with micro-PL measurements prior to fabrication in order to check there were QDs present in the wafer. Figure 5.10A shows a high power micro-PL measurement of the

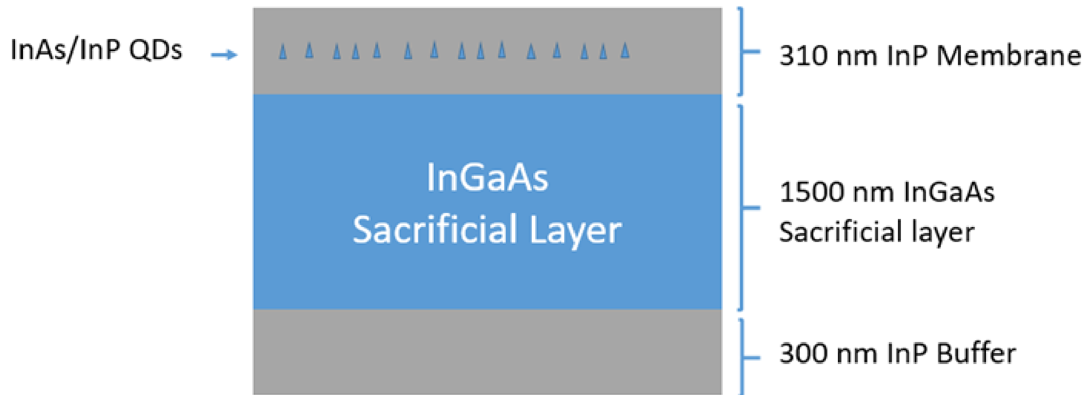

Figure 5.9: *Sample structure used for PhCC fabrication. The QDs are grown within a 310 nm thick InP membrane which is grown about a 1500 nm thick InGaAs sacrificial layer.*

sample. The QD ensemble type emission can be seen to start from 1400 nm. Emission from the InGaAs sacrificial layer accounts for the bright peak around 1550 nm. No emission from the InP can be seen, this is likely because the excitation laser does not penetrate down to the InP substrate or there is very efficient relaxation of carriers from the InP to the InGaAs and QDs (this is typically observed in these samples).

Figure 5.10B gives a low power spectrum showing single dot emission and confirming the presence of QDs across the range of measured wavelengths. Notable in this spectrum is the lack of InGaAs emission peak, this is likely due to more non-radiative recombination sites at low power which quenches the InGaAs emission.

5.2.2 Hard Mask Patterning

The hard mask is very important for PhC fabrication as it is used to transfer the EBL pattern from the EBL resist to the semiconductor membrane. During the semiconductor etch the hard mask is consumed and it is important that the hard mask is of a thickness such that it is not completely consumed during the semiconductor etch.

This is due to the fact that the hard mask protects regions on the sample that are not intended to be etched. If such regions were not protected, then they too would be etched which would thin the membrane. This would mean the device membrane would be thinner than intended which

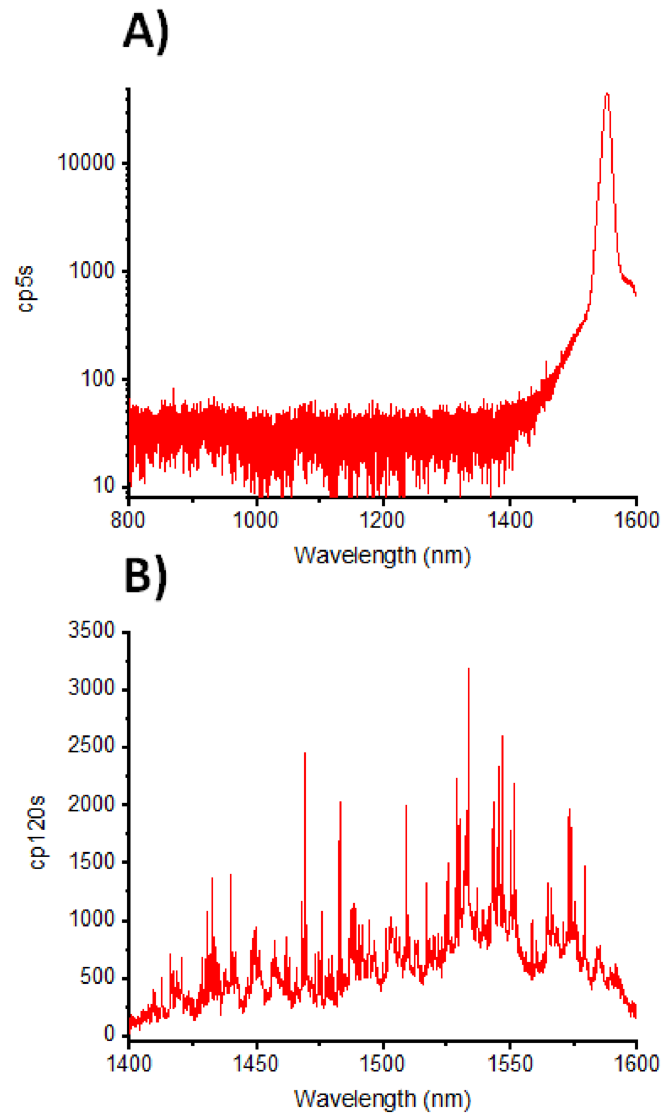

Figure 5.10: *A) High power micro-PL measurement of the sample to be used for fabrication. The QD-related emission can be seen from 1400 nm and emission originating from the sacrificial layer is seen at 1550 nm. B) Low power micro-PL spectrum of the same sample showing lines originating from the QDs.*

could unintentionally blue shift the PhCC modes. Furthermore, unintentionally etching the InP can introduce roughness to the smooth epitaxially-grown surface. This would reduce the confinement of light within the membrane, thus reducing the PhCC Q factor, as the membrane-air interface would no longer be smooth.

Previous fabrication of PhC devices in GaAs at the university of Sheffield have used hard masks with a thickness of 90 nm. A thin hard mask was appropriate due to the GaAs membranes being of thickness 140 nm. These relatively thin GaAs membranes mean that the hard mask is not completely consumed during the GaAs etch. We can see that the membrane thickness informs the choice of hard mask thickness used for PhC fabrication. In turn, the thickness of the hard mask also informs the thickness of the EBL resist that is used during EBL patterning. During the RIE etch of the hard mask the EBL resist is also consumed. With the thin hard mask for the GaAs work, 2:1 diluted CSAR was used which, after resist spinning, is of ∼200nm thickness.

The work presented here uses relatively thick InP membranes of 310 nm thickness. As such, a thicker hard mask would be required. Initially a 500 nm hard mask was used but it was found that the patterned holes did not etch through the full thickness of the hard mask and subsequently did not transfer to the InP membrane udring the InP etch. From these results a 200 nm hard mask was used which allowed for the patterning and etching of the holes through the hard mask. By using a thicker hard mask, it was necessary to use a thicker EBL resist. Undiluted CSAR was used for the EBL patterning as it was of a ∼400 nm thickness after spinning

Four blocks of H1 cavity arrays and seven blocks of L3 cavity arrays were then patterned onto the sample with EBL, these are shown in Figure 5.11.

The device parameters were varied for each block in order to maximise the parameter space fabricated and account for any potential fabrication variations, the H1 cavity parameters for each block are shown in Table 5.1.

Figure 5.11: *Blocks of H1 and L3 cavities. Also shown is a block of nanobeam waveguides but these will not be considered here.*

H1 Block Number	a_c/a	r_c/r
1	1.14	0.9
2	1.16	0.9
3	1.14	0.95
4	1.16	0.95

Table 5.1: *Values for the inner hole parameters for each H1 cavity block.*

The seven blocks of L3 cavities each had a variation in the shift of the third hole from the cavity between (0 -0.1)a in steps of 0.02a. The final block had unmodified L3 cavities.

Each block featured arrays of cavities, example arrays are shown in Figure 5.12. The H1 arrays, given in Figure 5.12A, had a variation in hole radius across the columns, with the first column having a hole radius of 50 nm and the final column having a hole radius of 100 nm. The lattice constant varied between 400 nm and 440 nm across the rows. The L3 cavities are shown in Figure 5.12B, they feature the same hole radius variation as the H1 cavities. The lattice constant varies across the rows from a = 435 nm to a = 415 nm. The sample also featured W1 waveguides and

nanobeam waveguides but they will not be considered here.

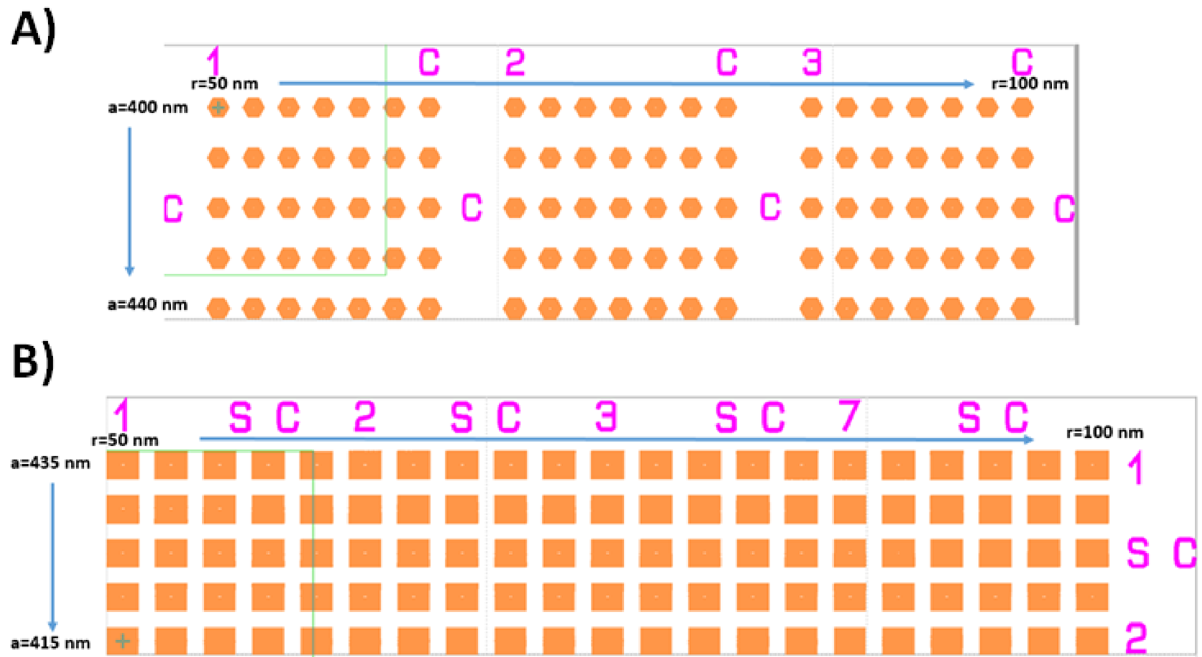

Figure 5.12: *Arrays of a) H1 and b) L3 cavities for EBL patterning. Both featured a variation in hole radius and lattice constant in order to account for any parameter changes introduced due to fabrication imperfections..*

Following EBL and resist development, the pattern was then transferred to the hard mask using RIE with an O_2 and CHF_3 based etch. Figure 5.13A shows an SEM image of an L3 cavity patterned into the hard mask after a 22 minute RIE etch and subsequent resist removal. This image shows the nano holes to be well defined and relatively uniform. This image is for a cavity at the end of the row so the design diameter is 200 nm, the hole diameter is measured to be ~214 nm which is close to the intended value.

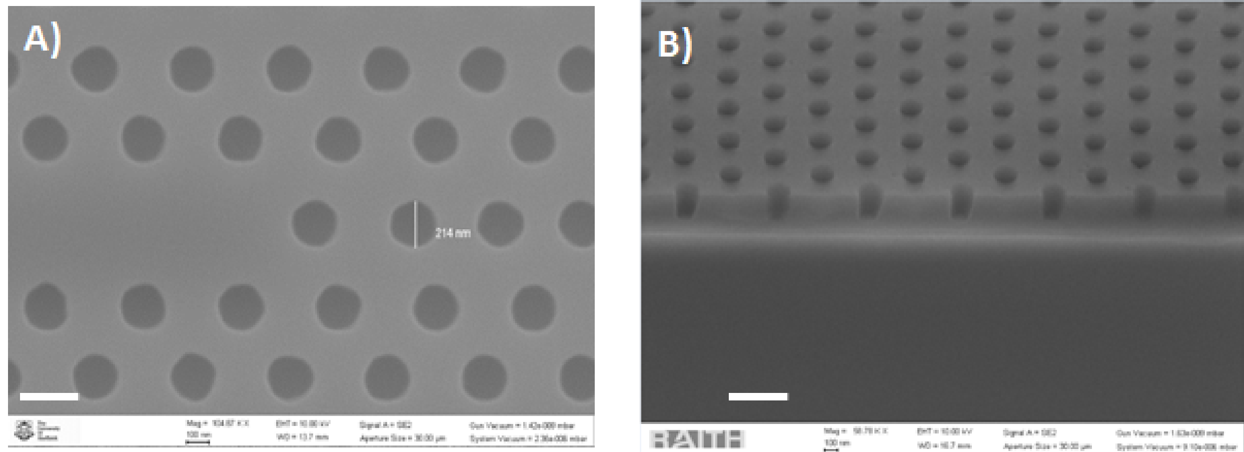

Figure 5.13: *A) SEM image showing of the hard mask after pattering and RIE etch. The holes are well defined and appear uniform. Scale bar is 200 nm. B) 30 degrees tilted SEM image. Scale bar is 800 nm.*

Figure 5.13B shows a 30 degrees tilted SEM image of a cleaved sample which shows the cross section of the holes. The sidewall angle, when accounting for the 30-degrees image tilt, is measured to be 7 degrees. This is relatively close to vertical so it was deemed to be acceptable. It should be noted that this image was taken at high magnification (59,000x) so the image is slightly distorted due to the sample moving during image acquisition.

5.2.3 InP Etch

The next step was to transfer the hard mask pattern into the InP membrane with ICP etching. We used an optimised recipe of $Ar/Cl_2/H_2$ of ratio 9/6/6 sccm, RF power of 150 W, ICP power of 900 W and chamber pressure of 3 mT [110] with all etch rates testing in advance on InP test pieces. Figure 5.14A shows a 45° tilted SEM image of an H1 cavity. The sample was cleaved in order to assess the quality of the holes etched into the InP. This image shows clearly defined holes etched into the InP. Figure 5.14B shows a zoomed in image, the holes are seen to have good verticality with a measured sidewall angle of 6°.

Using the sample growth parameters and thickness measurements from SEM images, the amount of remaining hard mask and etch depth of the holes can be calculated. The distance from the InP/InGaAs sacrificial layer interface, indicated in Figure 5.14A with a red dashed box, to the sample surface is measured to be approximately 1810 nm, correcting for the 45° tilt. Subtracting

the known thicknesses of the InP membrane and InGaAs sacrificial layer, 1500 nm and 310 nm respectively, gives the remaining hard mask thickness to be approximately 80 nm. For an original hard mask thickness of 200 nm, this indicates that the hard mask consumption rate is ∼40 nm/min. The presence of remaining hard mask on the surface can also be seen by orange appearance of the sample when looked at by eye.

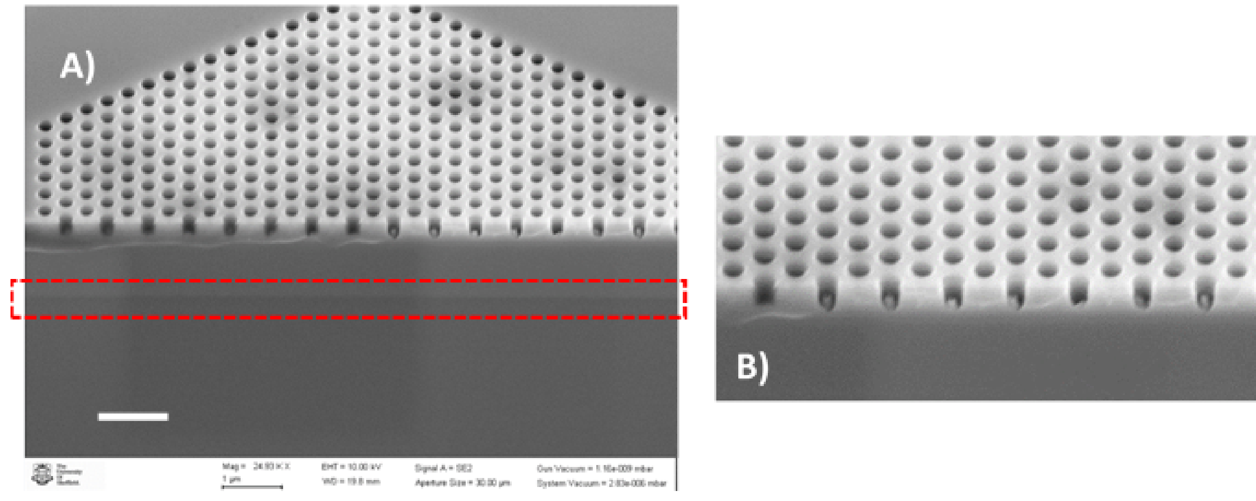

Figure 5.14: *A) Cleaved H1 cavity after the InP etc. The Scale bar is 1 μm. B) Zoomed in image showing holes having a good verticality.*

The etch depth is measured to be approximately 394 nm, subtracting the remaining hard mask thickness gives an InP etch depth of approximately 314 nm. This confirms that nano holes have etched through the InP membrane as desired. Additionally, there being 80 nm of hard mask remaining on the sample means the unpatterned InP surface will have been successfully protected during the etch.

It is very important to check the hole radii after the InP etch. Figure 5.15A gives an example SEM image of an L3 cavity after the hard mask etch and Figure 5.15B gives an SEM image of the same cavity after the InP etch. The hole diameter is measured to be 163 nm in Figure 5.13A and 208 nm in Figure 5.15B, indicating that the InP etch causes an increase in hole size. This was not a major issue due to the EBL patterning intentionally containing a range of hole sizes and lattice constants in order to account for any potential effects such as here. As can be seen in Figure 5.15B, holes in the InP of a diameter close to 210 nm were still fabricated due to the patterning of the smaller holes.

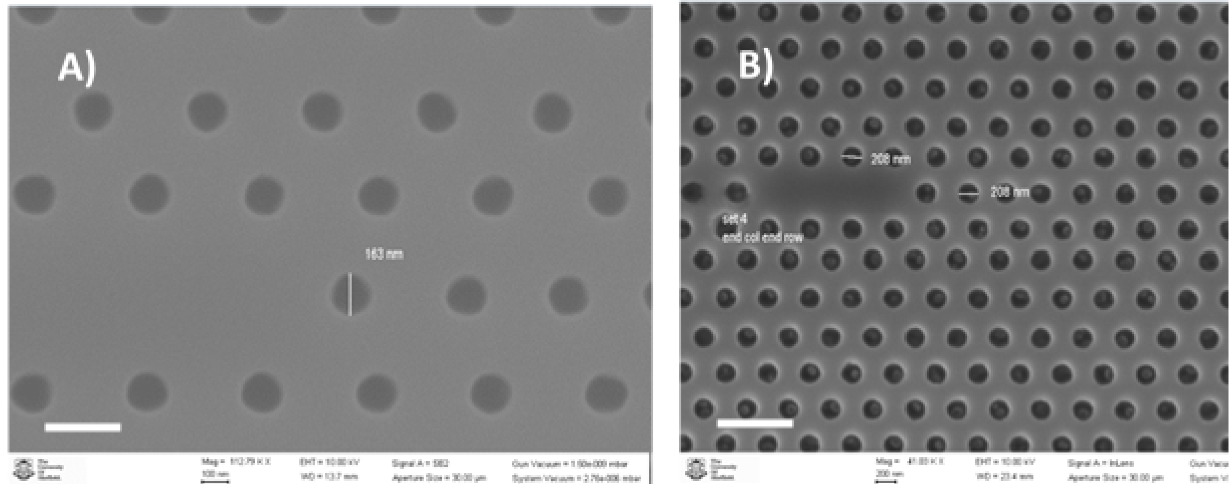

Figure 5.15: *A) SEM image of an L3 cavity patterned into the hard mask after RIE etch, the hole diameter is measured to be 163 nm. Scale bar is 200 nm. B) The same L3 cavity after the InP etch, the hole diameter increased to 208 nm. Scale bar is 400 nm.*

A later fabrication run featured a hard mask thickness of 235 nm which was due to a variation in the deposition rate of the PECVD. This sample did not exhibit the same type of hole increase after the InP etch. This is shown in Figure 5.16A and 5.16B where the hole size is 200 nm after the hard mask etch and shows only a slight increase to 208 nm after the InP etch. This indicates that the hole size increase seen previously is related to the hard mask thickness where there is a lateral etch into the InP for thinner hard masks. For future work it would therefore be preferable to use a slightly thicker hard mask (∼235 nm) in order to avoid this occurring.

5.2.4 Sacrificial Layer Removal

Prior to the undercut etch, the remaining hard mask is removed from the sample by dipping in 10% HF. For the InGaAs sacrificial layer removal, the undercut etch is performed with $FeCl_3$ (Ferric Chloride) which has been shown to etch InGaAs selectively to InP (selectivity >1200) when cooled to 7°C [111]. The Ferric Chloride was cooled to 7.6^{o}C using a chiller and a sample was initially submerged for 10 minutes. This was shown to not fully remove the InGaAs under the patterned areas so the time was increased to 20 minutes. To avoid collapse or bending of the suspended membranes the samples were then dried with CPD.

Figure 5.17A shows an SEM image of an H1 cavity and Figure 5.17B shows an SEM image of an

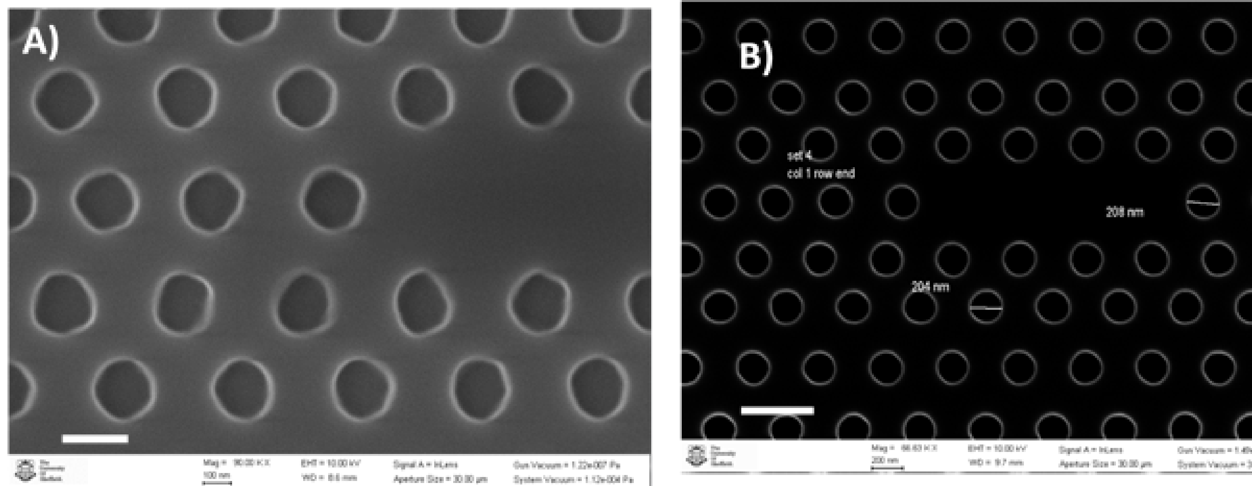

Figure 5.16: *Later fabrication run with an increased hard mask thickness of 235 nm. a) Holes of 200 nm diameter after hard mask etch. Scale bar is 200 nm. b) The same holes after InP etch with a size of 208 nm, only a small increase in size compared to the 200 nm thickness hard mask samples. Scale bar is 400 nm.*

L3 cavity after the CPD step. Both images show a contrast between areas close to the etched holes where the InGaAs has been removed (lighter) and areas where the InGaAs has not been removed (darker), this is highlighted with a red box.

These devices were produced after the optimisation of the fabrication process. It should be noted that there was a large amount of trial and error in the process development which is mainly attributed to equipment down time.

Overall it can be seen that H1 and L3 PhCCs have been fabricated and fulfil the aims of having holes in the InP with good verticality. Additionally, the Ferric Chloride under etch and subsequent CPD successfully produce suspended PhCCs.

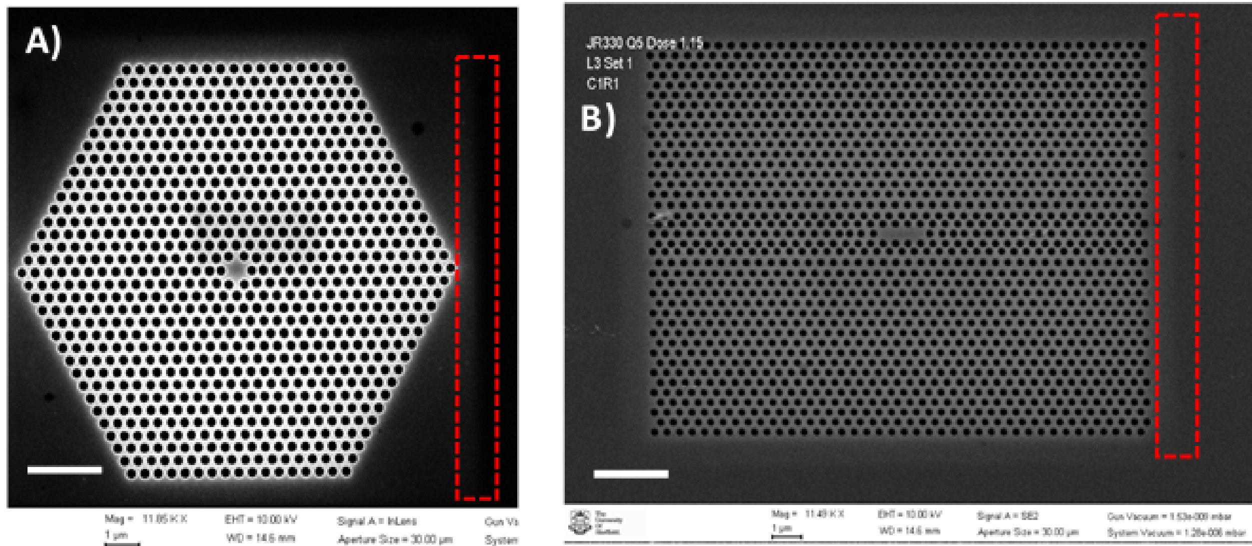

Figure 5.17: *Final under etched PhCCs A) H1 cavity, scale bar is 2 μm. b) L3 cavity, scale bar is 2 μm.*

5.3 Optical Characterisation of Photonic Crystal Cavities

The following section outlines the initial optical characterisation of samples from the first complete fabrication run. The previous section has shown, from visual SEM inspection, PhCCs that appear to have been successfully fabricated. The true test, however, comes from the optical measurements of the PhCCs. The aim here is to confirm the successful fabrication by measuring the cavity modes with good Q factors and then to measure single QDs within the PhCCs.

The optical characterisation was done by exciting the devices with high power, the broad QD ensemble and background emission then excites the cavity modes. Many H1 and L3 cavities were fabricated on the sample where the hole radii and lattice constant from the EBL patterning were varied. As stated before, this was to counteract any potential fabrication variations but also having PhCCs with varying mode wavelengths can increase the chances of finding a resonant QD due to the spread in QD emission wavelengths.

Figure 5.18 shows a high power micro-PL measurement of an example H1 cavity. The spectrum features two well defined modes which are attributed to the two polarisation states of fundamental mode. In simulation these modes are at the same wavelength due to the H1 cavity having perfect

symmetry about the cavity centre. The fabrication cannot reproduce this exact symmetry due to fabrication imperfections causing some variation in the PhC hole size. Therefore, the fundamental modes are non-degenerate [112].

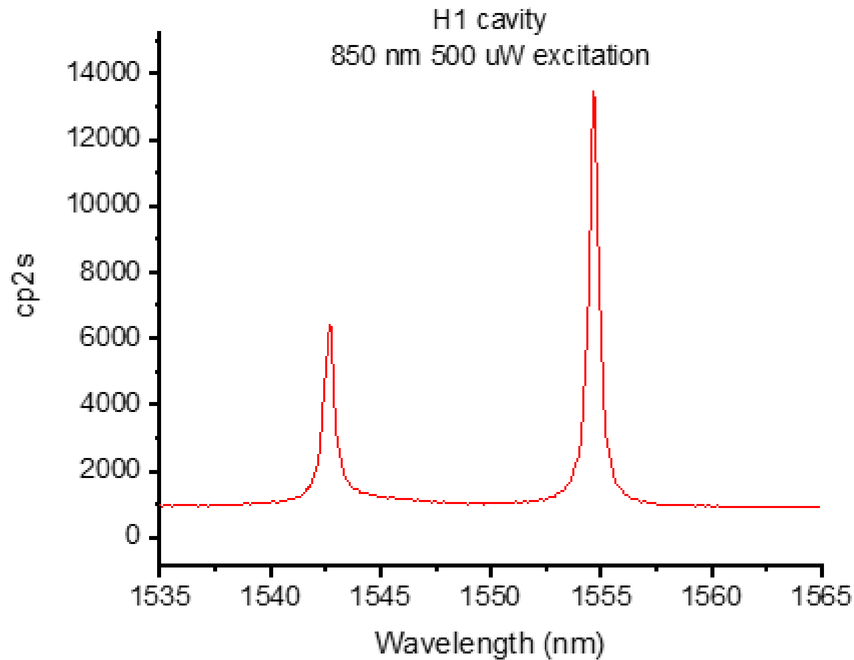

Figure 5.18: *H1 cavity spectrum measured using high power micro-PL. Two fundamental modes are seen near to 1550 nm which shows that the fabrication was a success. Data taken from H1 block 1.*

The low energy mode at 1554 nm has a Q factor of 3000 and the higher energy mode at 1542 nm has a Q factor of 2500. The presence of these cavity modes confirms that the fabrication of H1 cavities was successful. Furthermore, achieving Q factors of a few thousand indicates that overall the fabrication is of good quality. A key aspect of this is the hole uniformity which can be seen to be highly uniform in Figure 5.17. Also the etched hole verticality of 6° is indeed a good level. Additionally, we can infer that the sacrificial layer removal has not been overly detrimental to the quality of the PhC due to the selectivity of the $FeCl_3$ etch.

Looking at a range of cavities, Figure 18a shows the wavelength of the lowest energy mode for varying lattice constant. The mode red shifts with increasing lattice constant due to the size of the cavity increasing. Figure 18b shows the mode wavelength of this mode for different hole radii. The mode wavelength blue shifts with increasing hole radii due to reduction in size of the cavity,

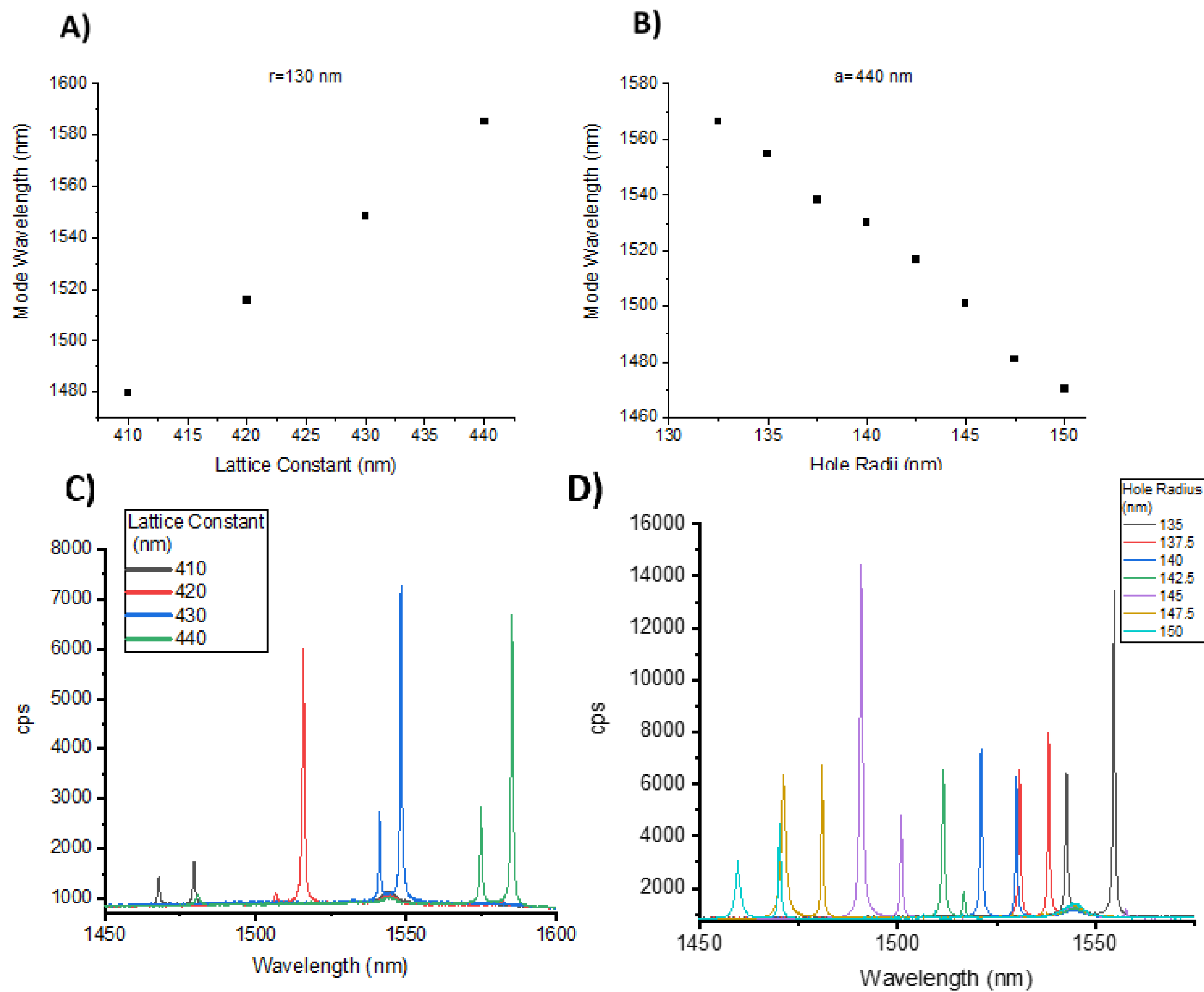

Figure 5.19: *A) Wavelength of lowest energy mode red shifts with increasing lattice constant. B) Wavelength of lowest energy mode blue shifts with increasing hole radii. C) Spectra for the lattice constant change data shown in panel A. D) Spectra for the hole diameter change shown in panel B. Data taken from H1 cavity block 1.*

matching the trend from the simulations shown in Figure 5.4.

Figure 5.20 gives an example high power spectrum of an L3 cavity, showing the single fundamental mode at 1525 nm with the higher order modes visible at 1491 nm, 1430 nm and 1407 nm. The fundamental mode gives a Q factor of 9700 demonstrating the L3 cavity fabrication to be of high quality.

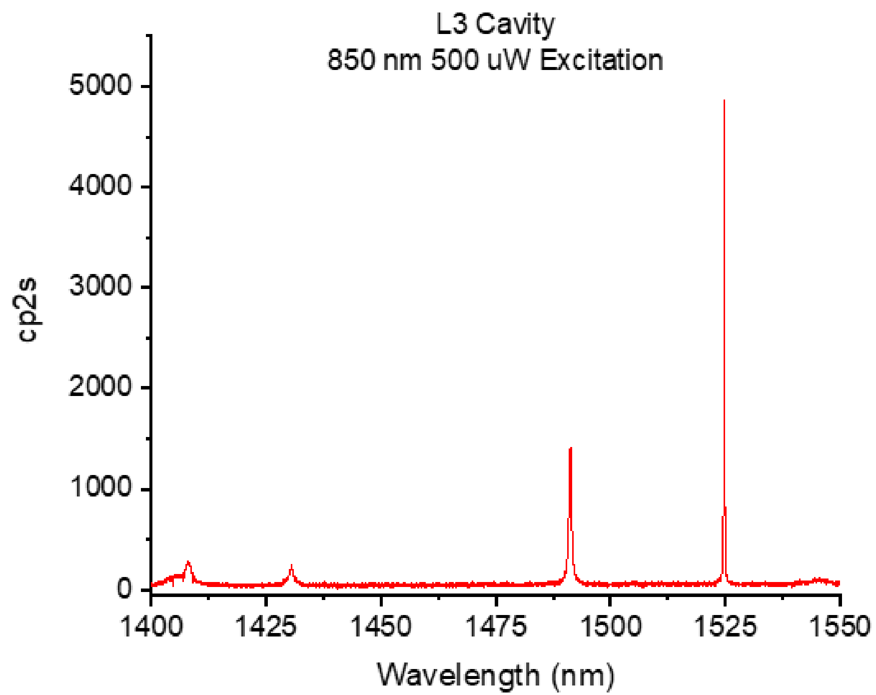

Figure 5.20: *L3 cavity spectrum, the fundamental mode is seen at 1525 nm and the higher order modes are seen at shorter wavelengths. Data from block with 0.8a hole shift.*

As with the H1 cavities, the fabricated L3 cavity lattice constants and hole radii were varied in order to achieve a range of fundamental mode wavelengths. Figure 5.21A and Figure 5.21b give the variation of fundamental mode wavelength as a function of lattice constant and hole radii, respectively. Overall these measurements demonstrate the successful and high quality fabrication of H1 and L3 PhCCs with mode wavelengths covering the C-band.

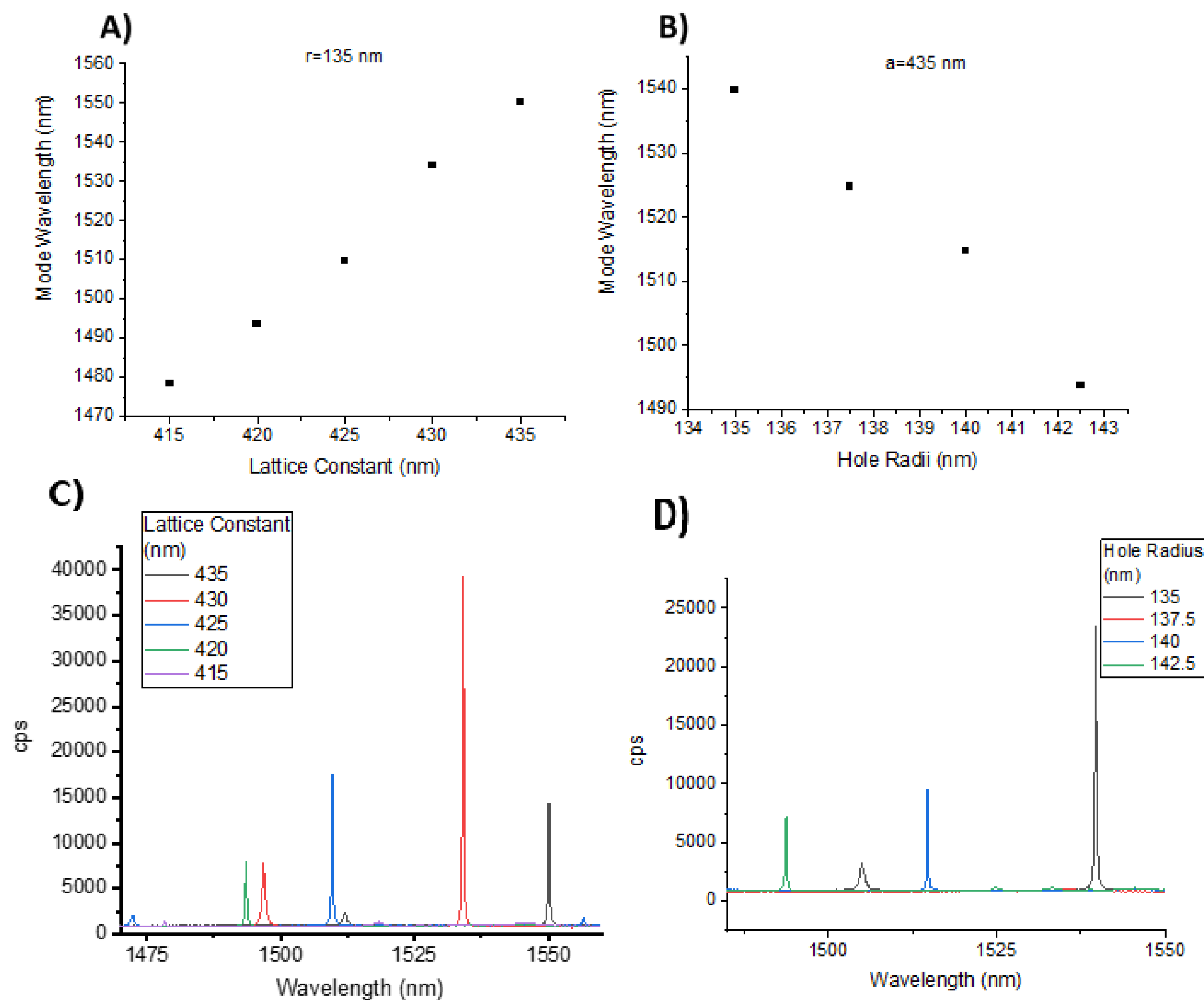

Figure 5.21: *a) Wavelength of fundamental mode red shifts with increasing lattice constant. b) Wavelength of fundamental mode with blue shifts increasing hole radii. Data from block with 0.8a hole shift. C) Spectra for the lattice constant change data shown in panel A. D) Spectra for the hole diameter change shown in panel B.*

Next, low power micro-PL measurements were required in order to find individual QDs in PhCCs, these measurements were taken on many H1 and L3 cavities but unfortunately no single QDs were found when measuring the structures. Measurements were taken on the bulk region of the sample, shown in Figure 5.22, which showed QD lines but fewer than for the initial characterisation piece presented in Figure 5.10B. This suggests that the particular area of the wafer that this fabrication piece was taken from had a lower QD density than expected.

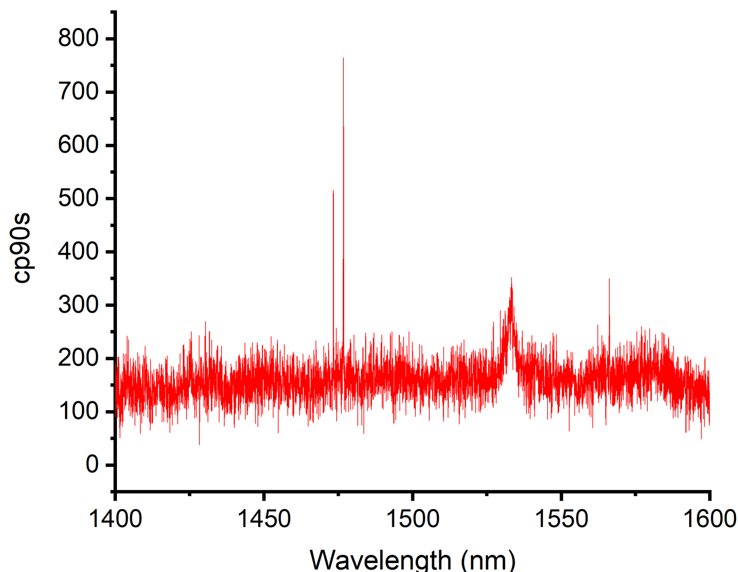

Figure 5.22: *Low power micro-PL spectrum of a bulk region of the fabricated piece. Fewer QD lines are seen compared to the piece measured in 5.10B, suggesting fabrication took place on a low density region of the wafer.*

The QD density in the sample used for the fabrication was ~9x10^8 cm^{-2}. Comparing to previous work by Birowosuto et al [87] on QDs in InP-based PhCCs used QD densities of the order of 10^{10} cm^{-2}. Furthermore, the work by Kors et al [88] also used QDs of a density of the order of 10^{10} cm^{-2} [113]. Both of these studies were able to demonstrate emission from QDs within PhCCs. Though the sample presented in this section appeared to have a lower than expected QD density, it appears that QD density for the recipe used (~9x10^8 cm^{-2}) is too low.

It is clear that an order of magnitude increase on the QD density used here would lead to an increased chance of measuring QDs in PhCCs. As seen in the previous chapter, higher QD densities of the order of 10^{10} cm^{-2} were accessible in this project by growing the QDs on interlayers. The fabrication of PhCCs using these growth structures will be presented in the next chapter.

5.4 Summary

Overall this chapter has presented the development of PhCCs operating around 1.55 μm in InP. PhCC devices were simulated using FDTD methods in Lumerical and these designs formed the basis

for the fabricated strcutures. The PhCC fabrication process has been adapted and developed from GaAs to InP and shown to be successful with the measurement of PhCC modes and high Q factors demonstrated. No QD lines were measured in low power micro-PL which has been attributed to the low density of QDs used in these structures. The next chapter will explore the integration of high density QDs with the PhCC fabrication.

Chapter 6

High Density Quantums Dots in Photonic Crystal Cavities

With an established process for the fabrication of PhCCs, a new growth structure was required to increase the likelihood of finding QDs within the structures and ultimately measure a Purcell enhanced QD. As we have previously established, a QD density of the order of 10^{10} cm^{-}2 has been shown to be required for increasing the likelihood of measuring QDs within PhCCs.

This chapter outlines PhCC fabrication using alternative growth structures which make use of QDs grown on interlayers in order to access a higher QD density. The fabrication of PhCCs only included L3 cavities, this was done due to L3 cavities being of a larger size than the previously fabricated H1 cavities. Having a larger cavity size increased the chance of spatial overlap between a QD a cavity, thus increasing the chances of a Purcell enhancement. Unless stated otherwise, micro-PL measurements presented in this chapter were taken in the closed cycle cryostat system. The vibrations in the system were low enough to make measurements on the small devices areas possible, realignment was done on a cavity after each measurement in order to account for any possible system drift.

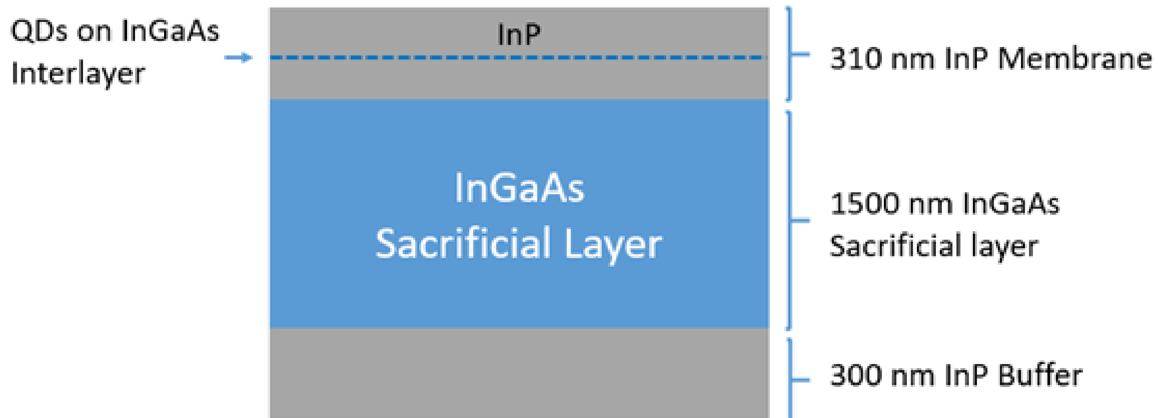

Figure 6.1: *New growth structure for high density QDs, QDs are grown on a 5 nm InGaAs interlayer within a 310 nm thick InP membrane. These are grown on top of a 1500 nm thick InGaAs sacrificial layer.*

6.1 InAs/InGaAs/InP QDs for Devices

At the time that work presented in this chapter had started the only option to increase the density of the QDs was to grow the QDs on a 5 nm InGaAs interlayer. This uses the growth parameters presented in Chapter 4 which allows for QD densities of $1\text{x}10^{10}$ $\text{cm}^{-}2$, over an order of magnitude higher density than the QD growth used for the initial set of PhCCs. Figure 5.9 shows the growth structure for the first high density dot sample.

As with the membrane structure presented in Chapter 5 this high density dot sample consists of a 300 nm InP buffer, 1500 nm InGaAs sacrificial layer and a 310 nm InP membrane layer. The QDs are grown on a 5 nm InGaAs interlayer which is grown in the centre of the InP membrane.

Prior to device fabrication the wafer was checked in micro-PL to confirm first the presence of QDs then the expected density and linewidths of QDs. Figure 6.2A gives a high power micro-PL measurement which reveals the InGaAs sacrificial layer emission peak sitting on top of the broad QD-related emission. The emission from the 5 nm InGaAs interlayer is not present in this measurement, this is likely due to the layer efficiently feeding the QDs. Figure 6.2B gives the corresponding low power micro-PL measurement showing a high density of QD lines as desired for this sample. Additionally, there is a high proportion of single lines at wavelengths greater than 1500

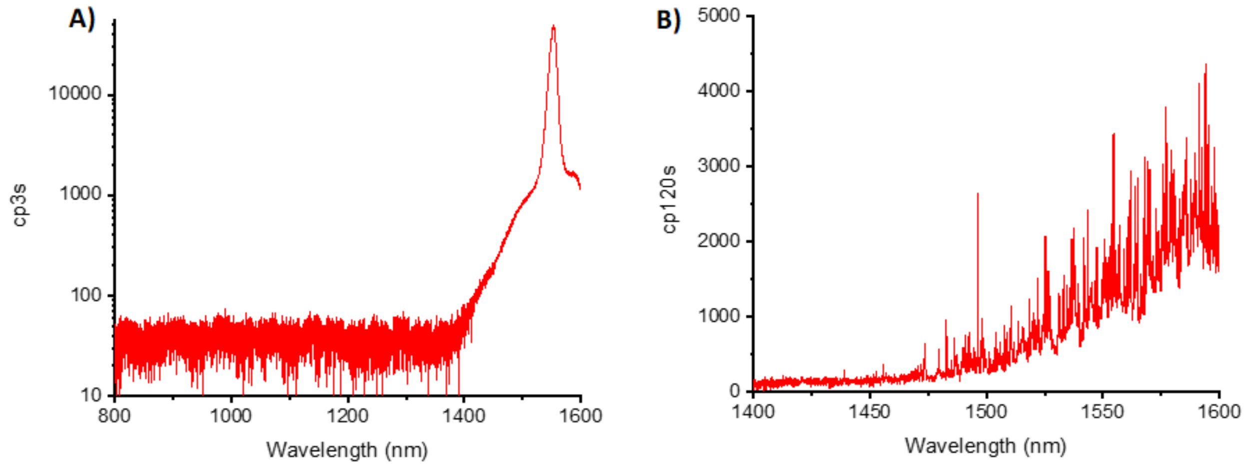

Figure 6.2: *A) High power micro-PL measurement of the new sample structure for PhCC fabrication. QD ensemble can be seen from 1400 nm and the InGaAs sacrificial layer is seen at 1550nm. B) Low power spectrum of the same sample showing sharp lines originating from the QDs.*

nm. The high density and longer wavelength of the QDs measured in this wafer indicates a good alternative recipe to the previous wafer for device fabrication.

6.1.1 Fabrication and Characterisation

Devices were then fabricated using this wafer with the same process as outlined in the previous chapter. The new sample structure presented a possible risk in that the QDs are grown on an interlayer of the same material as the sacrificial layer. After the InP etch the edge of this interlayer would then be exposed to the subsequent 20 minute $FeCl_3$ undercut etch, this is shown in Figure 6.3. The thickness of the interlayer was 5 nm so it was proposed that such a thin layer would have a reduced etch rate such that the interlayer etch would not negatively affect the dots. However, this turned out not to be the case.

Figure 6.4 shows SEM images of a set of nanobeam waveguides post-fabrication. This particular set of NB waveguides shows delamination of the InP membrane above the InGaAs interlayer, likely originating from the etching away of the interlayer.

Figure 6.5 shows an SEM image of an L3 cavity. Looking at the holes of the PhC, evidence for interlayer etching can be seen around the perimeter of each of the holes, a red circle gives a specific example. The etching appears to extend up to approximately 40 nm radially out from the holes

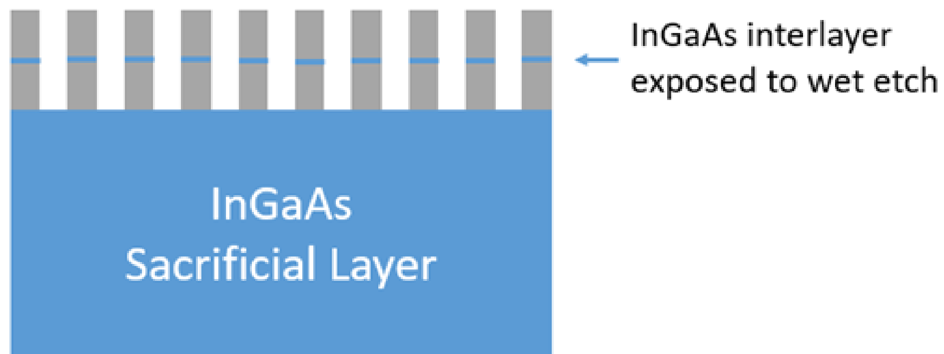

Figure 6.3: *Diagram showing the PhC after the InP etch. The InGaAs interlayer is exposed due to the InP etch and therefore will be exposed to the sacrificial layer wet etch.*

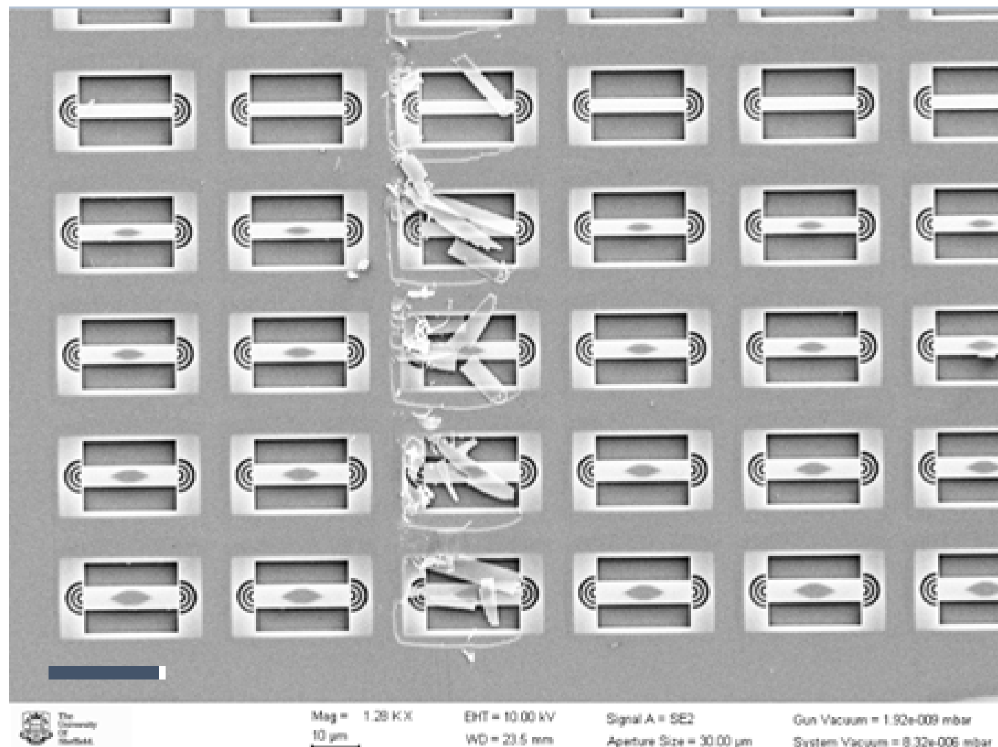

Figure 6.4: *SEM image of a set of nanobeam waveguides. One column shows clear evidence of delamination which indicates that the InGaAs interlayer has been etched during the sacrificial layer removal. Scale bar is 20 µm.*

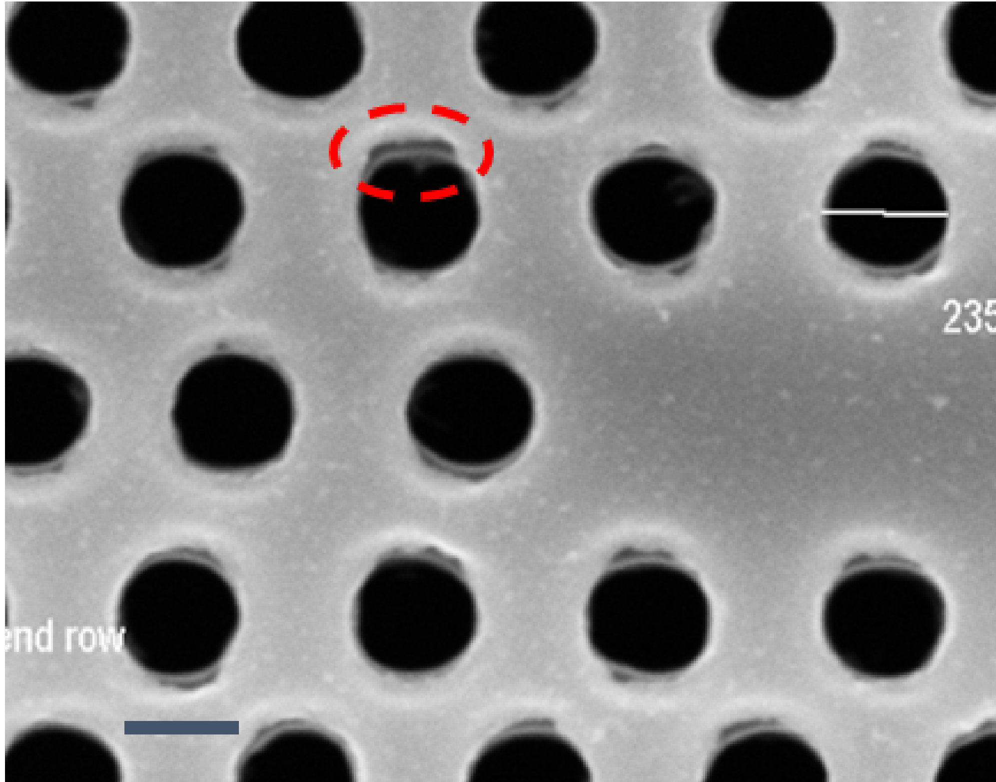

Figure 6.5: *SEM image of L3 cavity where etching of the interlayer is visible around the edges of the holes. A specific example is shown by the red dashed circle. Blue scale bar is 200 nm.*

and, as shown in Figure 6.5, the etching does appear to be different for each hole. Where some show a single clear notch and others multiple notches. Evidence for etching was seen to be present in all L3 cavities observed under SEM.

The post-fabrication SEM images showed evidence for the interlayer being etched but it was necessary to confirm the detrimental extent of this etching with optical measurements.

L3 cavities were measured in micro-PL but no evidence of cavity modes or QD emission could be found. This fabrication run included an additional sample that was fabricated at the same time, (hence same fabrication conditions) as the sample presented in this chapter. This piece was measured in the bath cryostat system and also showed no evidence of QD emission or cavity modes.

These measurements strongly indicate that the interlayer has been etched to such an extent that the device fabrication has not been able to reproduce the cavity modes measured in the previous chapter.

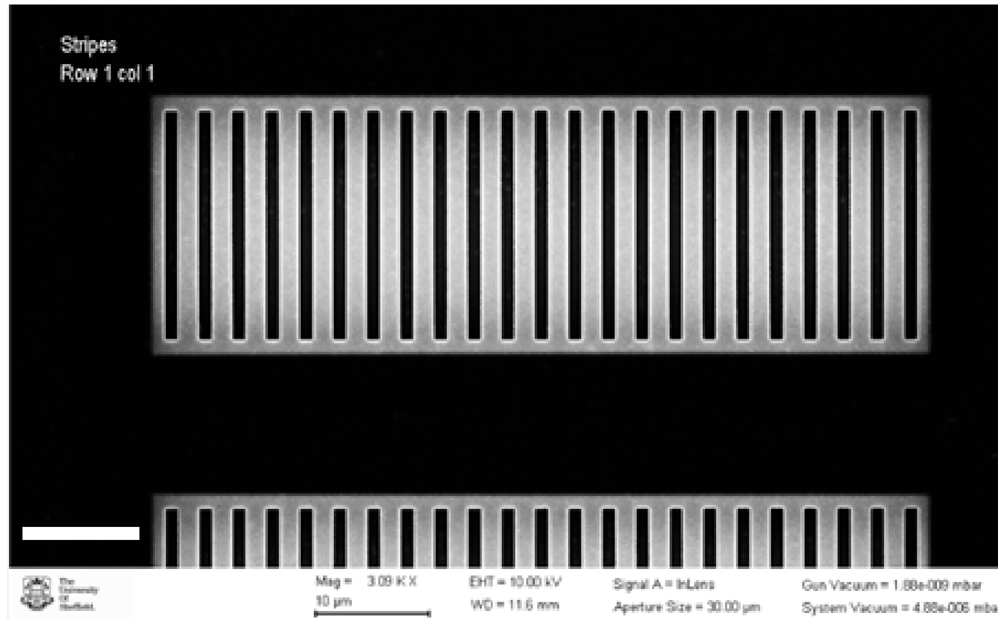

Figure 6.6: *Under etched stripes. Scale bar is 10 μm.*

To further investigate the extent of etching, measurements were taken on patterned stripes on the sample. The dimensions of the stripes were 2 μm width and 10 μm in length, which also appeared to be under etched, an SEM image of such a structure is shown in Figure 6.6. Micro-PL measurements on these features also showed no emission relating to the QDs. The dimensions of the non-etched parts of these stripes are much larger than the non-etched regions in the PhCCs with approximately a micron separating etched surfaces compared to approximately 100 nm for the PhCCs. The fact that there is no emission from the QDs shows that the interlayer attack is a problem on distance scales larger than PhCCs dimensions.

To ensure that we were not over etching the sample, a further fabrication run was performed with a shorter $FeCl_3$ undercut etch time. Originally it had been found that 10 minutes was too short to undercut the samples so 20 minutes was used in the established fabrication process. Here an undercut etch time of 15 minutes was used, in order to reduce the detrimental interlayer etching.

Figure 6.7 shows a high power micro-PL spectrum of a new L3 cavity with the shorter etch time. The peak at 1550 nm is attributed to remaining InGaAs sacrificial layer possibly under the InP membrane, located at the same wavelength as the InGaAs peak seen in bulk but being significantly weaker. In this example the peak count rate is approximately 600 cps whereas the bulk count rate is approximately 16,000 cps (see Figure 6.2A) for comparison).

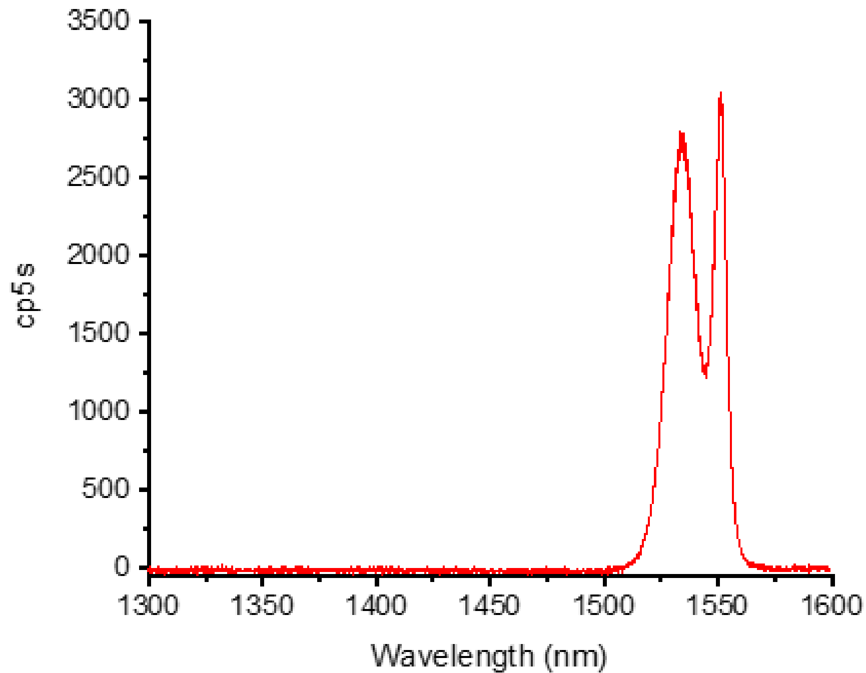

Figure 6.7: *High power micro-PL spectrum of an L3 cavity with a 15 minute undercut etch time. Emission from what is believed to be remaining InGaAs under the PhCC is seen at 1550 nm. A possible cavity mode is seen at 1534 nm.*

The origin of shorter wavelength peak at 1534 nm is likely a cavity mode being excited by the shorter wavelength tail of the InGaAs sacrificial layer emission. The sets of L3 cavities on this sample were organised into rows of decreasing PhC hole radii. This apparent cavity mode peak shows a red shift as the PhCC hole size decreases, matching the expected behaviour for a PhCC mode. The InGaAs peak stays at the same wavelength for each device.

The presence of cavity modes is an improvement for the 15 minute undercut etch compared to the 20 minute etch. However, the devices still do not show emission from the QDs, so whilst etching of the InGaAs interlayer was not completely destroying the integrity of the PhCC, it was enough to compromise any emission from the QDs in the cavity, and therefore the problem of optimising the etch process in these structures was deemed to be very challenging.

Shorter $FeCl_3$ under etch times were not considered due to the presence of the InGaAs emission which indicated that 15 minutes was too short a time to under etch the sample fully. Etch times between 15 minutes and 20 minutes were not considered due to a 15 minute undercut etch being long enough to effectively stop the QD related emission.

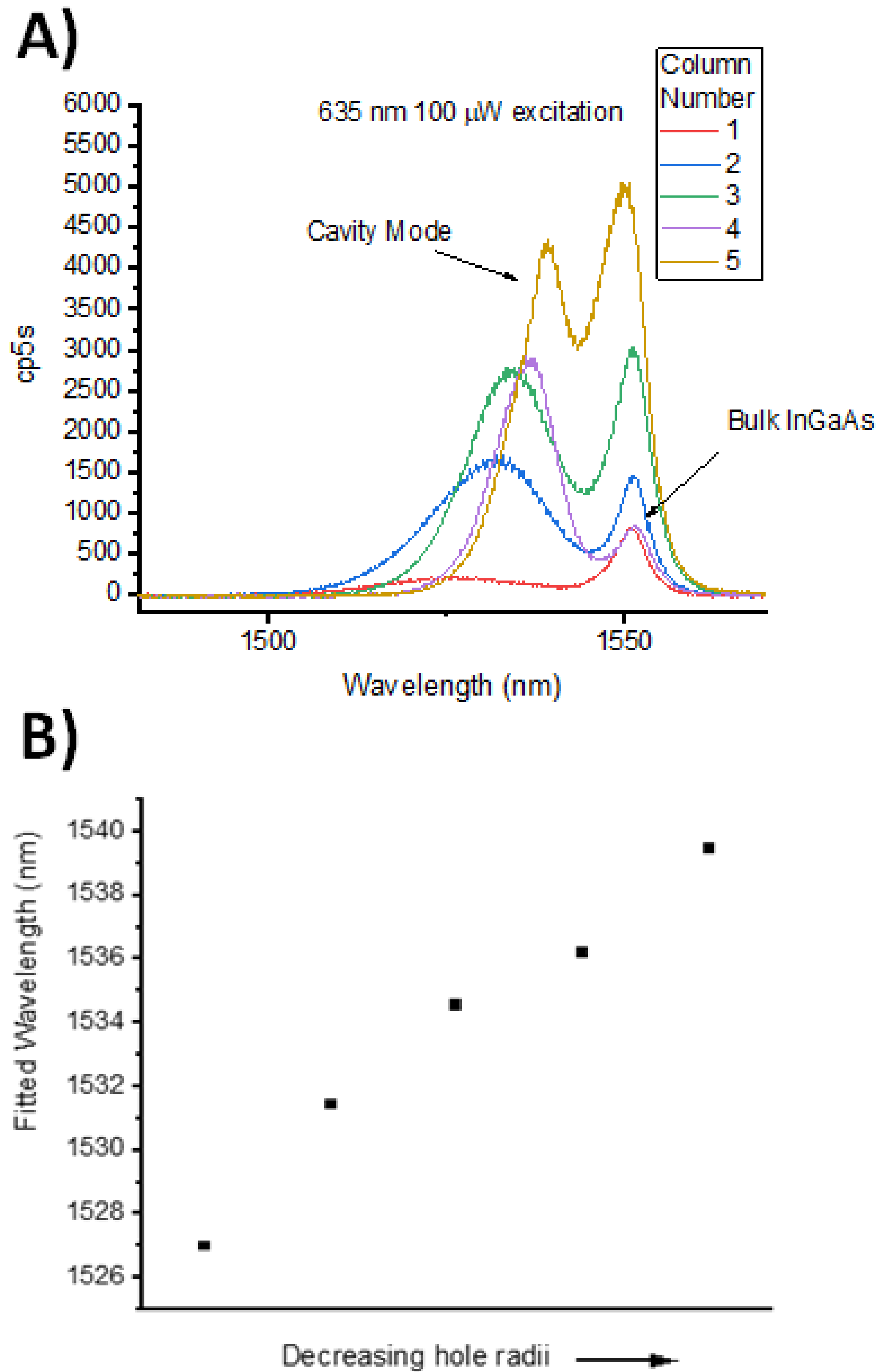

Figure 6.8: *A) Spectra for increasing hole sizes where column 1 has the smallest holes and column 5 has the largest holes. B) Wavelength of cavity modes for decreasing hole radii. The wavelength shows a clear redshift with decreasing hole radii.*

Sacrificial Layer	**Interlayer**
InGaAs	InGaAs
InAlAs	InGaAsP
AlInGaAs	

Table 6.1: *Possible interlayer and sacrificial layer options available for growth.*

6.2 Optimisation of High Density QDs in Devices

In order to solve the problem of the QDs not being optically active after the fabrication, a new approach was required. The first possible option was to alter the fabrication process by including a wet etch window. The second option was to change the sacrificial layer material and the third option was to change the interlayer on which the QDs were grown.

The first option is outlined in Figure 6.9. Rectangles near to the PhCCs would be included in the initial EBL patterning, these would then be etched into the hard mask and then the subsequent InP ICP etch would leave trenches. Another hard mask deposition would follow which would allow for the interlayer in the PhCCs to be protected from subsequent wet etching. Additional EBL patterning would then expose a central strip of the trenches with the sidewalls of the trenches protected. Opening up this trench would then create a wet etch window.

The undercut etch of the PhCCs would then take place through these windows and proceed bottom-up under each PhCC, leaving the interlayer and thus the dots in the PhCCs unaffected. A final BOE would remove remaining hard mask.

The second option involved using a different sacrificial layer to InGaAs in the growth structure and the third option was to change the interlayer from InGaAs to InGaAsP which required a development of the MOVPE epitaxy, but became available at this point in the project. These sacrificial layer and interlayer options are summarised in Table 6.1.

The aim here was to have a growth structure in which the sacrificial layer would etch faster than the interlayer during the undercut etch. It was desired that this would occur to the extent that the QDs would be optically active in devices after fabrication.

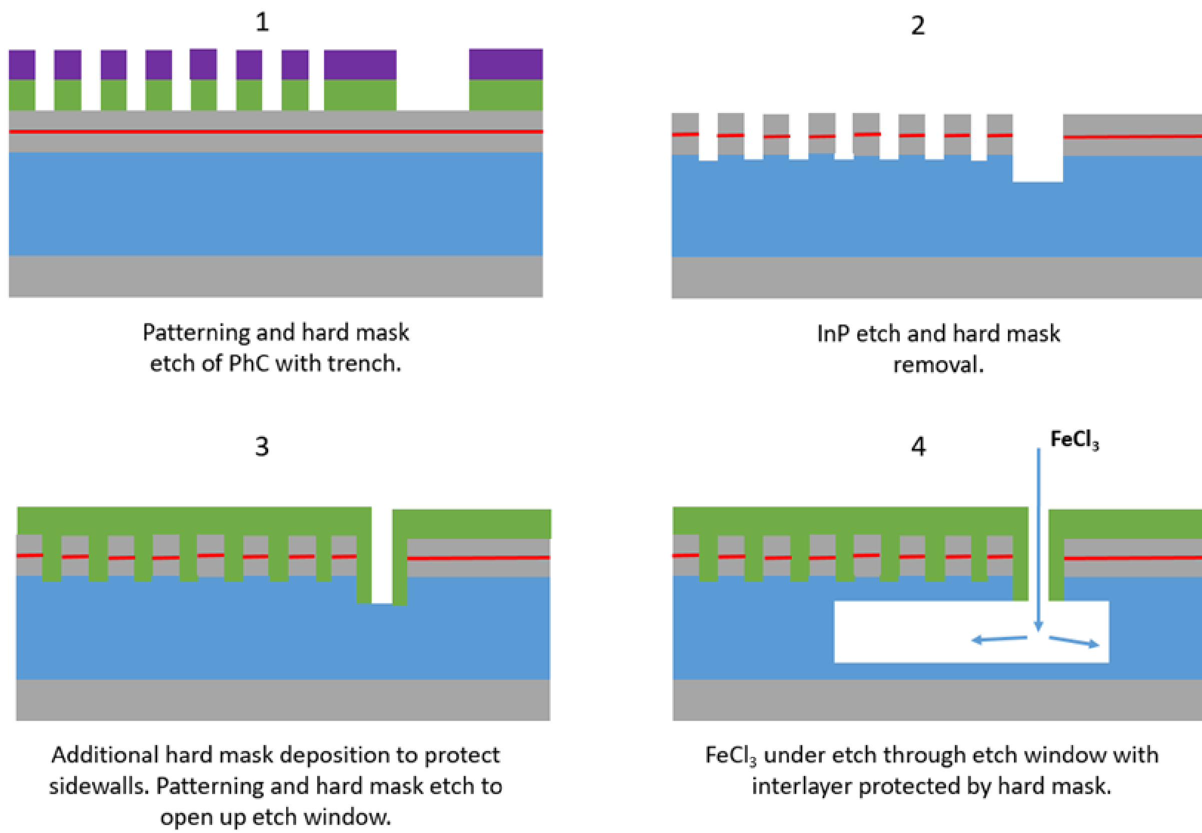

Figure 6.9: *Outline of alternative PhCC fabrication process which makes use of an etch window and protection of the InGaAs interlayer.*

As a starting point for option two, a study by O'Callaghan et al [114] has shown that InAlAs etches over 4 times faster than InGaAs when using $FeCl_3$ at 6 ^oC. This result indicates that an InAlAs sacrificial layer combined with the InGaAs interlayer would be an improvement over the InGaAs interlayer and InGaAs sacrificial layer combination. Additionally, the fabrication would not need to be significantly altered due to the use of the same $FeCl_3$ etchant. No studies looking at the etching of AlInGaAs with $FeCl_3$ were found in the literature so this would need to be investigated.

With regards to changing the interlayer to InGaAsP, succinic acid has been shown to etch InGaAs selectively to InGaAsP [115]. However, this etchant was not available at the University of Sheffield cleanroom facilities at the time this work was being carried out. As previously discussed, ideally a new sample structure would use the same etchant as in the established process. Therefore, investigations into its etching with the available $FeCl_3$ would need to be undertaken due to no published information being found on the etching of InGaAsP with $FeCl_3$.

It was decided that options two and three would be followed, where different growth structures for the PhCCs would be explored instead of changing the fabrication process. From the literature, an InAlAs sacrificial layer was shown to be a good alternative sacrificial layer option that used $FeCl_3$ as an etchant. Investigations into the etching of the possible interlayer and sacrificial layer options would need to be undertaken. This was deemed to be simpler than changing the fabrication process which would be hampered by the EBL experiencing significant downtime at this point in the project. Additionally, material for testing was readily available at this time in the project so this route could be explored relatively quickly.

6.2.1 Ferric Chloride Wet Etch Tests

The desired outcome of following options two and three was to have a structure where the sacrificial layer etched faster than the interlayer, to the effect that the QDs were optically active after the sacrificial layer removal. In order to investigate this, etch tests were performed on wafers containing the material presented in table 1 in order to compare their respective etch rates. The wafers comprised of a 300 nm InP buffer layer with 500 nm of either InGaAs, InGaAsP, AlInGaAs or InAlAs with a 20 nm InP cap. A general sample structure is shown in figure 6.10.

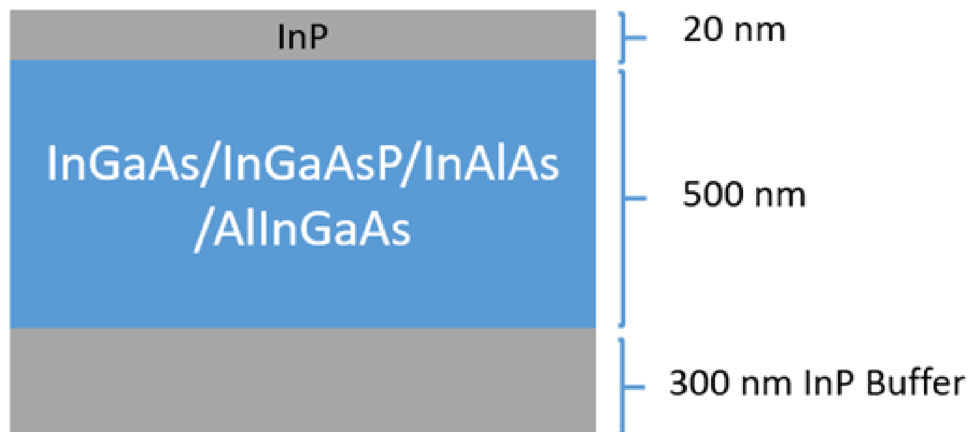

Figure 6.10: *Schematic of wafer used for wet etch testing. Each wafer comprised of a 300 nm InP buffer with 500 nm of either InGaAs, InGaAsP, InAlAs or AlInGaAs. This was completed with 20 nm of InP.*

The etch rates would be investigated by submerging each sample in $FeCl_3$ which can attack the exposed edges of the sample, as shown in Figure 6.11. By SEM imaging the samples edge on, the lateral etch distance for each material can be measured.

Wet etch tests were performed using $FeCl_3$ at 7 ^{o}C, the same etchant and temperature conditions as used previously. The samples containing InGaAs, InGaAsP and AlInGaAs were dipped in the etchant for 40 minutes whilst the sample containing InAlAs was dipped for 5 minutes due to the fast etch rate removing all the InAlAs in the 40 minute dip.

SEM Images for the InGaAs, InGaAsP, AlInGaAs and InAlAs samples are shown in Figure 6.12 A,B,C and D, respectively. It was found that the samples did not need to be SEM imaged edge on due to the presence of a clear line near the sample edges. This line originates from where the material had been etched and the lateral etch distance can be ascertained by measuring the distance from the sample edge to this line. It should be noted that the value for lateral etch distance is an approximation due to the samples not always being perfectly straight inside the SEM. It can be reasonably assumed that when the material of interest is removed the top InP layer falls away due to it being so thin.

The lateral etch distances for a 40 minute etch are summarised in Table 6.2. The value for the InAlAs containing sample is extrapolated from a 5 minute etch.

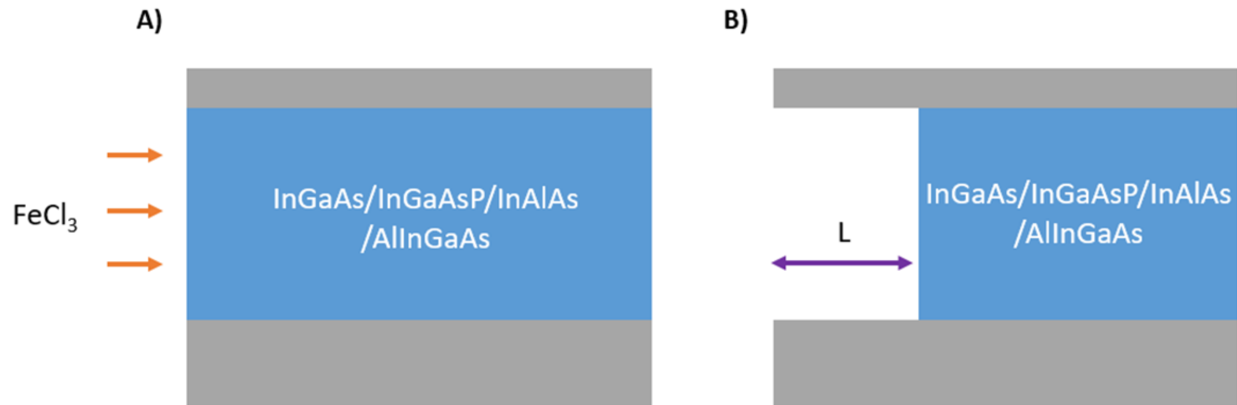

Figure 6.11: *Method to compare etch rates of the different materials. A) The FeCl3 attacks the exposed edges of the sample. B) The amount of etched material (L) can be determined by SEM imaging the sample edge.*

Material	Approximate Lateral Etch Distance (μm)
InGaAs	10
InGaAsP	0.72
AlInGaAs	28
InAlAs	38

Table 6.2: *Approximate lateral etch distances for each material tested.*

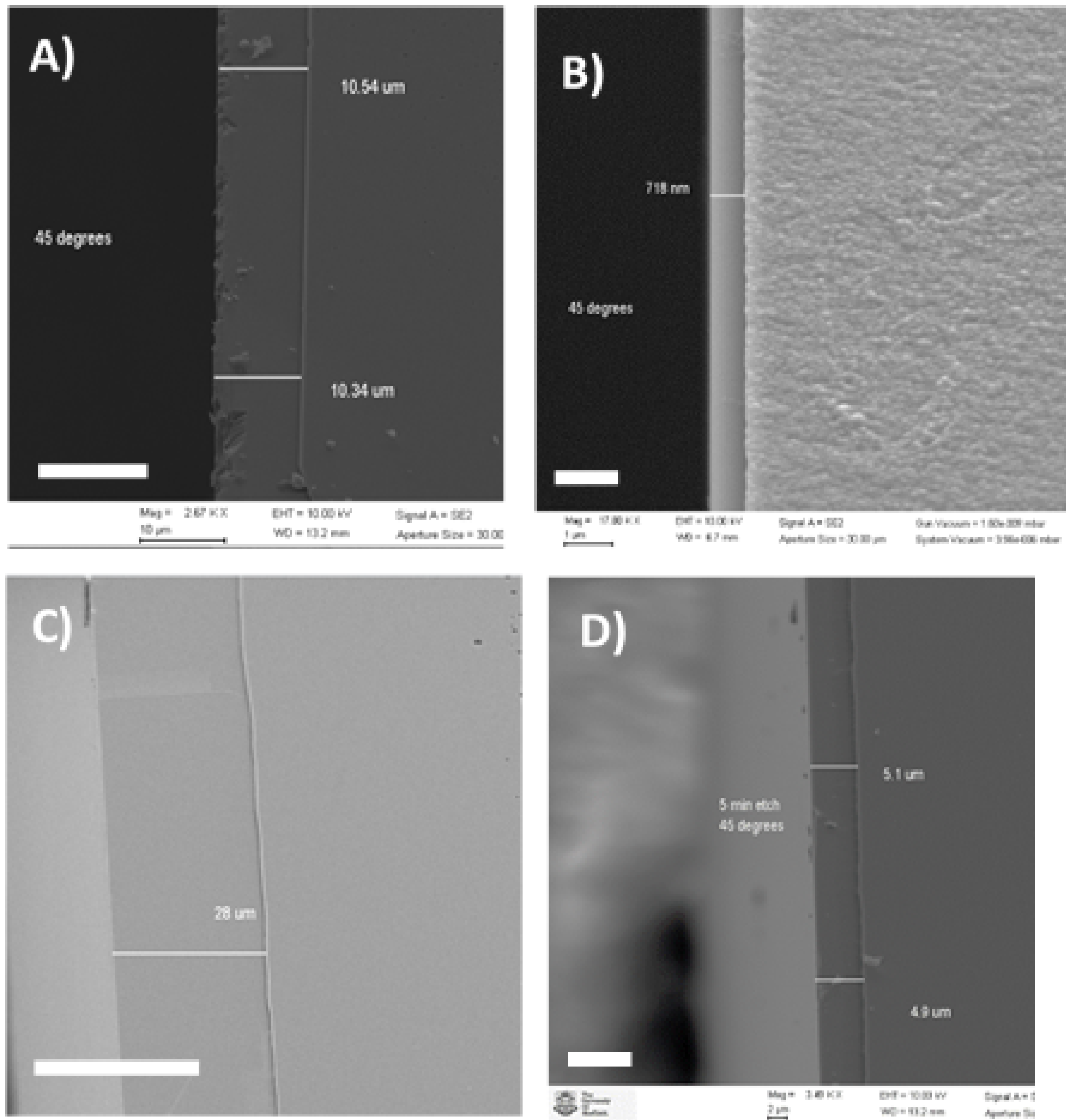

Figure 6.12: *45 degrees tilted SEM images of test wafers after wet etch. A) InGaAs with scale bar of 10 µm. B) InGaAsP with scale bar of 1 µm. C) AlInGaAs with scale bar of 30 µm. D) InAlAs with scale bar of 5 µm. Note the InAlAs sample was only etched for 5 minutes compared to the 40 minute etch for the other samples.*

These results show that InGaAsP has an etch rate approximately 13 times lower than InGaAs. Such a slow etch rate makes it the preferable choice for the QD interlayer as the layer will be etched significantly less than InGaAs and validates our aim to use the recently developed InGaAsP as the interlayer. This fulfils the target of reducing the interlayer attack and increasing the chances of having optically active QDs after the undercut etch.

With regards to the choice of sacrificial layer, the aim was to have it etch faster than the interlayer. This aim is met with InGaAs (sacrificial layer) etching 14 times faster than InGaAsP (interlayer) but is greatly improved upon with InAlAs and AlInGaAs. InAlAs has the highest etch rate compared to InGaAsP, etching approximately 53 times faster. This shows that InAlAs would be a good replacement for InGaAs as the sacrificial layer material. It can also be seen that the InAlAs etches approximately 3.8x faster than InGaAs which matches well with the results presented in [114].

From these results it was concluded that the new growth structure should contain QDs on an InGaAsP interlayer with an InAlAs sacrificial layer. Using this combination would reduce the interlayer etching due to the reduced etch rate of InGaAsP compared to InGaAs. Additionally, this choice would benefit from the reduced etch time required due to the increased etch rate of InAlAs compared to InGaAs. These two factors would greatly reduce the extent of any interlayer etching during the fabrication and increase the chance of the QDs being optically active post fabrication.

6.3 New Sample Structure and Fabrication

6.3.1 Wafer Characterisation

A new wafer for PhCC fabrication was grown which featured an InAlAs sacrificial layer and QDs on an InGaAsP interlayer. As with previously fabricated samples, the sacrificial layer is 1500 nm thick with the QD layer being in the centre of a 310 nm thick InP membrane. The sample structure is shown in figure 6.13.

Micro-PL measurements for the non-processed wafer at high and low power are presented in Figure 6.14. The high power measurement in Figure 6.14A shows an emission peak around 818 nm which originates from the InAlAs sacrificial layer [116]. The emission peak at 920 nm is attributed to

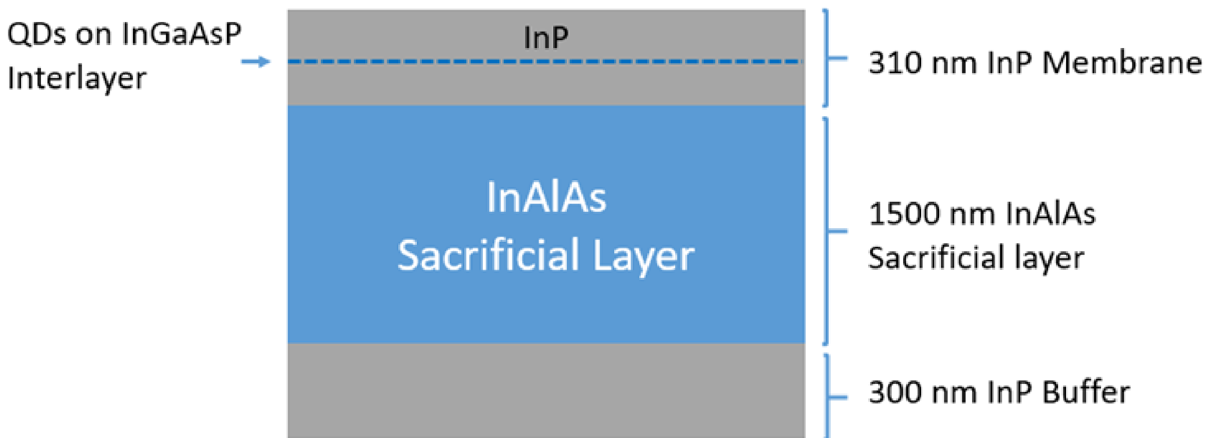

Figure 6.13: *New sample structure for the PhCCs based on the etch tests from the previous section. The QDs are grown on an InGaAsP interlayer and the sacrificial layer has been changed from InGaAs to InAlAs.*

recombination at the type-II interface between the InP membrane and the InAlAs sacrificial layer, which occurs due to the staggered band offset between the two materials [117]. Similarly, the emission peak at 1022 nm originates from the type-II interface between the InAlAs sacrificial layer and the InP buffer [116]. Finally, there is the broad and bright emission related to the QDs starting around 1250 nm.

Figure 6.14B shows the corresponding low power micro-PL spectrum revealing a high density of QDs and a broad range of QD emission lines from 1300 nm up to the detector cut off around 1600 nm. These measurements confirm that the wafer is appropriate for device fabrication due to the high density of emission lines and the emission lines up to the detector cut off at 1600 nm.

6.3.2 Unintentional Layer Problem

One of the advantages of revising the growth structure to achieve high density QDs in devices was the lack of changes required to the device fabrication process. As such, devices were fabricated using largely the same process established in chapter 5. The only change required was the undercut etch taking place for 2.5 minutes as opposed to the previously used 20 minutes. This alteration was done to take advantage of the InAlAs sacrificial layer etching approximately 3.8 times faster than the InGaAs sacrificial layer used in the previous wafer.

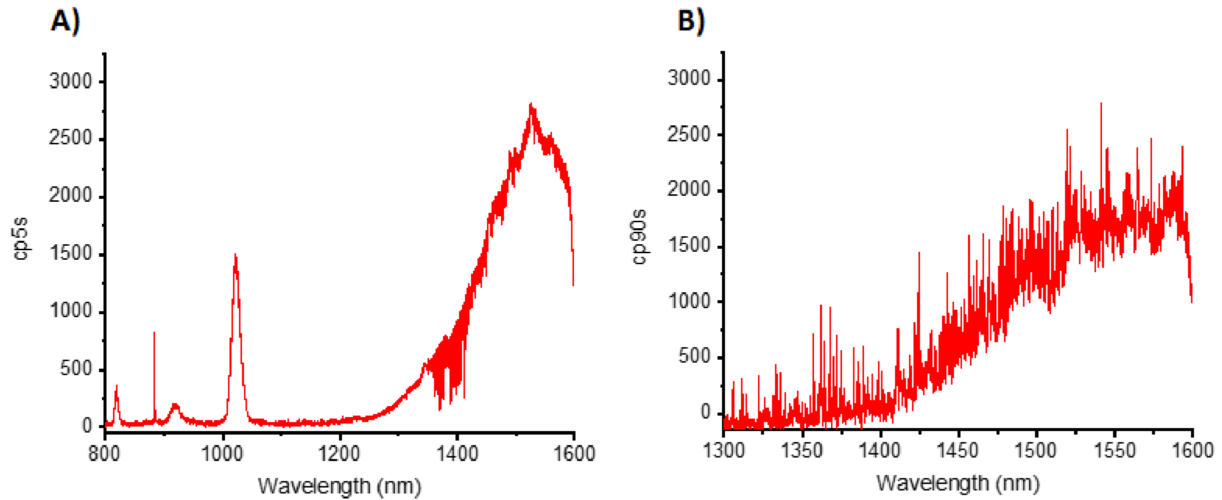

Figure 6.14: *A) High power micro-PL measurement of the new sample structure. This spectrum features emission from the InAlAs (818 nm) and InP (880 nm). Emission at 920 nm originates from the InAlAs/InP interface and the 1022 nm emission originates from the InP/InAlAs interface. Emission related to the QDs is from 1250 nm. B) Low power micro-PL measurement showing QD lines from 1300 nm to the detector cut off at 1600 nm.*

Figure 6.15 shows SEM images of L3 cavities taken after device fabrication had been completed. A layer of some unknown material can be seen on top of the InP membrane and was found across the whole sample. It can be seen that the layer features a similar pattern to the PhC but the holes appear to not be uniform and to be slightly larger than the those in the InP. From Figure 6.15B the layer thickness is approximated to be 145 nm and it also appears as if the layer is not uniformly in contact with the InP.

Such a layer was undesirable for the PhCCs as it would likely reduce the Q factor of the cavity modes. This would be due to the layer compromising the smooth InP membrane/Air interface which is important for device operation. Additionally, the layer appears highly inhomogeneous and could introduce unwanted scatter from QD emission, lowering the count rate of any potential QD measurements.

The fact that the layer has a pattern resembling the PhC holes indicates that the layer was present on the sample prior to the InP etch. It was thought this layer could be either residual SiNx hard mask or EBL resist as these were the only materials intentionally deposited on the wafer during the fabrication process.

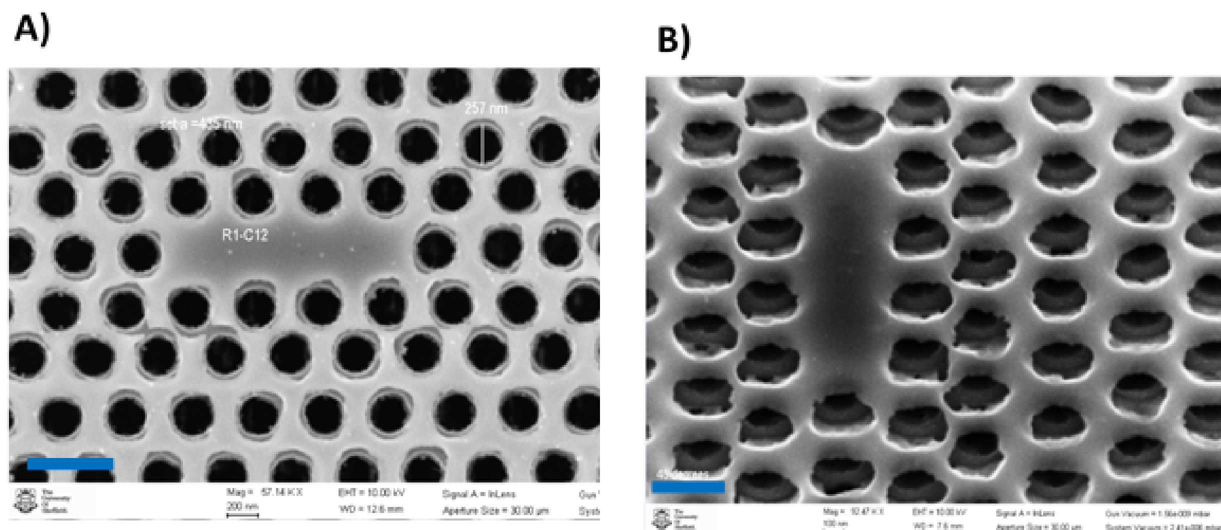

Figure 6.15: *A) Example L3 cavity in SEM showing a patterned layer of some unknown material. Scale bar is 400 nm. B) 45 degrees titled SEM image of an L3 cavity, the InP can be seen below the layer. Scale bar is 200 nm.*

In order to identify the origin of this unintentional layer, EDX measurements were performed on the sample in the SEM. Figure 6.16 shows the area of the sample that was measured in the EDX. The layer of interest is present in the area and can be seen between the etched holes.

This area can then be imaged with respect to the energy of the characteristic X-rays for specific elements. An image with respect to the Silicon, Carbon and Oxygen characteristic X-ray energies is shown in Figure 6.17 A,B and C respectively. These three elements were of interest because it was most likely to be hard mask, which is Silicon-containing, or EBL resist, which is an organic compound. The characteristic X-ray energy relating to Nitrogen, which would be found in the hard mask, was not considered because it is very close in energy to Indium and it was not possible to de-convolve these two emission peaks.

The Silicon image in figure 6.17A does not show any discernible pattern that matches the pattern of the unknown layer. The Carbon and Oxygen images, however, show a clear pattern very similar to the PhC pattern of the unknown layer. From this we can conclude that the layer is formed of an organic compound and likely to originate from EBL resist that was not fully removed from the sample.

Further resist stripping steps were repeated on this sample but the layer was still present. This

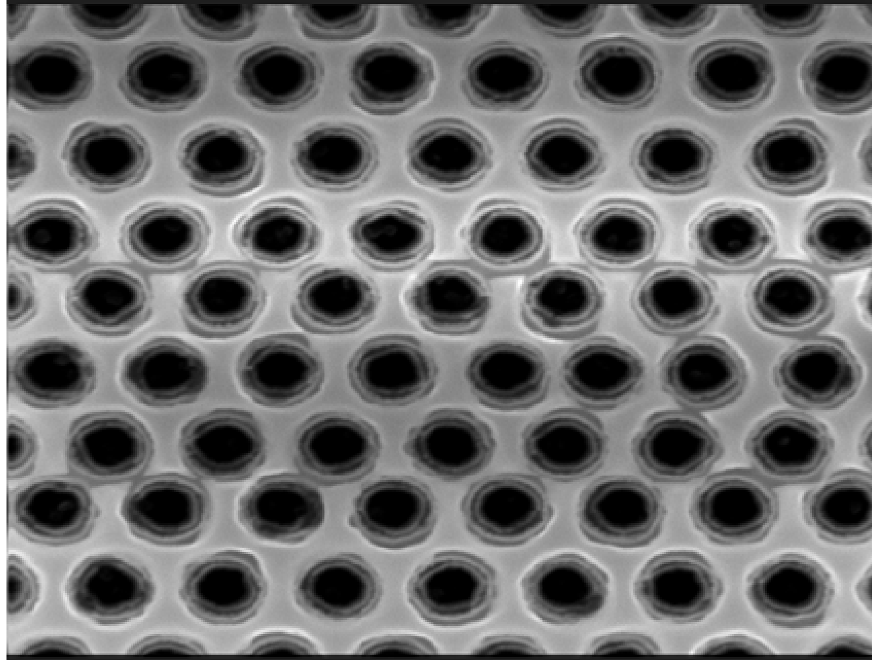

Figure 6.16: *Area of PhC imaged for the EDX measurements. The layer's PhC pattern is clearly visible.*

is likely due to the fact that during the original device fabrication run the EBL resist would have been on the sample during the ICP InP etch. During this dry etch the sample would have been at a very high temperature, curing the resist to such a degree that it was not possible to remove with the standard resist stripping process. Though the presence of this layer could be detrimental to the PhCC mode Q factors and the brightness of any potential QD lines, the samples were measured in micro-PL as it should still have been possible to test whether the QDs had survived the fabrication.

6.4 Micro-PL of Fabricated Structures

Fabricated devices were measured with micro-PL to assess whether the QD emission survived the fabrication. First the under etched stripes were measured, as done for the previous fabrication run with the InGaAs interlayer. This was to gauge whether there was emission from the QDs in these larger structures after the wet etch.

Figure 6.18 shows high and low power micro-PL measurements where excitation takes place on an area consisting of an etched stripe with the InAlAs sacrificial layer removed. These were the same

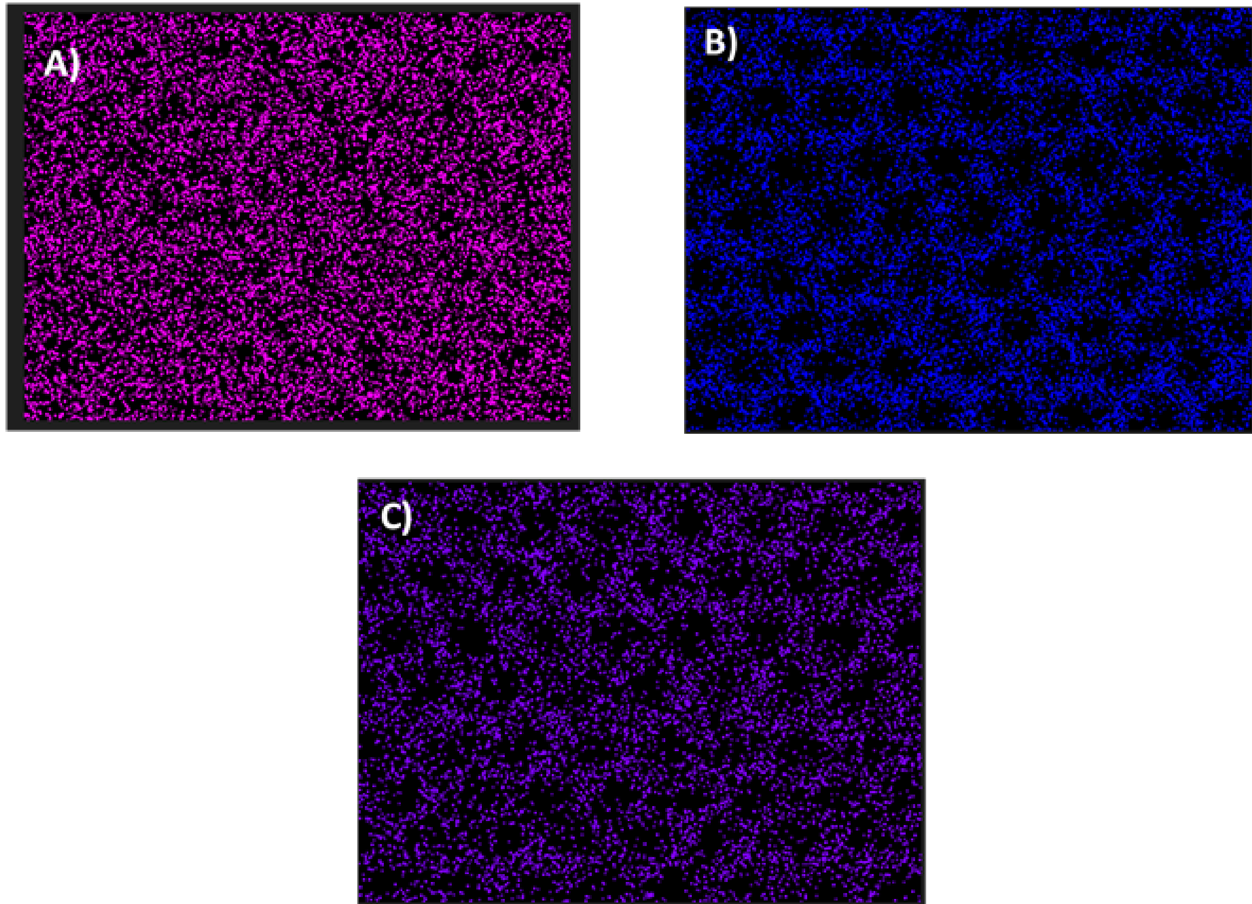

Figure 6.17: *PhC imaged areas for characteristic X-rays of A) Silicon energies B) Carbon energies C) Oxygen energies. The PhC pattern is clear for the Carbon and Oxygen but not visible for the Silicon. This indicates that the layer is organic in nature and likely to be EBL resist*

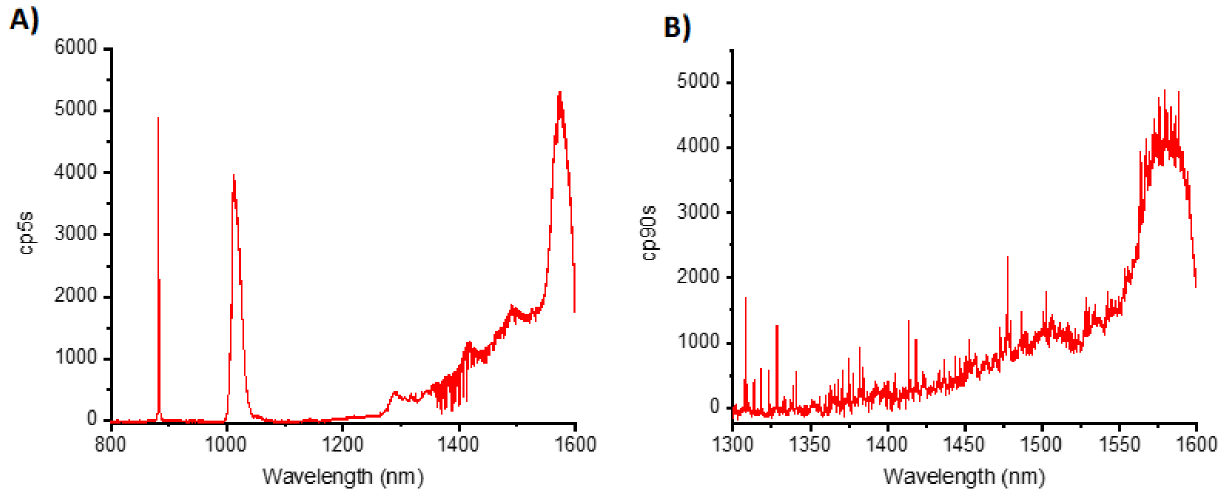

Figure 6.18: *A) High power micro-PL spectrum of the etched stripe. Emission from the InP is seen at 880 nm, emission from the InP buffer/InAlAs sacrificial layer interface is seen at 1022 and QD-related emission is seen for wavelengths greater than 1200 nm. The apparent peak around 1570 nm is attributed to the weak mirror effect from the air gap under the membrane. B) Low power micro-PL spectrum showing single QD lines across the measured range.*

structures presented in Figure 6.6. The high power spectrum in Figure 6.18A shows no InAlAs emission peak at 818 nm which confirms that the measurement location was on an under etched stripe. InP emission is seen at 880 nm. It is also clear that there is no emission peak at 920 nm measured in this location. This is expected due to the wet etch removing the InAlAs sacrificial layer/InP membrane interface.

The high power spectrum also features emission at 1022 nm which originates from the InP buffer/InAlAs sacrificial layer interface as seen in the unprocessed wafer measurements presented in Figure 6.14A. This indicates that there may be a small amount of InAlAs at what would be the start of the sacrificial layer. The QD-related emission is clear for wavelengths greater than 1200 nm. Additionally, there is an apparent peak at around 1570 nm, this is attributed to the air gap under the measured strip causing a weak mirror effect for a given wavelength range.

The low power micro-PL measurement presented in Figure 6.18B is taken in the same location as the high power measurement in figure 6.18A. The graph shows that presence of sharp QD emission lines across the full wavelength range. There is an apparent peak at 1570 nm, this is attributed to an increase in counts due to the air gap under the slit causing a weak mirror effect.

These measurements on the etched stripes region show that altering the growth structure to feature QDs on an InGaAsP interlayer with an InAlAs sacrificial layer has recovered the QD emission for these simple and relatively large under etched structures. This is an improvement on the samples using an InGaAs interlayer for which no QD emission could be found in these structures. This is a positive result but the PhCCs needed to be measured in order to confirm whether this new structure was successful for such devices.

6.4.1 PhCC Micro-PL

With the overall project aim of achieving a Purcell enhancement of a QD transition from a PhCC, QDs in PhC structures must be achieved. This sample also contained sets of L3 cavities and initial micro-PL measurements of these PhCCs aimed to establish whether the cavity fabrication was a success by seeing if cavity modes were present in high power micro-PL.

An example high power micro-PL measurement is shown in Figure 6.19. This data shows the presence of cavity modes indicating the successful fabrication of L3 cavities using the InGaAsP interlayer and InAlAs sacrificial layer wafer. The Q factor for the fundamental mode, at 1563 nm, is approximately 2700 which confirmed that the EBL resist still present on the sample was not overly detrimental to the Q factors of the L3 cavities.

In order to investigate whether QDs were present within the fabricated PhC structures, low power micro-PL measurements were performed on many cavities. Figure 6.20A gives a representative low power micro-PL spectrum of an L3 cavity. The data shows a QD line among cavity mode peaks, the linewidth is 136 μeV which is to be expected for these QDs. This line is only seen at low excitation power and was not seen at high excitation power, whereas the other peaks were seen for both power levels. The excitation power dependent intensity of the line is plotted in Figure 6.20B, this shows the saturation behaviour that is characteristic of QDs. Here the intensity of the QD line initially increases with increasing excitation power as more e-h recombination occurs. The QD line then saturates due to the lifetime of the transmission limiting how much e-h recombination can occur in a given time period. Finally the intensity reduces as the QD line is masked by an increasing background and QD ensemble.

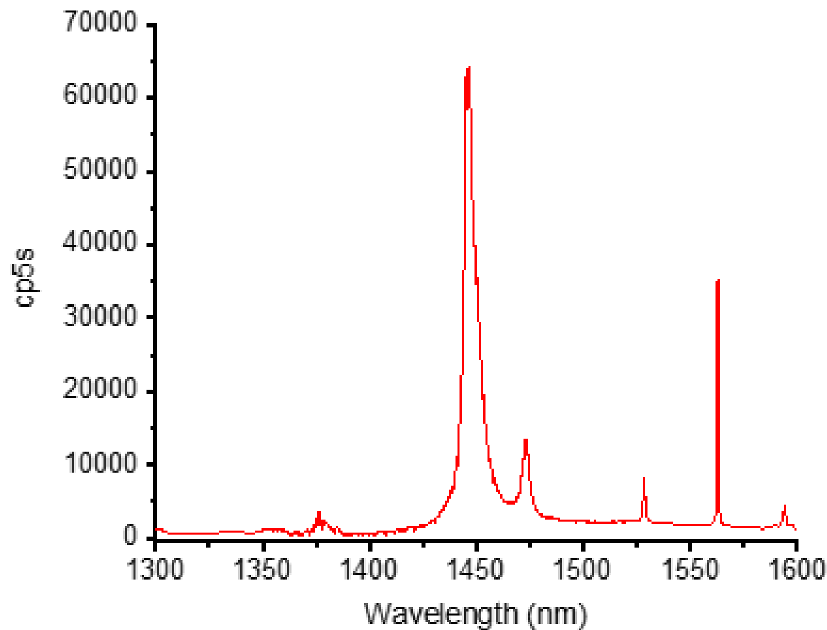

Figure 6.19: *Example high power micro-PL measurement of an L3 cavity in the InAlAs sacrificial layer and InGaAsP interlayer wafer. The presence of cavity modes indicates that this sample structure is superior to the InGaAs sacrificial layer and InGaAs interlayer wafer.*

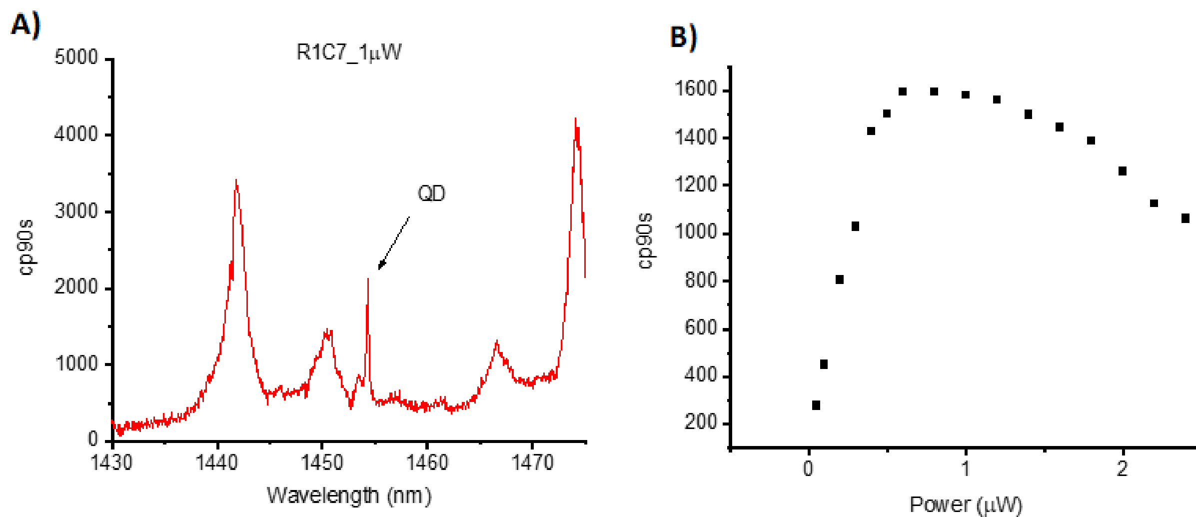

Figure 6.20: *A) Low power micro-PL spectrum of an L3 cavity showing a QD line at 1454 nm. B) Power dependence measurement of 1474 nm QD line intensity showing the saturation behaviour typically seen in QDs.*

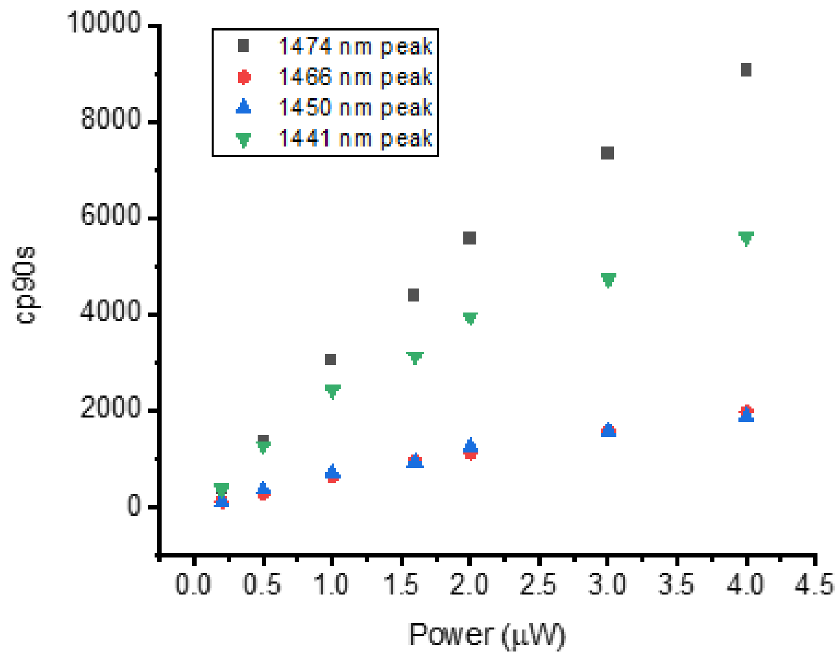

Figure 6.21: *Excitation power dependence of the cavity modes seen in Figure 6.20A. All peaks do not show that same saturation power behaviour as the QD, this allows us to distinguish between the QD line and the cavity mode peaks.*

The presence of this behaviour allows the line to be distinguished from cavity modes which did not exhibit a saturation of intensity with increasing power at these power levels, this is shown in Figure 6.21. Here, all the peaks are seen to still be increasing in intensity at an excitation power of 4 μ.

We can see that QDs have been measured when exciting the L3 cavities but it is important to consider where the QD emission originates. The dot could be within the fabricated device itself, which includes the cavity and the surrounding PhC, or the bulk regions near to the devices. The area of the devices is approximately 70 μm^2 which is larger than the excitation area of 20 μm^2. This means we can be confident that only the devices are being excited. As such, the QD lines measured must either be in the cavity itself or in the PhC surrounding the cavity.

The measurement of QDs indicates that the QDs survived the full fabrication process and that adjusting the growth structure to include QDs on an InGaAsP interlayer with an InAlAs sacrificial layer has recovered the QD emission in the PhCC devices.

For these initial L3 cavity characterisation measurements, a total of 41 cavities were measured with

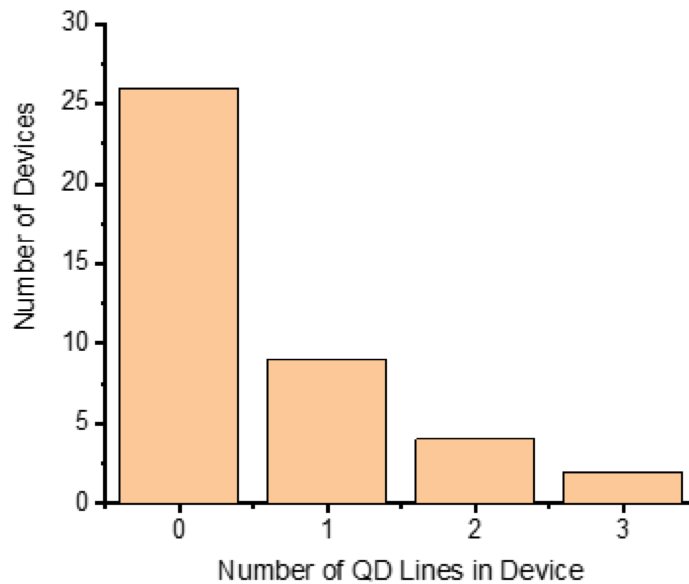

Figure 6.22: *Bar chart of the number of PhC devices and the number of QD lines measured in the devices. The majority showed no QD lines present.*

low power micro-PL. Figure 6.22 shows a bar chart for the number of cavities and their respective number of QD lines. From these 41 L3 cavities, 26 were found to have no QD lines present and 15 were found to have between 1 and 3 QD lines present.

If we consider the micro-PL measurement on the non-processed wafer presented in Figure 6.14B, there are 148 QD lines found within the 1300-1600 nm measurement range. With an excitation spot size of 5 μm diameter, this corresponds to an excitation area of $\sim$20 μm^2. If we consider the case emission lines originating from QDs located only in the cavity, then an area of $\sim$0.8 μm^2 is excited. This excitation area corresponds to 4% of the excitation area for a bulk measurement, from this we can estimate there should be typically $\sim$6 QD lines in the excitation area of each of the cavities.

This lower than expected number of QD lines measured in devices is problematic due to the fact that it reduces device yield, so it is important to consider the cause of this issue and ways to address it. The first possibility is that the issue is related to the presence of the EBL resist layer on these devices. As discussed previously, there is a possibility that this layer would be detrimental to the QD measurements due to it causing scattering of the QD emission. This could result in an apparent loss of QD lines due to their low brightness causing them to not be measured.

In order to test this the fabrication would need to be repeated, ensuring that the resist layer is fully cleaned from the sample after the hard mask etch. Then the L3 cavities can be surveyed and the proportion of cavities showing QD lines can be compared to the sample presented in this chapter.

We can also consider that the InGaAsP interlayer is being etched which is detrimental to the QD emission, similar to what was happening with the previously used InGaAs interlayer. We know that $FeCl_3$ will etch the InGaAsP interlayer as seen with the $FeCl_3$ etch tests. Though clearly the InGaAsP interlayer etching is less than for the case of the InGaAs interlayer due to the successful measurement of QDs in devices.

Going back to the InGaAs interlayer etching, it was seen from Figure 6.5 that the interlayer etching appeared to extend approximately 40 nm out from the PhC holes. There was no clear sign of interlayer etching for the InGaAsP interlayer PhCCs when viewed in the SEM, but it should be noted that the presence of the EBL resist made imaging the PhC holes challenging.

We can estimate how much etching there could be based on the relative etch rates of the InGaAsP and InGaAs from the $FeCl_3$ etch tests. InGaAsP was shown to have an etch rate 13 times lower than InGaAs and the etch time for the InGaAsP interlayer PhCCs was 4 times shorter than for the InGaAs interlayer PhCCs. This due to the inclusion of the InAlAs sacrificial layer. We can then estimate that overall there would be a factor of 52x less interlayer etching for the InGaAsP interlayer sample compared to the InGaAs interlayer sample. This would result in < 1 nm of InGaAsP interlayer etching when comparing to the $\sim$40 nm etching seen for the InGaAs interlayer. Though a reduced amount of etching, this still may be detrimental to the QDs.

In order to address any possible interlayer etching, the thickness of the InGaAsP interlayer could be reduced which would reduce the amount of etching of this layer. Though this would require initial investigations into the growth of the QDs on thinner InGaAsP interlayers. Alternatively, any interlayer etching could be completely stopped by altering the fabrication to include a wet etch window as presented previously in Figure 6.9.

Finally, there is the more general possibility that the ICP etching of the PhC holes and the proximity of QDs to the etched surfaces is detrimental to their emission. For example, the etched surfaces can result in crystal defects and dangling bonds which can create charge trap states on the surface

[118]. These charge traps could result in a change in the distribution of charge in the sample which may mean that charged excitons states are not observed from the QDs. This could account for the low number of QD lines observed in the PhC samples presented here.

Spectral wandering could occur for QDs which are near to these surfaces. Indeed, this has been observed for GaAs-based QDs, where a QD within a 100 nm diameter etched pillar, so within 50 nm of an etched surface, was measured. The emission wavelength was observed to vary over 4 nm in a 300s measurement, this was attributed to high levels of spectral wandering caused by the proximity to etched surfaces [119].

It is possible that this could be occurring within the PhCCs presented here as there will be QDs within 50 nm of etched surfaces, such large amounts of spectral wandering would make it difficult to measure the QDs. This is because the micro-PL measurements performed here take place over timescales of minutes, similar to the timescale of spectral wandering measurement seen in [119]. If spectral wandering was occurring to the large extent as seen in [119] then QD lines would not be measured due to the counts being spread out over such a large wavelength range.

In the case of [119], surface passivation was employed to address the problem. In this process the semiconductor surface is treated and the density of surface defect states is reduced [120] which can significantly reduce the effect of the spectral wandering. This was achieved by the deposition of a 15 nm Al_2O_3 capping layer on the etched column was shown to stabilise the QD emission.

For the InP PhCCs presented in this thesis, surface passivation could be investigated as a way to recover the QD emission. This could negate the possibility that charged states are not being measured and any potential spectral wandering effects. In the InP material system, surface passivation can be achieved by combining Al_2O_3 with a phosphorus oxide [121]. Another option is to investigate the use of pin structures where an electric field can be applied across the devices. This would enable control of the charge environment of the QDs which could negate any potential charge distribution changes and spectral wandering from the etched surfaces.

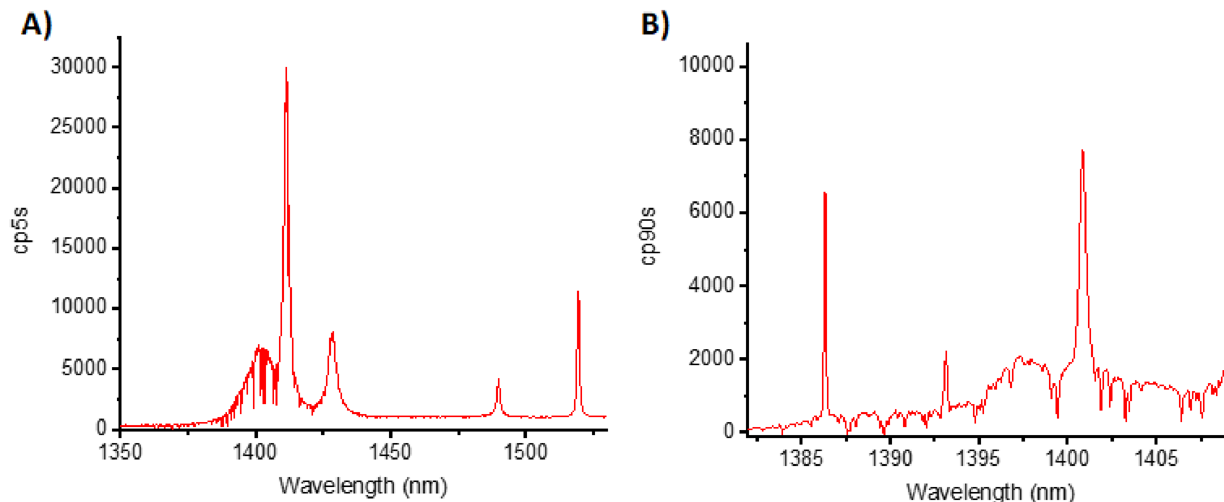

Figure 6.23: *A) High power micro-PL measurement of an L3 cavity showing the cavity modes. The mode at 1402 nm with a Q of ∼100 is of interest B) Low power micro-PL measurement showing three QD lines overlapping spectrally with the low Q mode. Note that the spectra show water absorption for wavelengths <1425 nm.*

6.5 Initial Candidates for Purcell Enhancement

Though the PhCCs presented in this chapter show fewer QDs than expected, devices were found where QD lines spectrally overlapped with cavity modes. The following section gives an initial analysis of devices measured during the survey of L3 cavities outlined in the previous section. It should be noted that the first two devices were measured in the flow cryostat system so the option to measure the lifetimes of the QD lines with time resolved measurements was not available.

6.5.1 First Device

Figure 6.23A shows a high power micro-PL spectrum of an L3 cavity which shows L3 cavity modes. Measuring the same cavity with low power micro-PL, shown in Figure 6.23B, revealed three QD lines which spectrally overlap with the broad cavity mode (Q∼100) centred at 1402.4 nm. Notably, the QD lines at 1386 nm and 1400 nm have count rates of ∼88 cps and ∼74 cps respectively. Both of these count rates are significantly higher than the typical <10 cps seen for bulk QDs measured in this thesis. The combination of spectral overlap with a cavity mode and high count rates make these QD lines possible candidates for Purcell enhancement.

Kors et al [88] temperature tuned a QD line from out of resonance at 5K into resonance at 60K.

When the QD was brought close to resonance and in resonance with the cavity mode, the brightness of the QD line increased. The QD line brightness was a factor of 4 increased at 60 K when the QD was in resonance with the cavity mode compared to at 5K when the QD was far away from resonance. This indicated a Purcell enhanced QD transition as the line was brought into resonance with the cavity mode.

Temperature dependent measurements were therefore carried out on this device with a view to investigating the behaviour of QD emission lines as they red shifted closer into resonance with the cavity mode.

The integrated intensity and wavelength of each QD line is shown in Figure 6.24, for temperatures of 5, 15, 25 and 40 K. Both the 1386 nm and 1393 nm lines appear to show a reduction in intensity as they red shift closer to the cavity mode centre. The longest wavelength line at 1400 nm passes through the cavity mode centre between 25 K and 40 K but the intensity still shows a reduction. It should be noted that the 1393 nm line does not appear for the 40 K measurement.

The reduction in emission intensity from the QD lines as they red shift closer to the cavity centre wavelength does not match up with what is seen in [88]. This can be attributed to the increase in temperature where non-radiative processes become stronger and the radiative efficiency of the QD transitions is reduced. It is possible that if these QD emission lines are coupled to the cavity mode that any increase in intensity due to increased spectral overlap from the temperature tuning is being negated by the effect of the non-radiative processes.

As discussed in Chapter 2 an increase in saturation power of a QD line as it goes into resonance with a cavity mode is indicative of a shortening of the transition lifetime and therefore can be used to show that the QD line is Purcell enhanced. Therefore, power dependent measurements on the QD lines were also performed for the different temperatures with a view to investigating how the saturation behaviour of the QD lines changed as the QD transitions red shifted closer to the cavity mode centre wavelength. Power dependent intensity measurements for the 1386 nm QD line are shown for temperatures of 5, 15, and 25 K in Figure 6.25A and 40 K in Figure 6.25B.

The data are fitted with exponential curves, these curves were fitted for excitation powers where the QD intensities were increasing up to and including where the intensities appeared to saturate.

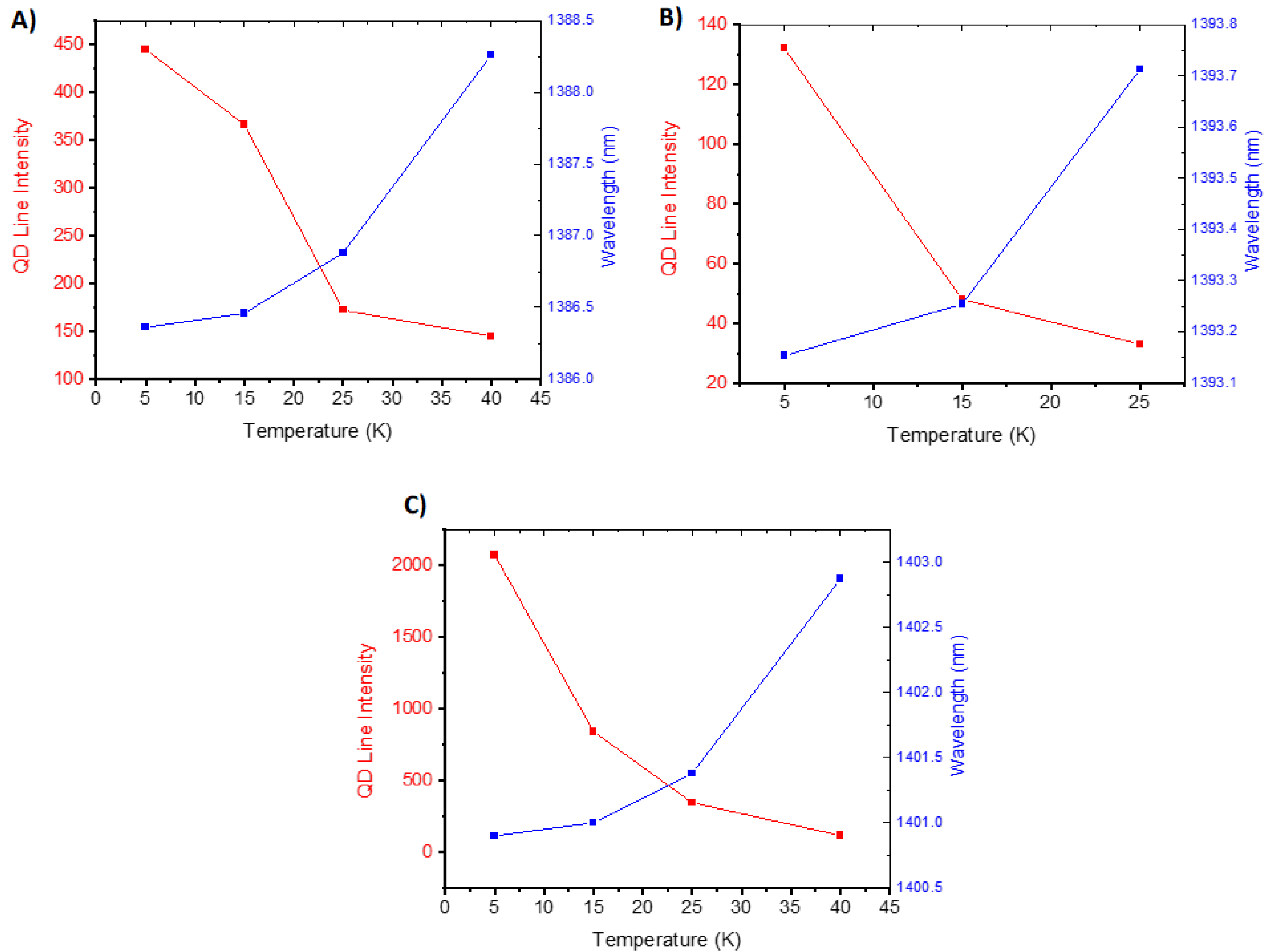

Figure 6.24: *QD line intensity and wavelength for 5, 15, 25 and 40 K. A) 1383 nm line B) 1393 nm line C) 1401 nm line. All lines show a reduction in intensity as they blue shift towards the cavity mode centre wavelength. It should be noted that the cavity mode shows a small redshift of 0.05 nm when the temperature is increased to 40 K which is much less than the redshift seen for the QD lines.*

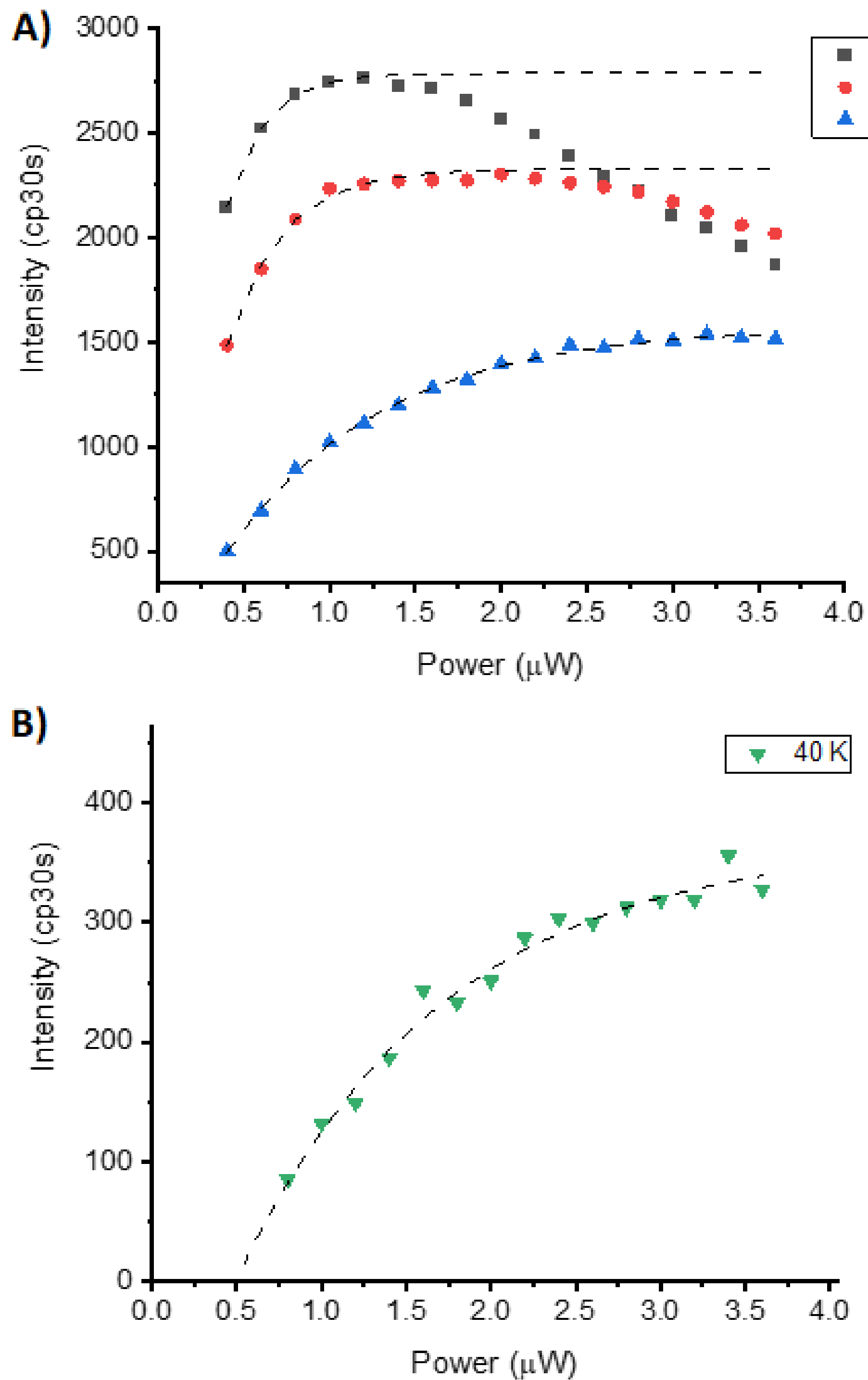

Figure 6.25: *Power dependent intensities for the 1386 nm QD line. A) For 5, 15, and 25 K B) 40 K measurements. The line appears to saturate at a higher power for the 25 and 40 K measurements.*

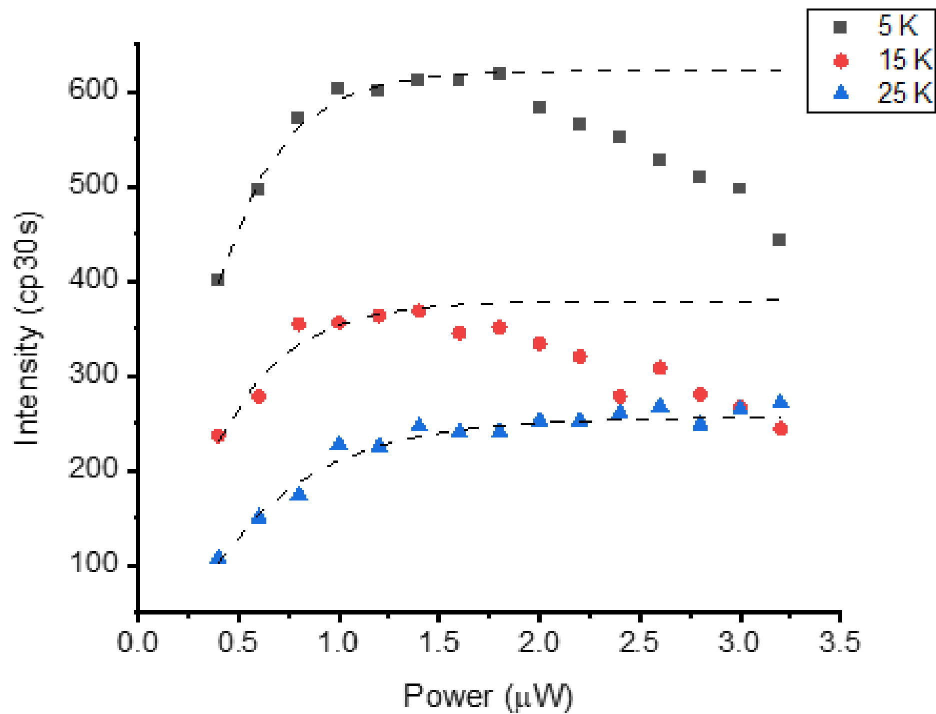

Figure 6.26: *Power dependent intensities for the 1393 nm line for temperatures of 5, 15 and 25 K.*

The saturation power was then extracted from the fit. It can be seen that for the 5 K and 15 K measurements the saturation power is at 1.2 μW. For the 25 K measurement, the saturation power increases to 3 μW. Finally, the 40 K measurement appears to show the line saturating beyond the maximum power of 3.6 μW.

The data for the 1393 nm line taken during the same experiment are presented in Figure 6.26. The measurements 5 and 15 K both show saturation at a power of 1 μW. The 25 K appears to show a slight increase to 1.5 μW.

Finally, the data for the 1401 nm line is presented in Figure 6.27. For the 5 K measurement the line saturates at a power of 2.5 μW, for the higher temperatures the line does not saturate within the power range used here. Again, this implies that the saturation power increases with increasing temperature.

These increases in saturation power indicate that the QD transitions have a reduced lifetime as the temperature is increased. If the lines are Purcell enhanced, then it is possible these apparent lifetime

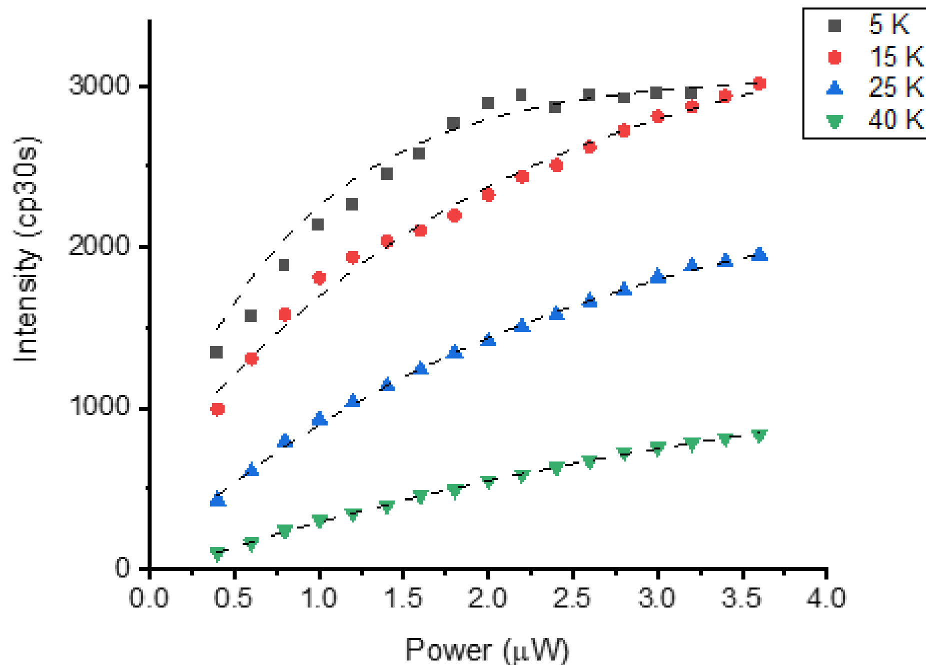

Figure 6.27: *Power dependent intensities for the 1401 nm line. The saturation power appears to increase out of the measurement range for temperatures above 5 K.*

reduction is due to the emission wavelengths red shifting closer to the cavity mode centre and the Purcell enhancement increasing. However, this observation may also be caused by the transition lifetime reduction from non-radiative processes mentioned previously.

An initial attempt was made to measure the saturation behaviour of a bulk QD line which could be used as a control against the previously presented saturation measurements. A bulk QD line would allow us to see the effect of temperature on the saturation behaviour without any influence of cavity modes. A low power micro-PL spectrum of bulk material is shown in Figure 6.28A where the dot of interest is at 1400 nm. The integrated intensity is seen to reduce with increasing temperature in Figure 6.28B which indicates that non-radiative processes are affecting the QD as the temperature is increased. Power dependent measurements were taken on this dot for temperatures of 5, 15 and 25 K and are shown in Figure 6.28B. The line appears not to saturate in the given power range for temperatures of 5 and 15 K but does saturate at approximately 1.2 μW for 25 K. This would indicate that the increase in temperature does not increase the saturation power and that the increase in saturation power for the first device may be due to the influence of spectral overlap with the cavity

mode.

These preliminary results merit further investigations, the saturation measurements should be repeated over a larger power range to fully characterise the saturation behaviour of each of the QD lines, unfortunately this was not done due to time constraints. Then saturation measurements for different temperatures on bulk QDs should be repeated in order to see the full effect of increased temperature on the saturation behaviour of QDs which are not in PhC devices.

Furthermore, the sample should be transferred to the bath cryostat system and the lifetimes of the QD lines should be measured. Then measurements of bulk QD lifetimes should be taken and compared to the QD lines of interest in order to directly measure a possible Purcell enhancement.

6.5.2 Third Device

As in the case of the InGaAs interlayer/ InGaAs sacrificial layer sample, two pieces were fabricated for the InGaAsP interlayer/ InAlAs sacrificial layer samples presented in this section. Devices from this piece were measured in the bath cryostat system by Dr Catherine Phillips, here we introduce a device with a candidate for Purcell enhancement from these measurements. Figure 6.29A shows a high power (500 μW) spectrum where cavity modes a seen for the given device. Figure 6.29B shows a low power (25 μW) spectrum of the same device which reveals a QD line at 1544.11 nm which is spectrally close to a cavity mode at 1545.96 nm (Q$\sim$1400).

The QD line was then measured at temperatures between 4.2 and 50 K in order to investigate the tuning behaviour with respect to the cavity mode. Figure 6.30 shows spectra for a selection of temperatures where the QD line is seen to red shift into the cavity mode up to 40 K. At 50 K it is possible that the QD line has tuned past the cavity mode centre but the spectrum is not clear.

The line intensity for the full temperature range is shown in Figure 6.31A, the intensity initially reduces but is seen to increase for temperatures greater than 20 K, this is plotted as a function of detuning from the cavity mode in Figure 6.31B.

The increase in intensity may be due to the increase in spectral overlap between the QD line and cavity mode which would indicate a Purcell enhanced QD line. Time resolved measurements will be presented in the next section.

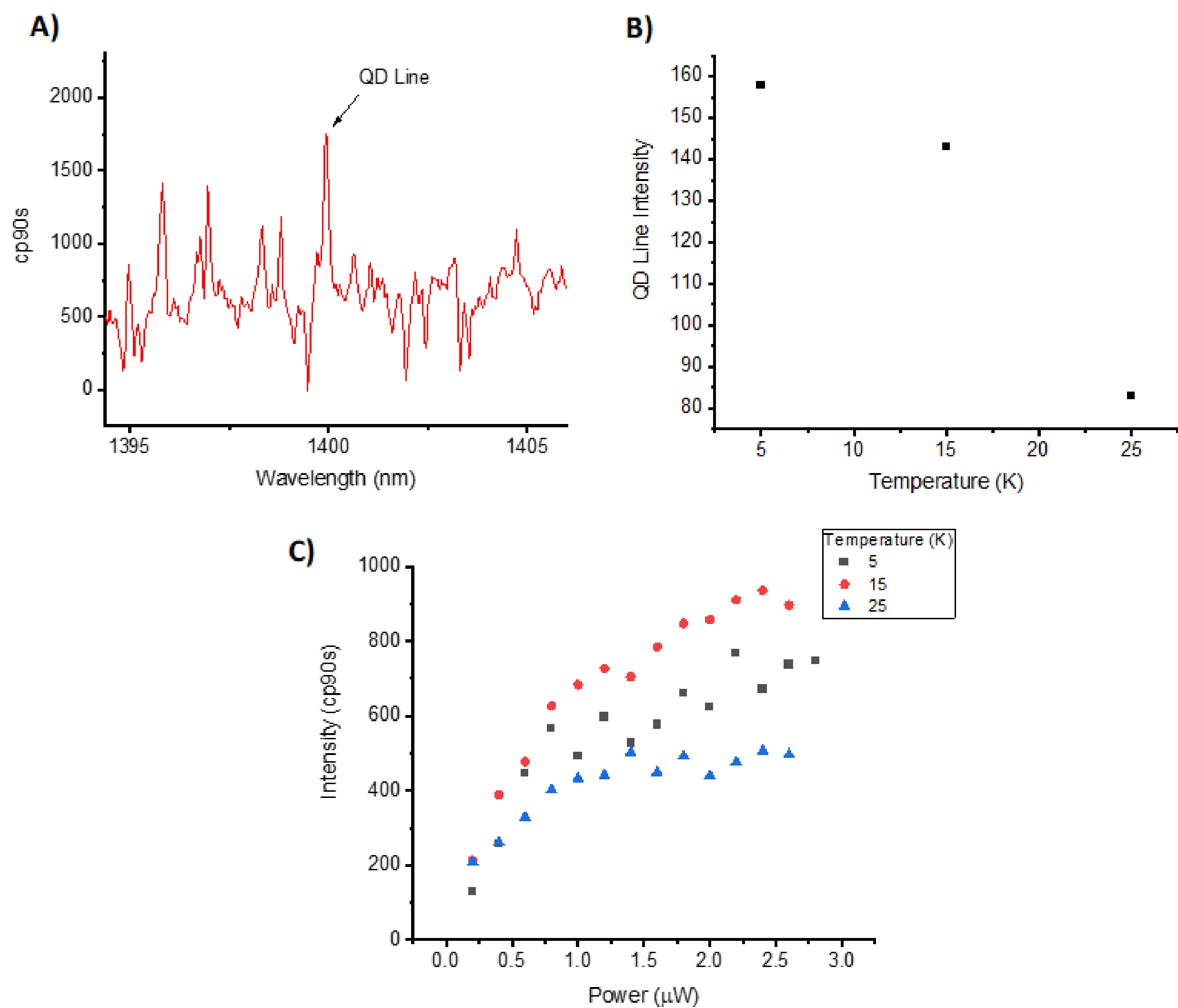

Figure 6.28: *A) Bulk QD line. B) Integrated intensity of the line with increasing temperature. C) Power dependent intensities of bulk line, there is an apparent reduction saturation power at a temperature of 25 K.*

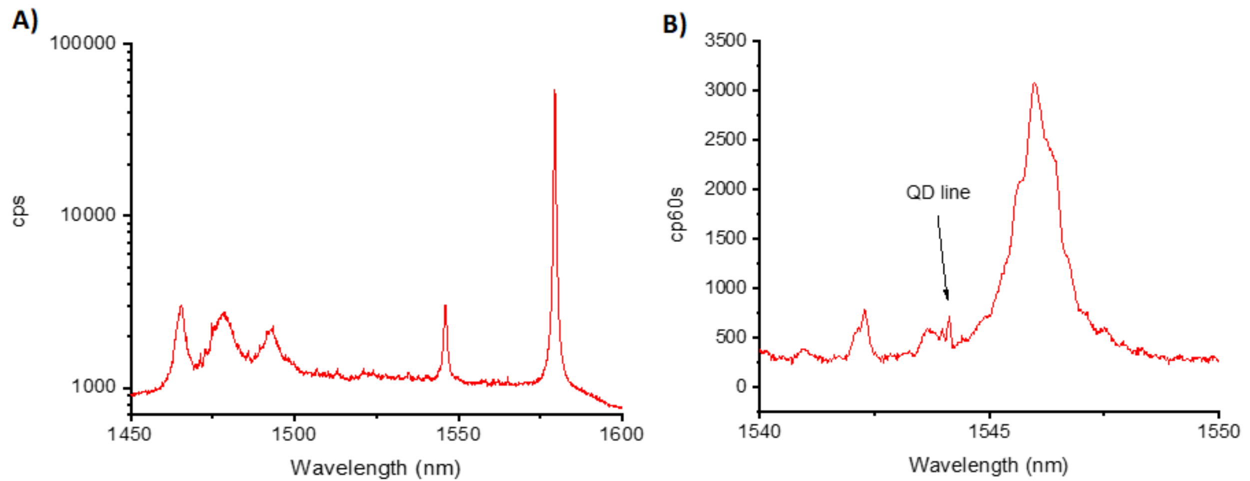

Figure 6.29: *A) High power micro-PL spectrum of a device of interest showing cavity modes. B) Low power spectrum of the same device showing a QD line close to a cavity mode. Spectra taken in the bath cryostat system.*

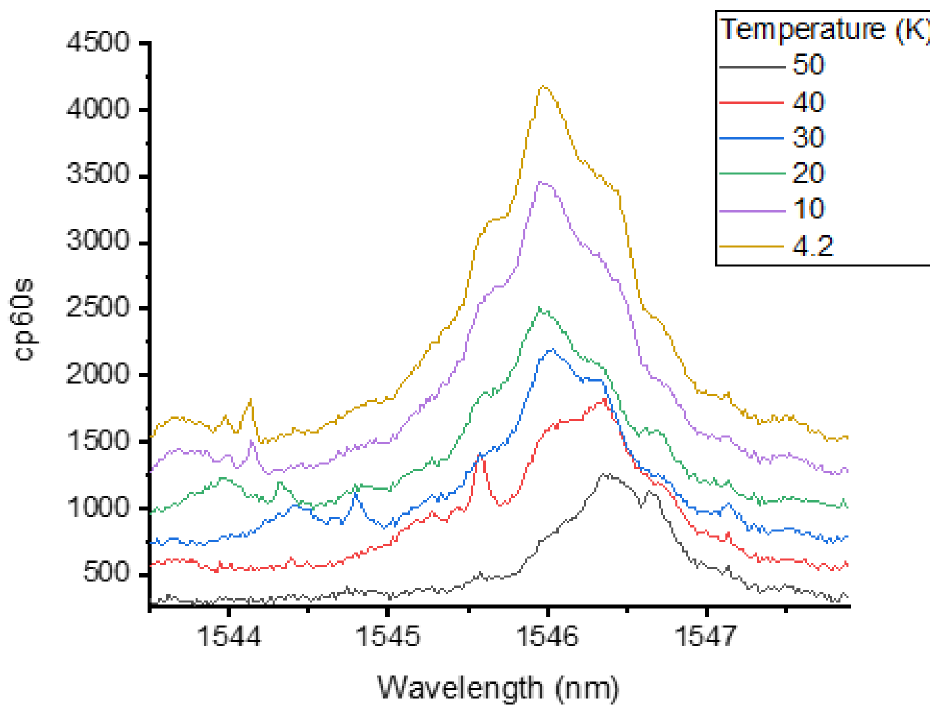

Figure 6.30: *Temperature dependent spectra of QD line of interest. The QD line is seen to redshift into the cavity mode with increasing temperature.*

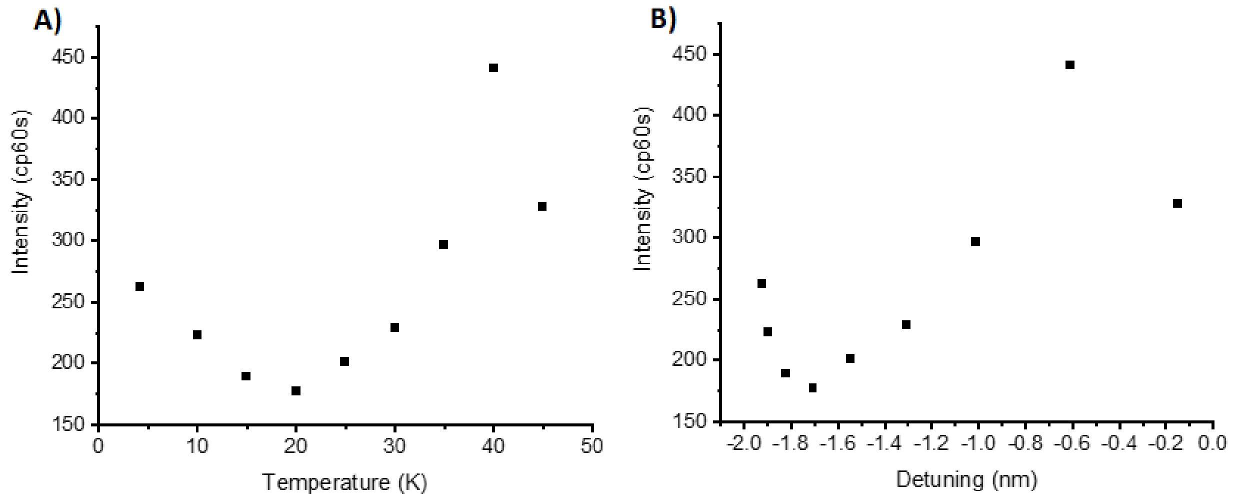

Figure 6.31: *A) Temperature dependent intensity of the QD line. After an initial decrease the intensity increases for temperatures less than 20 K. This is followed by an increase in intensity up to 40K. A) Same data but plotted as a function of detuning of the line from the cavity mode centre.*

Time Resolved Measurements

Time resolved measurements were performed on the QD line presented in Figure 6.30 for temperatures of 35, 40 and 45 K, where the QD line is redshifting into resonance with the cavity mode with increasing temperature. A spectral filter width of 0.112 nm is used for these measurements. A spectrum taken at 35 K using pulsed excitation with a power of 15 μW is shown in Figure 6.32A where the QD line can be seen overlapping with the cavity mode. A histogram of arrival times, with respect to the laser pulse, of photons within the detection window is shown in Figure 6.32B.

The photon arrival time data are fitted using a function comprising of the sum of two exponential decay curves which indicates that the photons being measured originate from two sources. One of these would be the QD line itself and the other could either be emission from the cavity, background emission or QD emission from the QD line that is not coupled to the cavity. It can be seen in Figure 6.32A that the QD line sits on emission from the cavity which makes the other source of light being measured likely to be the cavity emission originating from the background.

The two time constants, which give the lifetimes of each source, for the fits at each temperature are summarised in Table 6.3, where both are seen to reduce with increasing temperature. Without further information on the origin of the light for each time constant it is hard to draw any conclusions

Temperature (K)	$\mathbf{t}_1$ (ns)	$\mathbf{t}_2$ (ns)
35	0.52±0.01	1.74±0.02
40	0.34±0.005	1.60±0.006
45	0.32±0.003	1.51±0.005

Table 6.3: *Fitted time constants for 35, 40 and 45 K measurements for the two exponential decay functions used to fit the time resolved measurements.*

at present. It is possible that the reduction in lifetimes seen with increasing temperature is due to the increased spectral overlap with the cavity mode and indicative of Purcell enhancement. For this to be true the lifetimes of bulk QDs in the same temperature range needs to be measured in order to rule out the effect of non-radiative processes.

At present there have only been bulk lifetime measurements for InAs/InP QDs where the lifetime was measured at 4 K to be 1.72±0.008 ns, a spectrum and lifetime measurement are shown in Figure 6.33. This would indicate a potential Purcell enhancement when comparing to the reduced lifetime, t_1, presented in Table 6.3. Of course, this is not at all conclusive. We do not know whether it is t_1 or the longer lifetime t_2 that is related to the QD line of interest. The bulk measurement is for a different material system at a lower temperature and we do not know whether the exciton species of the QD line of interest and the bulk line are the same.

In order to measure a Purcell enhancement, the origins of the light for the lifetimes presented in Table 6.3 need to be identified. This could be achieved with time resolved measurements on only the cavity emission in order to quantify the contribution from the cavity to the time resolved measurements. Also QRE could be employed in order to reduce the amount of background cavity emission that would be measured during the lifetime measurement.

Once the lifetime and excitonic species of the QD is found then this can be compared to bulk lifetimes for the same excitonic species at the same elevated temperatures as the QD of interest. Comparing these lifetimes would allow a Purcell factor to be calculated.

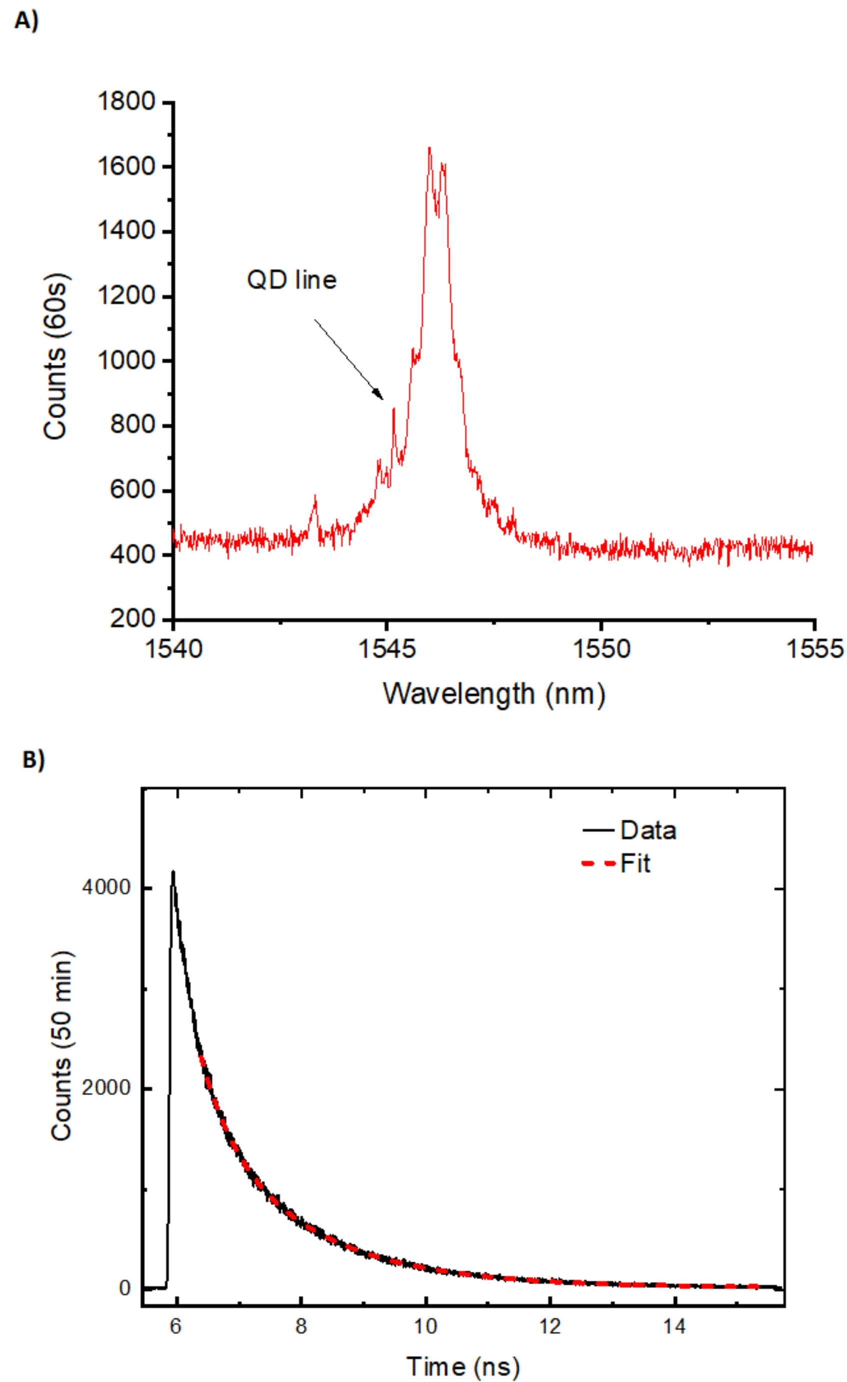

Figure 6.32: *A) Spectrum using pulsed excitation at 35 K, the QD line is labelled. B) Histogram of arrival times of photons in a 0.112 nm spectral window about the QD line centre wavelength. The data are fitted using the sum of two exponential decay curves which is shown with the red dashed lines.*

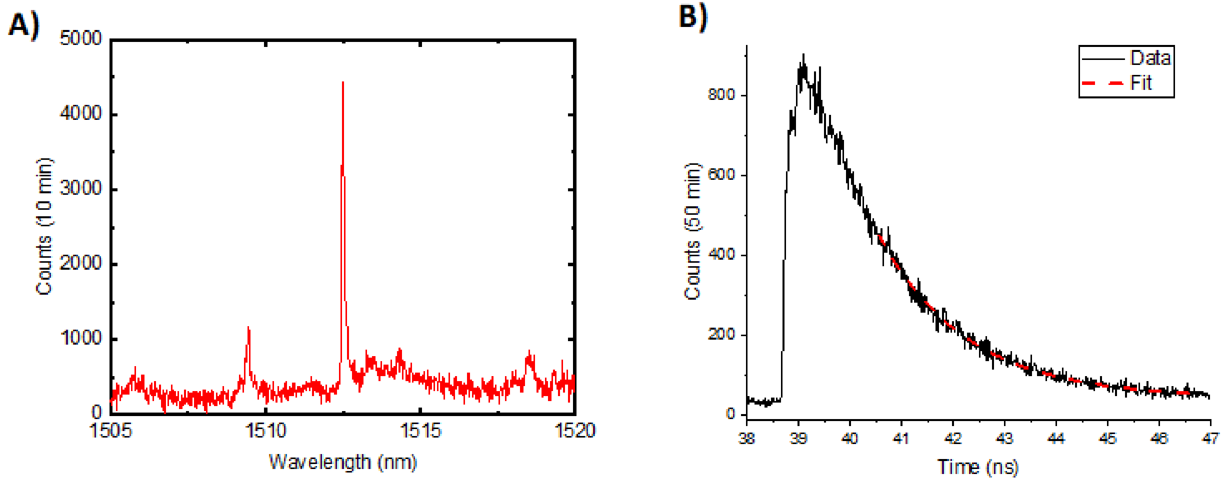

Figure 6.33: *A) Pulsed excitation spectrum of example bulk InAs/InP QD. Excitation power is 50 μW. B) Histogram of arrival time of QD line photons with respect to excitation laser pulse. The data are fitted with a single exponential decay curve shown by the red dashes.*

6.6 Initial Investigations into Electrical Tuning

So far temperature tuning has been used to investigate the effect of tuning emission lines into resonance with a cavity. As discussed in chapter 2, the ability to tune the emission wavelength of a QD transition using the QCSE allows for further flexibility for achieving spectral overlap between a QD emission line and a cavity mode. Demonstration of tuning in C-band QDs has been limited to date in the literature. Strain tuning has been shown to produce a wavelength change of $\sim$ 0.1 meV (0.25 nm) [58] for MMB-based QDs. Also tuning via the QCSE has been shown to produce a larger tuning range of $\sim$1 meV (2 nm) for InP based QDs [122]. On the other hand, GaAs QDs have demonstrated larger tuning ranges of $\sim$5.2 meV [83] and up to 25 meV when using AlGaAs barriers to stop carriers tunneling out of the QD [46].

Initial investigations into diode samples used diodes fabricated by Toshiba research Europe laboratories at the Cavendish Laboratory in Cambridge. These diodes used InAs/InGaAs/InP QDs. The sample structure consisted of a 1000 nm N-doped InP layer where the dopant was Si with a concentration of 2x10^{18} cm^{-3}, this was followed by 400 nm of undoped InP onto which high density QDs were grown on an InGaAs interlayer then 400 nm of undoped InP. The structure was finished with 1000 nm of P doped InP where the dopant was Zn of a concentration of 2x10^{18} cm^{-3}. The

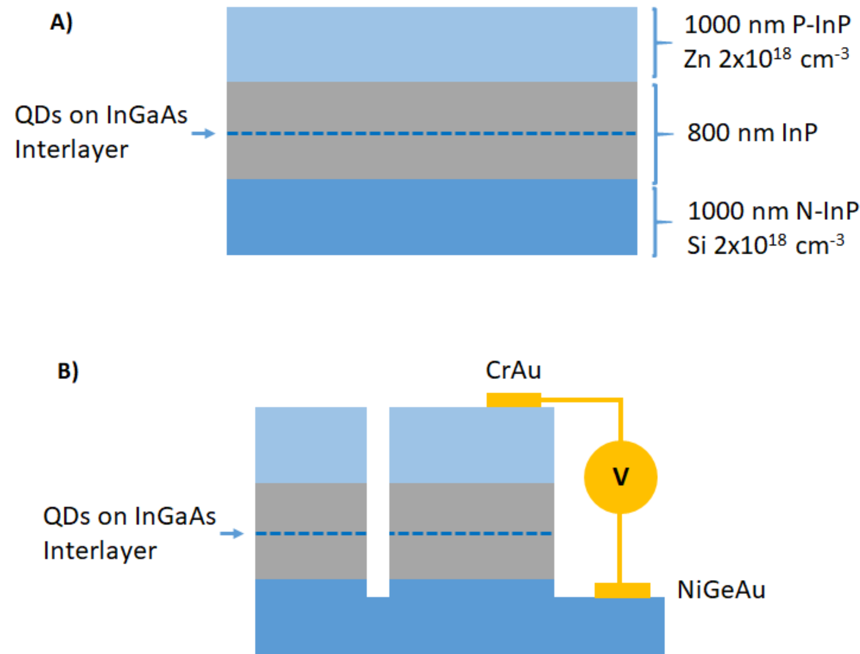

Figure 6.34: *A) Sample structure for diode wafer. B) Fabricated diodes with metal contacts on the p and n layers.*

sample structure is shown in Figure 6.34A. Mesas were wet etched down to the N-InP layer and it should be noted that the wet etch problems encountered earlier in this chapter were not an issue for these devices due to the mesas being of a size of hundreds of microns. CrAu contacts were evaporated onto the P-InP and NiGeAU contacts were evaporated onto the N-InP, a schematic of a diode is shown in Figure 6.34B. The sample was then mounted onto a ceramic sample holder and wire bonds were installed to electrically connect the sample to the holder. IV curves were measured which showed the expected behaviour for a diode, as shown in Figure 6.35. The ideality factor of the diode is 2.3

Figure 6.36A shows an example QD line found in low power micro-PL for the diode sample, Figure 6.36B shows the wavelength of the line for biases between 1.5 and -7 V. The wavelength of the emission line is seen to red shift from 1443.24 to 1443.45 nm within the applied bias range. This tuning range of 0.21 nm $\sim$ 0.1 meV, though small, would help bring a QD that is already close to a cavity mode into resonance with the cavity mode, but a larger range is desirable.

It is possible that a small amount of tuning was seen due to the relatively thick InP layer (800

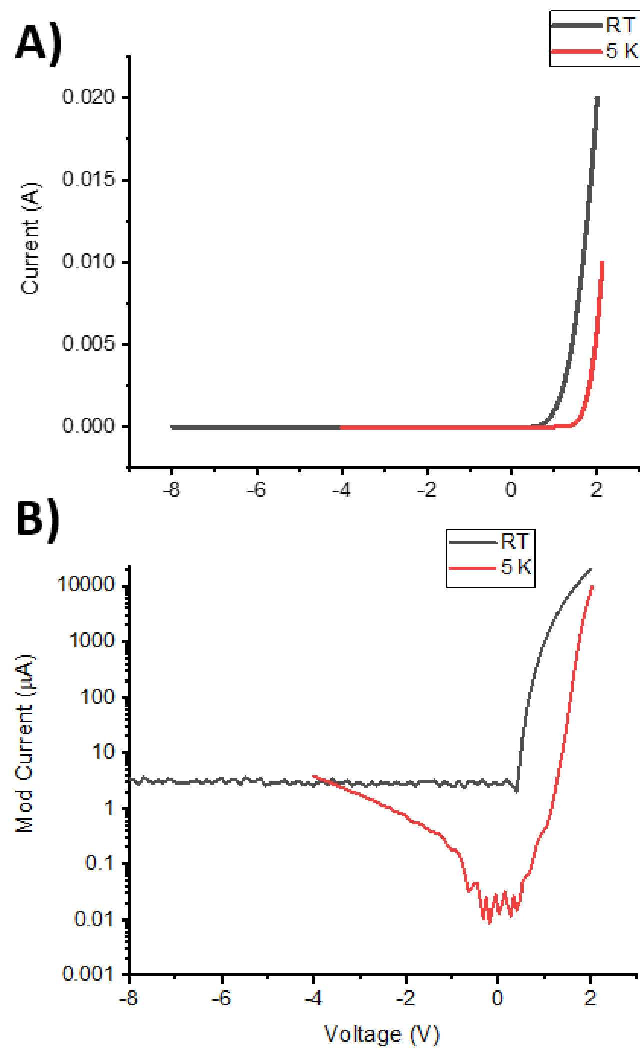

Figure 6.35: *IV curves for room temperature and low temperature, both show diode behaviour. A) Current in linear scale B) Current in log scale.*

nm) used causing a smaller electric field across the QD, where previous InP-based work [122] used thinner a intrinsic region (300 nm). Overall it does appear that InP-based QDs in the C-band show less tuning than GaAs-based QDs, which is not fully expected as QDs in InP would have a much higher barrier than GaAs QDs. It is not clear at present why this appears to be.

It would be beneficial to look at the tuning behaviours of the InAs/InP QDs and the InAs/InGaAsP/InP QDs in diodes to see the tuning behaviour of these material systems. As the current direction for PhCC fabrication uses the InGaAsP interlayer, it would be especially interesting to see how these QDs tune, with a view to later marrying tuneable QDs and QDs in PhCCs.

6.7 Summary

Overall this chapter has explored the integration of high density QDs into PhCCs. The use of an InGaAs interlayer and InGaAs sacrificial layer combination was shown to be detrimental to the fabrication of the PhCCs such that the QD emission was effectively destroyed by the wet etch attacking of the interlayer. This resulted in no cavity modes originating from the QDs being measured.

In order to recover the QD emission and the cavity modes, a change in the growth structure was employed. An InGaAsP interlayer and InAlAs sacrificial layer was chosen based on their relative etch rates with $FeCl_3$. Fabrication of L3 cavities was shown to be an improvement over the original high density QD growth structure due to the measurement of cavity modes. This was despite the presence of an unwanted EBL resist layer on the sample. Further low power micro-PL measurements revealed the QD emission lines originating from the PhC structures which indicated that the new growth structure was successful in recovering the QD emission.

It was found that devices contained fewer QD emission lines that expected which may be due to the unwanted EBL resist layer, the etching of the InGaAsP interlayer or the proximity of the QDs to etched surfaces. Ways to investigate these potential causes have been proposed.

Three devices have been presented which show possible candidates for Purcell enhancement on the QD lines present. Further measurements, especially time resolved measurements, are required in

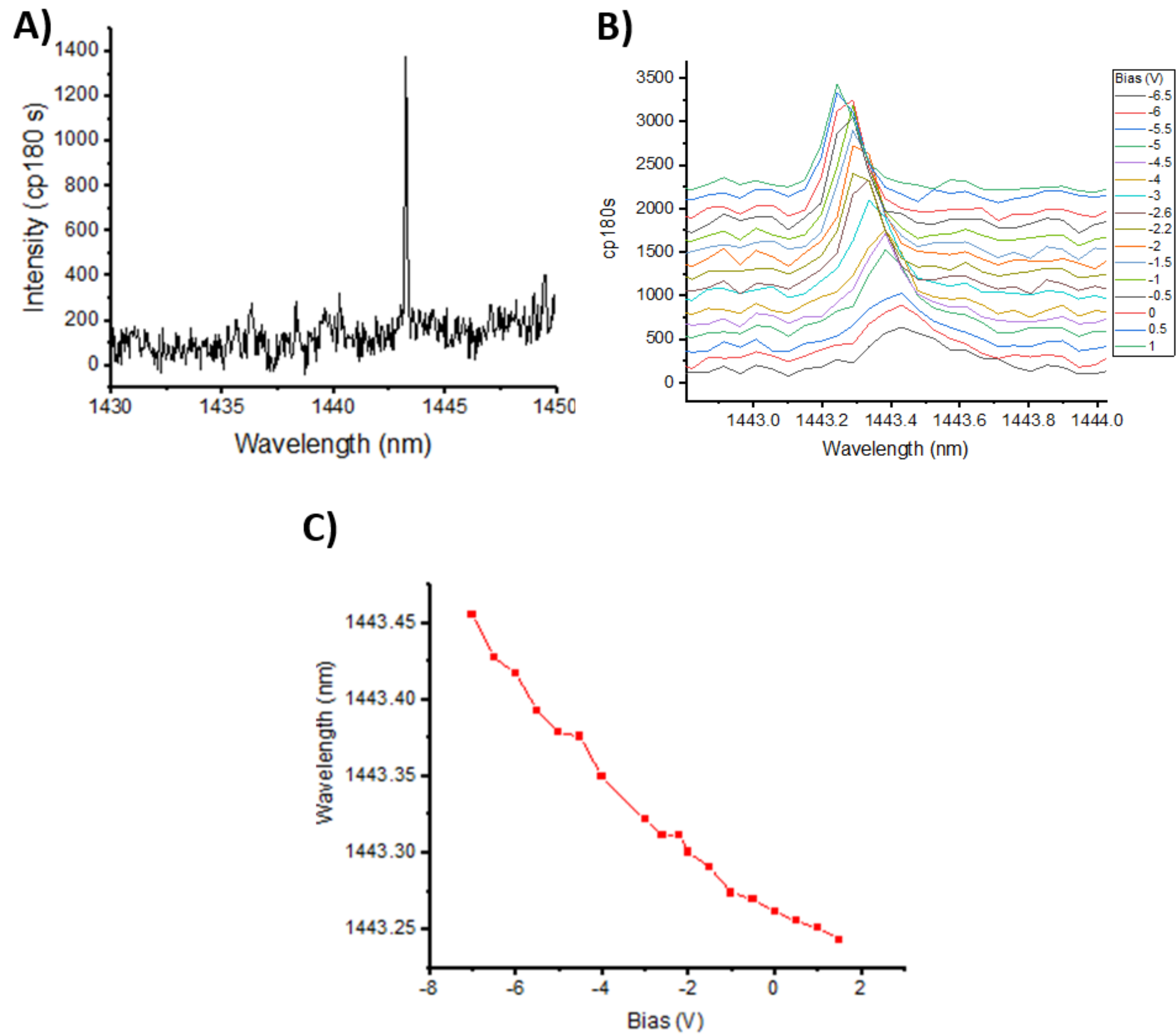

Figure 6.36: *A) QD line at 1443 nm found within pin diode device. B) Spectra of QD line at various biases. C) Emission wavelength with bias, the line red shifts over a 0.21 nm range with applied reverse bias.*

order to verify if these candidates are Purcell enhanced. More generally, more devices need to be measured in order to find further candidates.

Temperature tuning was used to bring QD lines into resonance in this chapter, electrical tuning forms a desirable alternative and initial work has been introduced where a tuning range <1 nm was found.

Chapter 7

Summary and Outlook

7.1 Summary

The overall aim of this PhD was to show Purcell enhancement for QDs in the telecom C-band. This thesis has demonstrated the optical characterisation of InAs DE QDs in the InP material system which emit near to and within the telecom C-band. A fabrication process was developed which successfully produced InP-based PhCCs.

Additional development of the PhCC fabrication process was then undertaken in order to integrate high density QDs with the PhCCs. This proved to be a challenge due to the etching of the InGaAs interlayer on which the high density QDs were grown which was detrimental to the emission properties of the structures.

This challenge was successfully overcome by changing the QDs to be on an InGaAsP interlayer and changing the sacrificial layer from InGaAs to InAlAs with QDs being measured in devices. Candidate QDs, with one in the C-band, for Purcell enhancement were then presented, forming good progress towards the overall project aim. More generally, the device fabrication and growth structure optimisation forms the basis for future InP-based PhC work at the University of Sheffield.

Chapter 4 presented optical characterisation of InAs/InP QDs which were shown to emit within the telecom C-band with narrow linewidths. A further study was performed which demonstrated the ability to blue shift the emission wavelengths of the QDs into the telecom O-band by reducing

the capping thickness during the QD growth. Next, QDs grown on an InGaAs interlayer were characterised which allowed for higher QD densities, though the linewidths were broader than the InAs/InP QDs. Measurements of QDs grown on an alternative interlayer of InGaAsP were also introduced.

Micro-PL measurements of InAs/InP QDs grown on a DBR showed enhancement of a background emission for the QDs which would be problematic for any single photon measurements of the QDs. Growth experiments to assess the constituent layers of QD samples with micro-PL indicated that the background emission originated from the growth of the QDs themselves. X-STM measurements and comparison to the literature indicated that the background emission may be related to the presence of arsenic in the InP capping layer due to the high crystallisation temperature used in the growth of the QDs.

Chapter 5 outlined the design of H1 cavities using FDTD methods, where cavities operating around the telecom C-band with reasonably high Q factors were simulated. Also a design for L3 cavities was presented. These designs formed the basis for the fabricated structures. Next the fabrication process was outlined and shown to produce PhCCs by SEM imaging. Successful fabrication of the cavities was demonstrated by the measurement of PhCC modes for both sets of devices with modes that were around the telecom C-band and of high Q. This fabrication process will form the basis for future PhCC fabrication in InP at the University of Sheffield. No QD lines were measured from devices in low power micro-PL, with the comparatively low QD density being proposed as the reason for this.

In Chapter 6 a new growth structure was studied for the fabrication of PhCCs. This structure featured QDs grown on an InGaAs interlayer in order to increase the density of QDs with the aim of increasing the chances of measuring QDs within the PhCC. This was shown to be detrimental to the fabrication due to the etching of the InGaAs interlayer which in turn meant that no cavity modes or QDs were measured from the devices.

A further growth structure was developed which consisted of QDs on an InGaAsP interlayer with a sacrificial layer of InAlAs. Fabrication of PhCCs was shown to be a success from measurements of cavity modes and QD lines measured within the devices. Although the PhCCs showed fewer QD lines than expected, and possible reasons for this were outlined, QD lines were found which

overlapped with cavity modes and were the basis for investigating Purcell enhancement. Evidence for Purcell enhancement was found for QD lines close to 1400 nm but it is not definitive due to the competing non-radiative processes. An additional device also showed evidence for Purcell enhancement in the C-band but further measurements are required to fully explore this.

7.2 Outlook

This work has presented major steps towards achieving a Purcell enhancement for QDs emitting in the telecom C-band. The following section will summarise directions for future work, starting with improvements to the QD growth followed by addressing the issues identified in the final PhCCs that were fabricated as part of this work. We will then look further ahead to methods for deterministic device fabrication.

7.2.1 The Background Emission Problem

It was found that the InAs/InP QDs and InAs/InGaAs/InP QDs both exhibited a background optical emission that would ultimately be problematic for single photon sources. The presence of this background was particularly notable for InAs/InP QDs grown within a DBR structures which are used to enhance the single photon extraction efficiency. From the investigations in this thesis, the origin of the background appears to be related to the temperature at which the QDs were crystallised during their growth and the corresponding presence of arsenic segregation in the InP cap.

It would be beneficial to gain further information about the origin of the background which could be achieved by employing PLE measurements. Here the amount of background emission for a given location could be measured with respect to the excitation wavelength. Any increases in background for a given excitation wavelength would give information on the relaxation of carriers and the possible origin of the background.

With the current proposition that the background is related to the crystallisation temperature of the QDs, further growth experiments are required. In these the crystallisation temperature

should be reduced and the other growth parameters explored. These include Arsine flow during crystallisation, the crystallisation time and the Indium deposition time. This however is a multi-dimensional optimisation problem, because it is evident from the extensive work carried out up to now on growth that the growth parameters for high efficiency, narrow linewidth QDs in the C-band are narrow.

7.2.2 Improving the Number of QD Lines in Photonic Crystals

The use of an InGaAsP interlayer and InAlAs sacrificial layer was shown to successfully integrate QDs into the devices. However, fewer QD lines than expected were measured, which has the effect of reducing the chances of finding candidates for Purcell enhancement. The first possible origin of this was the presence of the unwanted EBL resist layer which may have been detrimental to any QD emission due to possible scattering. It would be beneficial to simply repeat the fabrication ensuring that the resist was fully cleaned off.

Another option is to investigate the growth of QDs using InGaAsP interlayers of thickness <5 nm. The devices presented in chapter 6 will have experienced some etching of the InGaAsP interlayer which could have been detrimental to the QD emission. By using a thinner InGaAsP interlayer, any detrimental etching will be reduced. Initial growth experiments could include interlayer thicknesses of 1 and 3 nm to investigate whether the QD emission is affected by this. Should this be successful, then more PhCCs can be fabricated and surveyed to deduce whether a thinner InGaAsP interlayer increases the number of devices with QD lines.

The reduction in measured QD lines may also have been due to the proximity of the QDs to etched surfaces. This could have either caused a change in the distribution of charge on the sample, leading to charged excitons not forming, or large amounts of spectral wandering making QDs near to the etched surfaces not detectable. Future devices could be made from pin structures in which a bias would be applied across the QDs, this could allow a level of control over the charge environment around the QDs and negate the effects of any spectral wandering. Additionally, surface passivation of the PhCCs could also negate any effects of spectral wandering and charge build up.

7.2.3 Further Measurements of Photonic Crystal Cavities

Candidates for Purcell enhancement were presented in Chapter 6, though only initial measurements were performed on these. It would be beneficial to move the sample to the bath cryostat system in order to measure the lifetimes of the transitions and compare to bulk QDs. This would enable verification and measurement of any potential Purcell enhancement. The nature of this work does rely on the chance of having a QD that is in the correct spatial location and emits in the correct wavelength range with respect to a PhCC mode. As such, more devices should be fabricated and measured in order to find further candidates for Purcell enhancement.

7.2.4 Deterministic Device Fabrication

In order to reduce the relying on chance for QDs in cavities, QD registration represents a possible long term route for future work. The flow cryostat system features the possibility to integrate closed-loop micrometre stages which would enable movement of a known distance across a sample. By fabricating alignment markers on the sample, QD locations with respect to the markers can be mapped. Furthermore, the emission wavelengths of the QDs would also be recorded. Using the QD spatial and spectral information, PhCCs designed to emit at the same wavelength as given QDs can be fabricated at the same locations as the QDs. Though challenging due to the spatial accuracy required, this represents a viable route to begin deterministic fabrication of Purcell enhancing structures in the telecom C-band.

Another route for better scale-up of device fabrication would be to use full site control of QDs. Work on this has been carried out at the University of Sheffield, this was done by patterning InP substrates with nano holes which deterministically control the location of Indium droplet formation and the subsequent QDs. The particular challenge with this work, however, is that no sharp line emission has been seen from individual site controlled quantum dots. Solving this issue would make the integration of site controlled QDs and devices a feasible future direction for work [123].

Appendix A

Appendix

A.1 Optical Setups

Here follows further details on the equipment used in the micro-PL setups.

A.1.1 Flow Cryostat System

Cryostat Montana Instruments Cryostation s100

Spectrometer Princeton Instruments TriVista double stage spectrometer

Detector Princeton Instruments PyLoN-IR InGaAs photodiode linear array (1024 pixels).

Grating Princeton 600 g/mm, 1μm blaze wavelength, standard grating. Resolution $\sim$48 μeV at 1550 nm.

Lens 100X Mitutoyo Plan Apo NIR Infinity Corrected Objective 0.5 NA

Camera Thorlabs DCC1545M CMOS imaging camera

Laser Thorlabs 4-Channel Fiber-Coupled Laser Source. 635 nm used in this work (MCLS1-635).

Souce Measure Unit Kiethley 2400 Graphical Touchscreen Series SMU

A.1.2 Bath Cryostat System

Laser Santec TSL-770 - Tuneable CW, PriTel UOC-S-MM-0.5-20G -Tuneable pulsed, tsunami Ti:Sapphire

Spectrometer Princeton Instruments TriVista single stage spectrometer pulsed laser 850 nm and 850 nm diode laser.

Camera Raptor Photonics– OWL 640 M– InGaAs Camera

Grating Princeton 300, 600, 1000 g/mm, 1μm blaze wavelength, standard grating.

Detectors Princeton Instruments PyLoN-IR InGaAs photodiode linear array (1024 pixels). Single Quantum Superconducting Nanowires: 1550 nm and 900 nm channels

Lens Thorlabs C230TMD-C- f = 4.51 mm, NA = 0.55, Mounted Aspheric Lens

Bibliography

[1] Max Planck. On an improvement of Wien's equation for the spectrum. *Ann. Physik*, 1:719–721, 1900.

[2] Manjit Kumar. *Quantum: Einstein, Bohr and the great debate about the nature of reality*. Icon Books Ltd, 2008.

[3] Jonathan Pritchard and Stephen Till. UK Quantum Technology Landscape 2014. *Defence Science and Technology Laboratory, DSTL/PUB75620*, 2014.

[4] Richard P Feynman. Simulating physics with computers. In *Feynman and computation*, pages 133–153. CRC Press, 2018.

[5] Peter W Shor. Algorithms for quantum computation: discrete logarithms and factoring. In *Proceedings 35th annual symposium on foundations of computer science*, pages 124–134. Ieee, 1994.

[6] Ronald L Rivest, Adi Shamir, and Leonard Adleman. A method for obtaining digital signatures and public-key cryptosystems. *Communications of the ACM*, 21(2):120–126, 1978.

[7] Nicolas Gisin, Grégoire Ribordy, Wolfgang Tittel, and Hugo Zbinden. Quantum cryptography. *Reviews of modern physics*, 74(1):145, 2002.

[8] Oliver Benson, Charles Santori, Matthew Pelton, and Yoshihisa Yamamoto. Regulated and entangled photons from a single quantum dot. *Physical review letters*, 84(11):2513, 2000.

[9] Peter Michler, Alper Kiraz, Christoph Becher, WV Schoenfeld, PM Petroff, Lidong Zhang, Ella Hu, and A Imamoglu. A quantum dot single-photon turnstile device. *science*, 290(5500):2282–2285, 2000.

[10] Charles Santori, Matthew Pelton, Glenn Solomon, Yseulte Dale, and Yoshihisa Yamamoto. Triggered single photons from a quantum dot. *Physical Review Letters*, 86(8):1502, 2001.

[11] Daniel Huber, Marcus Reindl, Johannes Aberl, Armando Rastelli, and Rinaldo Trotta. Semiconductor quantum dots as an ideal source of polarization-entangled photon pairs on-demand: a review. *Journal of Optics*, 20(7):073002, 2018.

[12] Andreas V Kuhlmann, Jonathan H Prechtel, Julien Houel, Arne Ludwig, Dirk Reuter, Andreas D Wieck, and Richard J Warburton. Transform-limited single photons from a single quantum dot. *Nature communications*, 6(1):1–6, 2015.

[13] Lukas Hanschke, Kevin A Fischer, Stefan Appel, Daniil Lukin, Jakob Wierzbowski, Shuo Sun, Rahul Trivedi, Jelena Vučković, Jonathan J Finley, and Kai Müller. Quantum dot single-photon sources with ultra-low multi-photon probability. *npj Quantum Information*, 4(1):1–6, 2018.

[14] Alisa Javadi, I Söllner, Marta Arcari, S Lindskov Hansen, Leonardo Midolo, Sahand Mahmoodian, G Kiršanskė, Tommaso Pregnolato, EH Lee, JD Song, et al. Single-photon nonlinear optics with a quantum dot in a waveguide. *Nature communications*, 6(1):1–5, 2015.

[15] D Leonard, M Krishnamurthy, CMv Reaves, Steven P DenBaars, and Pierre M Petroff. Direct formation of quantum-sized dots from uniform coherent islands of InGaAs on GaAs surfaces. *Applied Physics Letters*, 63(23):3203–3205, 1993.

[16] G Wang, S Fafard, D Leonard, JE Bowers, JL Merz, and PM Petroff. Time-resolved optical characterization of InGaAs/GaAs quantum dots. *Applied physics letters*, 64(21):2815–2817, 1994.

[17] Artur Zrenner. A close look on single quantum dots. *The journal of chemical physics*, 112(18):7790–7798, 2000.

[18] Wilfried Blanc and Bernard Dussardier. Formation and applications of nanoparticles in silica optical fibers. *Journal of Optics*, 45(3):247–254, 2016.

[19] Kazuya Takemoto, Yoshihiro Nambu, Toshiyuki Miyazawa, Yoshiki Sakuma, Tsuyoshi Yamamoto, Shinichi Yorozu, and Yasuhiko Arakawa. Quantum key distribution over 120 km using ultrahigh purity single-photon source and superconducting single-photon detectors. *Scientific reports*, 5(1):1–7, 2015.

[20] Sheng-Kai Liao, Wen-Qi Cai, Wei-Yue Liu, Liang Zhang, Yang Li, Ji-Gang Ren, Juan Yin, Qi Shen, Yuan Cao, Zheng-Ping Li, et al. Satellite-to-ground quantum key distribution. *Nature*, 549(7670):43–47, 2017.

[21] M Avesani, L Calderaro, M Schiavon, A Stanco, C Agnesi, A Santamato, M Zahidy, A Scriminich, G Foletto, G Contestabile, et al. Full daylight quantum-key-distribution at 1550 nm enabled by integrated silicon photonics. *npj Quantum Information*, 7(1):1–8, 2021.

[22] Anthony Mark Fox, Mark Fox, et al. *Quantum optics: an introduction*, volume 15. Oxford university press, 2006.

[23] CK Hong and Leonard Mandel. Experimental realization of a localized one-photon state. *Physical Review Letters*, 56(1):58, 1986.

[24] Thomas M Babinec, Birgit JM Hausmann, Mughees Khan, Yinan Zhang, Jeronimo R Maze, Philip R Hemmer, and Marko Lončar. A diamond nanowire single-photon source. *Nature nanotechnology*, 5(3):195–199, 2010.

[25] Jörg Bochmann, Martin Mücke, Gunnar Langfahl-Klabes, Christoph Erbel, Bernhard Weber, Holger P Specht, David L Moehring, and Gerhard Rempe. Fast excitation and photon emission of a single-atom-cavity system. *Physical review letters*, 101(22):223601, 2008.

[26] Akihiro Ishii, Xiaowei He, Nicolai F Hartmann, Hidenori Machiya, Han Htoon, Stephen K Doorn, and Yuichiro K Kato. Enhanced single-photon emission from carbon-nanotube dopant states coupled to silicon microcavities. *Nano Letters*, 18(6):3873–3878, 2018.

[27] F Pelayo García de Arquer, Dmitri V Talapin, Victor I Klimov, Yasuhiko Arakawa, Manfred Bayer, and Edward H Sargent. Semiconductor quantum dots: Technological progress and future challenges. *Science*, 373(6555):eaaz8541, 2021.

[28] Peter Michler. *Single semiconductor quantum dots*, volume 28. Springer, 2009.

[29] Peter Lodahl, Sahand Mahmoodian, and Søren Stobbe. Interfacing single photons and single quantum dots with photonic nanostructures. *Reviews of Modern Physics*, 87(2):347, 2015.

[30] Kristjan Leosson, Dan Birkedal, and Jørn Märcher Hvam. Dephasing in self-organized InAlGaAs quantum dots. *Physica Scripta*, 2002(T101):143, 2002.

[31] J Houel, AV Kuhlmann, L Greuter, F Xue, M Poggio, BD Gerardot, PA Dalgarno, A Badolato, PM Petroff, A Ludwig, et al. Probing single-charge fluctuations at a GaAs/AlAs interface using laser spectroscopy on a nearby InGaAs quantum dot. *Physical review letters*, 108(10):107401, 2012.

[32] R Mark Stevenson, Robert J Young, Paola Atkinson, Ken Cooper, David A Ritchie, and Andrew J Shields. A semiconductor source of triggered entangled photon pairs. *Nature*, 439(7073):179–182, 2006.

[33] Michał Zieliński. Vanishing fine structure splitting in highly asymmetric InAs/InP quantum dots without wetting layer. *Scientific Reports*, 10(1):1–13, 2020.

[34] RM Stevenson, RJ Young, P See, DG Gevaux, K Cooper, P Atkinson, I Farrer, DA Ritchie, and AJ Shields. Cancellation of fine-structure splitting in quantum dots by a magnetic field. *Physica E: Low-dimensional Systems and Nanostructures*, 32(1-2):135–138, 2006.

[35] JD Mar, XL Xu, JS Sandhu, AC Irvine, M Hopkinson, and DA Williams. Electrical control of fine-structure splitting in self-assembled quantum dots for entangled photon pair creation. *Applied Physics Letters*, 97(22):221108, 2010.

[36] Thomas Lettner, Samuel Gyger, Katharina D Zeuner, Lucas Schweickert, Stephan Steinhauer, Carl Reuterskiold Hedlund, Sandra Stroj, Armando Rastelli, Mattias Hammar, Rinaldo Trotta, et al. Strain-controlled quantum dot fine structure for entangled photon generation at 1550 nm. *Nano letters*, 21(24):10501–10506, 2021.

[37] YH Huo, A Rastelli, and OG Schmidt. Ultra-small excitonic fine structure splitting in highly symmetric quantum dots on GaAs (001) substrate. *Applied Physics Letters*, 102(15):152105, 2013.

[38] Y Toda, O Moriwaki, M Nishioka, and Y Arakawa. Efficient carrier relaxation mechanism in InGaAs/GaAs self-assembled quantum dots based on the existence of continuum states. *Physical Review Letters*, 82(20):4114, 1999.

[39] T Miyazawa, K Takemoto, Y Nambu, S Miki, T Yamashita, H Terai, M Fujiwara, M Sasaki, Y Sakuma, M Takatsu, et al. Single-photon emission at 1.5 μ m from an InAs/InP quantum dot with highly suppressed multi-photon emission probabilities. *Applied Physics Letters*, 109(13):132106, 2016.

[40] A Malko, MH Baier, KF Karlsson, E Pelucchi, DY Oberli, and E Kapon. Optimization of the efficiency of single-photon sources based on quantum dots under optical excitation. *Applied physics letters*, 88(8):081905, 2006.

[41] Robert Heitz, Michael Veit, Nikolai N Ledentsov, Axel Hoffmann, Dieter Bimberg, Viktor M Ustinov, Petr Sergeevich Kop'ev, and Zh I Alferov. Energy relaxation by multiphonon processes in InAs/GaAs quantum dots. *Physical Review B*, 56(16):10435, 1997.

[42] Sonia Buckley, Kelley Rivoire, and Jelena Vučković. Engineered quantum dot single-photon sources. *Reports on Progress in Physics*, 75(12):126503, 2012.

[43] Zhiliang Yuan, Beata E Kardynal, R Mark Stevenson, Andrew J Shields, Charlene J Lobo, Ken Cooper, Neil S Beattie, David A Ritchie, and Michael Pepper. Electrically driven single-photon source. *science*, 295(5552):102–105, 2002.

[44] AJ Bennett, P Atkinson, P See, MB Ward, RM Stevenson, ZL Yuan, DC Unitt, DJP Ellis, K Cooper, DA Ritchie, et al. Single-photon-emitting diodes: a review. *Physica status solidi (b)*, 243(14):3730–3740, 2006.

[45] Alberto Boretti, Lorenzo Rosa, Andrew Mackie, and Stefania Castelletto. Electrically driven quantum light sources. *Advanced Optical Materials*, 3(8):1012–1033, 2015.

[46] Anthony J Bennett, Raj B Patel, Joanna Skiba-Szymanska, Christine A Nicoll, Ian Farrer, David A Ritchie, and Andrew J Shields. Giant Stark effect in the emission of single semiconductor quantum dots. *Applied Physics Letters*, 97(3):031104, 2010.

[47] M Bayer, G Ortner, O Stern, A Kuther, AA Gorbunov, A Forchel, Pawel Hawrylak, S Fafard, K Hinzer, TL Reinecke, et al. Fine structure of neutral and charged excitons in self-assembled In (Ga) As/(Al) GaAs quantum dots. *Physical Review B*, 65(19):195315, 2002.

[48] Stefan Seidl, Martin Kroner, Alexander Högele, Khaled Karrai, Richard J Warburton, Antonio Badolato, and Pierre M Petroff. Effect of uniaxial stress on excitons in a self-assembled quantum dot. *Applied Physics Letters*, 88(20):203113, 2006.

[49] S Varoutsis, S Laurent, P Kramper, A Lemaître, I Sagnes, I Robert-Philip, and I Abram. Restoration of photon indistinguishability in the emission of a semiconductor quantum dot. *Physical Review B*, 72(4):041303, 2005.

[50] Raúl J Martín Palma and Akhlesh Lakhtakia. Nanotechnology: a crash course. SPIE, 2010.

[51] Ivan Pelant and Jan Valenta. *Luminescence spectroscopy of semiconductors*. OUP Oxford, 2012.

[52] Massimo Gurioli, Zhiming Wang, Armando Rastelli, Takashi Kuroda, and Stefano Sanguinetti. Droplet epitaxy of semiconductor nanostructures for quantum photonic devices. *Nature materials*, 18(8):799–810, 2019.

[53] Mark Fox. Optical properties of solids, 2002.

[54] Blandine Alloing, Carl Zinoni, Val Zwiller, LH Li, Christelle Monat, M Gobet, G Buchs, Andrea Fiore, E Pelucchi, and E Kapon. Growth and characterization of single quantum dots emitting at 1300 nm. *Applied Physics Letters*, 86(10):101908, 2005.

[55] ES Semenova, R Hostein, G Patriarche, O Mauguin, L Largeau, I Robert-Philip, A Beveratos, and A Lemaître. Metamorphic approach to single quantum dot emission at 1.55 μ m on GaAs substrate. *Journal of Applied Physics*, 103(10):103533, 2008.

[56] Matthias Paul, Fabian Olbrich, Jonatan Höschele, Susanne Schreier, Jan Kettler, Simone Luca Portalupi, Michael Jetter, and Peter Michler. Single-photon emission at 1.55 μ m from MOVPE-grown InAs quantum dots on InGaAs/GaAs metamorphic buffers. *Applied Physics Letters*, 111(3):033102, 2017.

[57] Fabian Olbrich, Jonatan Höschele, Markus Müller, Jan Kettler, Simone Luca Portalupi, Matthias Paul, Michael Jetter, and Peter Michler. Polarization-entangled photons from an InGaAs-based quantum dot emitting in the telecom C-band. *Applied Physics Letters*, 111(13):133106, 2017.

[58] Katharina D Zeuner, Matthias Paul, Thomas Lettner, Carl Reuterskiöld Hedlund, Lucas Schweickert, Stephan Steinhauer, Lily Yang, Julien Zichi, Mattias Hammar, Klaus D Jöns, et al. A stable wavelength-tunable triggered source of single photons and cascaded photon pairs at the telecom C-band. *Applied Physics Letters*, 112(17):173102, 2018.

[59] Ming Gong, Kaimin Duan, Chuan-Feng Li, Rita Magri, Gustavo A Narvaez, and Lixin He. Electronic structure of self-assembled In As/ In P quantum dots: Comparison with self-assembled In As/ Ga As quantum dots. *Physical Review B*, 77(4):045326, 2008.

[60] JM Garcıa, L González, MU González, JP Silveira, Y González, and F Briones. InAs/InP (0 0 1) quantum wire formation due to anisotropic stress relaxation: in situ stress measurements. *Journal of crystal growth*, 227:975–979, 2001.

[61] G Sęk, P Podemski, A Musiał, J Misiewicz, S Hein, S Höfling, and A Forchel. Exciton and biexciton emission from a single InAs/InP quantum dash, 2009.

[62] Andrei Kors, Johann Peter Reithmaier, and Mohamed Benyoucef. Telecom wavelength single quantum dots with very small excitonic fine-structure splitting. *Applied Physics Letters*, 112(17):172102, 2018.

[63] Kazuya Takemoto, Yoshiki Sakuma, Shinichi Hirose, Tatsuya Usuki, and Naoki Yokoyama. Observation of Exciton Transition in 1.3–1.55 μm Band from Single InAs/InP Quantum Dots in Mesa Structure. *Japanese journal of applied physics*, 43(3A):L349, 2004.

[64] Toshiyuki Miyazawa, Kazuya Takemoto, Yoshiki Sakuma, Shinichi Hirose, Tatsuya Usuki, Naoki Yokoyama, Motomu Takatsu, and Yasuhiko Arakawa. Single-photon generation in the 1.55-μm optical-fiber band from an InAs/InP quantum dot. *Japanese Journal of Applied Physics*, 44(5L):L620, 2005.

[65] Toshiyuki Miyazawa, Shigekazu Okumura, Shinnichi Hirose, Kazuya Takemoto, Motomu Takatsu, Tatsuya Usuki, Naoki Yokoyama, and Yasuhiko Arakawa. First demonstration of electrically driven 1.55 μm single-photon generator. *Japanese journal of applied physics*, 47(4S):2880, 2008.

[66] Francesco Basso Basset, Sergio Bietti, Marcus Reindl, Luca Esposito, Alexey Fedorov, Daniel Huber, Armando Rastelli, Emiliano Bonera, Rinaldo Trotta, and Stefano Sanguinetti. High-yield fabrication of entangled photon emitters for hybrid quantum networking using high-temperature droplet epitaxy. *Nano letters*, 18(1):505–512, 2018.

[67] Joanna Skiba-Szymanska, R Mark Stevenson, Christiana Varnava, Martin Felle, Jan Huwer, Tina Müller, Anthony J Bennett, James P Lee, Ian Farrer, Andrey B Krysa, et al. Universal growth scheme for quantum dots with low fine-structure splitting at various emission wavelengths. *Physical Review Applied*, 8(1):014013, 2017.

[68] M Anderson, T Müller, J Skiba-Szymanska, AB Krysa, J Huwer, RM Stevenson, J Heffernan, DA Ritchie, and AJ Shields. Coherence in single photon emission from droplet epitaxy and Stranski–Krastanov quantum dots in the telecom C-band. *Applied Physics Letters*, 118(1):014003, 2021.

[69] T Müller, J Skiba-Szymanska, AB Krysa, J Huwer, M Felle, Matthew Anderson, RM Stevenson, J Heffernan, David Alastair Ritchie, and AJ Shields. A quantum light-emitting diode for the standard telecom window around 1,550 nm. *Nature communications*, 9(1):1–6, 2018.

[70] M Anderson, T Müller, J Huwer, J Skiba-Szymanska, AB Krysa, RM Stevenson, J Heffernan, DA Ritchie, and AJ Shields. Quantum teleportation using highly coherent emission from telecom C-band quantum dots. *npj Quantum Information*, 6(1):1–7, 2020.

[71] C Bentham, D Hallett, N Prtljaga, B Royall, D Vaitiekus, RJ Coles, E Clarke, AM Fox, MS Skolnick, IE Itskevich, et al. Single-photon electroluminescence for on-chip quantum networks. *Applied Physics Letters*, 109(16):161101, 2016.

[72] John D Joannopoulos, Pierre R Villeneuve, and Shanhui Fan. Photonic crystals. *Solid State Communications*, 102(2-3):165–173, 1997.

[73] Adil Karim, Joachim Piprek, Patrick Abraham, Dan Lofgreen, Yi-Jen Chiu, and John E Bowers. 1.55-/spl mu/m vertical-cavity laser arrays for wavelength-division multiplexing. *IEEE Journal of Selected Topics in Quantum Electronics*, 7(2):178–183, 2001.

[74] HW Dinges, H Burkhard, R Lösch, H Nickel, and W Schlapp. Refractive indices of InAlAs and InGaAs/InP from 250 to 1900 nm determined by spectroscopic ellipsometry. *Applied surface science*, 54:477–481, 1992.

[75] Tien-Chang Lu, JY Tsai, Hao-Chung Kuo, and SC Wang. Comparisons of InP/InGaAlAs and InAlAs/InGaAlAs distributed Bragg reflectors grown by metalorganic chemical vapor deposition. *Materials Science and Engineering: B*, 107(1):66–69, 2004.

[76] Martin Connor Patrick Felle. *Telecom Wavelength Quantum Devices*. PhD thesis, University of Cambridge, 2017.

[77] Steven G Johnson, Shanhui Fan, Pierre R Villeneuve, John D Joannopoulos, and LA Kolodziejski. Guided modes in photonic crystal slabs. *Physical Review B*, 60(8):5751, 1999.

[78] Dirk Englund, David Fattal, Edo Waks, Glenn Solomon, Bingyang Zhang, Toshihiro Nakaoka, Yasuhiko Arakawa, Yoshihisa Yamamoto, and Jelena Vučković. Controlling the spontaneous emission rate of single quantum dots in a two-dimensional photonic crystal. *Physical review letters*, 95(1):013904, 2005.

[79] Ginny Shooter, Zi-Heng Xiang, Jonathan RA Müller, Joanna Skiba-Szymanska, Jan Huwer, Jonathan Griffiths, Thomas Mitchell, Matthew Anderson, Tina Müller, Andrey B Krysa, et al. 1GHz clocked distribution of electrically generated entangled photon pairs. *Optics Express*, 28(24):36838–36848, 2020.

[80] M Kaniber, A Kress, A Laucht, M Bichler, R Meyer, M-C Amann, and JJ Finley. Efficient spatial redistribution of quantum dot spontaneous emission from two-dimensional photonic crystals. *Applied Physics Letters*, 91(6):061106, 2007.

[81] Mathieu Munsch, Alexis Mosset, Alexia Auffèves, Signe Seidelin, Jean-Philippe Poizat, J-M Gérard, A Lemaître, I Sagnes, and P Senellart. Continuous-wave versus time-resolved measurements of Purcell factors for quantum dots in semiconductor microcavities. *Physical Review B*, 80(11):115312, 2009.

[82] Momchil Minkov and Vincenzo Savona. Automated optimization of photonic crystal slab cavities. *Scientific reports*, 4(1):1–8, 2014.

[83] Feng Liu, Alistair J Brash, John O'Hara, Luis MPP Martins, Catherine L Phillips, Rikki J Coles, Benjamin Royall, Edmund Clarke, Christopher Bentham, Nikola Prtljaga, et al. High Purcell factor generation of indistinguishable on-chip single photons. *Nature nanotechnology*, 13(9):835–840, 2018.

[84] Pascale Senellart, Glenn Solomon, and Andrew White. High-performance semiconductor quantum-dot single-photon sources. *Nature nanotechnology*, 12(11):1026–1039, 2017.

[85] Luca Sapienza, Marcelo Davanço, Antonio Badolato, and Kartik Srinivasan. Nanoscale optical positioning of single quantum dots for bright and pure single-photon emission. *Nature communications*, 6(1):1–8, 2015.

[86] Antonio Badolato, Kevin Hennessy, Mete Atature, Jan Dreiser, Evelyn Hu, Pierre M Petroff, and Atac Imamoglu. Deterministic coupling of single quantum dots to single nanocavity modes. *Science*, 308(5725):1158–1161, 2005.

[87] Muhammad Danang Birowosuto, Hisashi Sumikura, Shinji Matsuo, Hideaki Taniyama, Peter J van Veldhoven, Richard Nötzel, and Masaya Notomi. Fast Purcell-enhanced single photon source in 1,550-nm telecom band from a resonant quantum dot-cavity coupling. *Scientific reports*, 2(1):1–5, 2012.

[88] A Kors, K Fuchs, M Yacob, JP Reithmaier, and M Benyoucef. Telecom wavelength emitting single quantum dots coupled to InP-based photonic crystal microcavities. *Applied Physics Letters*, 110(3):031101, 2017.

[89] Lucas Rickert, Bert Fritsch, Andrei Kors, Johann Peter Reithmaier, and Mohamed Benyoucef. Mode properties of telecom wavelength InP-based high-(Q/V) L4/3 photonic crystal cavities. *Nanotechnology*, 31(31):315703, 2020.

[90] Naoki Kobayashi and Yasuyuki Kobayashi. In situ control of heterointerface quality in MOVPE by surface photo-absorption. *Journal of crystal growth*, 124(1-4):525–530, 1992.

[91] FDTD Solutions. Lumerical Inc. *Suite*, 201:1290, 2019.

[92] GD Pettit and WJ Turner. Refractive index of InP. *Journal of Applied Physics*, 36(6):2081–2081, 1965.

[93] M Yacob, JP Reithmaier, and M Benyoucef. Low-density InP-based quantum dots emitting around the 1.5 μ m telecom wavelength range. *Applied Physics Letters*, 104(2):022113, 2014.

[94] Kazuya Takemoto, Motomu Takatsu, Shinichi Hirose, Naoki Yokoyama, Yoshiki Sakuma, Tatsuya Usuki, Toshiyuki Miyazawa, and Yasuhiko Arakawa. An optical horn structure for single-photon source using quantum dots at telecommunication wavelength. *Journal of applied physics*, 101(8):081720, 2007.

[95] Elisa Maddalena Sala, Young In Na, Max Godsland, Aristotelis Trapalis, and Jon Heffernan. InAs/InP quantum dots in etched pits by droplet epitaxy in metalorganic vapor phase epitaxy. *physica status solidi (RRL)–Rapid Research Letters*, 14(8):2000173, 2020.

[96] Paweł Holewa, Shima Kadkhodazadeh, Michał Gawełczyk, Paweł Baluta, Anna Musiał, Vladimir G Dubrovskii, Marcin Syperek, and Elizaveta Semenova. Droplet epitaxy symmetric InAs/InP quantum dots for quantum emission in the third telecom window: morphology, optical and electronic properties. *Nanophotonics*, 11(8):1515–1526, 2022.

[97] Samiul Hasan, Han Han, Maxim Korytov, Marianna Pantouvaki, Joris Van Campenhout, Clement Merckling, and Wilfried Vandervorst. InAlGaAs encapsulation of MOVPE-grown InAs quantum dots on InP (0 0 1) substrate. *Journal of Crystal Growth*, 531:125342, 2020.

[98] Elisa M Sala, Max Godsland, Aristotelis Trapalis, and Jon Heffernan. Effect of Cap Thickness on InAs/InP Quantum Dots Grown by Droplet Epitaxy in Metal–Organic Vapor Phase Epitaxy. *physica status solidi (RRL)–Rapid Research Letters*, 15(9):2100283, 2021.

[99] Giovanni Costantini, Armando Rastelli, Carlos Manzano, P Acosta-Diaz, Rudeeson Songmuang, Georgios Katsaros, Oliver G Schmidt, and Klaus Kern. Interplay between thermodynamics and kinetics in the capping of InAs/GaAs (001) quantum dots. *Physical review letters*, 96(22):226106, 2006.

[100] P Paki, R Leonelli, L Isnard, and RA Masut. Excitons in ultrathin InAs/InP quantum wells: Interplay between extended and localized states. *Journal of Vacuum Science & Technology A: Vacuum, Surfaces, and Films*, 18(3):956–959, 2000.

[101] Raja Sekhar Reddy Gajjela, Elisa Maddalena Sala, Jon Heffernan, and Paul M Koenraad. Control of Morphology and Substrate Etching in InAs/InP Droplet Epitaxy Quantum Dots for Single and Entangled Photon Emitters. *ACS Applied Nano Materials*, 2022.

[102] Elisa M Sala, Max Godsland, Young In Na, Aristotelis Trapalis, and Jon Heffernan. Droplet epitaxy of InAs/InP quantum dots via MOVPE by using an InGaAs interlayer. *Nanotechnology*, 33(6):065601, 2021.

[103] Heedon Hwang, Sukho Yoon, Hyeok Kwon, Euijoon Yoon, Hong-Seung Kim, Jeong Yong Lee, and Benjamin Cho. Shapes of InAs quantum dots on InGaAs/ InP. *Applied physics letters*, 85(26):6383–6385, 2004.

[104] Margaret A Stevens, Stephanie Tomasulo, Sergey Maximenko, Thomas E Vandervelde, and Michael K Yakes. Surface diffusion measurements of In on InGaAs enabled by droplet epitaxy. *Journal of Applied Physics*, 121(19):195302, 2017.

[105] PW Yu, BW Liang, and CW Tu. Deep center photoluminescence study of low-temperature InP grown by molecular beam epitaxy. *Applied physics letters*, 61(20):2443–2445, 1992.

[106] Raja SR Gajjela, Niels RS van Venrooij, Adonai R da Cruz, Joanna Skiba-Szymanska, R Mark Stevenson, Andrew J Shields, Craig E Pryor, and Paul M Koenraad. Study of Size, Shape, and Etch pit formation in InAs/InP Droplet Epitaxy Quantum Dots. *Nanotechnology*, 33(30):305705, 2022.

[107] RJ Coles, N Prtljaga, B Royall, Isaac John Luxmoore, AM Fox, and MS Skolnick. Waveguide-coupled photonic crystal cavity for quantum dot spin readout. *Optics express*, 22(3):2376–2385, 2014.

[108] Se-Heon Kim, Sun-Kyung Kim, and Yong-Hee Lee. Vertical beaming of wavelength-scale photonic crystal resonators. *Physical Review B*, 73(23):235117, 2006.

[109] Yoshihiro Akahane, Takashi Asano, Bong-Shik Song, and Susumu Noda. High-Q photonic nanocavity in a two-dimensional photonic crystal. *nature*, 425(6961):944–947, 2003.

[110] Sean L Rommel, Jae-Hyung Jang, Wu Lu, Gabriel Cueva, Ling Zhou, Ilesanmi Adesida, Gary Pajer, Ralph Whaley, Allen Lepore, Zane Schellanbarger, et al. Effect of H 2 on the etch profile of InP/InGaAsP alloys in Cl 2/Ar/H 2 inductively coupled plasma reactive ion etching chemistries for photonic device fabrication. *Journal of Vacuum Science & Technology B: Microelectronics and Nanometer Structures Processing, Measurement, and Phenomena*, 20(4):1327–1330, 2002.

[111] Ruggero Loi, James O'Callaghan, Brendan Roycroft, Cedric Robert, Alin Fecioru, Antonio Jose Trindade, Agnieszka Gocalinska, Emanuele Pelucchi, Christopher A Bower, and Brian Corbett. Transfer printing of AlGaInAs/InP etched facet lasers to Si substrates. *IEEE Photonics Journal*, 8(6):1–10, 2016.

[112] IJ Luxmoore, E Daghigh Ahmadi, BJ Luxmoore, NA Wasley, AI Tartakovskii, M Hugues, MS Skolnick, and AM Fox. Restoring mode degeneracy in H1 photonic crystal cavities by uniaxial strain tuning. *Applied Physics Letters*, 100(12):121116, 2012.

[113] Andrei Kors. *InP-based quantum dots for telecom wavelengths ranges*. PhD thesis, 2019.

[114] James O'Callaghan, Ruggero Loi, Enrica E Mura, Brendan Roycroft, António José Trindade, K Thomas, A Gocalinska, Emanuele Pelucchi, Jing Zhang, Günther Roelkens, et al. Comparison of InGaAs and InAlAs sacrificial layers for release of InP-based devices. *Optical Materials Express*, 7(12):4408–4414, 2017.

[115] Putu Pramudita, Hoon Jang, Indra Karnadi, Hwi-Min Kim, and Yong-Hee Lee. Self-aligned nanoislands nanobeam bandedge lasers. *Optics Express*, 25(6):6311–6319, 2017.

[116] P Abraham, MA Garcia Perez, T Benyattou, G Guillot, M Sacilotti, and X Letartre. Photoluminescence and band offsets of AlInAs/InP. *Semiconductor science and technology*, 10(12):1585, 1995.

[117] M Sacilotti, P Abraham, M Pitaval, M Ambri, T Benyattou, A Tabata, MA Garcia Perez, P Motisuke, R Landers, J Morais, et al. Structural and optical properties of AlInAs/InP and GaPSb/InP type II interfaces. *Canadian journal of physics*, 74(5-6):202–208, 1996.

[118] Leonard J Brillson. *An essential guide to electronic material surfaces and interfaces*. John Wiley & Sons, 2016.

[119] Jin Liu, Kumarasiri Konthasinghe, Marcelo Davanço, John Lawall, Vikas Anant, Varun Verma, Richard Mirin, Sae Woo Nam, Jin Dong Song, Ben Ma, et al. Single self-assembled InAs/GaAs quantum dots in photonic nanostructures: The role of nanofabrication. *Physical review applied*, 9(6):064019, 2018.

[120] Abhiroop Chellu, Eero Koivusalo, Marianna Raappana, Sanna Ranta, Ville Polojärvi, Antti Tukiainen, Kimmo Lahtonen, Jesse Saari, Mika Valden, Heli Seppänen, et al. GaAs surface passivation for InAs/GaAs quantum dot based nanophotonic devices. *Nanotechnology*, 32(13):130001, 2021.

[121] LE Black, A Cavalli, MA Verheijen, JEM Haverkort, EPAM Bakkers, and WMM Kessels. Effective surface passivation of InP nanowires by atomic-layer-deposited Al2O3 with PO x interlayer. *Nano letters*, 17(10):6287–6294, 2017.

[122] S Gordon, M Yacob, JP Reithmaier, M Benyoucef, and Artur Zrenner. Coherent photocurrent spectroscopy of single InP-based quantum dots in the telecom band at 1.5 μm. *Applied Physics B*, 122(2):1–7, 2016.

[123] Young In Na. *Growth and characterisation of site-controlled InAs/InP quantum dots by droplet epitaxy in MOVPE*. PhD thesis, University of Sheffield, 2021.